Neuronal Organization of the Olfactory Bulb in Adult Zebrafish

Inauguraldissertation

zur

Erlangung der Würde eines Doktors der Philosophie

vorgelegt der

Philosophisch-Naturwissenschaftlichen Fakultät

der Universität Basel von

Nila Rebecca Mönig

aus Riedlingen, Deutschland

Basel, 2024

Genehmigt von der Philosophisch-Naturwissenschaftlichen Fakultät

auf Antrag von

Prof. Dr. Rainer Friedrich

(Fakultätsverantwortlicher und Dissertationsleiter)

Prof. Dr. Stephan Neuhauss

(Korreferent)

Basel, den 26.4.2022

Prof. Dr. Marcel Mayor

Dekan

Für Miu, Noko & Finja

Möge eure Reise voller Neugier, Wunder und Freude sein!

„So kommt es, dass die meisten Menschen gar nicht wissen, wie schön die Welt ist und wie viel Pracht in den kleinsten Dingen, in irgendeiner Blume, einem Stein, einer Baumrinde oder einem Birkenblatt sich offenbart. [...] Es geht eine große und ewige Schönheit durch die ganze Welt, und diese ist gerecht über die kleinen und großen Dinge verstreut."

Rainer Maria Rilke, im Brief an Helmuth Westhoff, 12. November 1901

"[...] We followed the dreamer through the purple hazy clouds

He could control our sense of time

We thought we were lost but no matter how we tried

Everyone was in peace of mind [...]"

Judas Priest, „Dreamer Deceiver", *Sad Wings of Destiny*, Gull Records, 23 March 1976

Acknowledgements

Gratitude is an emotion so complex and strong that it can but lose by the concreteness of words. Hence, I struggled finding the right ones and the following should be considered a mere attempt.

First of all, I would like to thank those that made this study possible for their advice and support, that is the members of my thesis committee, Stephan Neuhauss, Andreas Lüthi, and above all my thesis advisor Rainer Friedrich, who has given the word "Doktorvater" true justice. I want to thank Rainer for his guidance, for sharing his seemingly endless knowledge with me and for opening my eyes to different perspectives and approaches that make the complex simple. I would like to thank him for his untouchable optimism and having an open ear (and usually a practical solution) to all sorts of problems. Above all, I am grateful that Rainer gave to me most generously one of the most precious things humans can exchange – trust!

One of the upsides of a longish PHD is, one gets to spend more time with the fascinating fellow scientists. I have grown a lot in my time at FMI thanks to all current and past members of the Friedrich group. It has been a stimulating and enriching experience to work alongside and with these creative, knowledgeable, and keen-minded people from so many different fields and backgrounds. And it has been a particular pleasure and privilege to work and exchange with so many fellow female scientists from all over the world. Sharing their experiences with me has expanded my horizon. Thank you!
I highly appreciate the pleasant, supportive, attentive, and accepting environment within the Friedrich group. Especially the members joining in the past few years, Bo Hu, Nesibe Temiz-Karayol, Claire Meissner-Bernard, Kim Palacios-Flores, Tommaso Caudullo, Jan Eckhardt, Ruth E. Montaño Crespo, Lukas Anneser, Alexandre Javier and Tomáš Gancarčik have brought rejuvenating enthusiasm and liveliness to the lab. Thank you for all the laughs, for normalizing long decision processes – and of course - the good coffee!
I want to extend my gratitude to some of the lab members in particular. I would like to thank Iori Namekawa, Thomas Frank and Chie Satou for the instructive, productive, and efficient collaboration building and setting up the odor discrimination training and proving its worth using it to explore Dp function. Special thanks go to Gilad Jacobson for mentoring me during my first step at FMI. I greatly enjoyed the weekly discussions with Bo Hu, Nesibe Temiz-Karayol, Rainer Friedrich and Ruth E. Montaño Crespo in our Tuesday meeting. Them, I also want to thank them for their patient and diligent work as "human classifier" of bulbar neuron types. I would like to thank Stephan Gerhard and Benjamin Titze for their help and input in the connectomics project and plentiful of contemplative conversations. Many thanks to Kathi Steuer and Ruth E. Montaño Crespo for being my "guinea pigs" with the agglomeration proofreading tool and their help with the reconstructions. Further, I want to thank Martin Nägeli for keeping the fish facility in order and up and running. Thanks to Jan Eckhardt for his immediate response to all those small questions and requests and all those nice chats. I would

like to thank Estelle Bouldoires-Arn for keeping the lab in check, for making the plants next to my desk blossom and for her attentive care for every single person in the lab! I am grateful to Adrian Wanner,

whose work has been crucial for establishing connectomics in the Friedrich lab and who continues to help me out, whenever I have questions or need help. It has been truly inspiring and compelling for me to witness his work and progress in the Friedrich Lab. The same holds for Peter Rupprecht. It was a real pleasure to work alongside him, and I am very grateful for his deliberate advice and feedback. Peter's help and support continues way beyond our time together at FMI. And then, I want to thank Anastasios Moressis, my brother from another mother, for dirty jokes and sarcasm, emotionally and mentally anti-correlating to me and just everything!

I am deeply grateful to Markus Rempfler for most patiently teaching me some fundamental principles of programming, for making me comfortable to ask any question, even a second time and for letting me experience and appreciate how beautiful well-written code can be. Without his help I might not have been able to create the agglomeration proofreading tool. I want to thank Christel Genoud for many enriching chats, her (moral) support and for being a role model in leadership. Further, I am very grateful to numerous members of the FMI core facilities, who have assisted me many times during my PHD, in particular Jan Eglinger, Alan Naylor, Stefan Grzybek, Sjoerd van Eeden, Enrico Tagliavini, Thierry Vioget & Thomas Nyffenegger. I also would like to thank Paul Argast for his excellent work and his creative support in building the behavior setup. Many thanks to Elida Keller and Jitka Steuer for all the help and support with administration. Finally, I am deeply grateful to Piera Cicchetti, whose guidance and mentorship has been crucial to the successful completion of my PHD.

It is impossible to put in words the sentiment when, after more than one year of manual skeleton tracing in an EM volume, one has the opportunity to see the volumetric rendering of a reconstructed neuron for the very first time! It is truly overwhelming! The collaboration with the Connectomics team at Google has been a real stroke of luck for me. Foremost, I want to thank Michał Januszewski for his excellent work on the segmentation, for his swift and continuous help and support and for patient explanations and guiding me on this unknown territory of working with segmentation data. My gratitude and respect go to Jeremy Maitin-Shepherd for the creation and maintenance of *neuroglancer*, for near instantaneous bug fixes and realization of feature requests and in particular for all elaborate explanations and ideas the helped me use *neuroglancer* for my purposes. Similarly, I want to thank Tim Blakely and Laramie Lewitt for their support in using the *Brainmaps API*. These four people have enabled me to do things I literally did not know were possible. Thank you!

I want to thank Anna Boss for shining like the sun in my life and for a friendship that defies time and space. I would like to thank Ewelina Bartoszek-Kandler and Steffen Kandler for their friendship, for opening up their home to me and feeding me.

I want to thank my mother, Marianne Phan-Mönig, who raised me to believe that there is nothing I cannot do, if I only set my mind to it. By her example I learned the perseverance, pragmatism, and stubbornness to realize this. Most of all I want to thank her for opening my eyes to the beauty of nature and teaching me appreciation of the little things in life. I want to thank my father Ulrich Mönig for

being living proof that it is never too late, that there is always a second chance and importantly, for introducing me to the Blues. And I want to thank his wife, Anne Mees, for being there for him.

I would like to thank my brothers Minh Phan and Julian Mönig for loving me just and exactly the way I am, and most of all for making me laugh. They and my sister(-in-law), Ana Bravo-Ferrer Acosta, I want to thank for always having my back and supporting me. I would like to thank Walter and Christel Bätz for taking me into their family and being like parents to me. I want to thank Florian Bätz for becoming a partner and ally in raising our progeny and one of my best friends. I greatly appreciate all his help and advice in programming, formatting, and other aesthetic emergencies.

Finally, I want to thank the three undoubtfully most beautiful, most lovable, funniest, and weirdest human beings to roam this earth, Finja, Miu and Noko Mönig! You make me laugh and cry! You make me feel so old and turn me into a child! You ground me, you make me dream, you unleash unbelievable powers in me! You are my love, my life, my world, my everything!

TABLE OF CONTENTS

1. PREFACE

From an evolutionary perspective the brain can be considered as an organ that serves to control the state of an organism within its environment [1]. Through selective pressure that optimizes the interaction of organisms with their particular environment, a rich diversity of nervous systems has evolved across the Eumetazoa [2]. These nervous systems vary in structure, complexity, versatility, and – particularly noteworthy for their potential to broaden an organism's behavioral spectrum, and thus the ability to adapt to various and varying environments – neuronal plasticity. Evolution can act through modifications of the nervous system on different levels. These adaptations may occur as alterations on the molecular level (e.g., odorant receptors [3, 4]), at the ultrastructural level as specializations of neuronal subcompartments (e.g., the specialization of apical and basal dendrites in pyramidal neurons [5, 6]), and through the emergence of novel neuron types up to transformations affecting the brain architecture. The impact of these adaptations unfolds on the behavioral level, changing the potential to control the organisms state or interact with the environment. Notably, complex cognitive behaviors have emerged from fundamentally different brain structures in different taxa such as cephalopods, birds, and primates [7, 8]. Conversely, similar circuits can be due to a similar solution, optimized to meet common environmental and functional demands imposed onto diverse organisms, rather than a common origin.

The olfactory system of invertebrates and vertebrates is such a case of convergent evolution [9, 3, 10]. In arthropods, fish and mammals, similar principles have been identified with respect to the expression and turnover of odorant receptors in olfactory sensory neurons (OSNs) and the morphology of OSNs. Likewise, OSN projections show an equivalent organization into glomeruli within the respective first olfactory relay centers, the antennal or olfactory lobe of insects and crustaceans, respectively, or the olfactory bulb (OB) in vertebrates. These centers exhibit a comparable neuronal circuit organization and have been shown to perform the same types of computations and transformations on their inputs [3, 10]. Odorants carry diverse information vital for an organism's survival and species continuity: Odors help locating and identifying desirable objects, like food, mating partners, home territory or mating grounds and can warn of dangers, e.g., predators, fire, inedible foods, etc. Moreover, odorants represent an important means for communication with conspecifics, they can signal e.g., territorial boundaries, kinship, hierarchy, and many more. Whether airborne or aquatic, these odorants are usually complex mixtures of multiple different molecules and little variation in composition can alter identity and meaning of the signal. The challenge of correctly parsing these complicated, but crucial signals in order to execute the appropriate behavioral response is comparable for all species, which may be the reason for the organizational similarity of the olfactory system across taxa.

1. PREFACE

The work presented here focuses on evolution's substrate and objective in an olfactory system, namely the neuroanatomy of the olfactory bulb and olfactory behavior in adult zebrafish.

Section 2 covers the neuroanatomical part of this thesis, a comprehensive study of neuronal diversity in the OB of adult zebrafish. Single neuron reconstructions from the same animal are based on volumetric neurite segmentation in an EM volume. I developed a software tool to proofread this segmentation and reconstructed more than 200 neurons from all layers of OB. Based on these reconstructions, I extracted a detailed description of neuron morphology and defined neuron classes based upon this analysis. Further, I provide a qualitative investigation of the connectivity between defined interneuron classes and principal neurons in adult zebrafish OB.

The second project of my thesis is described in section 3. This study aimed at providing a tool which permits neuroscientists to functionally explore components of the olfactory system in adult zebrafish by means of a reproducible and scalable behavioral assay. I developed an olfactory discrimination paradigm for adult zebrafish in collaboration with Iori Namekawa. This study has been published with equal contribution first authorship [11]. I contributed to the design of the behavioral setup and developed the software and apparatus for automating the stimulation procedure, which allowed to scale up the number of animals per training. Further, I developed and optimized the discrimination training and control procedures, trained more than 85% of fish, determined the optimal set of behavioral features, analyzed all behavioral data and together with Rainer Friedrich developed a behavioral population score. Iori Namekawa designed the training apparatus, designed, and developed the software for movie recording, offline fish tracking and feature extraction and trained the remaining fish. Rainer Friedrich wrote the manuscript with minor contributions from the other authors.
This olfactory discrimination paradigm has been used in a study led by Thomas Frank, who showed that a major target of the OB contains a low-dimensional representations of odor valence that can be modified by conditioning and relies on inhibition [12]. I trained fish for this study together with Chie Satou and analyzed all behavioral data. I am a co-author of this publication, but I did not include it in my thesis because the main contribution to the study was made by Thomas Frank.

2. ANATOMY OF THE ZEBRAFISH OB

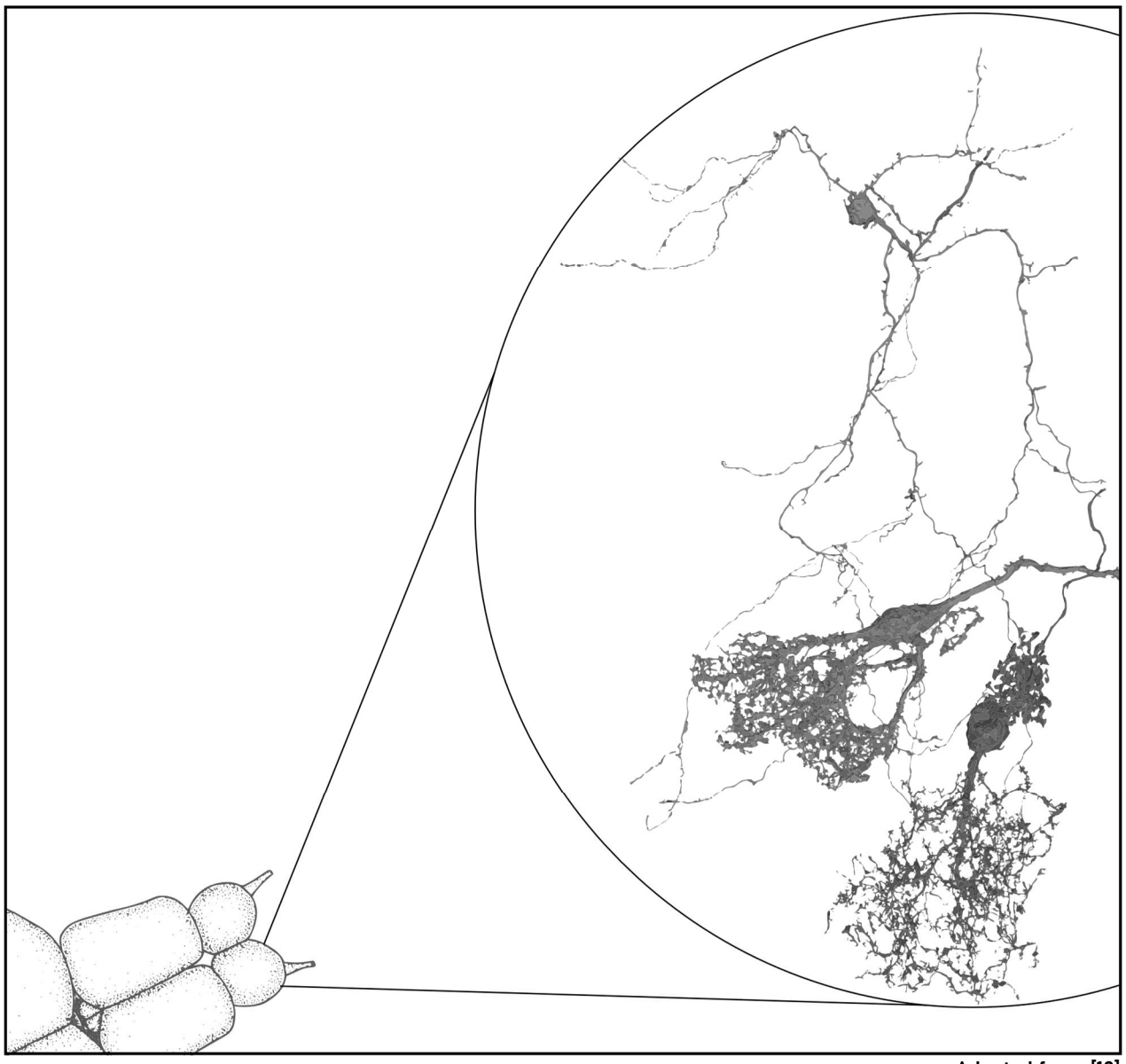

Adapted from [13]

2.1 INTRODUCTION

This section reviews the current understanding of the anatomical organization of olfactory bulb and its functional role in olfactory processing. It introduces volumetric EM reconstruction, a recent technique for neuroanatomical and circuit investigation and motivates its use in the investigation of the neuronal diversity in the adult zebrafish olfactory bulb.

2.1.1 REQUIREMENTS ON EARLY SENSORY PROCESSING

In a natural environment, information that is vital for survival can be encountered in a variety of different contexts, can be localized to varying degrees and may be experienced across a wide range of intensities. A fundamental task of early sensory processing is to detect this information and to find representations of sensory stimuli that facilitate fast and reliable processing. In olfaction, due to the complex and high dimensional nature of odorants this task is intriguingly challenging.

In vertebrates, odorants are sensed in the peripheral olfactory epithelium (OE), where individual odorant molecules bind to receptors of the primary sensory neurons. Each olfactory sensory neuron (OSN) expresses only a single type of olfactory receptor (OLFR) (rule of "*one sensory neuron-one receptor*"). OSNs expressing a particular OLFR project their axons in bundles to the olfactory bulb (OB), where they expand, and form defined globular structures called glomeruli (rule of "*one glomerulus-one receptor*") [14, 15]. Here, synapses with principal neurons (PNs) and interneurons (INs) of the OB are formed. Individual odorant molecules bind to a variety of odorant receptors with different affinities, thus exciting multiple different types of OSNs to varying degrees. In consequence, even a single molecule odor can stimulate numerous glomeruli in OB and with increasing concentration more and more glomeruli are activated [16, 17, 18]. Furthermore, similar odor molecules show an overlapping spectrum of affinities to odorant receptors. Thus, information about the olfactory environment arrives as a complex pattern of glomerular activation in OB, which in turn depends on both odor identity and intensity.

The neural circuit of OB has been described to make several transformations of this input: 1. Despite notable changes in glomerular activation, both the distribution and pattern of activated OB projection neurons (PNs) remains stable across a wide range of odor concentrations [19, 20, 21, 22], which is consistent with perceptual concentration invariance observed behaviorally [23, 24]. 2. Similar odors evoke initially highly correlated activity patterns in PNs, which decorrelate rapidly after stimulus onset such that representations of individual odors become more distinct [25, 26, 27, 28]. Experience and training enhance this pattern decorrelation [29, 30]. 3. The representation of mixtures by PNs reflects a nonlinear combination of the response pattern to individual components [31, 19]. Together, these input transformations result in an odor representation that is optimized for odor identification, associational and memory tasks, which are supposedly mediated by the cortical downstream targets of OB [32, 33, 34, 35]. A central role in performing the underlying computations has been attributed to local INs of OB, both theoretically and experimentally [36, 37, 38, 39, 20, 40, 21, 27, 28].

2.1.2 ORGANIZATION OF THE VERTEBRATE OB

The olfactory system is a phylogenetically old system and is well conserved across a wide range of species. However, notable differences are apparent in the repertoire of OLFR genes: While rodents possess > 1200 genes, dogs have ~ 800, humans ~ 400 and zebrafish ~ 200 - 300 OFR genes [4, 41]. In the OE, OSN position is organized along a dorsoventral axis correlating with the glomerular projection site in OB [42]. The rodent OE contains 5 Mio OSNs [43], which converge onto ~ 1800 - 2400 glomeruli in OB resulting in approximately 1 – 2 glomeruli per OLF type [44, 45]. Adult zebrafish OB has ~ 140 glomeruli, but the loose organization of OSN axons in the ventrolateral portion of OB complicates a precise count in the latter [46].

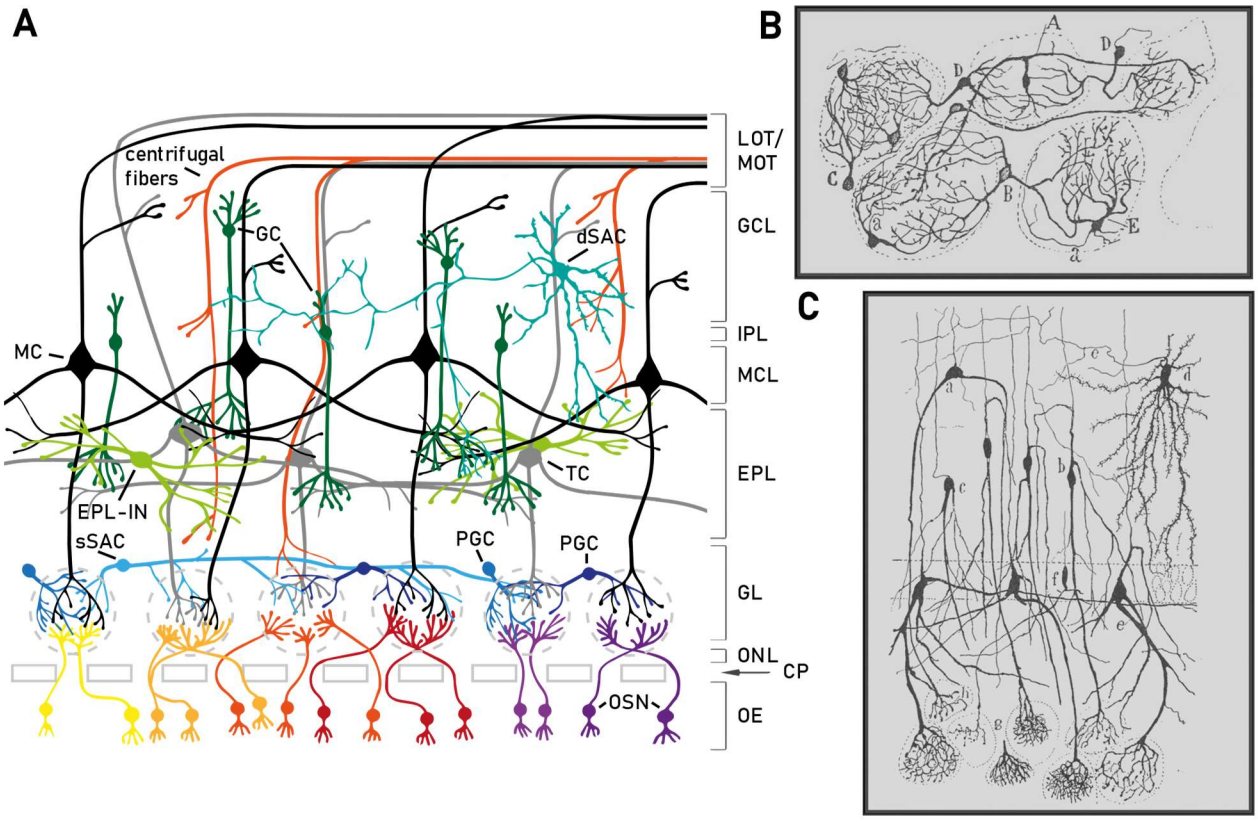

Figure 1. Architecture and neuron diversity of mammalian OB. A: Scheme of the mammalian olfactory bulb, ETCs are not shown (adapted from [47]). B. INs of GL: Mono- and multiglomerular PGCs in a one-month-old cat. Both axonal and axonless INs can be seen. Drawing by T. Blanes, from [48]. C. Neurons of the OB of a 20-day-old cat: Several MCs and TCs (a-c, e, f) expanding their primary dendrite in individual glomeruli (bottom) can be seen. The IN of the deep layer (d) is likely to be a dSAC. Drawing by T. Blanes from [48]. Abbreviations: CP: cibriform plate, dSAC: deep short axon cell, EPL: external plexiform layer, EPL-IN: interneuron of EPL, GC: granule cell, GCL: granule cell layer, GL: glomerular layer, IPL: internal plexiform layer, LOT: lateral olfactory tract, MC: mitral cell, MCL: mitral cell layer, MOT: medial olfactory tract, OE: olfactory epithelium, ONL: olfactory nerve layer, OSN: olfactory sensory neuron, PGC: periglomerular cell, sSAC: superficial short axon cell, TC: tufted cell

The mammalian OB can be divided into six layers (fig. 1). The superficial most, the olfactory nerve layer (ONL) contains the OSN axons and no neurons. The periglomerular region of the glomerular layer (GL) contains somata of cells projecting into glomeruli and short-axon cell (SAC) dendrites. It is

the primary target of all non-sensory, axonal projections to GL. The latter originate locally from tufted cells (TCs), superficial and deep SACs and periglomerular cells (PGCs) and remotely from centrifugal fibers [49]. Within a glomerulus OSN axons synapse onto neurons of the local OB circuit. The mammalian PNs, the mitral (MCs) and TCs, project their tufty primary dendrite into a single glomerulus. Three heterogenous classes of INs in GL have been reported: external tufted cells (ETCs), PGCs and superficial SACs (sSACs). ETCs are monoglomerular, glutamatergic INs that are a major source of excitation and synchrony within a glomerulus by providing input through synapses and gap junctions to PGCs, sSACs, MCs, TCs and other ETCs [50, 51, 52, 53]. Different subgroups of ETCs have been described based on physiological and morphological properties [54, 53]. Representing the most abundant GL neuron, PGCs are small GABAergic INs, which innervate a single or very few glomeruli [55] and have a broader odor tuning than MCs/TCs [56]. PGCs comprise several subtypes, which differ in their primary input source: OSN driven PGCs (~ 20%), which may co-express dopamine (DA) [57], and ETC driven PGCs (~ 80%), which further subdivide into calretinin$^+$ and calbindin$^+$ PGCs. The latter connect with all excitatory neurons of a glomerulus and have been shown to provide strong recurrent inhibition within a glomerulus [58]. PGCs are considered the main source of inhibition in GL, receive centrifugal input, and can mediate presynaptic inhibition of homotypic OSN axons [59]. The term sSAC has been used to describe large INs in the periglomerular region of GL which participate in interglomerular connections [60, 61, 55, 62]. This group is morphologically and molecularly very heterogeneous and a coherent definition is still lacking [63, 62]. The majority of sSACs is ETC driven, but some receive direct OSN input [59]. Oligo- (< 10 innervated glomeruli) and polyglomerular (10 - 50) sSACs co-expressing GABA and DA have been described [55]. These INs mediate concentration invariance in rodents [21] and fish [20] by boosting weak responses at low concentrations through gap junction coupling and by inhibiting strong responses at high concentration through chemical synapses, thereby stabilizing the mean and equalizing the variance of the PN output pattern across a wide range of concentrations [20, 21].

The secondary dendrites of MCs and TCs stretch far through the neuropil-rich external plexiform layer (EPL), where they form reciprocal synapses with the gemmules of granule cells (GCs) [64, 65]. In addition, EPL contains the somata of TCs, descending axon collaterals of MCs and a heterogeneous group of INs, which are not well investigated. These are subdivided into internal SACs and axonless INs of the EPL (EPL-IN) [59]. EPL is bounded by the mitral cell layer (MCL), which is densely packed with the somata of MCs and some TCs. MCs and TCs differ in response properties and the projections targets [66, 63, 67]. Whereas projections of MCs extend throughout the olfactory cortex, TCs projections are limited to the anterior portions, namely the anterior olfactory nucleus (AON) and the olfactory tubercle (OT). Further subdivisions of MCs and TCs are based on their position along the superficial-deep axis, which appears to correlate with the subtype of GCs they connect to [67]. A subgroup of EPL-INs spreads widely through EPL and connects reciprocally with a multitude of MCs and TCs which are associated with different glomeruli [68, 69]. These EPL-INs are broadly tuned, provide divisive inhibition to MCs and are considered important for gain control [70].

The internal plexiform layer (IPL) is a thin layer which contains mostly myelinated axons but also

somata and dendrites of the GL targeting deep SACs (GL-dSAC). Their axons project to GL, where they extend widely and branch heavily, traversing several glomeruli [71]. Receiving convergent input from ETCs and cholinergic centrifugal input, they strongly inhibit PGCs, ETCs and TCs [72].
The central GC layer (GCL) is predominantly occupied by GCs, which represent the by far largest group of bulbar INs, and also contain two further types of deep SACs (dSACs), the EPL targeting dSAC (EPL-dSAC) and the GCL targeting dSAC (GCL-dSAC) [71]. Both EPL-dSACs and GCL-dSACs broadly inhibit GCs, each innervating up to 10^3 GCs with 12-30 synapses [73]. They do not appear to innervate MCs and TCs [71, 73], and have been proposed to serve to disinhibit PNs [59]. GCs can be identified by a compact, thin spiny proximal dendrite and a single, spiny, primary dendrite that projects to EPL. In EPL, the primary dendrite branches into a tuft and forms large spines, the gemmules, which make reciprocal synaptic connections with MCs and TCs [74, 75]. GCs emerge during postnatal development and are, like many other OB INs, continuously added throughout adulthood [76]. A broad spectrum of morphological phenotypes has been described for GCs, e.g., several different types of GCs have been identified based on the position and extent along the superficial-deep axis as well as on the section of the EPL to which they project their primary dendrite [63]. GCs receive strong centrifugal input [77] and there is evidence suggesting that they are involved in pattern decorrelation and support odor discrimination in difficult tasks [78, 27].

The architecture of the teleost OB is very similar to the mammalian OB but layers are less distinct. Similar to mammals, teleost OSN axons rarely branch [79] and project from OE to the outer ONL in OB. Besides ONL teleost OB comprises three layers, the glomerular layer (GL), the plexiform layer (PL) and the granule cell layer (GCL) [80, 81, 82]. Next to the glomeruli in which sensory axons terminate, GL contains the somata of MCs, ruffed cells (RCs), the second PN of teleosts, and small GABAergic INs, some of which co-express DA [82, 83]. In contrast, to mammalian MCs, teleost MCs do not make secondary dendrites, but give rise to one or possibly more primary dendrites forming tufty branches that immerse into one or possibly multiple glomeruli [84, 85, 81, 86]. The classification of neurons in OB is less advanced in teleosts than in mammals. In goldfish, two IN types located in GL have been described morphologically [87]: The perinest cell (PNC) is a small IN closely associated with the neuropil surrounding the RC ruff. The mixed synapse cell (MSC) receives MC input onto cup-shaped appendages; these synapses are often associated with gap junctions [87]. The inner PL is a neuropil rich layer with few cell bodies. The central GCL is densely packed with small somata of GABAergic neurons [81, 88], and contains somata of presumed SACs [80].

2.1.3 UNCHARTED NEURONAL DIVERSITY IN ZEBRAFISH OB

Diverse evidence suggests that information processing in the OB exhibits many similarities in mammals and fish. As mentioned above, equivalent computations that critically depend on IN activity,

namely equalization of OB output and decorrelation of sensory input are performed in both zebrafish and rodent OB [25, 37, 27], mediated by presumably homologous IN types [20, 21]. Furthermore, the systems match in architecture and organization (see above). The adult zebrafish has been estimated to contain 20,000 – 30,000 INs [38] and 1500 MCs [89], thus INs outnumber PNs ~ 15 – 20 fold, a ratio similar to the mammalian bulb (~1.3 Mio INs : 50,000 PNs, ~26:1 reported in [59]). Apart from the GABAergic/DAergic sSACs [20] no other homologies to mammalian INs have yet been established. Histological and molecular studies suggest a rich variety of IN types in the OB of zebrafish [82, 83]. Yet, precise information about the diversity of neuron types in zebrafish OB is lacking.
In mammalian OB, most IN classes are heterogeneous and contain both axon-bearing and axonless subtypes. The axonless INs, e.g., subtypes of PGCs, EPL-INs or GCs, usually make reciprocal synapses with PNs. Early correlative light and electron microscopy studies of the anatomy of teleost OB considered all INs with reciprocal connections to MCs to be GC homologues [87, 81]. About 32% of the synapses of MCs in adult zebrafish are reciprocal [90]. However, it has not been determined whether these synapses originate from a homogeneous class of INs. Further, the densely packed GABAergic INs in zebrafish GCL are commonly considered homologues of the mammalian GCs [91], but this assertion is not well substantiated. Therefore, the diversity of INs in GCL of zebrafish remains largely unexplored.

In mammalian OB the secondary dendrites of MCs and TCs extend over long distances in EPL allowing widely distributed activation of GCs. As multiple MCs converge on a single GC, this anatomical organization has been considered a scaffold for lateral inhibition between distant MCs through a disynaptic motif mediated by GCs [92]. The morphology of teleost MCs differs markedly from mammalian MCs: They form a globular, tufty primary dendrite covering a glomerulus, but they do not make secondary dendrites [85, 81]. This localized dendritic organization raises the question whether a similar scheme of disynaptic reciprocal inhibition between remote MCs is realized in teleosts.

Computations like the pattern decorrelation observed in OB can be implemented on different circuits [40]. In larval OB three classes of INs have been described. At this developmental stage deep layer INs are still lacking and PNs outnumber INs 3:1 [93, 28]. Despite this stark difference in basic circuit organization, the larval zebrafish bulb shares computational functions with the adult OB. Here, decorrelation of OSN input and equalization of pattern variance has been shown to depend on a specific scheme of disynaptic reciprocal inhibition between similarly tuned MCs [28]. To appreciate how certain computations arise from a specific circuit, it is vital to know and understand both the individual components and their interaction. Comparing and understanding the differences between larval and adult OB, more specifically the function of deep layer INs, absent in larvae, as opposed to the superficial INs, first requires a detailed inventory of the neuron diversity in the adult.

Ruffed cells (RCs) seem to be unique to teleosts. They have been reported to represent about 5% of PNs in zebrafish OB [94] are not expected to receive sensory input and make many reciprocal synapses at their ruff [95, 94]. Beyond that, little is known about how this cell type is distributed in OB, about the input received by RCs or about how this cell type is embedded in the OB circuit.

2.1.4 FROM STRUCTURE TO FUNCTION

Since its beginning, neuroanatomic research, founded on the principles of observation and description, has provided the basis for functional insight. Already the earliest neuroanatomists remembered today, Herophilus of Chalcedon and Erasistratus, considered the brain the seat of intellect, distinguished sensory and motor nerves and derived the relationship between nerve signaling and muscle contraction as bequeathed by Galen of Pergamon [96]. The works of Andries van Wesel (1543), who explored and illustrated nervous system, and the full description of whole brain anatomy by Félix Vicq d'Azyr (1786) grace anatomical literature to date [97]. It was only with the discovery of neurons varying in appearance in different brain region by Jan E. Purkyně (1839) and the discovery of the Golgi stain (1873), that more detailed descriptions and understanding of neuronal networks began to emerge. The arguably most impressive example of determining function from structure in neuroscience is the Spanish neuroanatomist Santiago Ramón y Cajal (1852 - 1934). From rigorous and exhaustive description and critical observation of neuronal circuits across various brain regions and species, Cajal concluded, that neurons are discrete anatomical and functional units (*Neuron Doctrine*). He further deduced the direction of the activity flow within a neuron from the anatomical separation of dendrite, soma and axon (*Law of Dynamic Polarization*), identified dendritic spines, described aspects of structural neuronal plasticity in his *Neurotropic Theory*, and he proposed a canonical circuit underlying reflex and voluntary control of behavior [43, 98].

Beside an unprejudiced approach to the investigation of the biological structures at hand, a crucial factor to Cajal's success was a technical improvement of the Golgi method, thus a visualization of individual neurons. The introduction of electron microscopy (EM) has opened novel possibilities for modern neuroanatomy, as for example proof for the existence of synaptic connections [99]. In its latest advance, today volumetric EM, namely the imaging of large volumes of brain tissue at nanoscale resolution, and subsequent segmentation and neuron reconstruction is being used to investigate circuits and connectomes [100, 101, 102, 103, 104, 105] with the ultimate aim of reconstructing whole brains [106].

For large scale volumetric EM, stacks of images are obtained either by cutting the tissue sample into ultrathin serial sections which are then imaged (e.g. serial sectioning tomography EM (ssTEM) and derivatives) or it is imaged in a destructive fashion by *en-bloc* sectioning in the imaging chamber using serial block-face EM (SBEM) [107]. Volumetric reconstructions of neurons from this image stack are obtained through automated volume segmentation [108, 100, 109, 110] and consecutive manual proofreading [111, 112, 103]. Automated identification and detection of synapses can provide access to the wiring diagram of the circuit at reasonable time scales [113, 114, 115, 116]. These techniques overcome limitations imposed by previous anatomical approaches, which combined a low-resolution overview and larger samples size (e.g. via histochemistry) with selected, localized EM imaging, and required using heuristics to map the high-resolution information onto cell types described at the lower resolution level [74, 75, 60, 117, 85]. Instead, the newer approaches for neuronal circuit reconstruction based on volumetric EM allow to study all components of a neuronal circuit across

multiple levels of anatomical details from coarse topology to ultrafine structure within one and the same individual. Thus, large scale volumetric circuit reconstructions provide anatomical information at unprecedented detail and completeness. In *Drosophila*, one of the best described model organisms in neuroscience, about half of the 25,000 reconstructed cells in the hemibrain reconstruction [101] had not been known before [106]. For the human brain, the reconstruction, albeit incomplete, of a 1 mm^3 sample of human cortex has revealed previously unknown motifs of inhibition [105] and uncovered multiple examples of cells and neurite structures unseen before or disagreeing with prior knowledge (see e.g., supplementary figures 6 and 7 in [105]).

2.1.5 PROJECT OBJECTIVES & SUMMARY

Knowledge of the individual circuit components and their interactions is of fundamental importance for understanding how a network operates. Previous work suggests that the vertebrate OB is endowed with a rich diversity of neuron types, which shape the high-dimensional sensory input into a representation optimized for downstream cognitive processing. Yet, especially in zebrafish, but also mammals, knowledge about the true spectrum of neuron types in the OB is incoherent and very incomplete. This impedes the functional interrogation of OB circuit by targeted manipulation.

The goal of this project is to provide a detailed description and quantitative inventory of the neuronal diversity of adult zebrafish OB. To approach this, I exploited a previously imaged SBEM volume, which comprises about 18% of the adult zebrafish olfactory bulb [93, 90], and collaborated with Google to perform an automated segmentation of neuronal structures [100]. I developed software to proofread the automated segmentation which I used to obtain full volumetric ultrastructural reconstruction of 239 neurons encompassing all layers of OB. Using human and machine-based classification approaches I discovered ten morphological classes of INs, which can be further categorized in subclasses. Furthermore, I found the zebrafish MCs to be composed of three subclasses. The reconstruction of hundreds of neurons within the same brain allowed me to determine RCs to be an integral part of a zebrafish glomerulus and uncover anatomical evidence implicative of a paracrine interaction between MCs and RCs.

Further, this investigation revealed that the majority of IN types contradict the *Law of Dynamic Polarization*, i.e., axonless IN classes making reciprocal, dendro-dendritic synapses clearly dominate in zebrafish OB. In addition, I found the large and widespread anatomy of deep layer INs in agreement with a widely distributed interaction with MCs as it has been proposed for mammals.

Besides the morphological description of neuron types, I provide a qualitative characterization of synaptic and non-synaptic physical interaction between PNs and INs of the zebrafish OB. These analyses revealed systematic differences in the connection scheme between superficial and deep INs. Moreover, I discovered a striking preference in individual IN classes for interacting with one of the two mayor PN types of the zebrafish OB.

2.2 METHODS FOR NEURON RECONSTRUCTION & CLASSIFICATION FROM EM DATA

This section describes methodological approaches applied in this study. In light of the novelty of the cell reconstruction method, which required the development of novel and the adaptation of existing approaches, it furthermore aims to give the reader an introduction and well-founded understanding of the existing methods as well as their extension.

First, I will give a description of the segmentation procedure and briefly explain briefly different methods employed to reconstruct neurons from the SBEM stack. The software tool developed to proofread the segmentation will be discussed in detail in the next section (2.3).

To classify the reconstructed neurons, I assessed a multitude of morphological features, which are then used in for automatic classification approach described here. Additional anatomical measurements and qualitative assessments of connectivity that guide the manual classification are explained.

2.2.1 VOLUMETRIC NEURON RECONSTRUCTION

Volumetric neuron reconstructions are obtained by segmentation, a computation that identifies voxels belonging to individual neurites in an image volume. The performance of this automated procedure is controlled by skeletons, which are line representations reflecting the geometrical and topological properties of the neuron. These skeletons are created by manually tracing the neuron within the image data. To compensate human reconstruction error, usually, several independent, redundant tracings are transformed into a ground truth skeleton [118].

In this study, reconstructions of altogether 239 neurons were created using different approaches combining automated segmentation, manual skeleton tracing and proofreading. Manually created skeleton reconstructions of neurons served as a reference to evaluate and choose the best automated segmentation version. Altogether, 50 neurons were manually skeletonized with different redundancy (threefold: 18, twofold: 29, single: 3, see MANUAL SKELETON RECONSTRUCTION). Thirty-four skeletons served to assess segmentation quality, see fig. 2A.

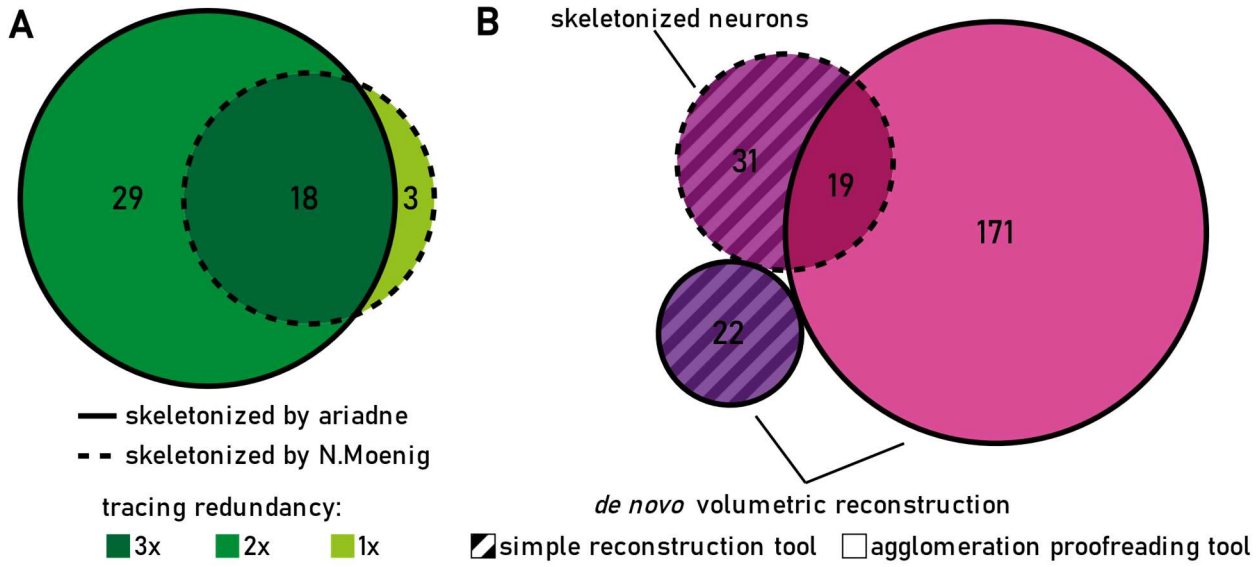

Figure 2. Overview of neurons reconstructed using different approaches. A: Skeletonization of 50 neurons at different redundancy B. Volumetric reconstruction of 239 neurons

The final agglomerated segmentation does not deliver perfectly reconstructed neurons but has to be proofread. This involves the correction of two types of errors: false splits, i.e., a neurite being represented by two objects and false mergers, i.e., two neurites being represented by one object. To obtain a volumetric reconstruction, I first developed a simple reconstruction tool that enabled correction of false splits. This tool was used to proofread 31 of the skeletonized neurons and to reconstruct 22 neurons de novo (see VOLUMETRIC NEURON RECONSTRUCTION & fig. 2B). I then created a more elaborate software tool, which also allowed correction of false merge errors (see AGGLOMERATION

PROOFREADING and section 2.3). This tool was used to proofread the volumetric representation of 19 skeletonized neurons and to reconstruct 171 additional neurons.

AUTOMATED NEURITE SEGMENTATION

A large SBEM volume of the adult zebrafish OB had been recorded previously [118] [90]. The volume represents ~18% of the single adult OB (288 x 173 x 98 μm^3, resolution: 9 x 9 x 25 nm^3).

ALIGNMENT

The segmentation performance depends on the quality of the preceding alignment. To optimize the alignment the data was aligned with iterative Nonlinear Keyframe-based Alignment (iNKA) as described in ([119], in preparation) by Stephan Gerhard et al.. In brief, data was first contrast corrected through histogram equalization. Several sections were removed due to recording artefacts contributing to misalignment. Image tiles were organized based on stage coordinates and then rigidly translated to maximize the cross-correlation of overlapping regions and between neighboring sections. Alignment errors were automatically detected based on a tile-specific measure taking into account the pixel-wise displacement across tiles. Sequences of tiles ("chains") exhibiting high levels of deformation were identified and nonlinear distortion corrections were applied to these chains while keeping the two keyframes surrounding the chain fixed. This procedure was iteratively applied to the stack resulting in alignment quality that displayed few artefacts upon visual inspection and was found to result in an 11-fold increase in the expected run length (ERL), a measure of segmentation performance (see box1).

AUTOMATED SEGMENTATION

The raw data was segmented by Michał Januszewski, our collaborator at Google AI, using flood filling networks (FFN) [100]. A concise description of the FFN procedure is given in box1.

The FFN was trained with three densely labelled ground truth stacks from the adult OB dataset. The first stack (640 x 640 x 100 pixel) was generated manually and served to train convolutional neuronal networks (CNN) to generate labels in two additional subvolumes (each 512 x 512 x 128 pixel) as described in [119]. All 3 stacks were reviewed in Armitage, a custom web-based voxel painting tool created by our collaborators at Google (unpublished).

Some modifications to the methods described in [100] were introduced to generate the segmentation at hand. First, an additional local realignment that dynamically aligned subvolumes during FFN inference was applied (for a detailed description see [120]). Upon large distortions between sections the movement of the FFN field of view (FOV) was, however, still restricted to avoid mergers. Second, separate FFN models were trained for the full resolution and for a dataset that was 2 x downsampled in plane. The base segmentation represents the oversegmentation consensus of segmentations at 9 x 9 x 25 nm and 18 x 18 x 25 nm resolution in standard and reversed seed order, respectively (see

box1). The agglomeration procedure was performed as described in [100] for all segments > 1000 voxels.

Box 1 | Segmentation using Flood Filling Networks

The Flood Filling Network segmentation approach uses 3D CNNs to segment single objects at a time across multiple network iterations. The voxel classification procedure is initiated from seed points placed at locations distant to putative cell membranes and takes into account both image data and predictions from previous inference runs.

During training the state of network weights are stored at regular intervals. For every such **checkpoint** a FFN inference is run on the entire dataset. The segmentation quality is evaluated by comparing the segmentation to manually created ground truth skeletons. Performance is quantified by the **ERL**, a measure of the average error free neurite length and the **edge accuracy**, measuring the proportion of skeleton edges correctly contained in the segmentation relative to edges in which the segmentation has an error.

Three types of segmentation errors can occur. An unsegmented neurite is referred to as omission error. If a neurite is contained in two different segments a **split error** occurred. If an object covers (parts of) two neurites, this is referred to as **merge error**. The correction of merger errors is much more time consuming than that of split errors. The FFN approach therefore aims at first producing an oversegmentation that contains very few false mergers. To achieve this, several segmentations created from the best performing checkpoints are combined to an **oversegmentation consensus**, the **base segmentation**, in which all splits are accepted.

In a consecutive **agglomeration** procedure, the number of false splits is reduced to improve object continuity. For agglomeration, for any given pair of segments that lie within a certain radius from each other two independent FFN inference runs are started from seeds in the two objects. The objects are then merged, if the predictions overlap sufficiently. All merge decisions are stored in an **agglomeration graph**.

An agglomerated segmentation can have two types of merge errors. In a **true segmentation merger,** the base segmentation exhibits spillage across neurites. An **agglomeration merge error** refers to a false decision of the agglomeration procedure, in which two or more base segmentation objects are assigned to one agglomerated object.

TISSUE CLASSIFICATION

Transitions between neuropil and other tissue structures e.g., blood vessels can impair the segmentation result. A tissue mask for restricting seed point placement (see box1) and the FFN FOV movement to relevant neuropil was created, adapted to the particular requirements of the data set at hand. To this end, I generated ground truth (GT) by sparsely labelling neuropil, cell bodies, blood vessels, sensory axons, extracellular space (ECS), and out-of-bounds (OOB) areas in 2D image sections,

distributed throughout the stack, using Armitage. Our collaborator used this GT to train a semantic segmentation model analogous to [100]. The training was done iteratively. After each training round predictions were generated, classifying each voxel in the volume to one of the tissue labels according to maximum likelihood. I assessed these predictions visually and generated additional GT to counter mistakes observed in the model's prediction. After 7 rounds the predictions were judged sufficiently precise for restricting seed point placement.

CHECKPOINT SELECTION

Manually reconstructed skeletons serve to evaluate the segmentation performance and to select the best performing checkpoint of the model by overlaying the segmentation and the skeletons analogous to [100]. I checked all mismatch points for which the distance between a segment and the closest skeleton node was larger than 3 µm and if the skeleton branch contained more than two nodes. Mistakes in the skeleton, i.e., either missing skeletal branches detected by the segmentation or wrongly traced branches, were manually corrected (see below).

PROGRESSION OF DIFFERENT NEURON RECONSTRUCTION APPROACHES

MANUAL SKELETON RECONSTRUCTION

Neurons were reconstructed by manual tracing using the software PyKnossos [118]. I initially reconstructed 21 neurons (10 putative projection neurons (PNs), 11 putative interneurons (INs)). Comparing these non-redundant cell reconstructions against segmentations from many different checkpoints, the skeletons were continuously updated and improved by tracing missed branches or removing falsely traced branches from the skeleton. Relative to the final skeleton length, on average 29.6 ± 21.6% (median 25.3%) had been missed in the non-redundant reconstruction and 2.3 ± 5.1% (median 0.3%) were wrongly traced. The total skeleton length of all neurons increased from 63.3 mm to 86.1 mm from first to final pass.

In addition, 47 neurons were reconstructed by an external tracing company, ariadne.ai ag (https://ariadne.ai/ see also [118]). This set comprised 29 additional neurons (7 putative PNs, 22 putative INs), if which 18 neurons were also part of the initial set of manually reconstructed neurons (9 putative PNs, 9 putative INs). These 29 neurons were reconstructed with two-fold redundancy using the CORE procedure described in [118]. In brief, each neuron was reconstructed by two independent human tracers and a consensus skeleton was generated. Mismatches between the individual tracings were resolved by two additional tracers, thus iteratively improving the reconstruction result. Further processing of CORE skeletons was needed before using them for automated segmentation evaluation and check point selection: First, in large compartments tracers

traced back and forth in order not to miss any side branches. As a result, large neurites were represented by two or more parallel skeleton branches, thus, skewing measures of segmentation performance, which are normalized to neurite length. This had to be manually corrected by replacing the parallel skeleton branches with one central branch. Furthermore, the original consensus skeleton calculation had been developed for three-fold redundant reconstructions [118] and the consensus of only two skeletons often resulted in branch points outside of the target neurite. To circumvent this problem, I created consolidated skeletons by visiting detected mismatch points and manually joining one of the original skeleton fragments created by a single tracer to the neuron's skeleton.

The set of skeletons to select the segmentation checkpoint was extended by 13 such consolidated skeletons (two presumptive PNs, 11 presumptive INs). Consecutive revision of mismatches against automated segmentation resulted in the addition of 2.2 ± 1.8% (mean ± s. d., median: 1.7%) missed skeleton length to, and the removal of 2.0 ± 2.7% (mean ± s. d., median: 0.8%) wrongly traced skeleton length from the skeletons traced with two-fold redundancy.
This final set of skeletons for segmentation evaluation encompassed 33 neurons (amounting to 121.5 mm neurite length) and spread through the entire SBEM volume to ensure that errors in the segmentation can be assessed throughout the data set.

VOLUMETRIC NEURON RECONSTRUCTION

To obtain a volumetric reconstruction of the 50 manually skeletonized neurons, the identity of the segment (id) in the agglomerated segmentation volume at each skeletal node position was retrieved. These reconstructions were further proofread: First, erroneously retrieved segments, which did not belong to the target neuron but did not represent agglomeration errors were removed. These wrongly added segments presumably originated either from rounding imprecision at a certain skeleton node position or some skeletal nodes were placed outside the target neurite. Second, they still contained agglomeration errors, which were mostly splits, but also some merge errors (see box1).

In addition, 22 neurons were reconstructed exclusively volumetrically using a program that I wrote, which allowed to control *neuroglancer* through Python. This script enabled to follow and "trace" neurons in the segmentation by storing the ids of segments a neuron contains. This tool was also used to review the segmentation – skeleton overlays of 31 neurons described above and to remove wrongly added segments from this neuron representation. This tool did not allow for correction of agglomeration errors.

AGGLOMERATION PROOFREADING

To fix the agglomeration splits in volumetric neuron reconstructions, potential partners involved in a split between neighboring segments were determined. For this purpose, Michał Januszewski skeletonized the agglomerated segments using the *TEASAR* algorithm [121]. The distance between skeleton nodes of any pair of skeletonized segments contained in a neuron was calculated. For all

segment pairs with nodes within a distance of > 500 nm, the segment ids and the voxel coordinates of the closest node pairs were stored. In ten neurons all locations were inspected and decisions to link a given pair of segments was made, if it was topologically correct. This revealed that topological correctness was given in the vast majority of segment pairs to be linked. Therefore, for the remaining 43 neurons for which a volumetric representation had been obtained (see above) all potential pairings were accepted and linked via the *Brainmaps API* (see section 2.3.4 → THE BRAINMAPS API). Altogether 150,920 links were set this way.

Agglomeration mergers in this set of neurons as well as the remaining agglomeration splits that were missed, because the distance between the involved segments was above threshold, were corrected using the agglomeration proofreading tool I developed. This tool is described in detail in section 2.3. This tool was also used to proofread the remaining 19 segmentation-skeleton overlays and to reconstruct and proofread another 171 cells from scratch. One cell contained a true segmentation merger to another neuron, which could not be split with the tools at hand. This neuron could still be reliably classified by humans and its skeleton was split (see below)

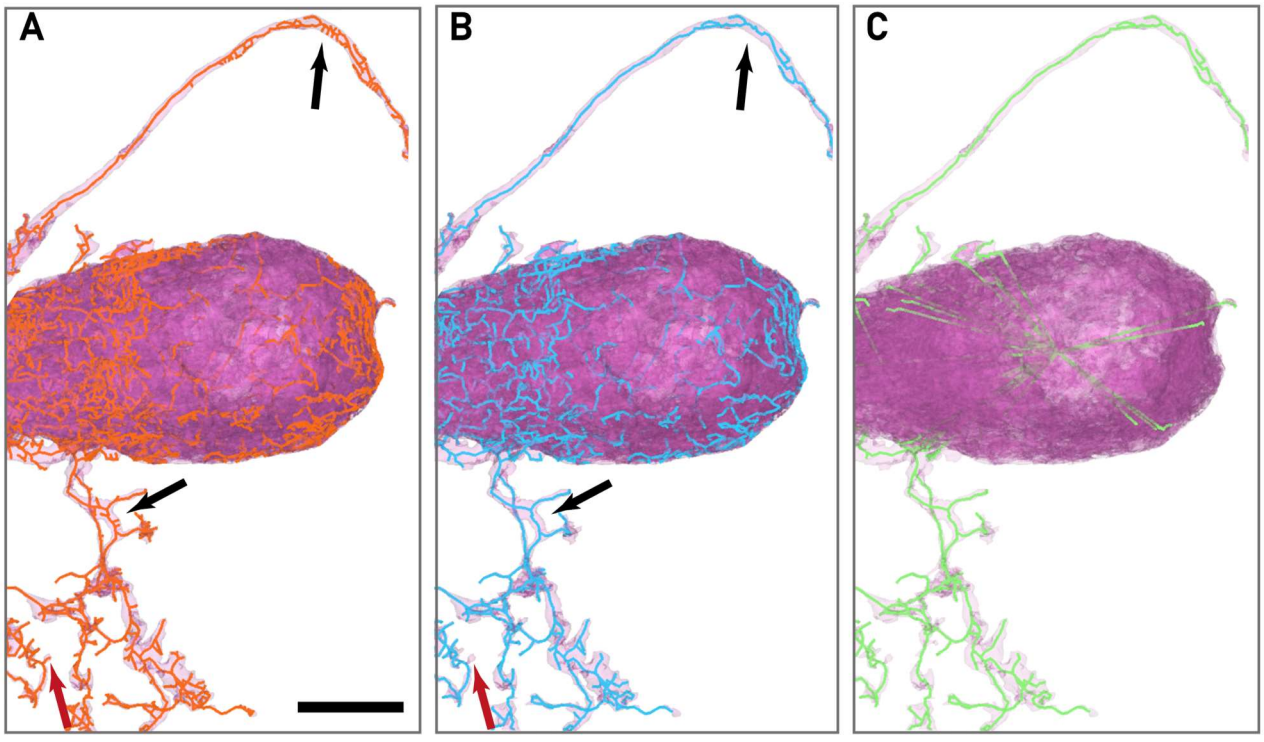

Figure 3. Postprocessing of automatically created TEASAR skeletons before extraction of morphological features. The original TEASAR skeleton (A) contained many small branches that reflected rather surface deflections than real branches (examples see black arrows). Their frequency was much reduced in the pruned skeleton (B). A tradeoff had to be made between maintaining short, real twigs and the removal of excess branches (see red arrow for erased real twig). The excess skeletal mesh at the soma was removed semi-automatically in the final version (C).

POSTPROCESSING OF TEASAR SKELETONS FOR FEATURE EXTRACTION

For morphological analysis and consecutive cell classification the volumetric representation of the reconstructed neurons was converted into skeletons using the *TEASAR* algorithm [121] by Michał Januszewski. These automatically generated skeleton reconstructions reliably reproduce the volumetric neuron representation topologically but differ notably from skeletons created by humans. In the *TEASAR* skeletons voluminous parts of the neuron like primary neurites and the soma are represented by an excessive network of tiny branches, that fills the spatial extent of the neurite, rather than reflecting real branching pattern (fig. 3A, black arrows). This property of the *TEASAR* skeleton is expected to bias the classification of neurons based on morphological features, which comprise measures of branching patterns. Therefore, skeletons were post-processed as described below. Skeletons were downloaded from the *brainmaps* servers as *networkx* graphs. To assess the modifications, skeletons were transformed into the precomputed format for visualization in *neuroglancer*.

PRUNING

Pruning presupposes a compromise between the removal of the excess branches reproducing neurite volume and the preservation of skeleton branches reproducing e.g., spine-like protrusions or true branches. An iterative procedure using first a threshold of 100 nm, then 400 nm was applied and finally all branches shorter than 1 µm in total sub-branch length were removed. The procedure was validated qualitatively by inspecting skeletons of neurons of various types. This confirmed reliable preservation of the skeletal representation of delicate neurite structures such as spine-like appendages as well as a reduction in overall occurrence of small, incorrect twigs (fig 3B).

REMOVAL OF EXCESS SKELETAL MESH AT THE SOMA

The copious skeleton network emerging from automated skeletonization of voluminous somata was largely unaffected by pruning because these branches were too long. To remove this mesh, but retain true branches and somatic spines, first, the coordinates of the approximate center of each soma were determined by hand. A sphere comprising the entire soma of individual neurons was identified by fitting neuroglancer ellipsoid annotations of different radii around the approximate center. The radius was chosen generously to encompass the base of large dendrites, which also produced copious skeletal branches, as well. Skeleton nodes within these spheres were extracted, and for each node position the label predicted by the tissue mask was queried. Nodes labelled as soma were removed and those branches remaining that exceeded a certain length (500 nm for INs and 2500 nm for PNs, respectively) were connected to the central soma node (fig 3C).

Unconnected components in the skeleton, originating e.g., from unsegmented parts of the neuron, were manually stitched in PyKnossos. During this process the segmentation merger encountered in one the neuron (see AGGLOMERATION PROOFREADING) was split in its skeletal representation. Skeletons were reviewed in *neuroglancer* and some remaining excess skeletal meshes were removed by hand in PyKnossos.

SPECIFICATIONS OF VOLUMETRIC NEURON RECONSTRUCTION

PROOFREADING TIME

The proofreading time was retrieved from time stamps in automatically saved files created by the proofreading tool (for details see section 2.3). These files were stored every 5 min only if changes to the previous state of the agglomeration graph were made. If two consecutive files were separated by more than 10 min, this was considered a pause between two proofreading blocks. The proofreading time was calculated as the sum of all blocks. This measure likely underestimates the true proofreading time because e.g., long intervals without changes to the agglomeration graph can occur while searching for objects involved in a merger. Due to a bug in the autosave procedure not all reconstructions could be used for the analysis of proofreading time. These reconstructions were excluded from the calculation of the proofreading time.

COMPLETENESS OF NEURONS

Limitations by Stack Size

I used visual inspection to assess the completeness of a given reconstructed cell in the imaged volume. The degree to which a cell was cut was evaluated while taking into consideration the extent of other cells within the same morphological class. Cells were graded in cutting degrees ranging from 0 to 3. A cell was graded with cutting degree (CD) CD0 if the dendritic arborization were fully represented in the image stack, even if an identified axon was cut. CD1 was used to describe a neuron that was minimally cut, e.g., if only distal parts of the dendritic tree were truncated and the comparison to similar cells suggested no major fraction of the cell were cut off. CD2 described a cell, which was notably cut, but could still be expected to be represented to ~75 % within the imaged volume. Cells subject to more substantial cuts, e.g., cuts at the soma, were rated CD3.

Fraction of Neurons Reconstructed by the Agglomeration

To calculate the fraction of the neurons which were represented by the agglomeration without proofreading the original agglomeration graph was retrieved for all base segmentation objects that were assigned to a given fully reconstructed neuron. This data was also used to calculate the number of split and merge errors corrected in the proofreading process (see section 2.4).
For volume calculation the voxel size of each independent agglomerated object was determined as the

sum of the voxel size of individual base segments. Next, the largest agglomerated object was determined and normalized to the total size of a neuron. For calculation of the neuron length the *TEASAR* skeletons of the base segmentation objects were retrieved. *TEASAR* skeletons had been created only for objects > 1000 voxels at a voxel size of 36 x 36 x 50 nm (~.065 μm^3). Skeleton length was calculated and accordingly the longest object determined and normalized to final length.

Reconstruction Accuracy of Neurons

Previously, reconstruction accuracy had been assessed by comparison of reconstructions to ground truth obtained at 26-fold redundant tracing [118]. Here, redundant volumetric reconstructions were not available. To get a notion of the completeness of my nonredundant neuron reconstructions, I compared the distribution of volume and neurite length between the reconstructions of neurons, that were first skeletonized with at least twofold redundancy (see VOLUMETRIC NEURON RECONSTRUCTION), to neurons reconstructed in the agglomeration proofreading tool. For this comparison a set of cells was required which was similar in terms of numbers and neuron location, which biases cell size in both conditions. This requirement was only be fulfilled for a specific cell type (DLIN, see section 2.4). Only neurons with CD < 3 were considered. Neurite length was obtained from the postprocessed *TEASAR* skeleton.

2.2.2 NEURON CLASSIFICATION

Three different approaches were used to classify reconstructed neurons: The main approach was a manual classification presented in section 2.4., which is based on exhaustive description of cellular morphology across different scales of resolution and inspection of interaction with other local neurons. The second approach is based on redundant classifications of the subset of neurons by several neuroscientists, who inspected the volumetric representation and grouped neurons based on similarity. The third classification approach uses clustering of neurons based on quantitative morphological features. These features were mostly obtained from the skeletal representation of volumetric neuron reconstructions.

HUMAN CLASSIFICATION OF NEURONS

Making use of the custom written *neuroglancer* viewer controls (see section 2.3) a software tool was implemented which allowed to examine and explore the 3D representation of reconstructed neurons visually in *neuroglancer* and to sort them into groups based on their appearance. Four neuroscientists with little or no previous exposure to the volumetric reconstructions (Bo Hu, Nesibe Z. Temiz-Karayol, Rainer W. Friedrich and Ruth E. Montaño Crespo) were asked to classify 125, in one case 108, reconstructed cells into maximally 12 groups plus an additional group for reconstructions, which

could not be confidently assigned to a group. No further instructions were given. My own preliminary morphological classification was also included in the evaluation. This set of 125 cells contained two cells that were later classified as glia based on morphological features and the absence of synaptic structures.

Individual classification results are represented as a graph, in which each neuron represents a node and neurons of one group are linked all-to-all with edges of weight 1. A combined representation is derived by summing edge weights across the graphs generated by different annotators.

EXTRACTION OF FEATURES FOR SEMI-AUTOMATED CLASSIFICATION

For automated classification, features describing neuron morphology were extracted from the skeleton as well as from the mesh representation of reconstructed neurons. The skeletons were transformed into directed graphs that were rooted around a node in the soma center. Triangle meshes of the volumetric neuron reconstruction were generated by our collaborators at a voxel resolution of 50 nm^3. All features were calculated using custom written software in python and are summarized in table 1. References to publications or software inspiring or underlying the feature calculation are given, where applicable.

Feature Name	Description	Ref.
Spatial extent of the neurite		
width (w), height (h), depth (d)	The extent in x, y and z of the neuron extracted from the PCA transformed point cloud of skeleton nodes.	
total length (len_{tot})	Total edge length of the automatically created, postprocessed skeletons	
longest branch length (len_{br})	Maximal path length in nm	
axialization (ax)	The axialization is a measure of elongation of the dendritic tree. It compares the ratio of the variances in the principal component space of the skeleton node coordinates. It is defined as $1 - \frac{sd2}{sd1}$ where sd1 and sd2 are the square root of the eigenvalue of PC1 and PC2, respectively.	[122]

Feature Name	Description	Ref.
flatness (fl)	Flatness is a measure of the extent of the dendritic tree along the axis perpendicular to the longest axis. It is defined as $1 - \frac{sd3}{sd2}$ where sd2 and sd3 are the square root of the eigenvalue of PC2 and PC3, respectively.	[122]
gyration radius (gr)	The radius of gyration is a measure of compactness of an object that can be described as a point cloud. It is defined as the root mean square distance of the points from the center of mass. $r_G = \sqrt{\frac{1}{N}\sum_{i=1}^{N} \lvert\vec{r_i} - \vec{r_S}\rvert^2}$	[123]
convex hull volume (Vol_{hull})	The convex hull volume [μm^3] was calculated around the point cloud of skeletal nodes.	
cell volume (Vol_{cell})	The volume of the neuron in μm^3. It was calculated as the sum of the voxel volume of individual segment objects comprised in the agglomerated object representing a neuron.	
surface area (A_{cell})	The surface area was calculated as the sum of the area of faces in the triangle mesh representation of a neuron.	
Branching features		
no. of branches (nbr)	total no. of branches > 1 µm	
no. of primary branches	The no. of branches emerging from the soma that are > 40 µm was automatically determined. This measure can include axon	
nbr on the longest branch	number of subbranches on the longest branch	
tip ratio	The ratio of the total length of tips, terminal branches, to the remaining skeletal length	
path length	The path length for each branch node was calculated as the shortest distance from the soma along the skeleton.	*
distance to soma	The Euclidean distance of each branch node to the soma node; this measure is equivalent to a Sholl analysis.	[124] *
tortuosity	The tortuosity was calculated as the ratio of path length to distance to soma for each terminal node. This measures how much neuron branches meander.	[124] *
branch order	For the end node of each branch the number of preceding branch nodes to the soma node along the shortest skeleton path was measured.	*
partition asymmetry	The partition asymmetry measures the asymmetry of branching at bifurcations only. It is defined as the ratio of the absolute difference and the sum of the numbers of tip branches of each subtree.	[124] *

Feature Name	Description	Ref.
others		
soma position	the x, y, z coordinates of the central soma node of all cells were transformed by PCA and for each neuron the first and second principal component used as feature	
soma surface area (A_{soma})	Vertices of the mesh representation lying within a sphere that encompasses the soma [see 2.2.1] are derived. The area of faces containing these vertices is calculated. The surface area of smaller neurites or spines lying within the sphere may be included in this measure.	
soma volume (Vol_{soma})	The number of voxels belonging to a neuron's volumetric representation that lie within a sphere encompassing the soma. The voxel number was converted into metric volume. This measure may include the volume of branches and spines belonging to a given neuron if these lie in the sphere.	
axon	binary, presence of an axon is determined by visual inspection (see 2.4.4)	
spine	binary, presence of any of the spines defined in 2.4.4	

Table 1. Summary of morphological features extracted from each reconstructed neuron. *: distributed features

DATA PROCESSING

The distributions of path length of branches and the distances to soma of branch points were binned in bins of 5 µm. The tortuosity and partition asymmetry distributions were binned in 0.025 bins. The path length and distance to soma of tip branches exclusively was also extracted. Furthermore, the distribution of several parameters was extracted in relation to one another: The no. of branches per branch order, the distance to soma and path length versus branch order as well as the partition asymmetry versus path length. The feature space was further expanded by the following feature ratios: len_{tot}/gr, Vol_{hull}/gr, len_{br}/gr, nbr/gr, len_{br}/len_{tot}, $nbr_{longest}/len_{br}$, fl/ax, len_{tot}/nbr, A_{cell}/nbr, A_{soma}/Vol_{cell}, Vol_{hull}/Vol_{cell}, len_{tot}/Vol_{cell}, nbr/Vol_{cell}, A_{cell}/Vol_{hull}, len_{tot}/Vol_{hull}, ax/Vol_{hull}, fl/Vol_{hull}, nbr/pa, tip ratio/pa, Vol_{soma}/A_{soma}.

Distributed features of individual cells (*) were combined by zero-padding and flattening. PCA was performed to reduce dimensionality and the first three principal component scores (PC1, PC2, PC3) entered into the feature array.

The final feature array contained 63 features for each neuron. Missing values were replaced by the distribution mean across all cells. The same was done for the cell volume and surface area entries of the neuron containing a segmentation merger in the volumetric representation. With exception of binary and count parameters all parameters were normalized to zero-mean and unit-variance using scikit-learn PowerTransformer [125]. To normalize count parameters, they were square rooted. All features were standardized through z-scoring across cells.

SEMI-AUTOMATED CLASSIFICATION

A total of 197 neurons (28 PNs, 169 INs) with a cutting degree (CD) < 3 was selected for further analysis. PNs were identified based on obvious morphological features described in prev. publications, e.g., myelinated axon, ruff, characteristic tufty dendrite, etc., [117, 85, 94, 84, 86], whereas all other cells were considered INs. The following 40 features were selected to determine morphological groups among all neurons and the subset of PNs: len_{tot}, tip ratio, nbr, number of primary branches, len_{br}, nbr on the longest process, ax, fl, h, w, d, pa, Vol_{hull}, gr, Vol_{cell}, A_{cell}, Vol_{soma}, A_{soma}, axon, spines, nbr per order (PC1), tortuosity (PC1), dist2soma (PC1), path length (PC1), tip path length (PC1), pa (PC1), distance vs order (PC1), pa vs path length (PC1), path length vs order (PC1), soma position (PC1), A_{cell}/nbr, A_{soma}/Vol_{cell}, Vol_{hull}/Vol_{cell}, len_{tot}/Vol_{cell}, nbr/Vol_{cell}, A_{cell}/Vol_{hull}, ax/Vol_{hull}, fl/Vol_{hull}, nbr/pa, Vol_{soma}/A_{soma}. The entire feature space was used to identify morphological types among INs alone.

The data was visualized using UMAP to project the 63-/40-dimensional feature space into a 2D space. The emerging clusters were inspected for homogeneity in morphological composition by visualizing individual members in neuroglancer. Clusters were found to be largely stable in composition across a range of the UMAP input parameter "number neighbors", which was varied from 5 to 60 (same random seed). KMeans (n_clusters=2-12) and HDBSCAN [126] (min_cluster_size=3, min_samples=3) clustering was applied to the original feature array as well as to the dimensionality reduced feature space (PCA, 20 components for KMeans; UMAP, varying no. of neighbors: 5-60 and no. of components: 5-40 for HDBSCAN). Clustering did not reveal qualitatively different results compared to the simple projection onto 2D space.

2.2.3 ADDITIONAL MORPHOLOGICAL ASSESSMENTS

GRANULE CELL LAYER OUTLINE

Using PyKnossos the outline of the GCL was traced in the xy image planes at 30 to 50 section intervals. Using custom software, the node coordinates were extracted and exported to a point cloud, which was then meshed using Meshlab [127]. The meshed representation was transformed to the *neuroglancer* precomputed format for rendering with *neuroglancer*.

SOMA DIAMETER

The soma diameter was assessed by fitting *neuroglancer* ellipsoid annotations (see above) tightly around the soma and doubling the radius. This diameter, thus, reflects the maximal extent of a soma in one axis. Average soma sizes for morphological classes reflect mean and standard deviation across representatives, excluding neurons with cut somata.

MEASURES OF DENDRITE DIAMETER, NEURITE LENGTH AND GLOMERULAR EXTENT

The diameter of dendrites was measured at their base, directly after emergence from the soma, using the scale bar provided in *neuroglancer*, resolving to 100 nm bins for structures ≤ 500 nm and 250 nm bins for larger structures. Averages for morphological classes reflect mean and standard deviation across representatives.

The extent of glomeruli, diverse dendrite trees as well as the length of diverse neurites as given in the cell class description were all measured using *neuroglancer's* scale bar. Glomeruli measures reflect the maximal extent in height, length, and width. Values indicate mean and standard deviation across measurements.

TABLES OF NEURON CLASS SPECIFIC FEATURES

Values report mean and standard deviation across representatives of a given neuron (sub)class. Except for the number of glomeruli innervated for PNs these were obtained from completely reconstructed neurons only. Measures of cell volume and total length, which are sensitive to the reconstruction completeness, were limited to neurons with CD ≤ 2. The number of glomeruli was only averaged across neurons reaching the GL. The spine frequency was rated by visual inspection.

ASSESSMENTS OF CONNECTIVITY

SYNAPSE DETECTION

839 synapses were manually annotated in 65 PN neurites and 193 IN neurites. The cell interior was screened at membrane contact sites between a given pair of cells for the presence of chemical synapse structures, namely a vesicles cloud in the presynapse, vesicles fused to the membrane and a close contact between the pre- and postsynaptic membrane. OB neurites are characterized by an extensive presence of vesicles and organelles of the endomembrane system potentially biasing towards false positives. The contact sites were carefully inspected in all 3 orthogonal viewports in *neuroglancer* and rated my confidence for the presence synapse on a scale of 1 to 5. Here, I only report synapses with a confidence of 3 and higher. These are structures that I would classify as a synapse in a binary decision.

GLOMERULUS SPECIFIC IN-PN INTERACTIONS

For all but the sGLIN1, the interaction of individual representatives of a morphological IN class was assessed by overlaying the IN mesh pairwise with all reconstructed PNs of a given glomerulus. Each pair was carefully screened for contacts sites, and contact sites were screened for synapses. Connections were considered only if the confidence of a synapse was >2. For pairs with a large number

of synapses, I recorded at least 4 synapses. The number of inspected INs per class as well as the number of glomeruli and the resulting number of IN-PN examined are summarized in table 2.

The description of glomerulus-specific MC-IN interaction summarized in table 10 was derived as follows: The glomerular innervation was considered as **monoglomerular**, if the mean number of innervated glomeruli for a respective IN class rounded to one and **multiglomerular**, if it was higher. MC selectivity was defined as **broad**, if an IN connected to more than 40% of reconstructed MCs within a glomerulus, and **selective** otherwise. If the IN projected only in one glomerular subcompartment, only MCs projecting to this subcompartment to calculate the percentage were considered. This was also reflected in the number of inspected IN - MC pairs given in table 2 above. The MC selectivity of an IN class was rated as broad or selective, respectively, if ≥ 60% of the IN-MC interactions were broad or selective, respectively, in ≥ 60% of the glomeruli inspected. The number of contacts per connected MC-IN pair was defined as high if the number of synaptic contacts between a given pair exceeded three. Reciprocal synapses were counted a as a single contact. The number of MC contacts for an entire IN class was rated **high** or **low** if ≥ 60% of the pairs had a high or low number of contacts, respectively. To calculate the fraction of connections of a given directionality only connected IN-MC pairs were considered. Independent of possible unidirectional synapses, a MC-IN pair was considered reciprocal, if it was connected through reciprocal synapses. Likewise, MC-IN pairs connected by spatially separated unidirectional synapses of opposing directionality were considered reciprocal.

type inspected	lGLIN1	GLIN2	GLIN3	PLIN1	PLIN2	rlPLIN3	vPLIN3	PLIN4	rDLIN1	lDLIN1	sDLIN1	cDLIN2	fDLIN2	sDLIN2	DLIN3	unclassified IN
glomeruli	4	2	3	1	2	2	5	4	3	2	2	7	2	2	3	2
IN	8	5	4	3	2	2	5	3	2	1	1	2	1	1	5	1
IN-MC pairs	92	21	53	12	13	14	42	52	52	19	24	76	28	24	73	21
IN-RC pairs	16	9	14	2	4	4	16	9	10	4	4	32	4	4	18	4

Table 2. Number of inspected glomeruli and IN-PN pairs for the examination of glomerulus specific PN interaction

2.2.4 DATA ACCESS AND ANALYSIS

Most segmentation data created by our collaborator at Google, e.g., image data, meshes and skeletons was hosted on a dedicated server, which can be accessed interactively via the *Brainmaps API* (see section 2.3.5). A python package making use of the *Brainmaps API* has been published on GitHub [128].

Additional information for individual segment objects that cannot be retrieved via the *Brainmaps API* e.g., voxel size and the bounding box was provided by Michał Januszewski via BigQuery.

I wrote all data analysis tools, as well as tools for data retrieval using Python3.8 [129] and the open source packages numpy [130], pandas [131], networkx [132], lxml [133], scikit-learn [125], matplotlib [134], seaborn [135], scipy [136], requests [137], umap-learn [138], hdbscan [126] and numpy-stl [139].

Volumetric renderings of the segmentation and as well as automatically created skeletons were visualized using *neuroglancer* [140].

2.3 AGGLOMERATION PROOFREADING TOOL FOR NEURON RECONSTRUCTION

This section introduces the software developed to reconstruct and proofread neurons in the agglomerated segmentation. It intends to give the reader a notion of the agglomeration errors and means to solve them. I briefly review existing proofreading options and give a detailed description of the organization and workflow of the tool I created.

The agglomeration proofreading tool was created to provide a means for reconstructing sparse subsets of neurons in the segmented EM volume. Through agglomeration the segmentation had achieved a high level of quality and already reconstructed large fractions of individual neurons with few large segment objects (see section 2.4.2). A full or near complete cell reconstruction, however, requires a more detailed proofreading. Errors in the agglomeration were mostly due to data quality, e.g., imaging or alignment artefacts or due to biological structures that were challenging to segment. The latter involved for example neurites coiling around each other, glial cells ensheathing several neurites or smaller branches and protrusions joined to the main neurite only through narrow conjunctions (see e.g., fig. 25A, fig. 45B). The agglomeration parameters were chosen to favor split errors over mergers, which are more difficult to correct. Segmentation mergers, in which two neurites are falsely segmented to one object, were still present, but rare.
Thus, the neuron reconstruction and proofreading required a tool which enables to identify and fix false splits and agglomeration mergers. This tool should permit the sparse reconstruction and review of a medium sized set of neurons at a reasonable speed and accuracy. The topological, morphological, and surface structure information that is accessible through the 3D representation of the neurites is highly instructive in identifying sites of false splits and verifying that a potential split substructure fits morphologically to the neuron. Furthermore, it is particularly valuable for the identification of false pairing of segments in agglomeration mergers (see fig. 5).

2.3.1 EXISTING PROOFREADING TOOLS

A variety of well-established and versatile skeleton tracing tools exist, like Catmaid [141], Knossos [142], PyKnossos [118] and WebKnossos [143], as well as commercial tracing services and approaches that crowdsource the proofreading of connectomic data to an online game (http://eyewire.org). For proofreading of segmentations of large datasets, however, only two tools were published, namely VAST [111] and NeuTu [144].

VAST [111] is a segmentation and annotation tool that offers elaborate voxel painting functionality and has been designed to create GT for automatic segmentation and to correct errors in automatic segmentations. False splits can be fixed through a merge operation and false mergers can be unmerged with aid of voxel painting and filling tools. The tool has, however, several drawbacks for our use case: With segmentations at the scale of our volume segment objects have to be individually streamed and copied into an image layer, a process that is particularly slow for large objects. VAST does not offer tools to specifically target agglomeration mergers, which do not require time-consuming painting, but require a simple retraction of the erroneous agglomeration decision. Furthermore, VAST relays mostly on XY display of image data. The 3D information about a neuron's morphology is very informative to guide the revision and the detection of erroneous locations and allows for much faster revision of neurons, compared to browsing through the image data. Lastly, there is no direct interface to commit the local corrections to the *Brainmaps* servers.

NeuTu [144] is a large-scale segmentation proofreading tool. It offers 3D visualization and annotation tools, as well as tools and heuristics to interactively resolve segmentation errors, and allows working collaboratively on the same segmentation volume. However, NeuTu expects data served by a specific server structure, DVID, a data management system developed at Janelia Research Campus to serve large scale connectome data [145]. It was beyond the scope of the project to implement such a system in our institute.

Since published tools did not meet the demands for proofreading of the current data or had infrastructural requirements that could not be met, I decided to write a dedicated proofreading tool using *neuroglancer* [140]. This tool addresses specific demands for proofreading of our dataset but can also be readily applied to proofread other dataset hosted on the *brainmaps* servers, or with minor adaptations to data that are hosted by one of many data sources supported by *neuroglancer.*

2.3.2 NEUROGLANCER: A WEB-BASED TOOL FOR VOLUMETRIC DATA VISUALIZATION

Neuroglancer [140] is a browser application that allows to view slices of volumetric image and segmentation data (xy) together with the cross-sectional views (xz and yz) alongside a 3D rendering of the meshed segmentation (fig. 4). *Neuroglancer* comes with a range of functions that allow to visualize, browse, and navigate through the image data. Multiple layers can be visualized simultaneously, similar to conventional image editing programs. Loading different segmentation versions with the raw image data, e.g., an agglomerated and original volume, to specific layers allows to explore them alongside each other (fig. 4). In the 3D viewport the mesh representation of multiple selected neurites can be explored from all sides at different levels of detail. The viewer can be controlled through keyboard and mouse input. These functions can be extended and overwritten using the *neuroglancer* python integration. This integration runs *neuroglancer* on a local web server and allows to customize and interactively update viewer settings and exchange data.

I created a python application to reconstruct neurons in a volumetric segmentation that uses neuroglancer as a viewer to guide the correction of agglomeration errors. The underlying idea is to fix agglomeration errors by adding or removing links in the agglomeration graph (see next section).

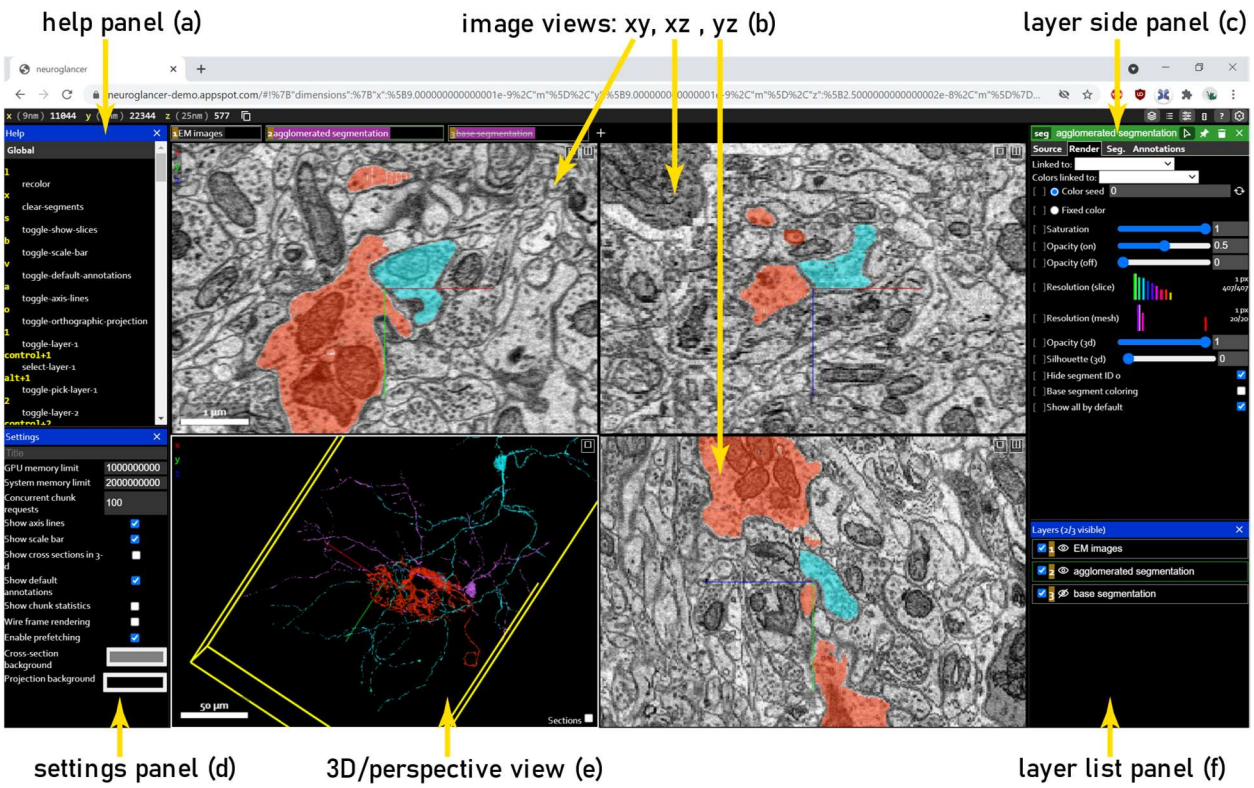

Figure 4. Overview of the neuroglancer web application with the most important viewports and panels. The image views allow to display the raw EM data alongside one or more segmentation layers in the three orthogonal axes (b). The 3D view displays the meshed segmentation (e). The proofreading workflow is facilitated by numerous built-in features: Any arbitrary combination of viewports can be displayed together. The zoom level can be adjusted individually for image and 3D viewports. Navigation is possible through scrolling as well as mouse click on meshes. The help panel (a) displays all built-in and custom keyboard and mouse short-cuts. The layer side panel (c) allows to change diverse display settings, e.g. for segmentation layers the opacity can be adjusted in 2D and 3D. The settings panel (d) allows to adjust basic viewport settings. The layer list panel (f) allows to toggle the visibility of layers.

2.3.3 THE AGGLOMERATION GRAPH

The result of the agglomeration procedure can be represented as a graph. Segments, which are agglomerated to an object with a shared id, form one connected component in the agglomeration graph. A false split is thus corrected by creating a (anatomically correct) link between two disjoint components (fig. 5A).

The challenge when resolving false mergers is to find the segments that are wrongly linked across components. Since false splits are easier to fix than false mergers, the segmentation is oversegmented, the areas in which two wrongly merged neurites overlap or touch are often composed of several segment objects that have then been agglomerated to one. Thus, the wrong link or links may have to be identified from a larger group of pairs potentially involved in the merger (fig. 5B).

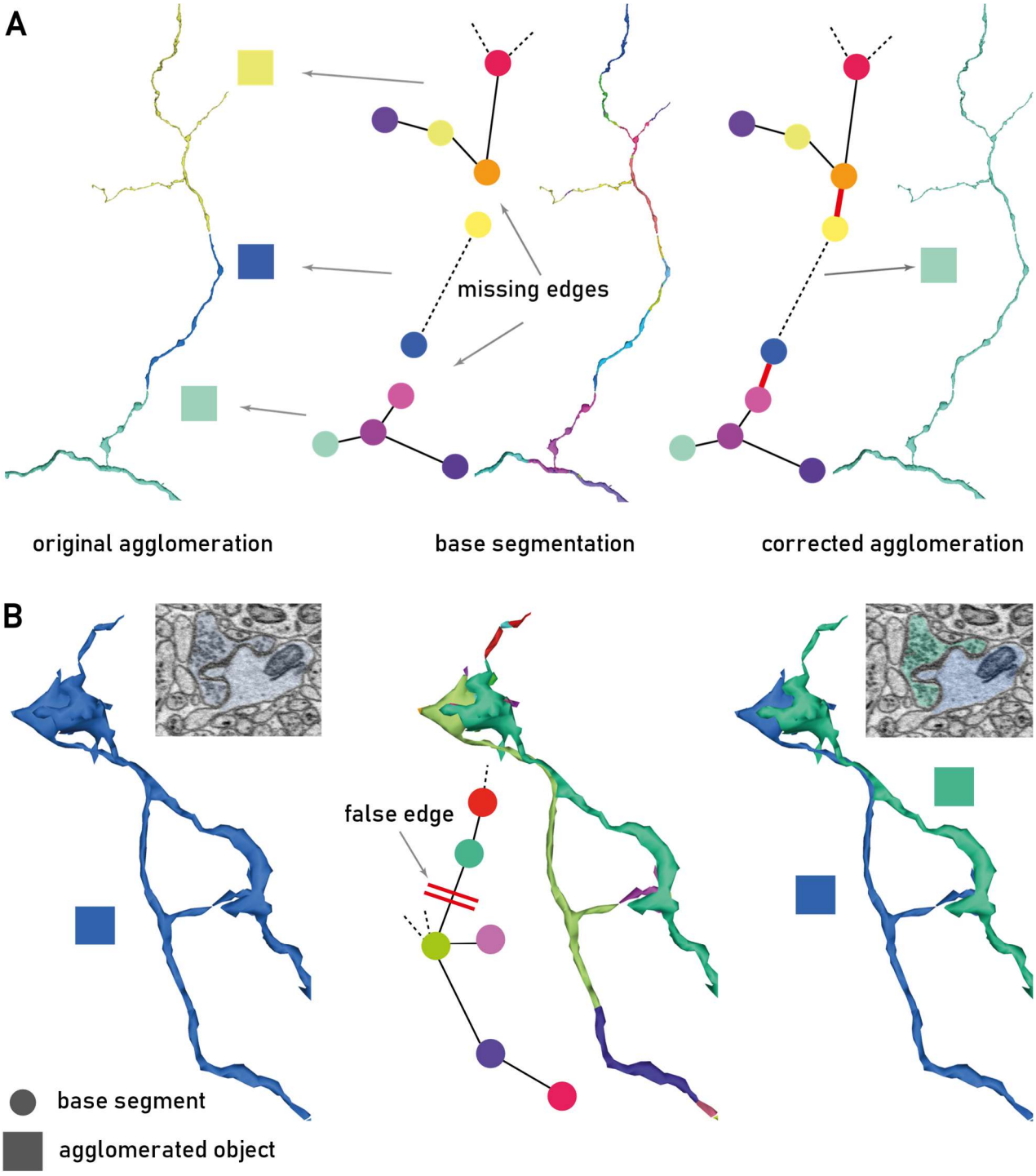

Figure 5. Illustration of agglomeration errors. A: Split errors: Left: A neurite is segmented into three agglomerated objects (squares). Center: The representation in the unagglomerated base volume. The segmentation can be represented as a graph with nodes depicting individual segments (circles). During the agglomeration process segments belonging to one neurite are determined and linked. False split errors are the result of missing edges. Right: By adding two edges the entire neurite is represented by a single connected component in the agglomeration graph. B. A merge error. Left: Two neurites have been falsely agglomerated to one object. Center: Representation of the object in the agglomeration graph. The challenge in correcting this error is to identify the falsely set edge(s). Right: After splitting the false edge, the two neurites are represented by two distinct objects.

2.3.4 THE PROOFREADING TOOL

The reconstruction of a subset of neurons in the densely segmented EM volume requires a tool that enables a fast resolution of the abundant split errors, while enabling the user to correct the less frequent merge errors. The proofreading tool provides an interface to quickly identify segmentation errors visually and correct them by modification of the agglomeration graph. This includes a toolset to address and correct split as well as agglomeration merge errors for individual neurons. The rarely occurring true segmentation mergers (see section 2.2.1 box1) cannot be fixed with this tool and have to be corrected externally through voxel painting.

The proofreading workflow is intended as follows: Single neurons are reconstructed at a time. The *neuroglancer* viewer (see section 2.3.2) displays the cells in the segmentation-raw data overlay and its mesh rendering. Starting at a soma, individual branches are followed and split off neurites are merged by means of two keystrokes. For a wide range of neurons, missing or cut branches can be easily detected from the topology of the meshed representation. Neurons with complex morphologies, like the tufty mitral cells (MCs) and ruffed cells (RCs), require more careful tracing through the segmentation-raw data overlay. In hard-to-resolve situations, the inspection of morphological and topological features of a potentially split branch in 3D can guide the merge decision. The proofreading tool comprises a branch point annotation function which allows to tag and store branching locations. Branch point annotation is helpful to structure the neuron reconstruction, especially for complex cells. Having reconstructed one of the subbranches, the function allows the user to immediately go back to the tagged branch point to complete the next subbranch.

In order to identify the segment pairs involved in an agglomeration merger, the original base segmentation volume has to be consulted. The viewer can be configured to display the original base segmentation alongside the agglomerated segmentation. The user can then display partners of a segment selected in the base segmentation volume and check whether one of its partners overlaps with the falsely merged neurite. This link can then be selectively split, and the updated agglomerated volume can be checked to see whether the merger is resolved. Functions to switch the viewer configuration and manipulate the display settings of the two segmentation volumes extend the available toolset of neuroglancer to support the reconstruction process.

2.3.5 ORGANIZATION OF THE PROOFREADING TOOL

The segmentation data is directly streamed from the *brainmaps* servers in *neuroglancer*, and several users can work on the dataset in parallel. Changes in the agglomeration graph, however, are handled locally. So, two users working on the same cell would be ignorant of the other user's input and a consensus would have to be calculated externally. The *Brainmaps API* allows to update the agglomeration graph on the server directly with these user-created changes.

THE BRAINMAPS API

The *Brainmaps API* is a private API that allows to retrieve data stored on the *Brainmaps* servers e.g., the segmentation in form of image data, triangular representations of meshes and skeletons or other metadata. The *Brainmaps API* also enables to interact with the agglomeration graph directly. Agglomeration information about individual segments can be queried, e.g., its immediate partners or its parent and the entire object the base segment has been assigned to in the agglomeration graph. Specific edges can be set and deleted.
The agglomeration proofreading tool makes use of a python package I created that ensures user authentication to access the *Brainmaps API* and implements interaction with the agglomeration graph, but also allows retrieval of image and segmentation subvolumes, skeletonized segmentation and mesh data.

LOCAL GRAPH REPRESENTATION

The *Brainmaps API* allows the modification of the agglomeration graph directly on the server. Thus, it is possible to update the graph with the user generated corrections online during proofreading. However, due to data caching in neuroglancer a reload of the data is necessary in order to visualize updates to the agglomeration graph made on the server. This procedure turned out to substantially interrupt and delay the proofreading workflow. Therefore, a strategy was chosen in which the graph modifications are handled locally.
This approach offers the advantage of storing and tracking changes of individual proofreaders easily and allows, in principle for redundant reconstructions of single cells. Furthermore, actions can be undone more conveniently without delays imposed by requests made via the *Brainmaps API*. The proofreading results can be screened or compared offline and then committed as a batch back to the server via the *Brainmaps API*.
In order to visualize the corrections made by the user, I made use of a feature of *neuroglancer* that allows to display distinct segment objects as a single object. When a segment is selected in the viewer, information about the agglomerated object, to which this segment belongs, is retrieved via the *Brainmaps API*. It is then both stored in a local graph representation and passed over to a dictionary structure in *neuroglancer*. This will trigger *neuroglancer* to stream the volumetric information of all segments but display them as one structure. During proofreading newly added branches are, thus, merged as components to the local graph. In case of an agglomeration merger the falsely set edges identified by the user are split in the local graph representation and *neuroglancer* is used to simulate the agglomerated object after the split.

CODE STRUCTURE

The code is composed of four main functional units:

LOCAL GRAPH REPRESENTATION

The agglomeration graph of the proofread neuron contains a local graph representation that is defined as a dictionary. This dictionary maps a list of connected partners onto individual segments. Built into this graph objects are functions that allow to modify the graph by adding or deleting edges and recomputing its connected components.

API INTERFACE

The API interface implements a set of graph tools that permit the retrieval of agglomeration graph information, e.g., directly connected partners or the index of the agglomerated object, for single or multiple segments.

As described above the proofreading tool uses a separate package to request information about the agglomeration graph through the *Brainmaps API*. This package is passed to the API interface and allows it to trigger requests. The proofreading tool itself does not depend on the original agglomeration graph to be stored on the *brainmaps* server. It could also be served from any other remote or local database.

NEUROGLANCER VIEWER CONTROL

A set of classes provides control over basic functionalities within *neuroglancer*, like assigning the data source or setting up the viewer layout and browser control. These classes also implement a variety of fundamental functions that permit e.g., passing messages to the users, setting and retrieving positional information, making annotations, linking keyboard and mouse input to callback functions or manipulating the viewer settings like the display and appearance of segments.

A subclass is tailored more specifically, but not uniquely limited to the demands of the proofreading tool. It creates a viewer with two segmentation volumes in a columnar layout and implements the functionality to switch columnar layouts of *neuroglancer*. These classes can be repurposed to control *neuroglancer* in other tools (see section 2.2.2 → HUMAN CLASSIFICATION OF NEURONS).

NEURON PROOFREADING

The proofreading class holds the local representation of the agglomeration graph of the neuron, provides the user access to functions to correct the graph and visualizes the update in *neuroglancer*. It implements functions to load and automatically save the local neuron graph and the edges to add or delete as defined by the user to file. To structure and support the proofreading flow the proofreading class realizes functions to set, move to and annotate branch points and functions that mediate tool-specific functions to interact with *neuroglancer*.

INSTALLATION

The tool can be cloned and installed from GitHub [146]. The tool only relies on open-source software, requires Python3 and Google Chrome to be installed and has been tested on the most common operating systems (Windows10, Linux (Ubuntu16.4, 18.4) and MacOS). In its current implementation the tool has to be started as a command line tool. This allows to set or overwrite default parameters, e.g., the data source address or the file path for local storage.

USAGE

The manual for the proofreading tool describes all options workflow for correcting false split or false merge errors, as well as additional features of the tool in detail. It can be found in the Appendix.

2.3.6 SUMMARY AND OUTLOOK

The proofreading tool allows proofreading neurons in an agglomerated segmentation by correcting split errors and false agglomeration mergers. In this study, it has been used to reconstruct 171 neurons in an agglomerated segmentation of the zebrafish olfactory bulb based on the agglomeration and proofread the agglomeration of 19 additional neurons, which were initially reconstructed by manual skeletonization (see section 2.2.1 and section 2.4.2).
The tool is designed for and permits proofreading of neurons by a larger group of proofreaders. The proofreading task can be easily learned and does not depend upon expert knowledge in neuroscience or programming. However, the following introduction into the usage of the tool should provide some intuition for a neuron's morphology to enable the proofreader to detect errors based on topological implausibility. The resolution of agglomeration mergers is more challenging than the correction of split errors and the training therefore demands more guidance and expert feedback.

The agglomeration proofreading tool is open source and can be readily used for proofreading datasets hosted by the *Brainmaps* servers. Otherwise, data has to be transformed and hosted by sources that are supported by *neuroglancer*. *Neuroglancer* is ever more widely used as a viewer for volumetric data even outside the field of connectomics and many open-source projects exist that provide tools to produce compatible data representation (e.g., https://github.com/seung-lab/igneous).

The agglomeration proofreading tool has some limitations. First of all, it does not permit the correction of segmentation mergers. However, since the segmentation was adjusted to favor split errors over merge errors, the segmentation merge rate was low in this volume. Only one segmentation merger was found in 239 reconstructed neurons. To resolve this, one could resort to voxel painting tools like VAST [111].
Due to preceding API requests to query agglomeration graph information the buildup of the mesh display is slower for the local simulation of agglomerated objects in *neuroglancer* compared to a direct

retrieval of the agglomerated object. This limitation is, however, only noticeable for very large objects, so that the advantages of the local simulation prevail.

Both speed and precision of the reconstruction and proofreading of neurons are affected by several factors. On the technical side, the better the data quality and the consecutive alignment preceding the segmentation, the better the segmentation. Better segmentation performance permits a more aggressive agglomeration procedure resulting in fewer splits without increasing the rate of false mergers. However, even with a more complete agglomerated segmentation, many neurons reconstructed in this dataset exhibit some morphological features that are challenging to segment and are unlikely to be reconstructed fully automatically without requiring human interaction. Among these are e.g., the thin peduncles of some spine types (fig. 45) or beaded neurites, in which the constriction between the beads become too thin to segment (fig. 45B).
The complex morphology of some neuron types, e.g., MCs or RCs with their tufty dendrites, makes the identification more difficult, requiring thus more proofreading time in order to achieve a comparable reconstruction accuracy as cells with simpler morphology. Ultimately, the compromise between reconstruction accuracy and speed has to be made with regard to the demand of the specific scientific question pursued. However, the possibility of cell type specific biases in completeness, which could e.g., result in a systemic underestimation of specific synaptic connections, may have to be taken into account for downstream data analysis.
There are several ways in which the proofreading and reconstruction efficiency could be optimized. Proofreading large, complex neurons is particularly time consuming because the neurons have to be followed in their entirety to detect false split errors. An alternative approach would be to detect potential split sites and inspect these selectively. Potential split sites could be determined by selectively inspecting pairs of segments within a certain range below the threshold for a merge decision. This could be done specifically and iteratively for a sparse set of cells targeted for reconstruction. While most agglomeration mergers are simple and easily resolved using this proofreading tool, identifying the false edges in a merger between large complex cells can become very cumbersome. To facilitate the split, heuristics which search and remove edges within a region of interest around the merge site closest to agglomeration threshold, could be employed.

Recently, Kornfeld et al. published a dense reconstruction of an SBEM volume of zebrafinch AreaX by first optimizing the agglomeration to specifically reduce the number of orphans [103]. Then the number of orphan branches was further reduced by manual inspection of their ends by human annotators. To correct agglomeration mergers, a subset of neurites was inspected and edges in the agglomeration graph were manually removed. Independently, the Seung lab recently published a proofreading workflow used in a series of publications [147, 148, 112, 109]. The approach makes use of a custom adapted version of *neuroglancer* for visualization and employs a custom graph representation that can be edited directly. Their approach is targeted for large scale proofreading and has been the basis for FlyWire, an open and crowdsourced proofreading platform for the FAFB dataset [112].

2.4 RESULTS

This section describes the findings of my neuroanatomical study in the adult zebrafish olfactory bulb. I give a detailed depiction of projection neurons and interneurons, which I characterize based on topological and morphological features. Based on this analysis I propose the existence of three subclasses of mitral cells and ten classes of interneurons, four of which can be further subdivided into ten subclasses.

An additional, qualitative investigation provides first insights into the interactions between representatives of the different interneuron classes and the projection neurons.

2.4.1 EM VOLUME OF ADULT ZEBRAFISH OB: DESCRIPTION OF THE DATASET

A large volumetric SBEM dataset of the zebrafish adult olfactory bulb (OB) was acquired previously, as described in [118] and [90]. In brief, the volume of the stack is a cuboid (288 x 173 x 98 μm^3) and contains ca. 4900 somata, covering about 18% of the adult zebrafish OB in volume and cell number [90]. The long axis of the cuboid extends from the surface of the ventro-lateral OB deep into the dorso-medial parts (fig. 6A). It encompasses the superficial glomerular layer (GL), the intermediate plexiform layer (PL) and the deep granule cell layer (GCL) (fig. 6B). A brief qualitative description of their appearance in the dataset is given in the following.

THE GLOMERULAR LAYER

The GL was dominated by neuropil composed of the darkly stained sensory axons and the dendrites of projection neurons (PNs) and local interneurons (INs). The sensory axons traversed the glomerular layer in bundles of several hundred individual axons [90], often enwrapped by thin glial sheaths. In the most peripheral parts of the GL these bundles assembled to even larger bundles traversing the stack from anterior to posterior. Sensory axons that entered the OB terminated in microglomeruli of varying size and shape [90]. The diffuse nature of sensory innervation and the absence of glomeruli proper has been previously reported as characteristic for the ventro-lateral region and the lateral plexus (LP) of the zebrafish OB [46]. Based on comparisons with light microscopic image stacks of labeled sensory axons [33], it can be assumed, that the volume was recorded in the transition region between lG and LP, just anterior to LP. Since the sensory axons were excluded from the neuropil segmentation to enhance segmentation performance, a volumetric reconstruction of individual sensory axons was not possible. The 3D rendering of the tissue mask created for sensory axons (see section 2.2.1), however, revealed that bundles of sensory axons, which were likely aggregated projections of OSNs that terminated in similar regions [79], followed quite complex trajectories (fig. 6D). Axon bundles branched frequently and formed bulbous local enlargements, where synaptic contacts to secondary olfactory neurons were formed, before they continue their course through the GL. The bulbous enlargements of sensory axons were mainly presynaptic and synapses between sensory axons were found (fig. 6F, G). Many axon bundles branched and formed complex loops, innervating quite separated parts of the imaged volume before reuniting (fig. 6E). Further investigation is needed to learn more about the origin and composition of sensory axon bundles, to determine the homogeneity of the presynaptic component of microglomeruli in this region of the OB of zebrafish. In between the neuropil isolated somata of various sizes and shapes belonging to superficial INs as well as ruffed cells (RCs), mitral cells (MCs), and glial cells, mainly astrocytes, were loosely distributed. Several blood vessels traversed the GL.

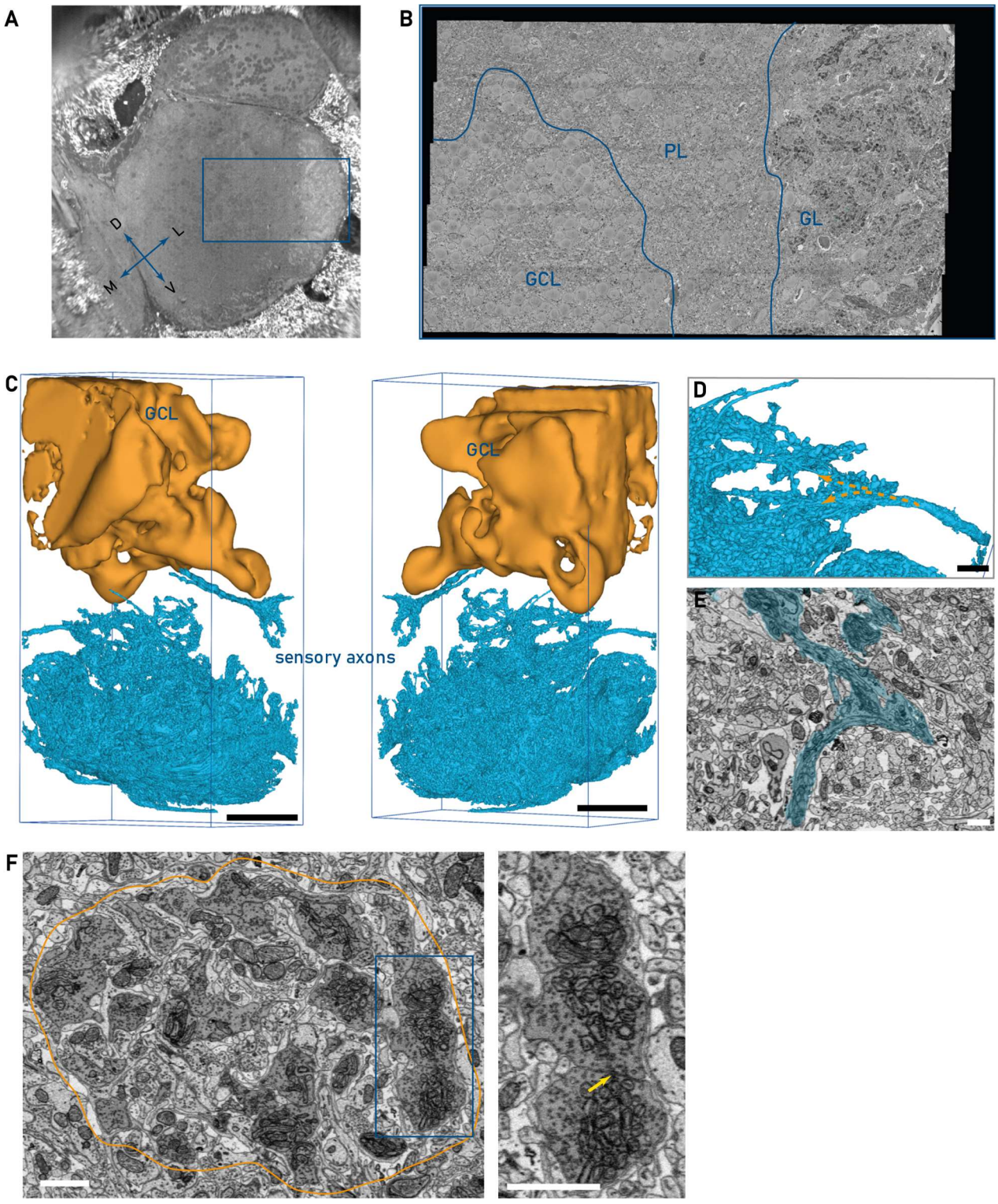

Figure 6. Composition of the dataset A. Positioning of the recorded EM volume in the OB (adapted from [90]). B. A central image section: the boundaries of GCL, PL and GL are outlined. C. Volumetric representation of the sensory axons bundles (blue) and the GCL (orange). D: Sensory axon bundles made complex trajectories bifurcating and reuniting. E: Image view on the bifurcation of the axon bundle shown in D. F. Left: Example of microglomerulus: Sensory axons stand out by the dark stain. The large boutons were filled with myriad mitochondria and synaptic vesicles and made synapses onto OB neurons. Right: Sensory axons made synapses onto each other (arrow). Scale bars: B & C: 50 µm, D: 10 µm, E–G: 1.5 µm.

THE PLEXIFORM LAYER

The plexiform layer stretched as a band in between GL and GCL and encompassed the GCL at the dorso-lateral and antero-lateral side (fig. 6B). The border region between the GL and the PL was often marked by a somewhat denser arrangement of somata belonging to MCs, RCs, and superficial IN, which innervated glomerular structures superficial to their cell bodies. Within the PL few somata can be found. These somata were usually isolated or occurred in small clusters on the order of five somata. Microglia were prominent in PL. However, the majority of the PL was dominated by dense neuropil. Dendrites of deep layer INs, which traversed the PL towards the GL, could be identified by their large diameter, clearly visible microtubules, and a relatively bright cytosol, which was populated by darkly stained ER. Very few myelinated axons passed through the PL. Many neurites filled with vesicles and synapses were abundant, indicating that the PL is an important location for local circuit computation.

THE GRANULE CELL LAYER

The GCL is located on the medial and ventro-medial side of the data set and covers around a third of the imaged volume (fig. 6B, C). It was distinguished by large clusters of ten and more, small to medium-sized somata, that were densely packed. The cell clusters were heterogeneous in that members could be representatives of various different kinds of morphological classes of deep layer INs (see IV. INTERNEURONS OF THE DEEP LAYER). Patches of neuropil of varying size could be found in between these cell clusters. The transition zone between PL and GCL was not very distinct, with large, dense cell clusters stretching well into the dorso-lateral PL. Similar to PL, the GCL neuropil was characterized by massive neurites of deep layer INs directed towards the superficial layers and an abundance of smaller vesicle-rich neurites.

2.4.2 LARGE-SCALE NEURON RECONSTRUCTION

To obtain a volumetric reconstruction of neurons of the adult zebrafish OB the SBEM image stack was automatically segmented by our collaborators at Google using flood-filling networks [100]. In brief, this machine learning approach uses 3D CNNs trained on volumetric GT. Manually created skeleton reconstructions of neurons serve as GT for the selection of segmentation versions. This method aims at an oversegmentation of the tissue to avoid merge errors, which is compensated by a successive agglomeration procedure (fig. 5, for details see section 2.2.1 box1).

The final agglomerated segmentation volume had an error-free path length (ERL) of 741 µm and an edge accuracy rate of 70%. The dataset had certain properties that are challenging to segment by FFNs, in consequence both ERL and edge accuracy are below the performance published [100]. On the technical side, there were small, but frequent and distributed misalignment issues that triggered a

halt of the flood filling algorithm and caused split errors (fig. 7B). Areas with unfocused images caused spillage of the segmentation across membranes, resulting in false mergers (fig. 7A). Further improvements of the alignment and additional GT from challenging areas is expected to improve the segmentation performance. In addition, intrinsic properties of the imaged biological structures impeded segmentation and agglomeration. Among these were for example very thin neurites or beaded neurites in which the lumen is separated by tight constriction (see e.g., fig. 25A, fig. 45B), both causing split errors, which needed to be fixed manually. Glial or neurite sheaths wrapping around branches or spines could result in merge errors (fig. 7D).

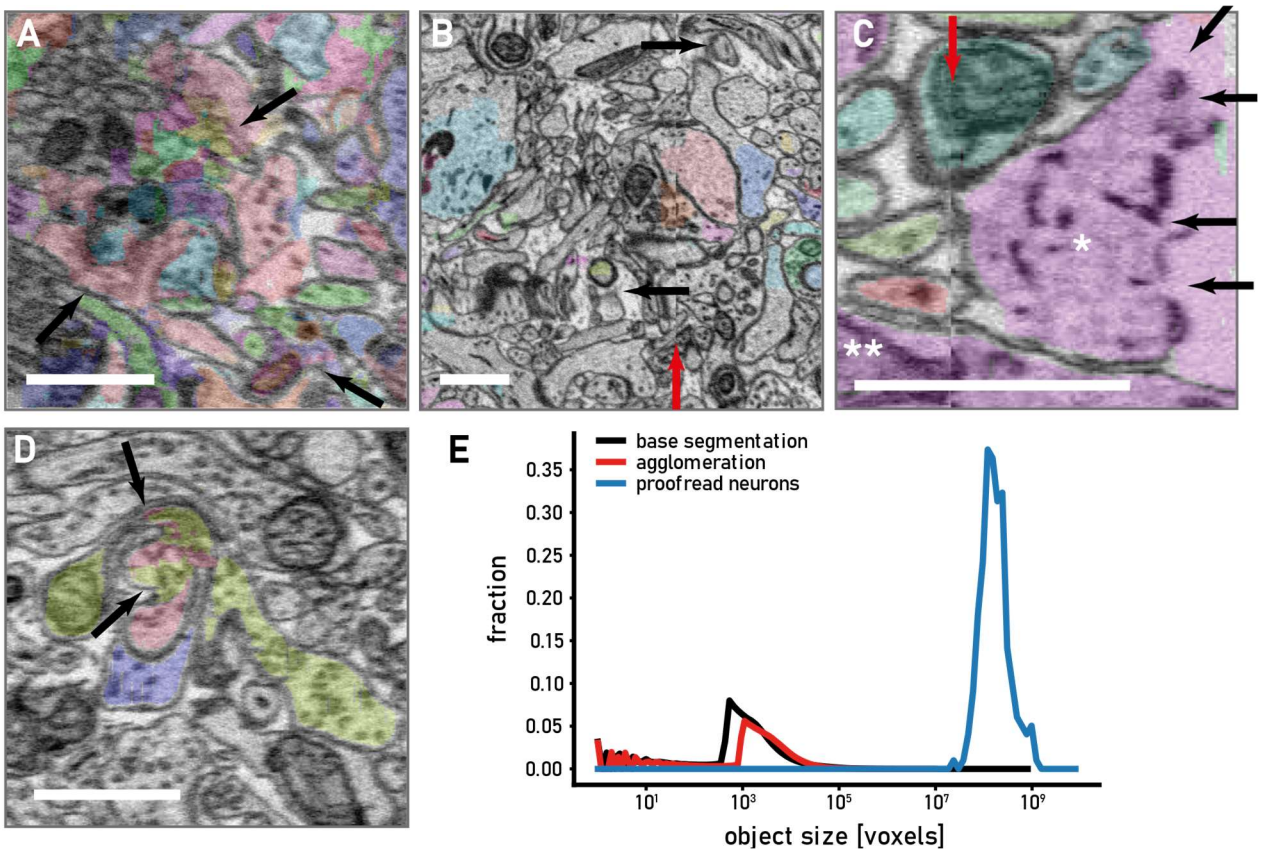

Figure 7. Technical and biological aspects impair segmentation quality. A. An unfocused area caused segmentation errors of the small neurites and spillage into the extracellular space (ECS). Ground truth targeting such areas could counter this. B. Example of substantial distortions within the image tiles (black arrows) and alignment artefacts at image tile borders (red arrow) resulted in a forced segmentation stop and omission errors in order to avoid false mergers. C. A ruptured membrane (black arrows) caused spillage of the segmentation into the ECS and caused a merger of the neurite (*) to the glial branch (**). The FFN pipeline was able to compensate misalignment artefacts, which were not too severe (red arrow: misalignment of tiles). D. Challenging properties of the biological tissue: A neurite (red) was "swallowed" by another (blue) and a third neurite (yellow) wraps around the resulting structure. The layers of membrane were difficult to segment and caused the segmentation to spill into the false neurites (arrows: red voxels in yellow object and vice versa). E. Distribution of voxel size of segments in the base segmentation (black), objects in the agglomeration (red) and of the fully reconstructed neurons (blue). Scale bars: 1 µm.

While small objects still dominated (fig. 7E) the agglomerated segmentation, many neurons were already well reconstructed by this segmentation. The fraction of a neuron represented by its largest

agglomerated object relative to its final size after proofreading is shown as a distribution for 239 neurons in fig 8A. The largest object represented on average 81.2 ± 0.1% in voxel size and 65.3 ± 0.1% in length of the *TEASAR* skeleton (see section 2.2.2). Whilst the agglomerated segmentation volume already reconstructed many cells very well, a complete or near complete neuron reconstruction required further manual proofreading. Therefore, I created a software tool that allowed me to reconstruct neurons by fixing both agglomeration split and merge errors. A scheme of the reconstruction procedure is shown in fig 9 (for a detailed description of the proofreading tool see section 2.3).

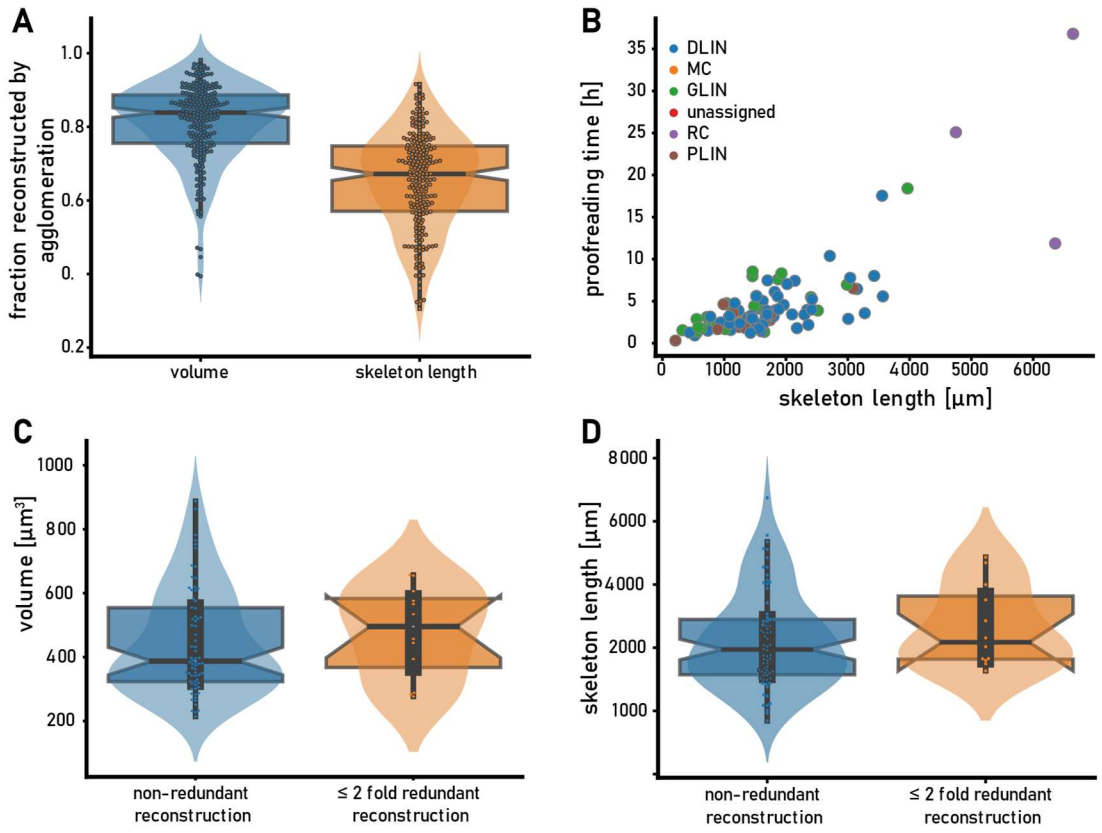

Figure 8. Analysis of the neuron reconstruction procedure. A: The fraction of a neuron represented by its largest agglomerated object in terms of volume and length. B. The proofreading time scales with skeleton length. Less complex neurons like the DLINs were by trend faster to reconstruct. C & D: Comparison of volume (C) and neurite length (D) distribution for DLINs with CD < 3 reconstructed in a non-redundant fashion vs. DLINs reconstructed with two or threefold redundancy as skeletons first. By trend the redundant reconstructions were larger. This difference is however not significant (students ttest: volume p=0.38, neurite length p=0.53).

I used this tool to reconstruct 244 cells. This set comprised 32 PNs, 61 INs of the GL, 36 INs of the PL and 110 INs of the GCL. Four cells were identified as glial cells by the lack of outbound synapses and morphological consistence with microglia. A single IN had a segmentation merger, which could not be split. This did not impair the manual classification and the neuron was treated accordingly for semi-automatic classification (see section 2.2). Altogether, for the reconstruction of 239 neurons 184,096 split errors and 317 merge errors were corrected.

Initially, I selected putative PNs for reconstruction. From these I identified synaptically connected INs and reconstructed those INs where the soma was located in the imaged volume. I extended the set by reconstructing partners of these INs. At later stages in the reconstruction process, I aimed at increasing the number of representatives of identified or presumed morphological neuron classes. The choice of neurons was thus biased towards classes connected to PNs and the set of reconstructed neurons should only coarsely represent the true distribution neuron classes in the OB. The neurons were preserved to different degrees within the imaged volume: I rated the completeness of neurons in a cutting degree (CD, see section 2.2.1) from fully preserved (CD0: 37/239 (15%)), minimally cut (CD1: 87/239 (36%)), considerably cut (CD2: 72/239 (30%)) to substantially cut (CD3: 43/239 (18%)).

2.4.3 SYNAPSE DETECTION

The resolution of the SBEM and the stain were appropriate for the identification of chemical synapses [93], but not gap junctions. However, the detailed annotation of synapses also had limitations. Because of the oversaturation of the lipid plasma membrane with osmium, the protein rich postsynaptic density was equally stained as other membrane regions and was not unambiguously identifiable. This prevented a distinction between symmetrical and asymmetrical synapses and thus the identification of inhibitory and excitatory synapses in this dataset. Moreover, synapse detection was complicated by the fact that most neurites in the OB are both pre- and postsynaptic structures. Furthermore, the abundance of vesicles in many neurites made the precise location and direction of synapses difficult to identify. Additional features such as the fusion of vesicles to the plasma membrane or a darkening of the synaptic cleft had to be considered as well for synapse annotation. Because of the high variability in the synapse assignment between and within annotators requires redundant annotations for reliable synapse detection.

A detailed analysis of synaptic connectivity between OB neurons is beyond the scope of this study. Nevertheless, inputs and outputs observed for particular morphological cell classes will be described based on non-redundant annotations of synapses in subsets of neurons. These observations are therefore not exhaustive but serve as a qualitative description of the richness of interactions of representatives of a morphological subclass with the surrounding OB network. Focusing primarily on PN-IN connectivity, I conducted an examination of interactions between INs and PNs within a specific glomerulus for each identified morphological IN class. This involved searching for contact sites between pairs of INs and PNs and validating the presence of a synapse in the image data in all or a subset of contacts (for details see section 2.2.3). An IN-PN connection was defined as broad, if the IN connected to more than 40% of that PN subtype, i.e., MC or RC, in a given glomerulus, and otherwise as selective. Furthermore, the number of contacts between a given IN-PN pair was considered high, if it exceeded three synapses, and low otherwise.

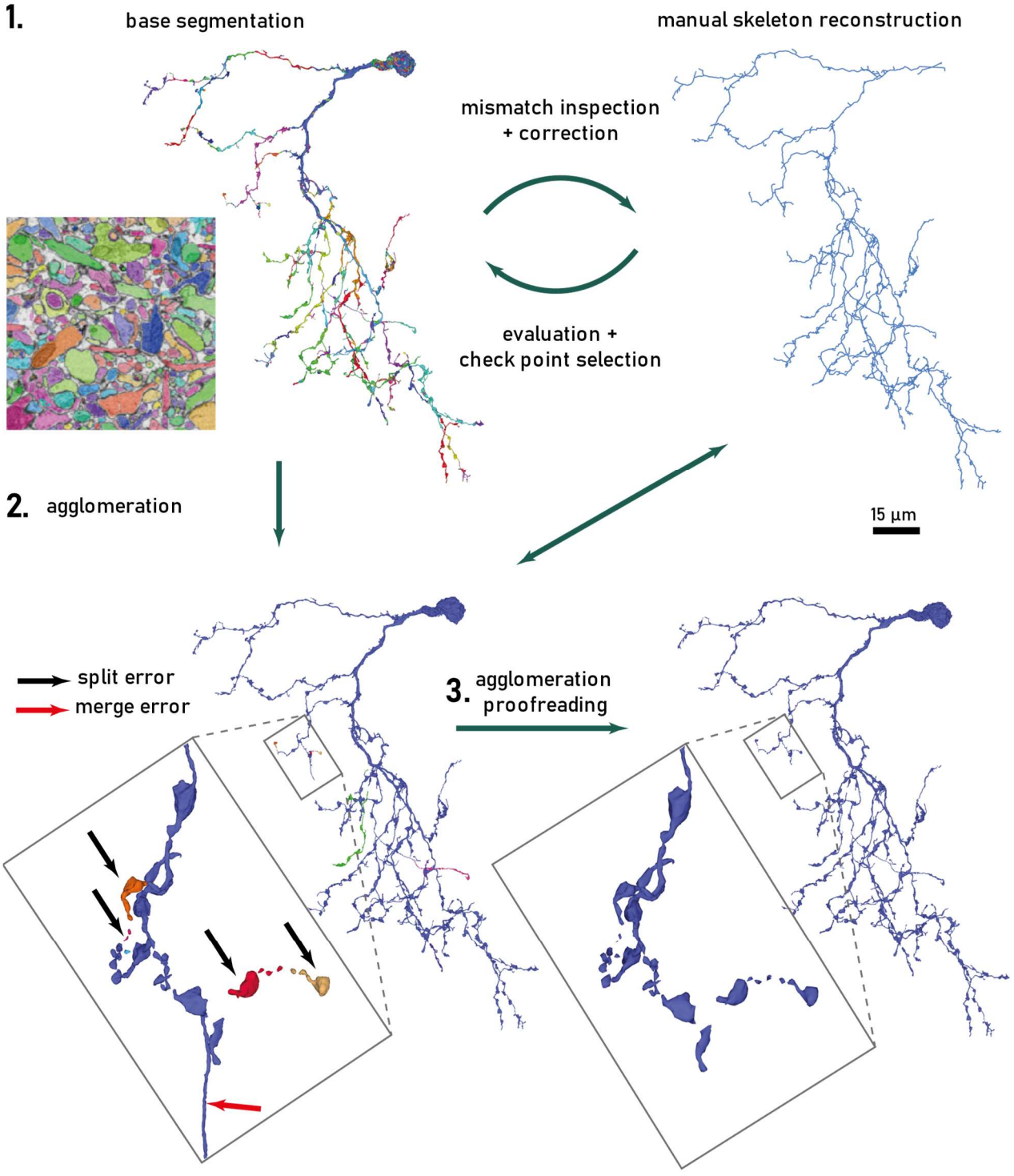

Figure 9. Scheme of the reconstruction pipeline: 1. Volumetric segmentations were automatically created by FFNs. To determine the segmentation version ("checkpoint") which best reconstructs neurites, manually traced skeletons served as reference. Juxtaposition of skeletons and segmentation revealed mismatches, which were inspected and mistakes in the skeletons were corrected. The base segmentation was oversegmented, i.e., biased towards split errors in order to avoid the introduction of false mergers, which are difficult to correct. 2. The oversegmentation of the base segmentation was countered by an agglomeration procedure, which combined segment objects presumed to be in the same neurite. Again, manual skeletons guided the choice of an optimal agglomeration volume. 3. Remaining mistakes in the agglomeration were corrected by proofreading individual neurons to obtain a full volumetric cell reconstruction.

2.4.4 MORPHOLOGICAL CLASSIFICATION OF OB NEURONS

The 239 reconstructed neurons exhibited diverse appearance suggestive of multiple different morphological classes of both PN and IN. However, little is known about the neuronal diversity in adult zebrafish OB. To delineate morphological classes, I first used a classical anatomical approach based on visual inspection. I thoroughly examined and described the reconstructed neurons in a qualitative manner, considering features across many different levels of detail that range from low resolution features like the position, size, extent, and shape of the neurite tree to more close-up features like the frequency and aspect of spines and varicosities, the shape of neurite cross sections or the surface structures to ultrastructural features like the appearance and distribution of cellular organelles. In addition, I selectively describe interactions representative of neuron classes. These interactions comprise not only connections mediated by chemical synapses but also observations of membrane contacts suggestive of some other form of cell-to-cell communication.

Furthermore, I recorded the presence of an axon or spines. Given omnipresence of pre- and postsynaptic structures in neurites of OB neurons, the term axon requires definition. The term neurite was used to refer to any branchlike neuron structure. A neurite was considered an axon if it was myelinated or comprised a ruff, but also, if it was morphological distinct from other neurites of that cell with features typical for axons, e.g., a smaller diameter, the absence of spine-like appendages, or the exclusive presence of presynapses. Following this definition, axons of OB neurons may receive input and make reciprocal synapses. All other neurites were referred to as dendrites and most neurons in the OB had dendrites that make outbound synapses.
I considered a neuron spiny, if it made multiple dendritic protrusions that could be roughly classified into known spine classes, i.e., mushroom, thin, stubby and filopodial [149], and if most of these structures were postsynaptic.

In addition to the description of PNs, I describe ten morphological classes of INs. These IN classes were denominated according to the respective OB layer in which the majority of reconstructed representatives of this class occurred and numbered them serially. The first class of INs of the glomerular layer is e.g., named GLIN1 and so forth. For nomenclature of subclasses, I assigned names that contained identifying characteristics that distinguish members, e.g. small GLIN1s and large GLIN1s.

2.4.5 MORPHOLOGICAL CLASSES IN ADULT ZEBRAFISH OB

PROJECTION NEURONS

Volumetric reconstructions of 32 PNs, 24 MCs and 8 RCs were obtained (CD0: 8, CD1: 19, CD2: 1, CD3: 4). PNs were identified based on features described as distinctive for MCs and RCs in the teleost OB in previous publications [117, 85, 94, 84, 86], namely the location of a comparably large soma in the glomerular layer, the presence of an axon and a tufted dendritic tree.

THE POSTSYNAPTIC GLOMERULAR ORGANIZATION

The 32 PNs could be divided into five distinct, self-contained groups based on the spatial organization of their dendritic trees, which overlapped substantially among PNs within each group but not across groups. To verify that the emergence of these structures was not a result of a bias towards neighboring neurons selected for reconstruction, an additional 54 PNs (45 MCs, 9 RCs) were coarsely proofread. In addition, six orphan branches identified as MC dendrites were reconstructed, to better delineate assemblies located at the border of the imaged volume. The coarse proofreading involved the removal of all obvious topological mergers and the fixing of splits to a degree that revealed the overall dendritic topology of the cell. This included correcting splits in major branches, carefully scanning the outline of the dendrites and adding all split branches found, but not thoroughly tracing along all the branches. Due to morphological differences (see I. CLASSES OF PROJECT NEURONS) this form of reconstruction results in a higher level of incompleteness for RCs than MCs. These reconstructions lack completeness in the fine structure and do not qualify for a quantitative connectomic analysis, but they are sufficiently precise to determine the morphological subtype and to appreciate the spatial extent of the dendritic tree.

The addition of the coarsely reconstructed cells confirmed the presence of the five self-contained dendritic assemblies and also revealed the presence of five additional clusters. The spatial organization of the dendrites suggests that members of a particular assembly share local in- and output through their dendritic synapses. Common OSN input to several PNs was confirmed. These clusters are henceforward referred to as glomeruli. The ten glomeruli were densely packed, nevertheless discrete, and filled almost the entire ventro-lateral GL in the stack. The composition of cells, the level of completeness in their representation and reconstruction, as well as the extent of each glomerulus is summarized in table 3.

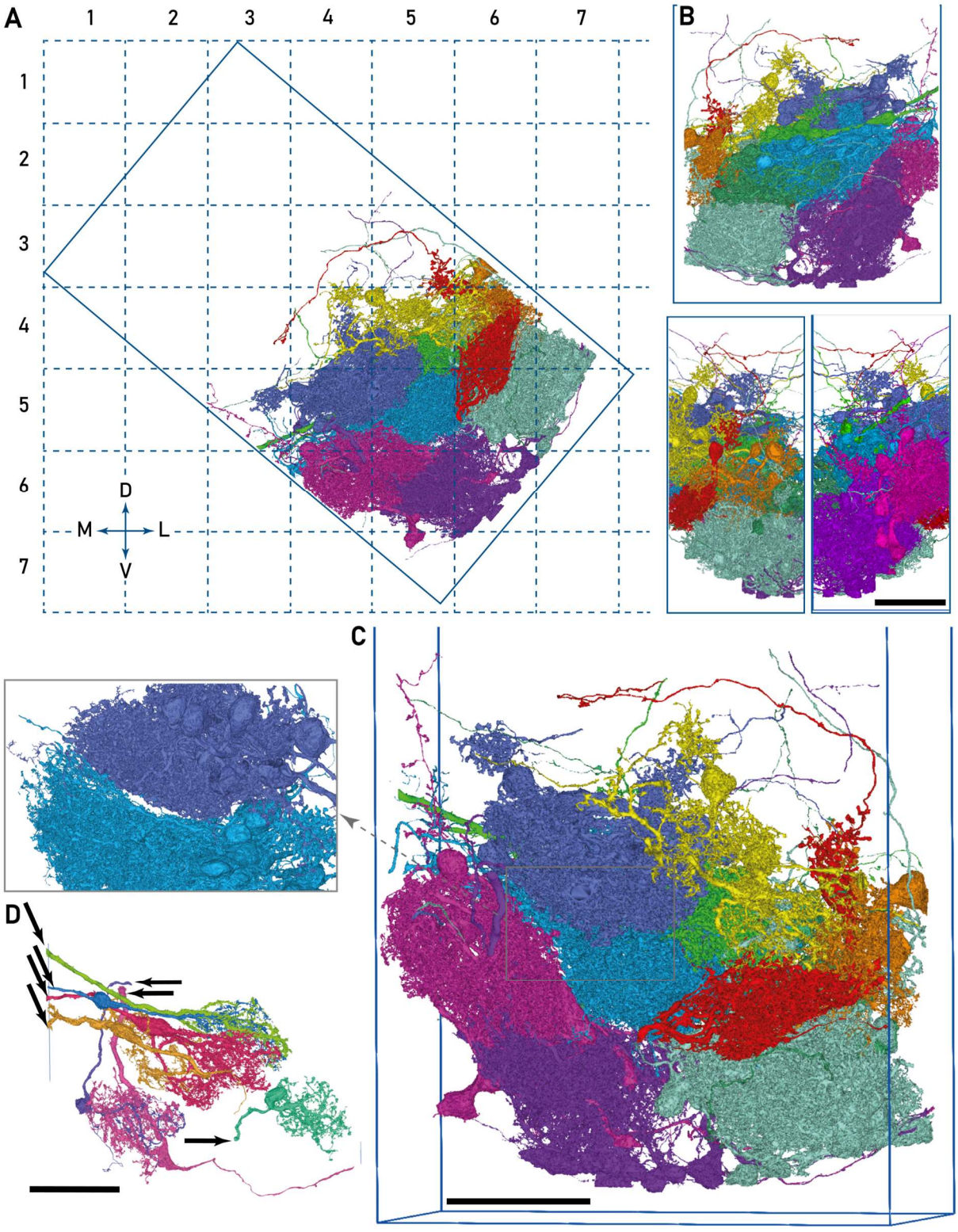

Figure 10. Glomeruli within the imaged volume. A: Embedding of the imaged volume within a grid of 50 µm oriented to the animal's body axis. All glomeruli are shown from the anterior side. B: View onto all glomeruli from posterior to anterior (top), dorso-lateral to ventro-medial (bottom left) & ventro-media to dorso-lateral (bottom right). C Higher resolution image of all glomeruli from the anterior side. Inset: Close-up on M45D45A1 (dark blue, top) and M5D5A12 (light blue, bottom), glomeruli were well-separated and self-contained structures. D: Some large and intermediate MCs were potentially multiglomerular projecting a large neurite out of the imaged volume (arrows). Scale bars: 50 µm

glomerulus	MC	RC	CD0	CD1	CD2	CD3	width [µm]	depth [µm]	height [µm]
M56D56A2	4 CR	2 CR	3	3			85	75	55-60
	11 ICR		1	3	5	2			
M45D56A1	4 CR			4			60	45	30
	3 ICR	2 ICR		3	1	1			
M5D5A12	11 CR	2 CR	5	5		3	80	70	40
	2 ICR					2			
M45D45A1	2 CR	3 CR		4		1	70	40	30
	7 ICR			1	5	1			
M5D4A12	4 ICR	1 ICR	2	1	1	1	40	60	20-30
M67D45A12	3 CR			3			75	80	50-60
	7 ICR	2 ICR	1	5	2	1			
M6D45A1	5 ICR	1 ICR		1	1	4	40-50	20	20-30
M456D4A1	3 ICR	2 ICR				5	70	30	30
M45D4A2	7 ICR			1	4	2	60	25	30
M6D34A12		1 CR		1			30	60	30-40
	2 ICR	1 ICR		1		2			

Table 3. Overview of glomeruli identified in the OB volume and numbers of associated PNs. Abbreviations: ICR: incompletely reconstructed, CR: completely reconstructed, CD: cutting degree, MC: mitral cell, PN: projection neuron, RC: ruffed cell.

In the context of this study, these glomeruli are labelled according to their position within a grid which is superimposed onto the imaged volume and has its origin at the anterior, medial and dorsal extreme of the stack (Fig. 10A). The medial to lateral axis and the dorsal to ventral axis are unitized into eight and seven sections of 50 µm, respectively. The anterior to posterior axis is split into two 49 µm sections. Thus, the M45D56A1 is a glomerulus which covers the 4th and 5th section along the medio-lateral axis, the 5th and 6th section along the dorso-ventral axis and remains within the first section of the anterior-posterior axis.

Located at the most ventral side, this well-defined glomerulus of moderate size enfolded an ovoid volume formed by the dendritic arbors of nine PNs. It was slightly cut at the left and anterior border of the image stack. In its center, M45D56A1 exhibited a hole through which a bundle of seven thick MC dendrites projected (Fig. 11B). M56D56A2 was a large glomerulus formed by 17 PNs which assembled their dendrites into a large ellipsoid with a closed surface to the ventral, medial, and anterior side, but cuts at the posterior side. The dorso-lateral and posterior side of this glomerulus displayed holes, where further PN reconstructions were missing. Two large MCs of this glomerulus projected a thick dendritic branch outside the glomerular and imaged volume (Fig. 11A). The central M5D5A12 was the best-preserved glomerulus with only minor cuts at the anterior side. It was constituted by 15 PNs which assembled to a large tassel, (Fig. 11K). At its medio-dorsal side lay M45D45A1, a large glomerulus composed of 12 PNs and notably cut at the anterior side (Fig. 11C).

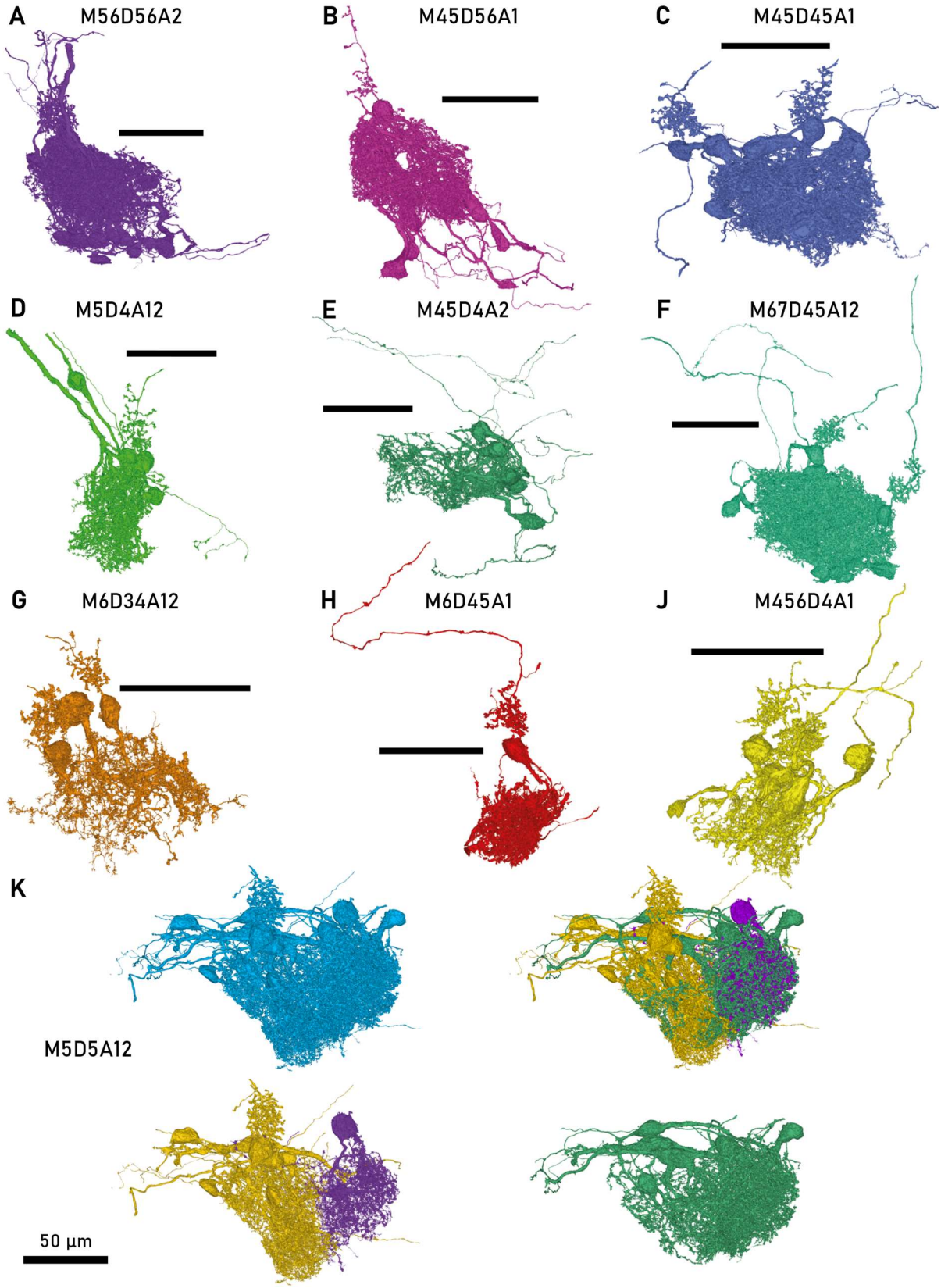

Figure 11. Individual glomeruli identified within the imaged volume (A–J). K: The central glomerulus M5D5A12 consisted of three PN subgroups (top right): Two self-contained subcompartments formed by eight and two PNs, respectively (bottom left) were linked by five large PNs projecting to both compartments (bottom right). Scale bars: 50 µm.

M5D4A12 was made up by five PNs, very compact and only slightly cut at the anterior side (Fig. 11D). M67D45A12 was a large, globular structure constituted by 12 PNs that was somewhat truncated at the posterior side (Fig. 11F). Four further glomeruli, M45D4A2, M6D34A12, M6D45A1 and M456D4A1, were located on the dorso-lateral portion of the imaged volume. These glomeruli were all only partially represented in the image stack and their true size could not be assessed (Fig. 11E, G-J). M45D4A2 also comprises at least one RC, which has, however, not been reconstructed, because of a severe merger with a glial cell that could not be corrected. None of the glomeruli were reconstructed to the entirety of the PNs they were composed of.

The sister cells belonging to one group substantially overlapped in the projection of their dendrites. With very few exceptions, MCs were entirely confined to one glomerulus, despite the close proximity to other glomeruli (Fig. 10B). A few RCs extended isolated dendrites out of the glomerulus. A closer examination of the central glomerulus, M5D5A12, indicated that the group might be composed of two subcompartments of eight and two PNs, respectively, which were joined by five larger members. These larger members themselves showed a bias towards projecting the majority of their dendrite to only one of the subcompartments, thus, creating a link through a single, yet still massive subbranch (Fig. 11K). Similar subcompartmentalization are present in two further, large glomeruli (not shown): The two compartments of M56D56A2 were made up by ten and two PNs, respectively, linked through five larger MCs. In M67D45A12, the overlap was much smaller with one MC joining two subcompartments composed of seven and three PNs, respectively.

Locally, neurons belonging to one glomerulus did not show a pronounced tendency to project their axons in a common direction.

I. CLASSES OF PROJECTION NEURONS

	PN class	cell count	axon collaterals	cell volume [µm³]	total length [mm]	soma volume µm³]	soma diam. [µm]	n glomeruli	sensory input	dendro-dendritic synapses
MC	small MC	8	++	542 ± 221	2.0 ± 0.8	217 ± 68	11.0 ± 1.2	1 (+)	+++	+++
	intermediate MC	4	+	1116 ± 350	4.1 ± 0.7	394 ± 69	12.9 ± 1.5	1 (+)	+++	+++
	large MC	12	-	1958 ± 522	7.0 ± 1.5	667 ± 244	15.2 ± 2.8	1	+++	+++
RC		8	-	1186 ± 318	6.3 ± 2.0	633 ± 109	14.1 ± 1.4	1	+	-

Table 4. Selected features of PNs. Abbreviations: –: absent, +: present, ++: pronounced, +++: very pronounced. Numbers given as mean ± standard deviation.

All glomeruli were composed of various quite distinct morphological subtypes of PNs that will be described in the following. Previous studies have subdivided zebrafish MCs based on the number of primary dendrites [81] or based on the number of glomeruli they innervate [83]. Here, I describe three morphological subclasses of MCs as well as RCs in detail. A schematic of PN classes that are part of a given glomerulus in zebrafish OB is shown in fig. 12, table 4 summarizes the main morphological features of these (sub)classes. The MC subclasses differed most notably in size (see table 4, fig. 13), but also expressed variation in some other morphological features.

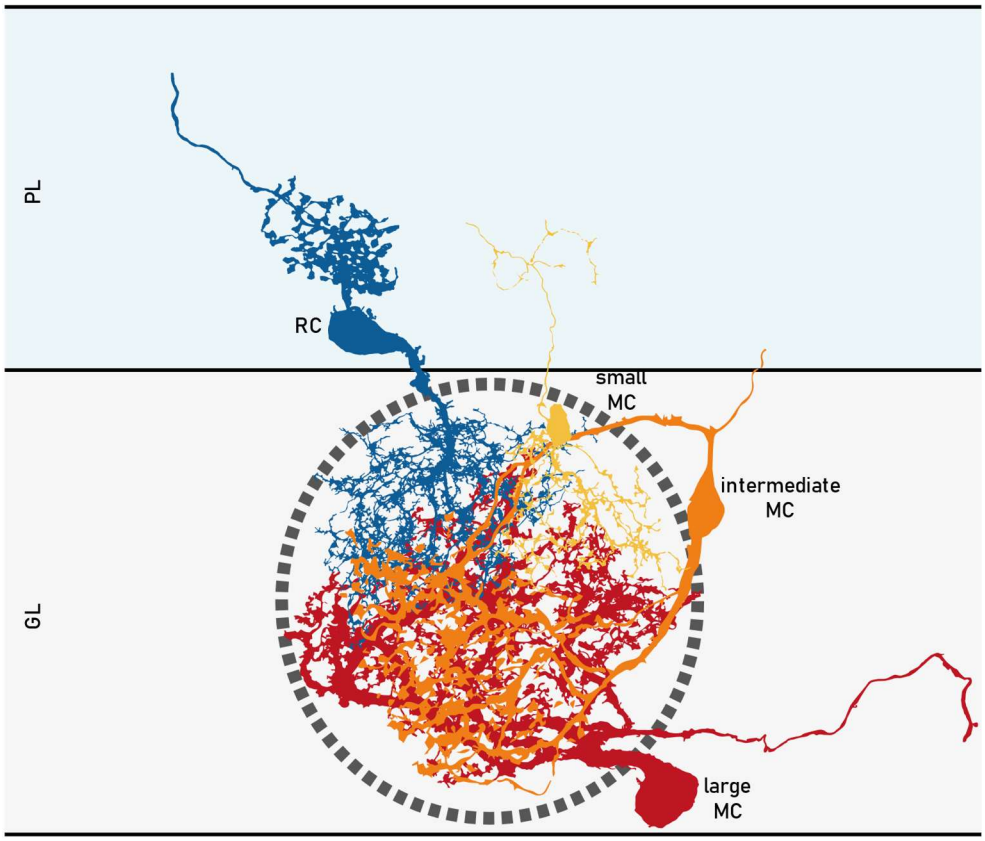

Figure 12. Schematic representation of PN classes of a glomerulus.

MITRAL CELLS

Before describing differences between MC subclasses, I will summarize their common features.

Morphology

The somata of MCs were located in considerable distance to the glomerulus they innervate, with sister MCs being distributed to all sides of the glomerulus. The cell bodies were confined to the GL and most superficial PL. Many MC somata were located at the very surface of the OB, where no cell bodies of other neurons could be found. MCs somata displayed a large diversity in shape: ovoid, triangular, globular and soma of very irregular outline were observed. The soma size varied across subclasses with cell size (see Fig. 13B). The nuclei were large, predominantly ovoid, frequently displayed a wrinkled and indented surface and contained several large nucleoli (see fig. 14D). The amount of

cytoplasm immediately surrounding the nucleus differed substantially between cells and seemed to relate to the overall soma size only loosely. In cells in which the nucleus was separated from the plasma membrane by only a thin layer, one or more large bulges of cytoplasm could be found at either pole of the soma, usually where a primary dendrite emanated. The perikarya were full of organelles. A myriad of ER cisternae, plenty of mitochondria, as well as lysosomes and endosomes at different stages could be observed. Multiple Golgi apparatus were noticeable, usually, but not exclusively, accumulating at the base of a primary dendrite. In larger cells with massive primary dendrites, organelles of the perikaryon spread well into the dendrite. In most MCs (24/25) a single primary cilium could be identified. These cilia arose from the soma or the base of the main dendrites, projected into the surrounding cytosol and were of medium length (0.5 - 4 µm, $\bar{x} \pm \sigma$: 2.7 ± 0.8 µm).

The axon could arise from either soma or a larger dendrite. Axons emanating from the soma could be recognized by the (relative) lack of cellular organelles reaching into the emerging branch and by their small diameter in comparison to dendrites. This relationship held across subclasses though the effective initial diameter varied from ~500 nm in small MCs to > 1 µm in large MCs. When the axon emerged from a dendrite, it usually branched off before the process ramified into a bushy dendrite. However, in rare cases a process also gave rise to several tufty side branches before tapering off and adopting an axonal appearance. The axons of 16 MCs exhibited myelination within the imaged volume. Axons usually travelled over tens of µm, before becoming myelinated. The direction of axons had a bias for a lateral projection. There was no pronounced tendency of axons to align or to form bundles, sometimes, though, myelinated axons travelled over some distance in small groups of <5 (see fig 15A). Due to the limited size of the stack, it could not be determined whether the tendency to fasciculate was more pronounced as MC axons approached their exit points of the OB. With the exception of two intermediate MCs, local collateralization had only been observed for members of the small MC subclass.

The most distinct feature of MC dendrites was the high variance in diameter due to frequent dilations and shrinking along the entire dendritic tree. This became particularly pronounced in distal processes of higher branch order, where thin, sometimes filamentous dendrites abruptly broadened into large varicosities (see fig 14B). In contrast to other neurites with repeated varicosities (see e.g., DLIN2), the structure of these branches did not resemble a pearl necklace. The varicosities were irregular in shape, uneven or ragged in surface and occasionally bore various excrescences. Very often these enlargements gave rise to several subbranches. The cytosolic composition distinguished these dendritic varicosities as sites of synaptic interaction (see fig. 14E). They contained at least one, but usually many, dark mitochondria of different sizes immersed in a large volume of cytosol. Further, an abundances of membrane structures of varying sizes and shapes could be found. Extensive membrane sacs with large lumen, often darkly stained, could be identified as cisternae of the ER. Smaller vesicular structures, clearly larger than synaptic vesicles, some globular, some rather ellipsoid, were scattered through the cytosol, often intermingling with synaptic vesicle clouds. These might be clathrin-coated reuptake vesicles, endosomes, or secretory vesicles. Synaptic vesicles were globular and appeared

larger than those found in neighboring IN. In many cases they were so numerous that it was difficult to distinctly outline a vesicle cloud and assign it to a specific synapse. MC dendrites did not taper towards the tip branches, but rather terminated in rod-shaped, sometimes bulbous structures. These rods were usually the location of sensory input (see fig. 14B). Despite the absence of any presynaptic structure many vesicles of the size and shape of synaptic vesicles were loosely distributed in the cytosol.

Large Mitral Cells

This subclass comprises 12 completely and ten coarsely reconstructed cells. Large MCs were massive compared to other neurons in zebrafish OB (soma size: ø: 12 - 24 µm, $\bar{x}$ ± σ: 15.2 ± 2.8 µm). Another characteristic was the rough, uneven, and craggy texture covering the entire cell except for the axon (ø: 0.75 - 2 µm, $\bar{x}$ ± σ: 1.1 ± .4 µm, see e.g., orange MC in fig 14). The surface often exhibited irregular indentations and fissures and bore pointy or frazzled excrescences, which did not resemble spines. Somata were mainly ovoid or triangular in shape and smoothly transition into large, primary dendrites, which had a diameter of up to 8 µm at their base (ø: 1 – 8 µm, $\bar{x}$ ± σ: 3.3 ± 1.9 µm). In some cells additional smaller dendrites arose from the soma to form a single, tufty branch. The primary processes usually maintained a large diameter along their entire length and did not taper off quickly (see e.g., orange MC in fig 14). The outline of the dendritic tree was more or less globular or bushy. Due to the heavy subbranching and the large varicosities, the morphology of the dendrites was highly complex and dense within the occupied volume.

Intermediate Mitral Cells

Four of the completely reconstructed MCs and 20 incompletely reconstructed neurons were categorized as intermediate cells (see fig. 14A). Their somata were of medium size (ø: 10 - 18 µm, $\bar{x}$ ± σ: 12.9 ± 1.5 µm) with irregular shapes and usually small perikarya dominating. These MCs were characterized by an overall finer and more delicate appearance of the dendrite, which occupied a smaller volume than the large MCs. The processes were still uneven and varicose and varied in perimeter, but despite occasional pointy excrescences, the surface of soma and dendrites appeared smoother. Intermediate MCs had two or more, long primary dendrites of medium diameter (ø: 0.75 – 4.5 µm, $\bar{x}$ ± σ: 2 ± 1 µm) that started ramifying after a considerable path length. These sometimes bent back, resulting in an overall tufty and bushy dendrite, which was still large, but the volume was not densely occupied with subbranches. Alternatively, they stretched out and diverged into a paint brush tip-like structure with the soma quite remote from the dendritic tuft.

Small Mitral Cells

I classified eight of the fully and 13 of the coarsely reconstructed PNs as small MCs (see fig. 14B). The somata of these cells were round or triangular and small in size and volume (ø: 9 - 13 µm, $\bar{x}$ ± σ: 11 ± 1.2 µm). One noteworthy feature of small MCs was the morphology of the axon. Axons could be identified in 18 of 22 small MCs and emerged as fine processes ($\bar{x}$ ± σ: 0.5 ± 0.2 µm) from the soma or, rarely, the primary dendrite. About half of them made local collaterals, which remained in the GL but occupied neuropil volumes distinct from the dendrite. Most axons bore bulbar varicosities, often with

short, pointy, filamentous processes (see e.g., red MC fig. 14B). These varicosities were quite distinct from dendritic varicosities and often resembled the varicose enlargements observed at the axons of the GLIN1 (see GLIN1). Both pre- and postsynaptic sites were present in these varicosities. None of the axons of small MCs showed myelination before reaching the stack boundaries. Most small MCs had multiple primary dendrites (ø: 0.3 – 4.5 µm, $\bar{x} \pm \sigma$: 1.7 ± 1.1 µm). The dendrites of most neurons occupied a volume of roughly globular shape, they were bushy and spread out close to the soma. Their appearance was delicate in comparison to the large MC subclasses. There was a large variation in the density of neurites within the dendritic volume; while some cells ramified intensely, others were very sparse.

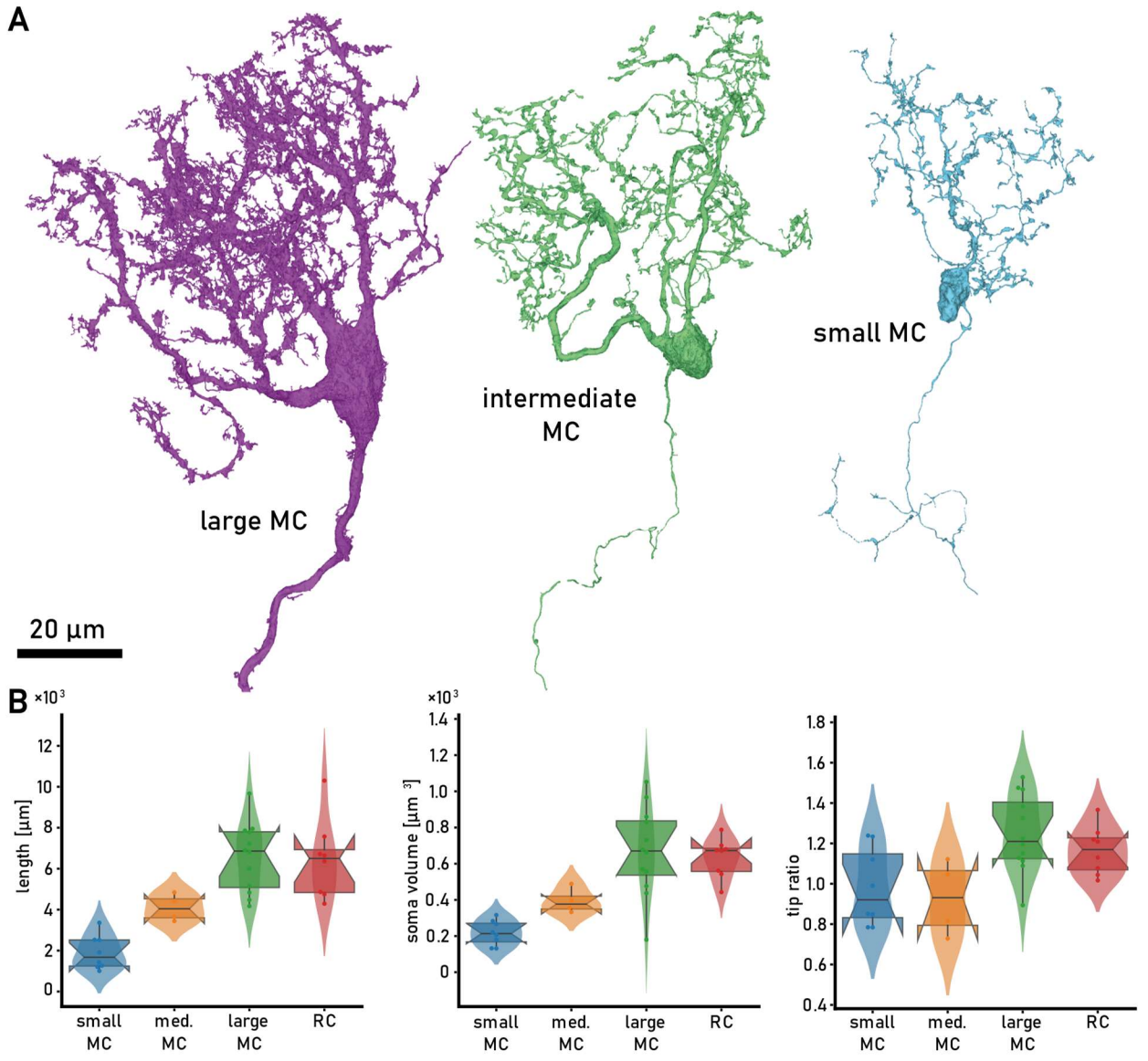

Figure 13. The morphology of MC subclasses in comparison. A: Examples of a large (left), intermediate (middle) and small MC (right). B. The individual (sub)classes of PNs showed differences across many morphological features, shown here exemplarily neurite length, soma volume and tip ratio.

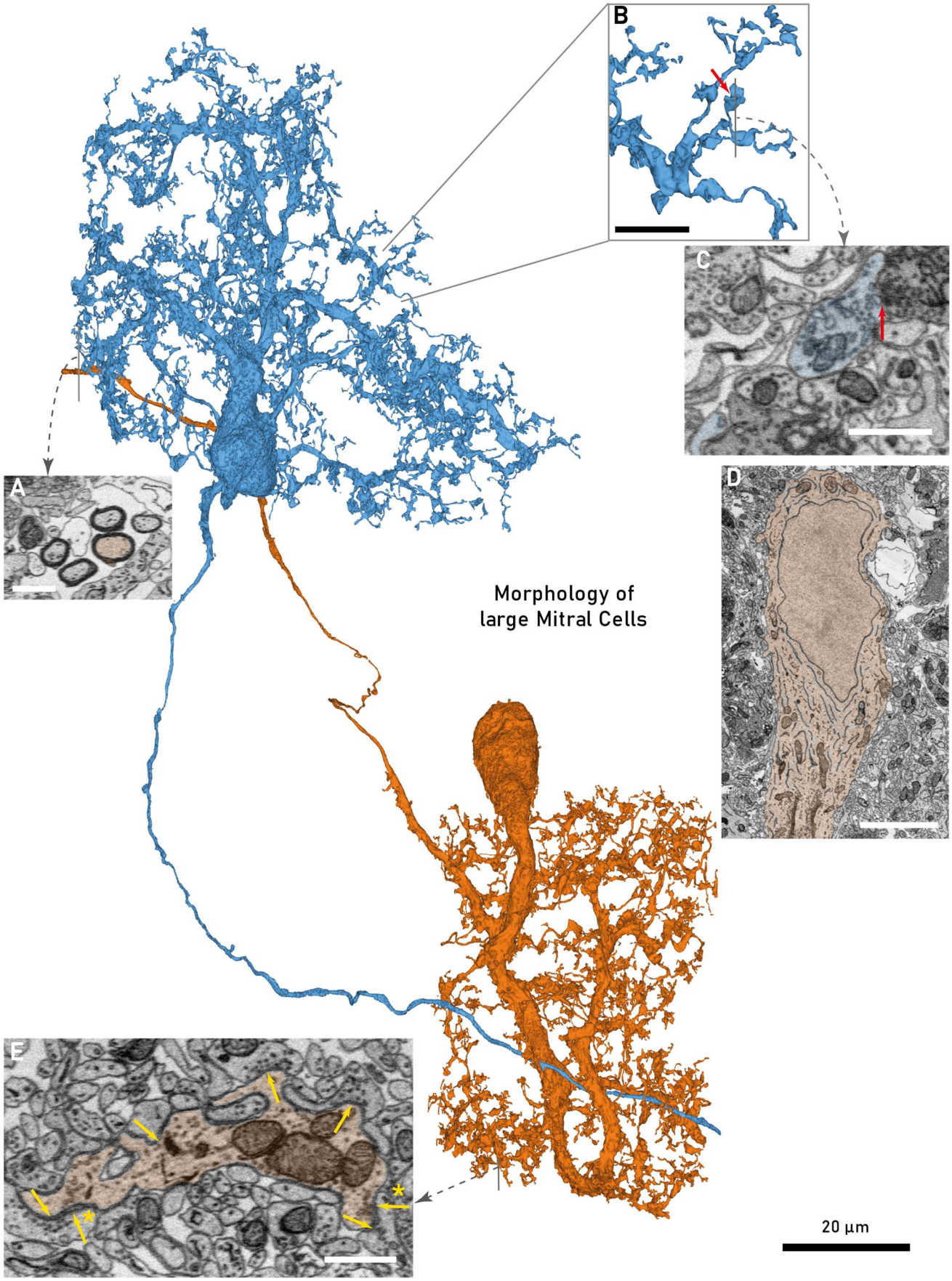
B
C
A
D
Morphology of
large Mitral Cells
E
20 µm

Figure 14. Morphology of large MCs at the example of two large MCs of glomerulus M67D45A12 (blue) and glomerulus M67D45A12 (orange). Insets: A: MC axons occasionally travelled in small bundles. B: Close-up on the distal dendrites with varicosities separated by thin dendrites. C: Sensory input onto a terminal dendritic enlargement (red arrow). D: An abundance of ER, mitochondria and vacuoles was found in the perikaryon. The Golgi apparatus stretched well into the proximal dendrite. E: Cross section of a distal varicosity in which of many in- and outbound synapses were found. Some synapses were reciprocal (asterisk). Scale bars: A, C, E: 1 µm, B, D: 5 µm

Interactions With Other Cells

Apart from one small and one large MC, which spread minor parts of their dendrites into a second glomerulus, all MCs were clearly monoglomerular. In glomeruli with multiple compartments only large and intermediate MCs were found to cross compartment boundaries. However, there were seven MCs that project a neurite of large diameter outside of the imaged volume (see Fig. 10D). From the topology of their dendrites, I assume that these MCs innervated remote glomeruli. Thus, multiglomerular MCs may exist, but they appeared to represent a minority of MCs.

For a small subset of MCs of this dataset broad synapse types, i.e., inbound, outbound, reciprocal, and sensory synapses, and their respective distribution had been described previously [90], confirming sensory input to target exclusively the distal most parts of MC dendrites, but revealing no pattern in the distribution of other synapse types. However, the identity of the synaptically connected neurons was not determined. In a qualitative examination, I found MCs to be connected to almost all morphological classes of INs described below. These findings are summarized in fig. 54. The large majority of these connections were made through dendro-dendritic synapses, and reciprocal synapses between MCs and members of eight of ten IN classes were found. There appeared to be two classes of outbound synapses made by MCs: synapses with small active zones and vesicle clouds were predominantly found in the large primary dendrite shafts and very voluminous varicosities. Larger synapses with large vesicle clouds were found primarily in the more distal varicosities (see fig 14E). An example of a large MC with all identified fully reconstructed partners is shown in fig 16.

The small MC subclass stood out by obvious local, axonal synapses. The axon collaterals of small MCs extended in GL and PL and did not overlap with the glomerulus innervated by the dendrites. I examined the local interactions qualitatively by tracing along all their collaterals and inspecting synaptic partners for one small MCs each of M45D4A2, M5D5A12 and M56D56A2. One of these cells stood out by a high frequency of vesicles along the entire axon. Distinct in- and output synapses appeared, however, restricted to the bulbar varicosities. The three MCs made axonal connections with a multitude of different INs (13, 26 and 47 connected neurites, respectively). Output synapses were more frequent than input synapses. The majority of connected partners were short neurite fragments that remained unidentified, many of which showed morphological features of the distal dendrites of DLINs and some PLINs (see below). Among the identifiable partners were INs from all layers of OB. These INs could innervate both the same and different glomeruli than the respective MC. Input was given to the dendrites of GLIN2s (see below), which also received input from dendritic synapses of the same small MCs. One MC gave input to the dendrites of a large GLIN1 (see below). I identified several vPLIN3s and multiple DLIN2s of different subclasses receiving input or making reciprocal synapses with the small MCs. Notably, none of the small MC axons received sensory input.

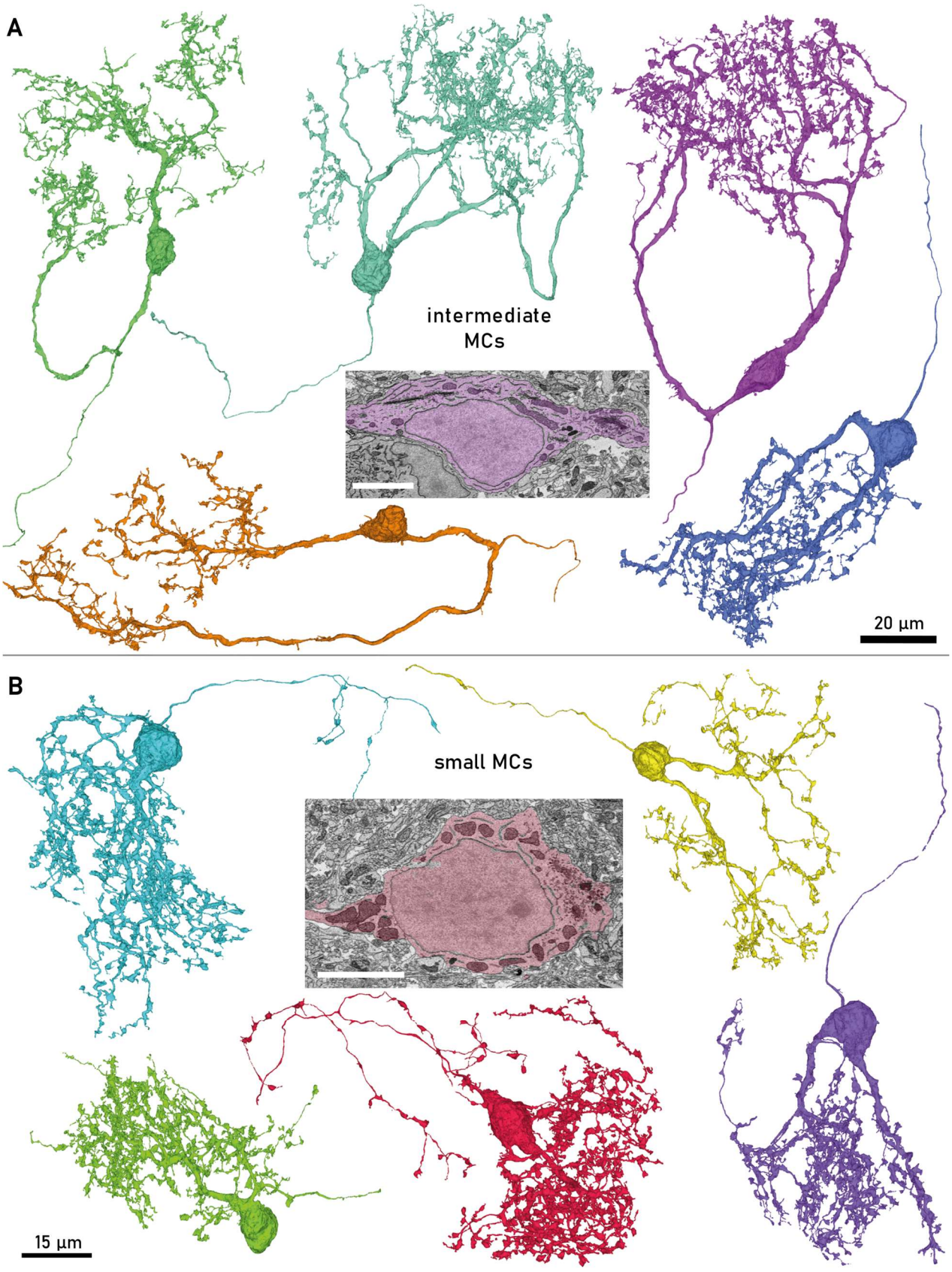

Figure 15. Morphology of intermediate (A) and small MCs (B) demonstrated by five cells. Scale bars insets: 5 µm.

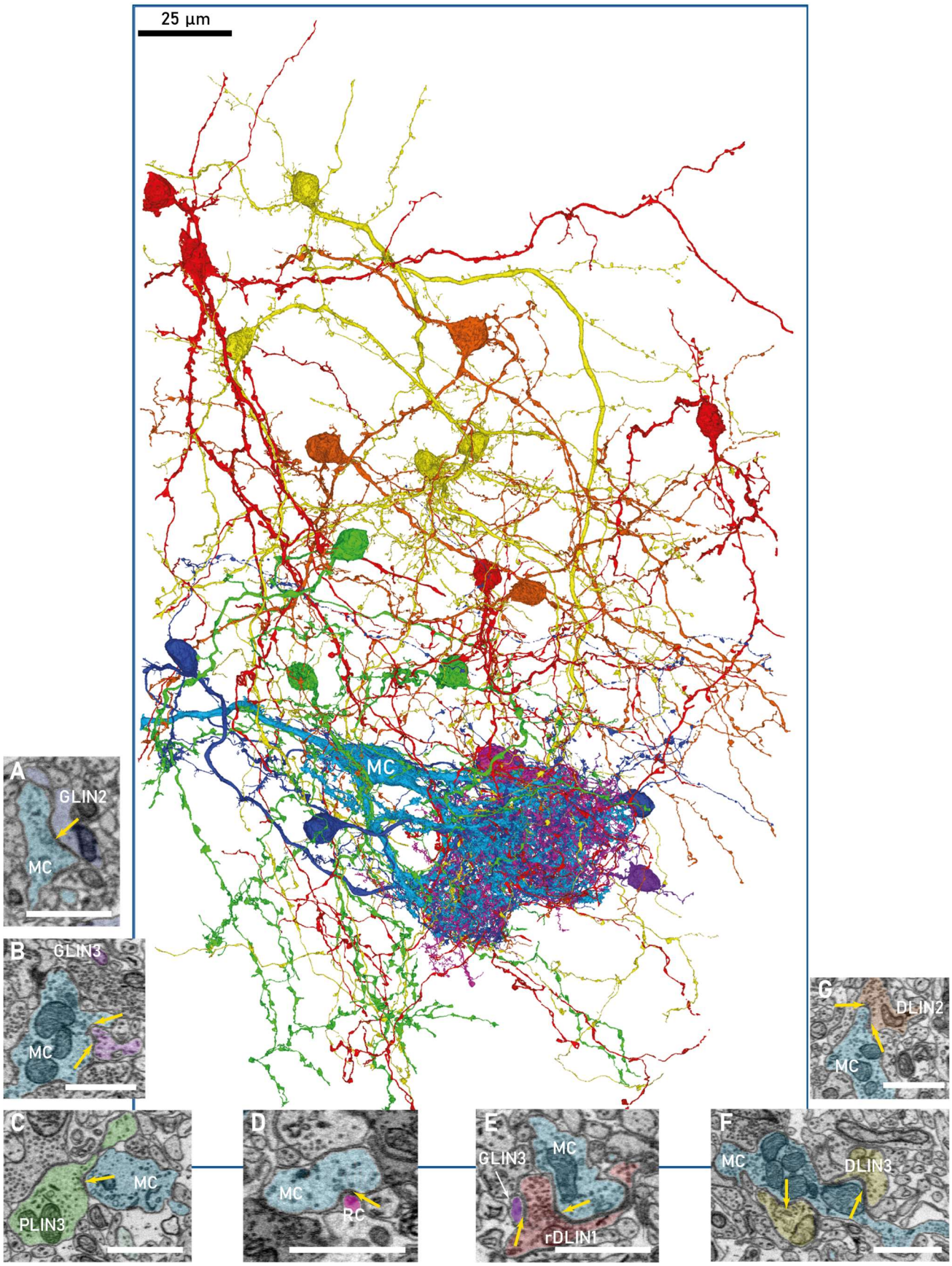
25 µm
MC
A
GLIN2
MC
B
GLIN3
MC
G
DLIN2
MC
C
MC
PLIN3
D
MC
RC
E
GLIN3
MC
rDLIN1
F
MC
DLIN3

Figure 16. Connectivity of MCs. A large MC (light blue) and 18 identified, reconstructed partners. The MC connected reciprocally to several representatives of all DLIN classes (yellow, orange, red), several PLIN3s (green) and a GLIN3 (purple) and gave input to several GLIN2s (dark blue) and a RC (pink). A. MC gave input to a filiform appendage of a GLIN2, it made multiple connections with this IN within the glomerulus. B. The MC made several reciprocal, as well as unidirectional in~ and output synapses with a small GLIN3. C. A PLIN3 gave input to a proximal dendrite of the MC. Other representatives of this class received input from this MC or were reciprocally connected. D. A synapse onto the tip of an RC neurite. Synapses onto RCs were usually very small. E. A synapse from a rough DLIN1 onto the MC. This IN also gave input to the GLIN3, which connected reciprocally to the MC. F. Input from a DLIN3 onto the MC. DLINs often enveloped MC dendrites and made very large synapses onto MCs. G. A reciprocal synapse with a DLIN2. Scale bar insets: 1.5 µm.

RUFFED CELLS

Morphology

First described in the OB of goldfish by Kosaka & Hama in 1979 [39], RCs have been reported in a multitude of other teleosts including zebrafish [150, 151, 152, 94]. RCs were characterized by the name-giving ruff, a structure of extensive protrusions at the axon initial portion with reciprocal synapses to local INs. They were described to make altogether few synapses with other neurons, surround mitral cell dendrites in a glial fashion and are expected not to receive OSN input [117, 153, 95]. I reconstructed eight RCs in detail and did a coarse reconstruction of an additional nine RCs. One of the completely reconstructed neurons was cut right at the base of its axon and its ruff was not preserved in the imaged volume. However, the cell was identified as an RC by the morphology of its dendrite. All other fully reconstructed RCs were either completely represented in the stack or only minimally cut (CD0:1, CD1: 6, CD2: 1). An overview on RC morphology is given in fig. 17.

RC somata could be identified with high reliability from the outline and make-up of the cytosolic composition of the perikaryon. The RC somata were densely populated with cellular organelles. Most characteristic was the ER, which formed concentric circles following the circular outline of the soma and traced a labyrinth into the perikaryon. Each soma contained multiple Golgi apparatus, which were typically not located at the base of emerging neurites but were rather embedded between the “walls” of the ER labyrinth. Endosomes and lysosomes were found, and the cytosol was filled with vesicles of various sizes and shapes. A myriad of mitochondria was located in the soma. These varied in size and shape, but they were typically smaller in diameter than the ones found in MCs. Characteristic for RC mitochondria was the light staining of the matrix that contrasted the christae and their round outline. The somata of RCs were globular and of medium to large size (ø: 12 - 16 µm, $\bar{x}$ ± σ: 14.1 ± 1.4 µm). They were distributed in the GL and superficial PL. The surface was mostly smooth and bore only a few short, thin, sometimes sheath-like excrescences that were neither pre- nor postsynaptic. RC cell bodies showed a tendency to be positioned deep with respect to the glomerulus they innervated with their dendrite. All RCs possessed at least one primary cilium. In most RCs (5/8), however, two primary cilia emerged from the soma in immediate proximity to each other (fig. 18E). On average, RC cilia were the longest of all OB neuron classes (2.5 – 6.5 µm, $\bar{x}$ ± σ: 4.6 ± 1.3 µm). The cilia often bent towards the soma and took a course parallel to the cell body (fig. 18E).

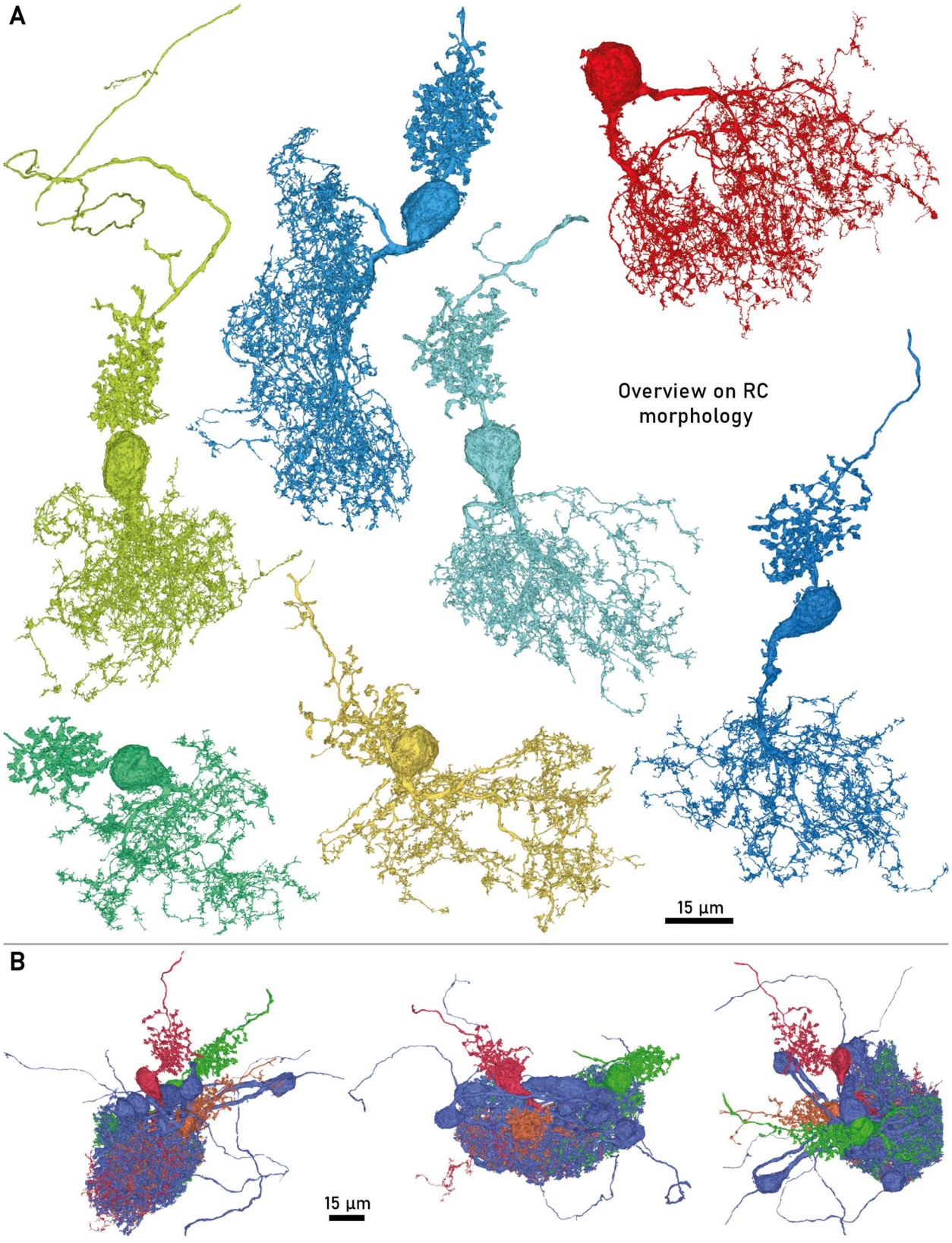

Figure 17. Overview on RC morphology. A. Seven completely reconstructed RCs. B. Immersion of three RCs in glomerulus M45D45A1. The ruffs were projected into neuropil deep to the glomerulus in PL. Scale bar: 15 µm.

The axon generally arose at the pole facing the deep layers and opposing the base of the primary dendrite(s). It was usually small in diameter (ø: 0.5 – 1.25 µm, $\bar{x}$ ± σ: 0.9 ± 0.2 µm) and in contrast to MC axons the base was filled with ER and vesicles of all sizes. Axons were initially directed towards the deeper layers, but then tended to bend laterally within the deep GL or superficial PL. Few collaterals and no myelination was observed within the imaged volume in the set of reconstructed RCs. In contrast to many other teleost species, in which the initial portion (IP) of the axon preceding the ruff may vary a lot in length [152, 151, 94], Here, the ruff was found to emanate within the first 5 µm of the axon, consistent with observations by Fuller & Byrd [94]. The ruff had a cylindrical or conical outline and extended over a length of 25 to 35 µm on the axon (fig. 17A). It consisted of multiple branchlike protrusions radiating all around the axon and typically ending in amorphous, varicose enlargements. With increasing distance to the soma, the ruff protrusions tended to become shorter and sparsen out. The protrusions diverged frequently and intermingled strongly, thus densely filling the volume delineated by the ruff. With their variance in diameter and their bumpy surface these branches were reminiscent of MC dendrites. However, they did not possess any pointy or frizzy excrescences, but showed rather rounded indentations and bulges. The cytosol of the ruff was filled with vacuoles, vesicles of various sizes, mitochondria, and ER christae with voluminous lumen. The central axonal strand could be made out because it accumulated large vesicles and was permeated by microtubules (fig 18C). Small and round synaptic vesicles filled the ruff protrusions and due to the small size of synaptic vesicle clouds, individual presynaptic sites were often hard to determine (fig 18A).

The dendritic tree of RCs was extensive and spanned a large volume. Due to the heavy branching combined with the delicacy of their branches, the topological outline of RC dendrites was reminiscent of a feather duster or besom that spreads towards the superficial parts of the GL. Primary dendrites emerged at the superficial pole of the RC soma. The majority of cells (9/13) gave rise to a single large primary dendrite (ø: 1.0 – 4.5 µm, $\bar{x}$ ± σ: 2.3 ± 1.0 µm) that branched immediately at its base into several sub-branches. These sub-branches branched mainly asymmetrically and could thus be clearly distinguished throughout their entire length. They were of moderate to small diameter, <1 µm, and tapered off with distance to soma. They were characterized by frequent large vesicular membrane structures, ER, mitochondria and clearly visible microtubule. This was not seen in the finer branches and in the small twigs, which covered the shafts in larger numbers. The finer branches were very delicate and had diameters of typically 100-200 nm. They meandered tortuously and often gave rise to sub-branches, but even more frequently to short twigs. At irregular intervals they dilated into round bulbar enlargements, giving rise to a beaded appearance of the dendrite. These enlargements were densely packed with mitochondria displaying a characteristic lightly stained intermembrane space. Almost no cytosol surrounded these mitochondria. Usually, multiple sub-branches or twigs originate from a bulbar enlargement. The RC distal branches and twigs were characterized by a very bright cytosol, rarely small strands of ER and no vesicles were found. This suggests that RC dendrites, in contrast to many other cell classes in the OB, are purely post-synaptic.

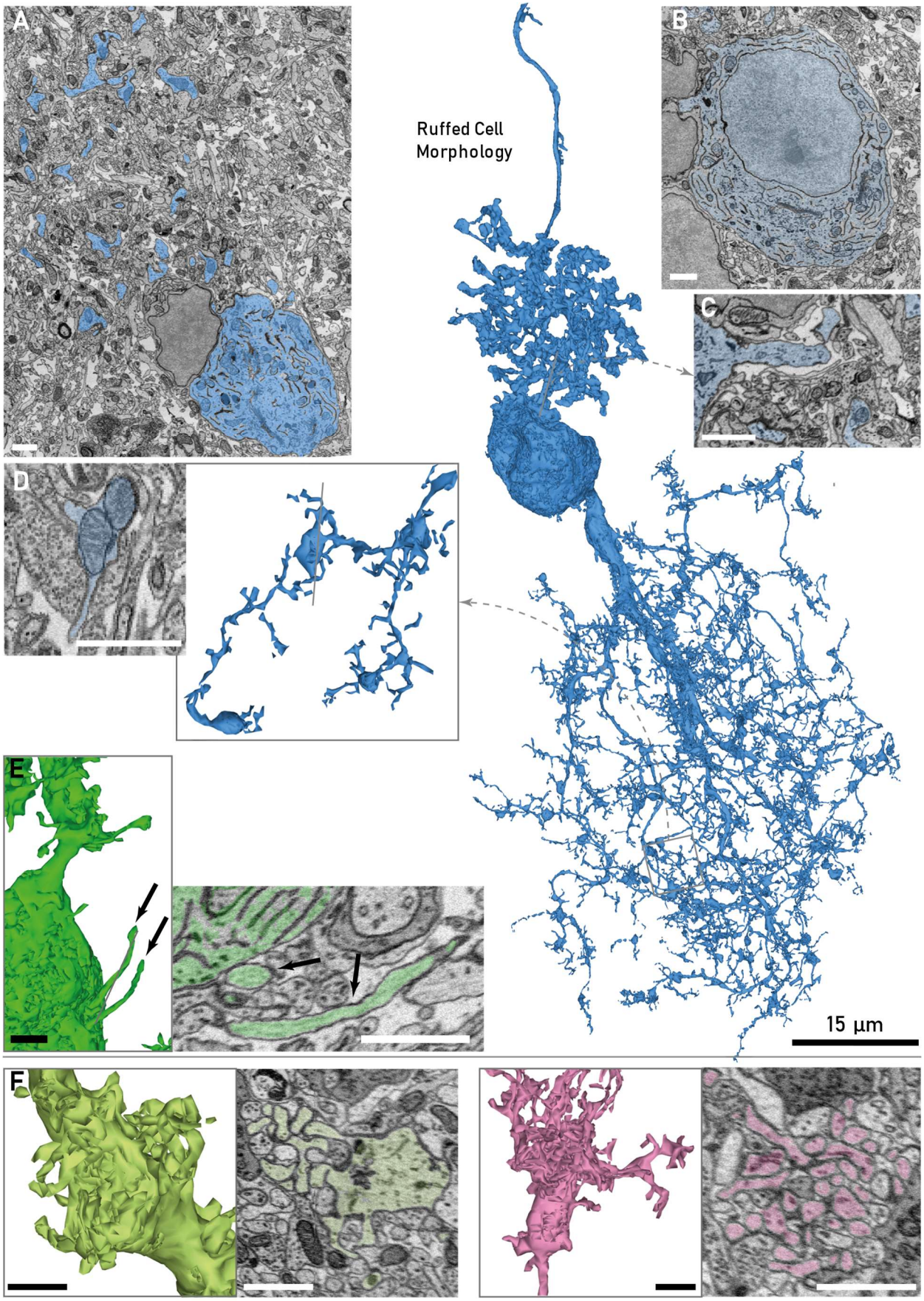
A
B
C
D
E
F
Ruffed Cell
Morphology
15 µm

Figure 18. Details of RC morphology. A: Cross section through the ruff and soma: the ruff covered in large volume of neuropil. B. Cross section of the soma showing the ER labyrinth and myriad organelles of the endomembrane system. C: The axon emerging from the soma was distinguished by large vesicular structures. D: The distal dendrites displayed bulbous enlargements containing the RC typical light mitochondria and thin tip branches. E: Close up on the soma of a RC from which two primary cilia arose (see arrows) F: Some RCs made excessive tip branches that wrapped around each other forming extraordinary structures. Scale bar: 1.5 µm.

The dendritic twigs were the most distinguishing feature of the RC dendrite, on average 54 ± 3% of a RCs skeletal length was contributed by twigs. They were thin and short, yet tortuous and typically end in a rounded head (fig. 18D). In a subset of RCs, the shafts of bigger dendrites were completely covered by twigs resulting in a very uneven appearance while other RCs gave rise to twigs predominantly in their distal dendrite. The twigs could be postsynaptic to IN or sensory axons, but often, they wrapped around other neurites and squeezed into synapses between two other neurons (fig. 20). Occasionally, the twigs were observed to wrap intensely around each other, which gave rise to the peculiar structures (fig. 18F).

Interactions With Other Neurons

Even in the most superficially positioned RCs the ruff extended into a volume of GL or PL neuropil, which was devoid of sensory axon terminals. The RC dendrite, in contrast, was fully immersed into a single glomerulus or glomerular compartment with only minor tip branches occasionally extending beyond. Early EM studies in goldfish suggested that RCs did not receive sensory input [85]. I found numerous synapses from sensory axons onto the RCs; these targeted predominantly the thin, terminal dendritic branches. Sensory synapses were, however, far less prominent than the inputs to MCs, first, in frequency and second, in their size (fig. 19B.2).

An intriguing aspect of the RC-glomerular interaction was their interplay with MCs: The delicate RC dendrites grew alongside and heavily entwined with MC dendrites, wrapping their thin side branches around the larger MC neurites (fig. 19A.1-3, B.1). This tight interaction was often stretched across a few microns of dendrite length, and usually observed across several distinct dendrite sections in a given MC-RC pair. Notably, RCs made this type of interaction with several MCs indiscriminate of MC subclass but not all MCs within the glomerulus or glomerular subcompartments they innervated. Despite this ample contact synapses were sparse and not of high confidence. Instead, RC dendrites were often found in close proximity to MC synapses onto interneurons (fig. 19A.2). RCs and MCs also received shared sensory and IN input.

RCs received substantial input from diverse INs of all layers on their dendritic tree (fig. 20). On their ruff these cells synapsed onto many INs, often reciprocally. A summary of a qualitative analysis of the RC interaction with INs is given in fig. 54.

Figure 19 (next page). Interaction between RCs and MCs. A. A RC (turquoise) received input from four different MCs of glomerulus M45D45A1. The RC tightly wrapped around the MC dendrites at multiple locations (A.1–A.4, 3D, A.1. bottom image, A.2 left image). The synapses from MCs to RCs were small (images A.1. top, A.3, A.4, arrows). RC dendrites "squeezed" in vicinity of MC synapses onto INs (A.2 image bottom, A3 image) and received input from the partners INs as well (A.2 image bottom, arrows). B: A RC of M5D5A12 (red) was tightly associated with an MC (overview, B.1). Both PNs received shared sensory input. Sensory synapses onto RCs were notably smaller than those on MCs (B.2). Scale bars 1.5 µm

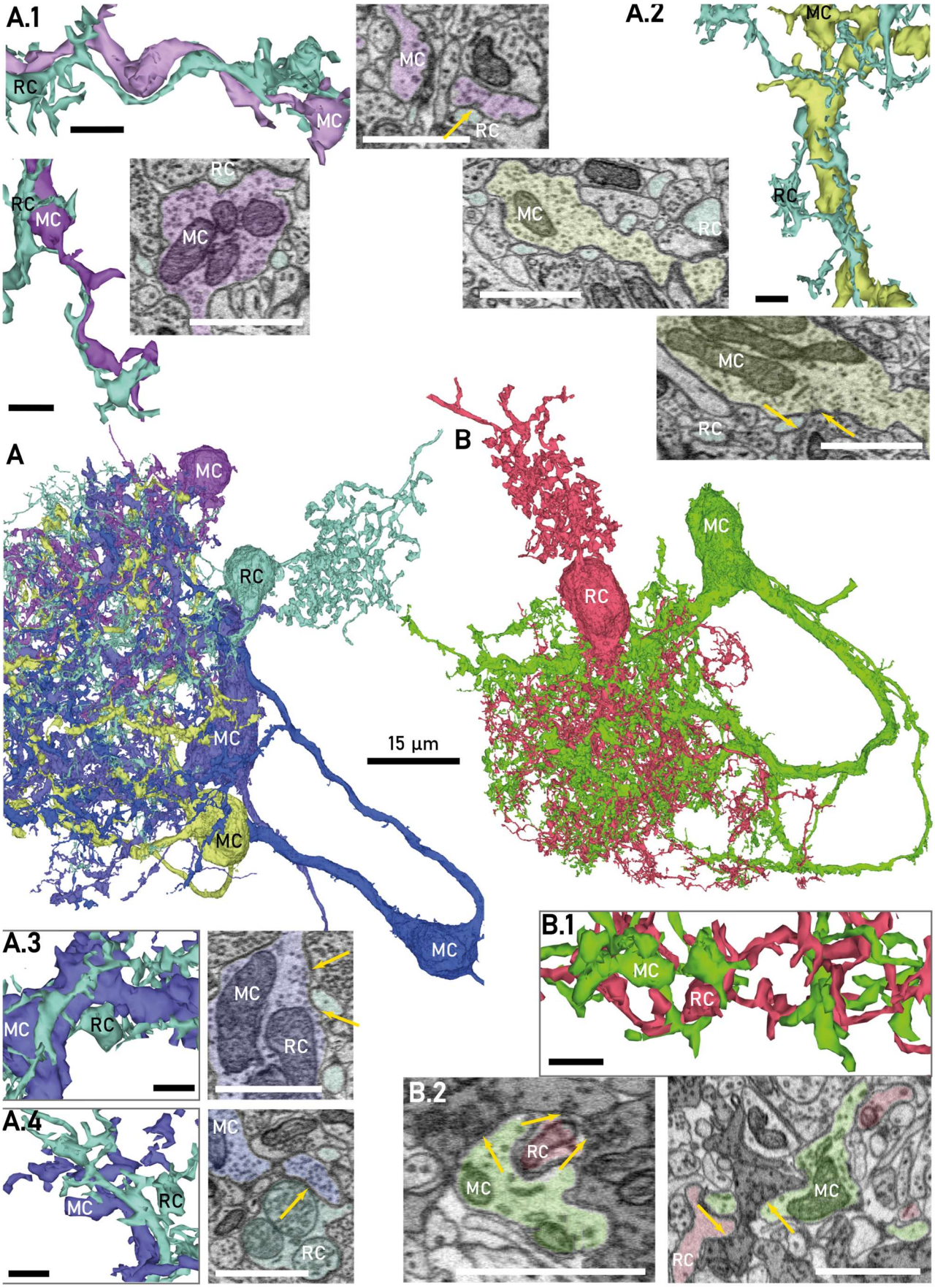
A.1
RC
MC
MC
RC
RC
MC
RC
MC
RC
A.2
MC
RC
MC
RC
MC
RC
A
MC
RC
MC
MC
MC
15 µm
B
MC
RC
A.3
MC
RC
MC
RC
A.4
MC
RC
MC
RC
B.1
MC
RC
B.2
RC
MC
MC
RC

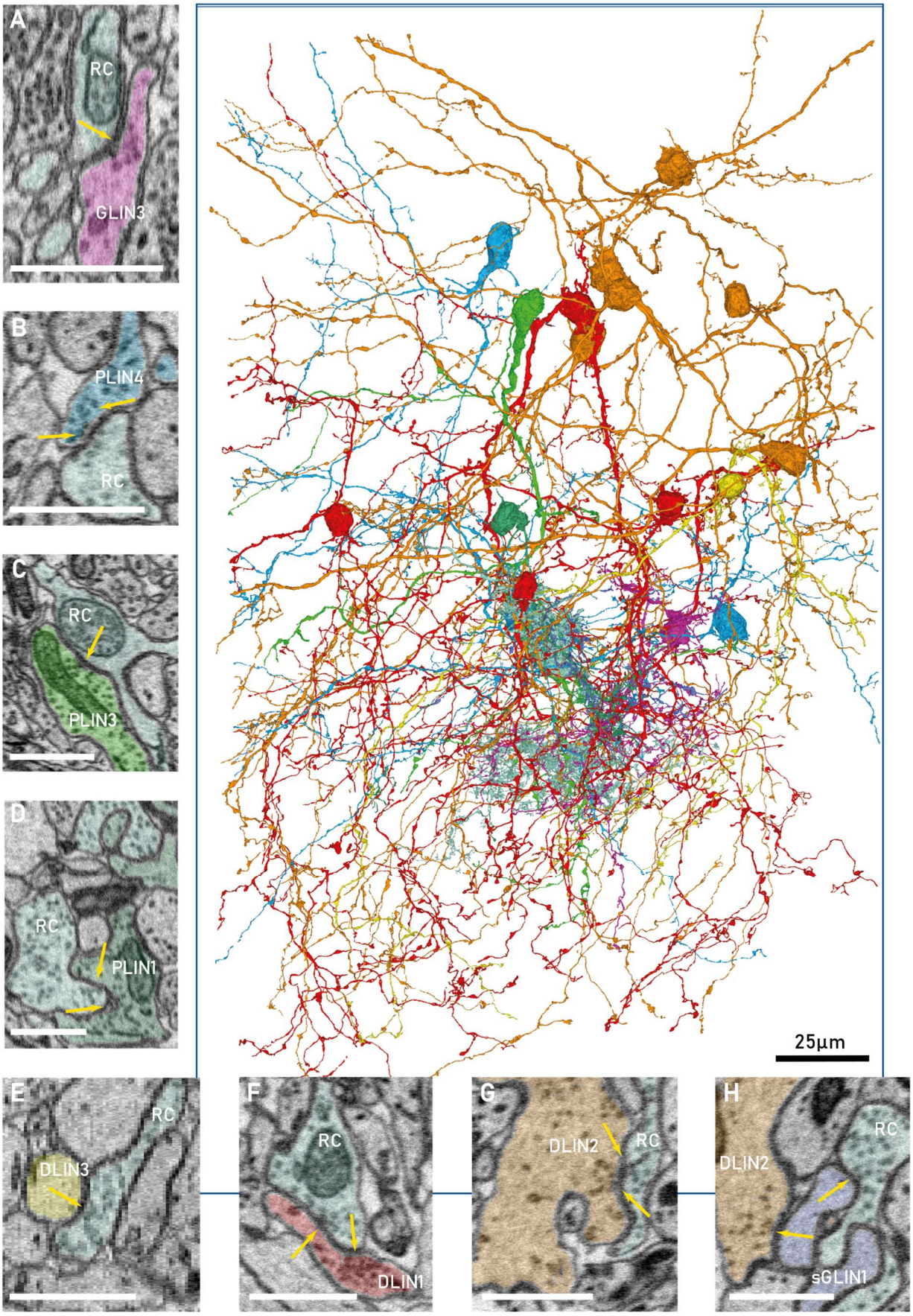
A
RC
GLIN3
B
PLIN4
RC
C
RC
PLIN3
D
RC
PLIN1
25µm
E
RC
DLIN3
F
RC
DLIN1
G
DLIN2
RC
H
RC
DLIN2
sGLIN1

Figure 20. Connectivity between RCs and INs. Example of a RC (turquoise) connected to 21 reconstructed INs. The RC was reciprocally connected to several representatives of DLIN1s (red) and DLIN2s (orange), several PLIN4s (light blue) and a PLIN1 (dark green). It received input from a PLIN3 (light green) and a GLIN3 (pink). The RC was presynaptic to several GLIN1s (purple) and a DLIN3 (yellow). This RC also received input from four MCs (see fig. 19). A. The RC received input from a GLIN3 at two locations. B. Reciprocal synapse with a PLIN4 at the ruff. This RC was connected to several PLIN4, either reciprocally or as presynaptic neuron to the PLIN4. C. Input from a PLIN3 onto a dendritic varicosity of the RC. D. Several reciprocal synapses with a PLIN1 were found. E. The RC gave input to a DLIN3 through a single synapse. F. A reciprocal synapse with a sparsely spiny DLIN1. Connections with five other DLIN1 of all subclasses were found, these include both reciprocal and unidirectional input connections G. A DLIN2 was reciprocally connected to the RC. The RC connected to five other DLIN2s. These connections involved reciprocal as well as in~ and output connections. H. The RC gave input to a small GLIN1. The same DLIN2 as in G gave input to this sGLIN1 in vicinity. Scale bars insets: 1.5 µm.

II. INTERNEURONS OF THE GLOMERULAR LAYER

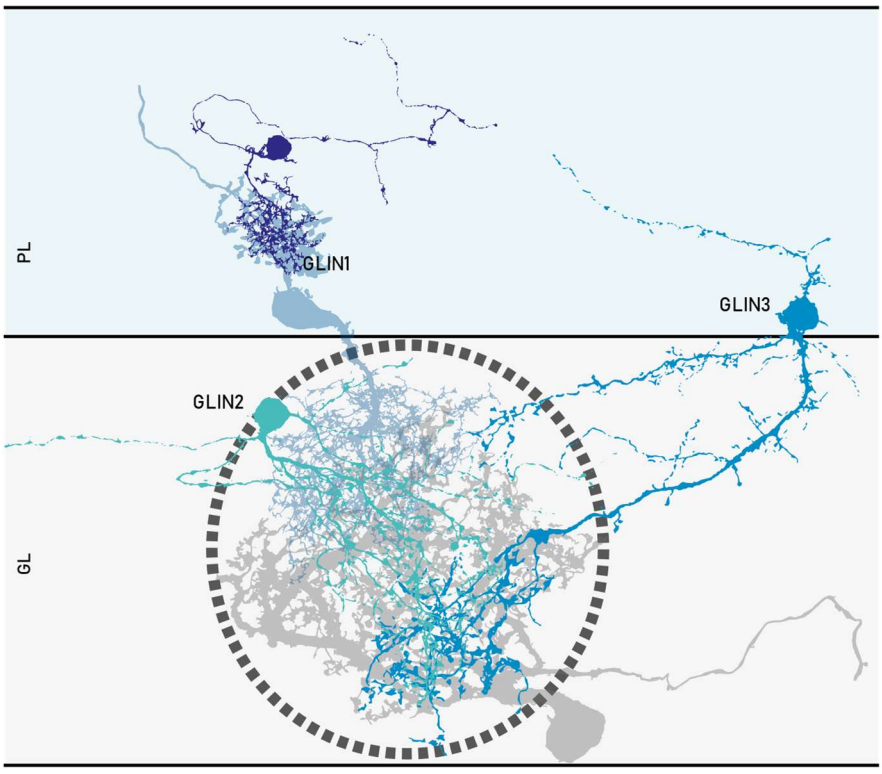

Figure 21. Schematic representation of IN classes in GL and their association to a glomerulus formed by PNs.

Due to the smooth transition between layers in the zebrafish OB the mapping of neurons to a particular layer was ambiguous. In addition, many of the superficial neurons were periglomerular and their somata were positioned in the vicinity of a glomerulus. Thus, neurons innervating deeper glomeruli often have their soma in PL. I consider a morphological class as part of GL, if the majority of the neurite mass targeted the GL and if at least one representative had its soma in GL. I describe three distinct morphological classes of INs in the GL, that are schematized in fig. 21. The GLIN1s comprises 31 neurons that were characterized by an overall small size, a spherical, mainly bushy dendrite, and the presence of a collateralizing axon. This class can be divided into two subclasses that can be distinguished mainly with respect to size. The smaller subclass of GLIN1s further stood out by an

intriguing interaction with RCs. The GLIN2s constitute a group of 18 large, axon-bearing INs, which were characterized by the presence of frequent, filiform, spine-like appendages. The third class, the GLIN3s, is composed of 11 axonless INs of varying size which possessed a spiny proximal dendrite and a bushy, beaded distal dendritic ramification. All GLINs were mainly monoglomerular. A brief summary of morphological characteristics is given in table 5.

IN class		cell count	axon	spine freq.	cell volume [µm³]	total length [mm]	soma volume [µm³]	soma diam. [µm]	n glomeruli innervated	reciprocal PN connections
GLIN1	sGLIN1	23	+	-	161 ± 40	0.8 ± 0.3	58 ± 17	7.5 ± 0.6	1.4 ± 0.6	-
	lGLIN1	8	+	-	192 ± 49	1.2 ± 0.3	65 ± 17	7.9 ± 0.6	1	-
GLIN2		18	+	+++	428 ± 185	2.1 ± 0.9	152 ± 61	9.1 ± 0.9	1	-
GLIN3		11	-	++	274 ± 101	1.7 ± 0.8	97 ± 34	8.3 ± 0.6	1.1 ± 0.3	+

Table 5. Features of GLIN classes. Abbreviations: -: absent, +: present, ++: pronounced, +++: very pronounced. Numbers given as mean ± standard deviation.

GLIN CLASS I

The first morphological class of GLINs (GLIN1) was composed of 31 small INs most of which were completely contained in the imaged volume (CD0: 26, CD1: 5).

Morphology

The GLIN1s represented the smallest neurons observed in the examined volumes. Their somata were found throughout the GL, though they appeared more frequently in the deeper GL and superficial PL. GLIN1s were found in small groups of three to five neurons near an RC; very often they sat directly on the RC soma or the ruff (fig. 23A). The somata were small (ø: 7 - 9 µm, $\bar{x}$ ± σ: 7.6 ± 0.6 µm) and ovoid or irregular in shape, rarely globular. Those cell bodies occurring in clusters were usually flattened at one or more sides. The nucleus filled the perikaryon almost completely and often exhibited profound invaginations of the cytoplasm. Cytosol was abundant at the base of the primary dendrite(s), where cellular organelles accumulated: endosomes, lysosomes, and various large vesicles, usually a single Golgi apparatus and few long strands of ER, as well as some small to medium-sized mitochondria. The mitochondria resembled those observed in RCs with a very light staining of the matrix. They were occasionally also found in other parts of the cell body, squeezed into the small cytoplasm space between nucleus and plasma membrane. The surface of the soma was smooth and, in most cases, did not exhibit any spine-like protrusions or indentations, except for occasional small twigs or sheath-like excrescences. These twigs squeezed in between the dense neuropil surrounding its soma and the ruff of an associated RC or wrapped around neurites and could receive synaptic input from multiple neurites. No outbound synapses from the soma were observed. However, occasional inputs from

neurites reminiscent of distal neurites of deep layer INs could be found. Short primary cilia were found in 21 of 31 GLIN1s (0.2 – 2 µm, $\bar{x}$ ± σ: 1.1 ± 0.5 µm), 7 of these cells gave also rise to a second nearby cilium (fig. 22A). In three cells without observable cilium centrioles were found in the perikaryon.
The axons of most GLIN1s were fully represented in the imaged volume and originated from the soma in 24 of 31 neurons as a very thin branch (ø: 100 – 500 nm). In the other neurons, it could arise at any position along the dendrite. The direction of axonal projections showed no obvious pattern. However, by trend GLIN1s belonging to the same cluster occupied a shared volume in their axonal spread. All axons collateralized frequently, projecting throughout the GL, PL and in some cases, collaterals reached into the superficial GCL. At irregular intervals these axons displayed enlargements of non-uniform appearance. The majority of neurons showed voluminous enlargements of variable length along the collaterals, whereas in a subset rather flat and sheath-like enlargements dominated. The latter wrapped around other neurites, while the voluminous enlargements often exhibit grooves, in which neurites of other cells are imbedded. The varicosities typically contained one or more mitochondria and small, round synaptic vesicles were dispersed through the cytosol. The axonal enlargements were typically sites of synaptic interaction with other superficial and deep INs. These synapses were predominantly reciprocal, but unidirectional pre- or post-synapses were also present. The voluminous enlargements usually carried one or several very thin (100-200 nm) extremities, which protruded into the surrounding neuropil. Occasional synapses onto these twigs were observed.

The GLIN1s expressed a large variability in dendritic topology in terms of spread and size. This also seemed to correlate with soma size. This morphological class could therefore be subdivided into two subclasses, which also functionally differed in the way they interacted with RCs (see below).
Most neurons (23 of 31) belonged to the subclass of smaller GLIN1s (sGLIN1). Characteristically, their dendrite spread directly adjacent to their soma ($\bar{x}$ ± σ: 7.5 ± 0.6 µm) and encompassed a small, globular volume on the order of 15 – 30 µm. The extent to which the dendritic branches filled this volume varied substantially. For the more prominent, denser, bushy versions, either a single dendrite that ramified immediately arose from the soma, or up to four dendrites emerged in close proximity of each other. The dendrites were already thin at their base (ø: 300 - 500 nm) and tapered off further to an average diameter between 100 and 200 nm. Similar to RC dendrites, short, meandrous twigs emerged from dendritic branches and sub-branches. Another similarity to RC dendrites exhibited by a subset of GLIN1s was the bulbous enlargements containing mitochondria (fig. 22). However, they were far less frequent than in RCs. The dendritic cytosol contained occasional strands of ER, but appeared to be devoid of any vesicles, suggesting that the dendrite of these cells is purely postsynaptic.

Figure 22 (next page). Morphology of GLIN1s. Three large (top) & three small GLIN1s (bottom). The two subclasses shared overall morphology but differed in size and distance between soma and dendrite. A: Close up on a soma of a lGLIN1 from which two small primary cilia emerge (see arrows). B: Detail of the GLIN1 dendrite displaying bulbar enlargement with light mitochondria. C: Detail of axonal enlargement(s) which made a reciprocal synapse. D: Cross of a soma of a sGLIN1. Scale bars A-D: 1.5 µm.

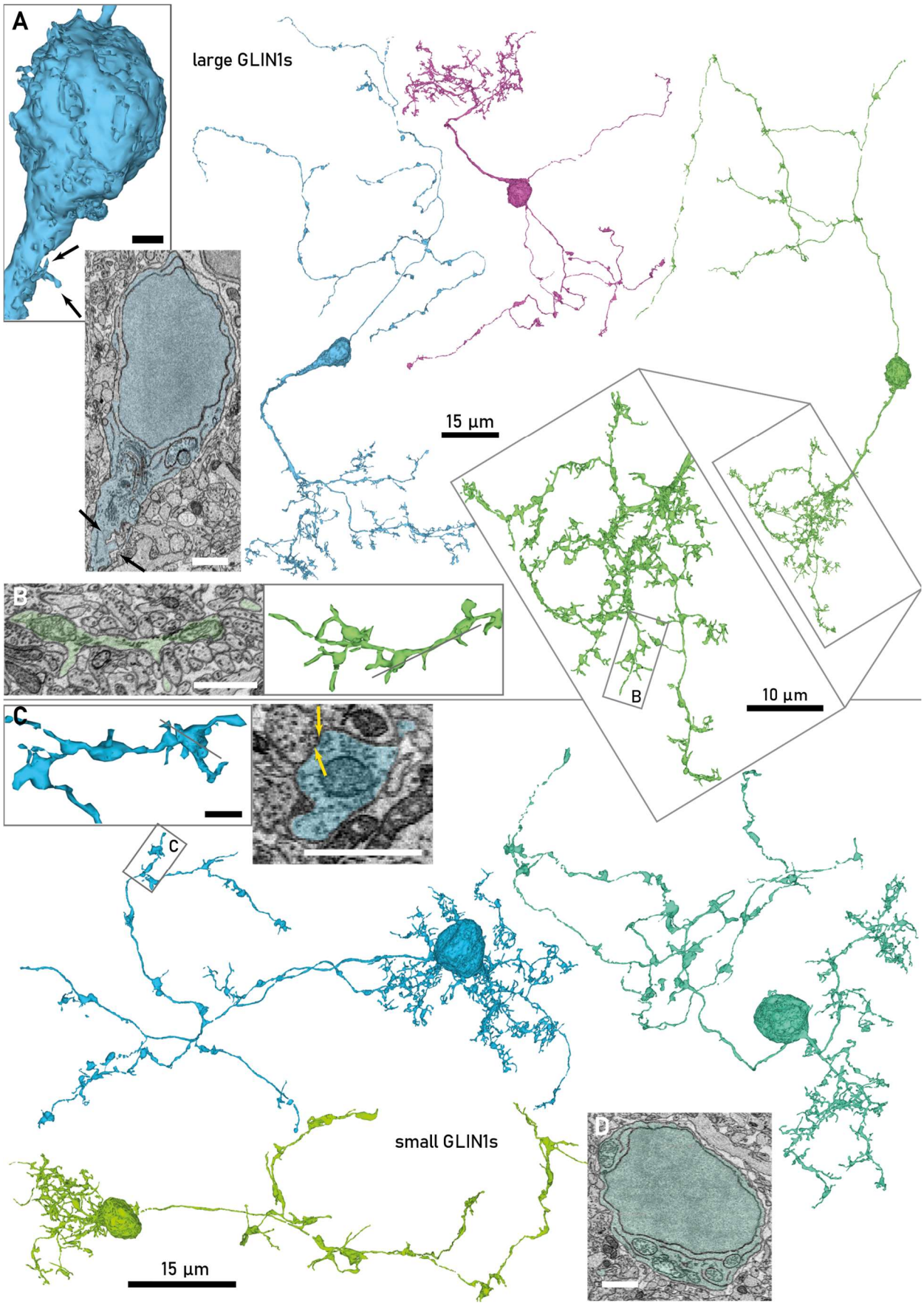
A
large GLIN1s
15 µm
B
10 µm
C
small GLIN1s
15 µm
D

While the majority of sGLIN1s (15 /23) had their soma in small cell clusters, the eight representatives of the larger subtype (lGLIN1) lay either freely in the neuropil or were attached to a RC. The somata of these cells were slightly larger ($\bar{x}$ ± σ: 7.9 ± 0.6 µm). The dendrite of these cells emerged as a single stalk, which ramified only at some distance from the soma. Apart from spreading over a larger volume, the dendrite resembled the dendrite of the smaller subtypes topologically (fig. 22).

Interactions With Other Neurons

Most characteristic for this IN class was their interaction with RC. In particular, most sGLIN1s interacted intimately with one or more reconstructed RCs (20 of 23 INs). These neurons were clustered in small groups that sat directly on a RC soma or adjacent to the ruff and immersed their dendrite fully into the ruff (fig. 23A, B). The appearance of this interaction was reminiscent of creeper plant climbing a tree by attaching with their tendrils: The dendritic branches of GLIN1s were closely attached to the RC, entwining the ruff branches and protrusions by clasping the RC neurites with the small twigs. Despite this vast amount of contact sites, very few distinct synapses from the ruff onto the IN dendrite were identified. Often, the small twigs of the IN protruded into the immediate vicinity of a synapse between a RC and another neurite. This made it difficult to distinguish whether RC vesicles next to the membrane contacted by GLIN1s formed an independent synapse or whether they belonged to the vesicle pool of the adjacent synapse with the other neurite. Yet, there were unambiguous instances of RC synapses onto GLINs. These synapses were usually small with very few vesicles (fig. 23B). Moreover, the interplay between RCs and GLIN1s extended to interactions with further neurons: The GLIN1s frequently received inputs to their dendrites from neurites that were either reciprocally connected to the RC or made unidirectional in- or output synapses with it. Many of these neurites belonged to deep layer INs (fig. 23B). The 3 sGLIN1s which were not found to immerse into a RC ruff were positioned very superficially in the volume, immersing their dendrite into a glomerulus.

None of the lGLIN1s showed interaction between their dendrites and a RC ruff. However, more than half of these cells tightly wrapped their dendrites around RC dendrites (fig. 23C). The smaller IN dendrite was most closely attached to the bigger RC dendrite and soma. This dendro-dendritic interaction usually spanned only a small fraction of the IN dendrites and was less pronounced than the interaction between RCs and sGLIN1s. Since the dendrites of both lGLIN1s and RCs were presumably purely post-synaptic structures, this suggests that the IN tracks the input to the RC. Indeed, several instances of synaptic inputs from a given neurite onto both RC and lGLIN1 were observed (fig. 23F). Yet, for a functional understanding of this interaction, further investigation is needed.

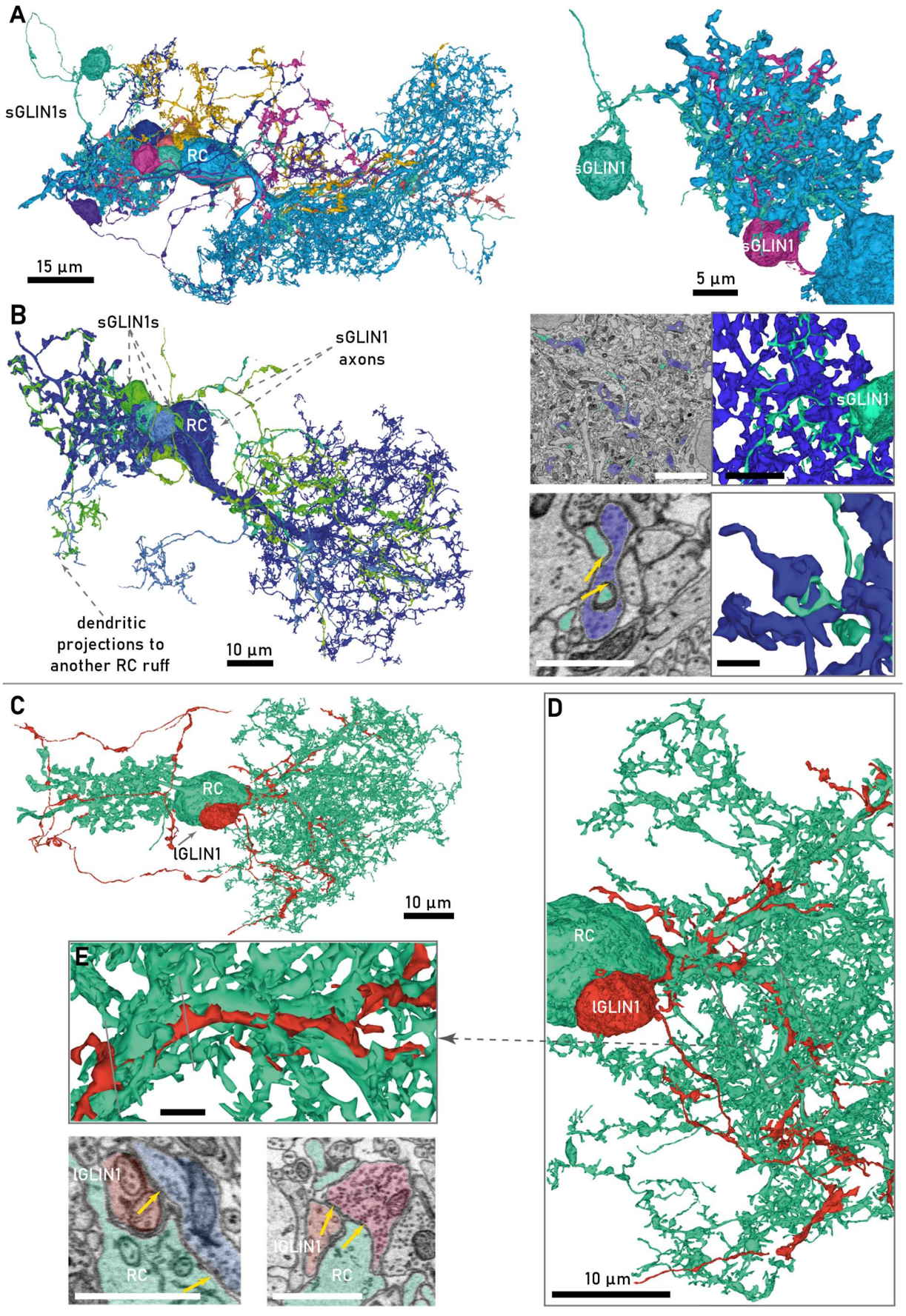
A
sGLIN1s
RC
15 µm
sGLIN1
sGLIN1
5 µm
B
sGLIN1s
sGLIN1
axons
RC
dendritic
projections to
another RC ruff
10 µm
sGLIN1
C
RC
lGLIN1
10 µm
D
RC
lGLIN1
10 µm
E
lGLIN1
RC
lGLIN1
RC

Figure 23. Interaction between RCs and GLIN1s. A. Left: RC associated with seven small GLIN1s, which immersed their dendrites into the ruff but did not interact with the RC dendrite. Right: Enlargement with two sGLIN1s showing the intense entanglement with the ruff. B: Left: Four sGLIN1s were immersed into the ruff of another RC. Insets: Top: Detail of the interaction of one sGLIN1s with the ruff. Scale bar 5 µm. Bottom: The sGLIN1 received input from the RC (arrows) and an IN, that was reciprocally connected to the RC (above, synapse not indicated). Scale bar 1.5 µm C: Association between a large GLIN1 and a RC. D: Enlargement showing the lGLIN1 curling around the RC dendrite. E: Top: Detail of the dendritic interaction. Bottom: Two examples of shared input to RC and lGLIN1. Scale bars: 1.5 µm.

The interaction of GLIN1s with glomeruli was intricate: Those GLIN1s immersing their dendrite into a ruff, dendritically connected to glomeruli only via RCs, since the ruffs were outside of the glomerulus, oriented towards deeper layers. Several neurons were found to interact with the ruff of multiple RCs. While these RCs arranged their ruffs in close-by volumes, the dendrites could project to different glomerular volumes. Thus, the sGLIN1s could presumably integrate information from more than one glomerulus ($\bar{x}$ ± σ: 1.4 ± 0.6 glomeruli). In contrast, the dendritic projections of lGLIN1s overlapped very well with the volume outlined by single glomeruli. The axonal projection pattern of GLIN1s was complex. A notable fraction of cells (12/31) projected their axons only to deeper layers, thus, not interacting with the glomerular volume. The axonal projections of the remaining neurons were not confined to a particular glomerular volume, but often appeared to be biased towards the volume occupied by a single glomerulus.

To further investigate the potential interactions between the GLIN1s and PNs, small groups of GLIN1s were overlaid with a single PN at the time. The neurite projection patterns were screened for potential contact sites and then searched for synapses. This was done for both completely and coarsely reconstructed PNs. Despite frequently observed overlap in the volumes covered by GLIN1 axons and RC dendrites, I did not detect any synapses from GLIN1s onto RCs. None of the tight interactions between RCs and GLIN1s could be found for MCs. No synapses were found between a MC and any of the sGLIN1. One MC of the small subtype was found to give input to two of the lGLIN1 from its axon collateral. However, given that only one pair was found to be connected among 92 pairs of MCs and lGLIN1s and none of the sGLIN1s, it is assumed that MCs do not represent a major input to this subclass of IN.

The axons of some GLIN1s were observed to form bundles. This was found for both neurons innervating the same RC as well as for pairs interacting with different RCs. I found both reciprocal as well as unidirectional synapses between these axons (fig. 24A). Furthermore, reciprocal connections to the same passing neurites were found from axons in the same bundle (fig. 24B). Some of these INs provided sparse input to another morphological class of superficial IN, the GLIN3s (see GLIN CLASS III). The sGLIN1s were found to interact with various deep layer INs as well (fig. 24C).

GLIN CLASS II

The second morphological class of GLINs was composed of 18 large, axon-bearing INs that were distinguished by a very characteristic form of spine-like appendages with filiform excrescences. Most of these neurons were well represented in the stack with presumably only little to moderate fractions of their dendrite cut (CD1: 7, CD2: 9, CD3:2).

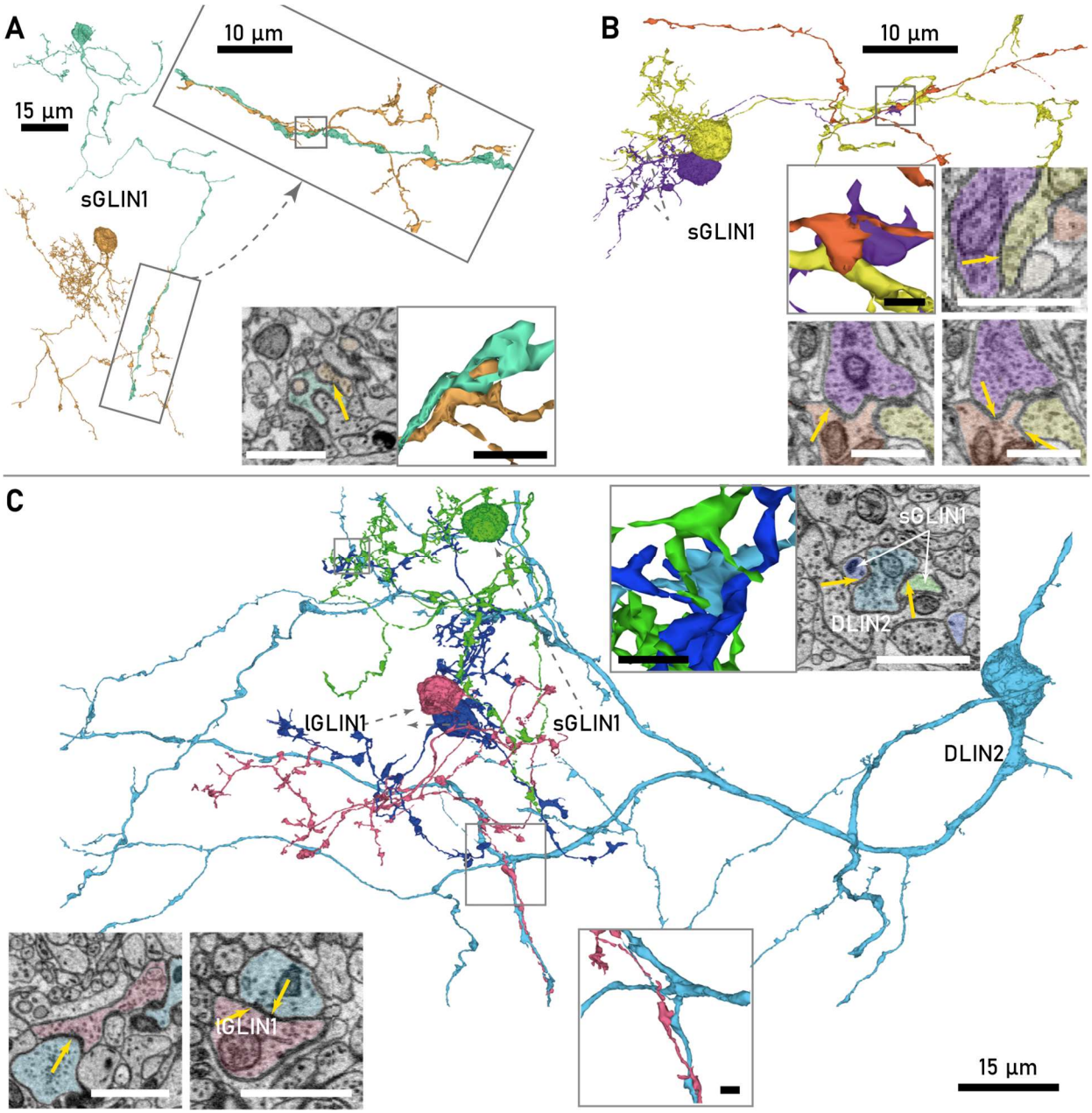

Figure 24. Interaction of GLIN1s with bulbar INs. A: Two small GLIN1s of different clusters bundled their axon. Inset: Detail of an axonal synapse between the two sGLIN1s. Scale bar insets: 1.5 µm B: Two sGLIN1s of the same cluster formed axon bundle. Insets: The two axons made reciprocal synapses with a third neurite and one sGLIN1 gave input to the other. Scale bar insets 1 µm C: A cDLIN2 (light blue) was reciprocally connected to a large GLIN1 (pink, inset bottom, see arrows) and gave input to the dendrites of two sGLIN1s in close proximity (dark blue, green, inset top see arrows). Scale bar insets: 1.5 µm.

Morphology

The somata of GLIN2s were loosely distributed in the neuropil of the GL, even at the surface, and in the very superficial PL. They only rarely clustered with other somata. Somata were globular to ovoid and medium-sized (ø: 8 - 11 µm, $\bar{x} \pm \sigma$: 9.1 ± 0.9 µm). The nuclei often had an undulated outline with mild indentation and were surrounded by a moderate, sometimes small amount of cytosol, from which it stood out by its dark staining. Altogether, the perikaryon had a rather light and clear appearance

and the mitochondria were remarkably small and very darkly stained. A handful of mitochondria were found distributed around the soma with a larger frequency at the root of primary dendrites. Few, rather short strands of ER cisternae surround the nucleus and relatively few, large vesicles and structures of the endo-membrane system were observed. The cells contained up to three Golgi apparatus, which could be very compact, but on other occasions stretched over a considerable length into the primary dendrites. A single primary cilium was present in the majority of GLIN2s (16/18, 1.5 – 6.0 µm, $\bar{x}$ ± σ: 3.4 ± 1.5 µm) The surface of the cell bodies was predominantly smooth and usually bore a few thin, filopodial excrescences. These were occasionally targeted by synapses. Direct input to the soma was also commonly observed, but no outbound synapses could be found.

In this morphological class, axons could be faithfully identified as the only neurite with outbound synapses. These synapses were confined to bulbar or voluminous enlargements, which emerged in all axons only at considerable distance from the soma (fig. 25A). Axons were distinguished in 14 of 18 GLIN2s. Among the remaining four neurons, two cell bodies reside close to the stack boundary, such that the characteristic bulbar enlargements carrying outbound synapses, which only occurred at considerable path length to the soma, might have been cut off. In the other two cells, no axon was identified despite thorough search. A possible explanation is that their neurites often became extremely thin, which complicated segmentation and reconstruction (see below).
Axons arose more often from the soma than from the dendrite (9:5). In the latter case, the axon could emerge from a proximal dendrite, as well as from a dendrite of higher branch order. Cells located in the deeper GL usually projected to the deep layers, while the axons of superficial neurons were directed predominantly laterally in GL. Unlike GLIN1s, no axon was represented fully in the stack. A few GLIN2s made local axon collaterals (5/14).
Synaptic vesicles seemed to be exclusively confined to the bulbar, voluminous varicosities, which varied considerably in frequency and size among neurons and gave the axon the appearance of a beaded chain. The varicosities had one or more presynaptic sites, but also received input and could make reciprocal synapses. No synapses onto the axonal shafts were observed. Even in enlargements with only one presynapse, vesicle clouds were very large. There appeared to be a bimodal distribution of vesicle size: larger round vesicles with visible light lumen were dispersed in between many small, dot-like vesicle (fig. 25A, black arrows).

All GLIN2s gave rise to several, round and slender primary dendrites. Up to three larger primary dendrites with a diameter varying between 750 nm and 3.5 µm emerged from the soma ($\bar{x}$ ± σ: 1.4 ± .7 µm). In addition, many cells had up to four smaller dendrites emanating of the soma (ø: 150 - 500 nm, $\bar{x}$ ± σ: 0.4 ± 0.1 µm). The path length from the soma at which the larger primary dendrite started branching varied significantly. While primary dendrites in some cells branched immediately at the soma, others extended a dendrite stalk up to ~90 µm from the soma before ramifying. In the majority of cells this stalk had a length between 15 and 30 µm. The branching pattern was asymmetric: primary dendrites were clearly discernible over a considerable length and tapered off slowly, while the emerging branches were as thin as the small dendrites arising from the soma.

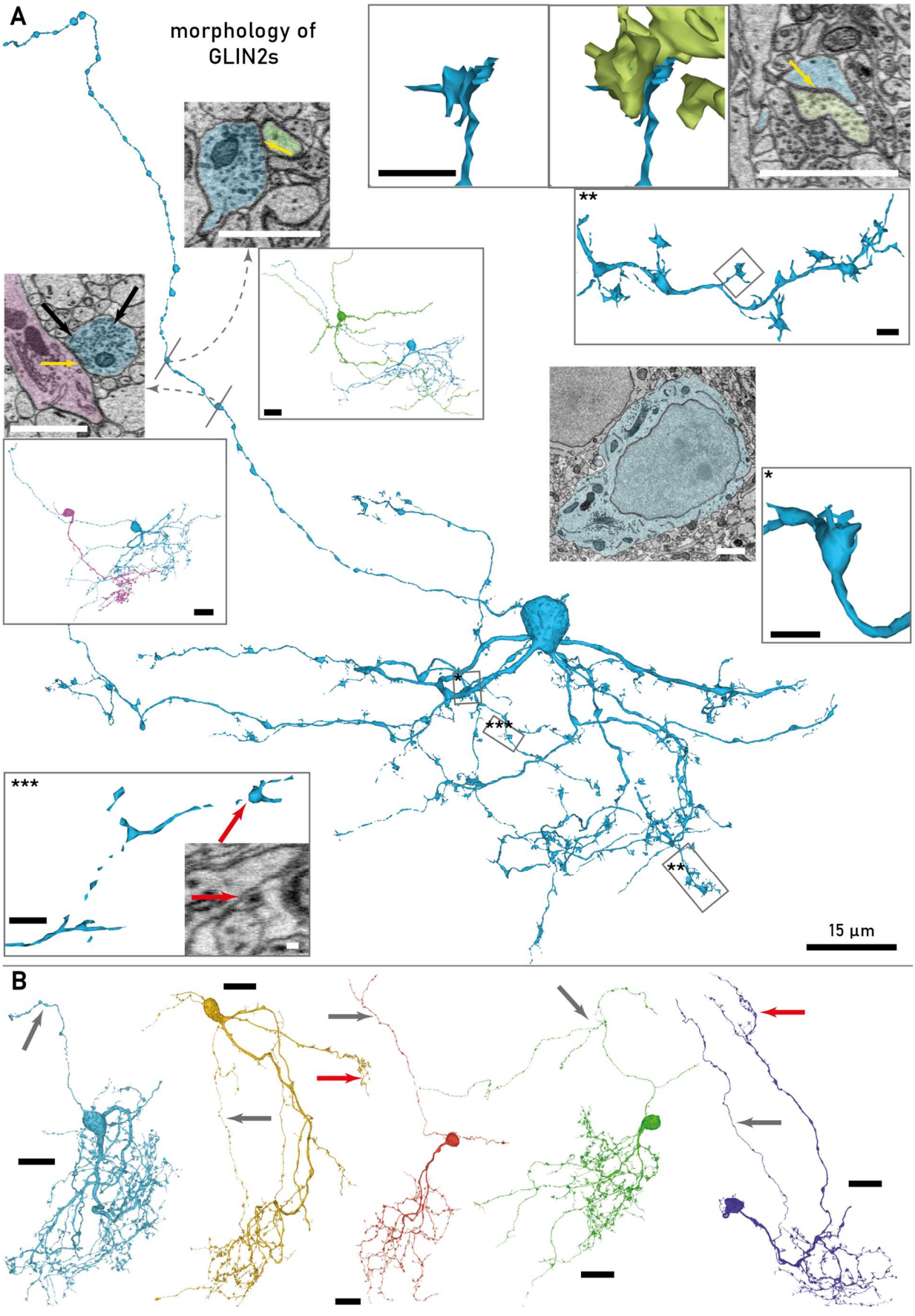
A
morphology of
GLIN2s
**
*
***
***
**
15 µm
B

Figure 25. The morphology of GLIN2s A: A GLIN2 of M45D45A1 with a roughly circular shaped dendrite. The beaded axon extended far into the PLIN at the dorsal side of the dataset and made synapses with local INs. Insets: left: synapse onto a GLIN3 (pink), right: synapse onto a DLIN1 (green). Scale bar image: 1.5 µm, 3D: 15 µm. Insets: * Enlargement of a sessile filiform protrusion. ** Enlargement of parts of the distal dendrite showing several filiform spines with long thin necks. Further enlargements: These spine-like protrusions wrapped around MC dendrites from which they received input (arrow). Scale bars 1.5 µm. * Example of a spine-like protrusion separated by a neck too thin to segment (red arrow). Scale bar image: 100 nm, 3D: 1.5 µm B: GLIN2s showed different topological appearances and size. Axons are highlighted by grey arrows. Two GLIN2 made a smaller secondary dendritic process (red arrows). Scale bars: 15 µm.**

In both larger and thin dendrites, regularly occurring dilations, containing few, small mitochondria, gave the dendrites a beaded appearance. The surface of the large dendrites was mainly smooth, but sparsely studded with protrusions. On the proximal part, these often resembled small stumps or branches. Filopodial protrusions, carrying the characteristic filiform appendages, covered the thin dendrites. On the larger dendrites, they became more and more frequent as the distance from the soma increased. In the thin side branches, these could emerge directly from the dendrite. In the thicker dendrites, the filiform appendages could have an appearance similar to sessile spines, thus, directly attached to the shaft (fig. 25A), but they mostly occurred at the end of a thin filopodial spine neck. The length of these varied considerably, from a few hundred nanometers to several microns. The neck could be extremely thin and was many times too thin to be segmented (fig. 25A). Naturally, this also impedes human reconstruction performance, since such thin protrusions are easy to miss and more likely to be lost during tracing. Since these appendages were major input sites, a higher imprecision in connectivity measures specific to this cell type may be assumed.

The appendages were distinguished by a voluminous enlargement which carried multiple thin filiform extensions. The arrangement was reminiscent of long-fingered hands clutching around the presynaptic partner(s): The filiform processes enclosed around one or more bypassing neurites, which synapsed onto the voluminous enlargements. Not all “fingers” clasped around other neurites, some merely stretched out into the surrounding neuropil. They were not observed to be targeted by synapses. Synapses were directed towards the bulky “palm”, which always contained darkly stained ER and, when larger, also one or more small darkly stained mitochondria. The ER was found throughout the entire length of the dendrites, thick and thin, with the filiform processes at the appendages as the only exception. No vesicles were observed anywhere in the dendrite, suggesting it was a purely postsynaptic structure.

The dendritic trees were entirely confined to the GL. Their overall shape varied considerably between cells (fig. 25B). The final outline of the dendrite seemed to be predominantly dictated by the shape of the primary glomerulus they innervate and the position of the soma. The more superficial representatives were often positioned laterally to their main glomerulus, sometimes at considerable distance. The dendrites of these cells adopted a fan- or tassel-like outline, sometimes more reminiscent of a flattened besom (fig. 25B, 2. from the left). Further inside the OB, GLIN2s were positioned at the deep side of their primary glomerulus. Their dendrites grew into a circular fashion, resulting in a donut-like shape (fig. 25A, B, left most). Despite the frequent and wide branching, the dendrite filled the volume it occupied only to a moderate extent.

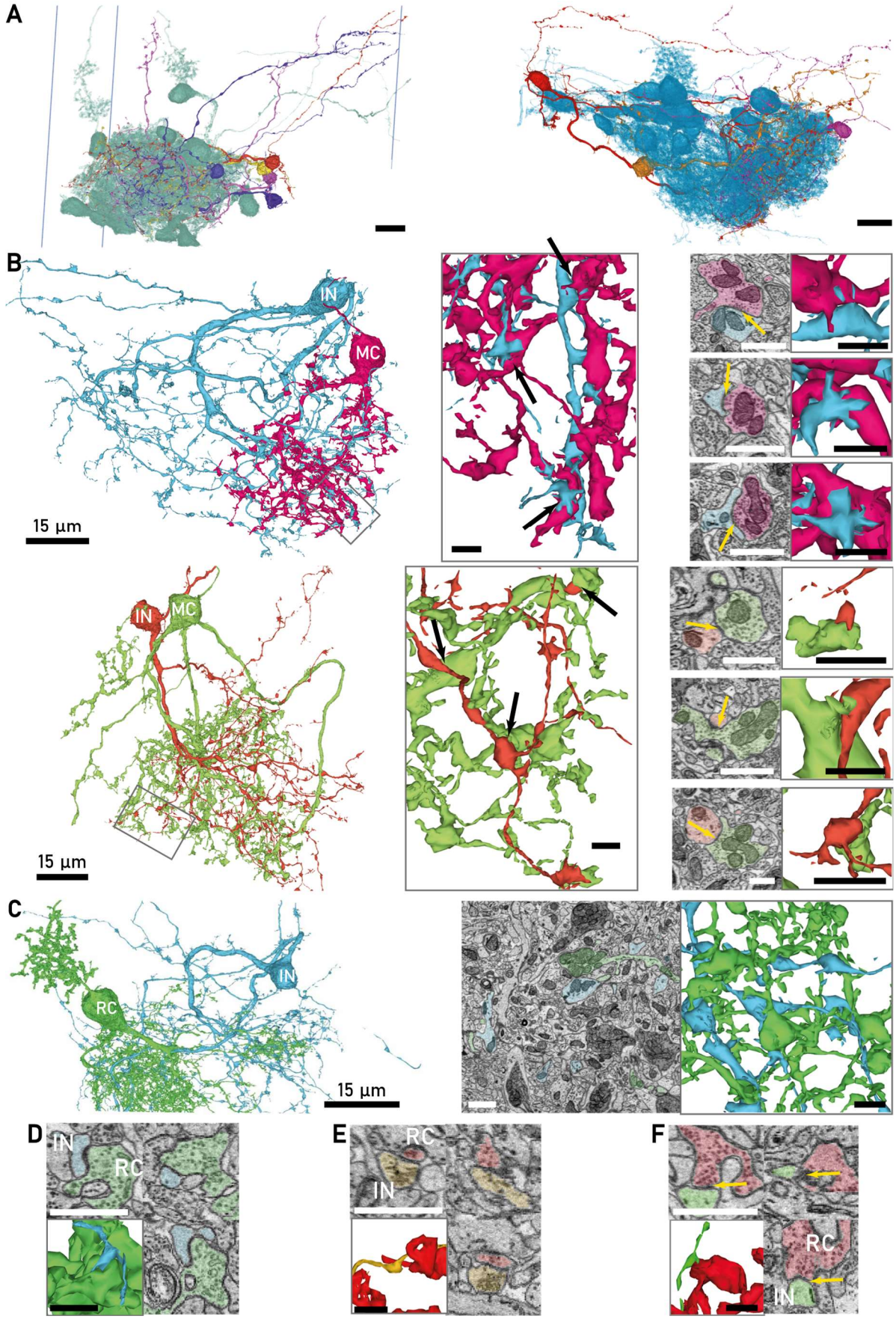
A
B
IN
MC
15 µm
IN
MC
15 µm
C
IN
RC
15 µm
D
IN
RC
E
RC
IN
F
RC
IN

Figure 26. Interactions between GLIN2s and projection neurons. A. Overlap of GLIN2s with glomeruli. Left: Two of the five GLIN2s innervating glomerulus M67D45A12 projected side branches to distal parts of the imaged volume. Right: Four GLIN2s innervating glomerulus M5D5A12 had smaller projections outside the glomerulus. B: Top: Interaction between a GLIN2 (blue) and a small MC (magenta) of glomerulus M45D45A1: the two cells made myriad contacts in which the MC synapsed onto the IN. Bottom: Overlay between a GLIN2 (red) and an intermediate MC of M5D5A12 (green). Contacts between this pair were fewer, but input from the MC to the IN was still frequent. C: Overlap between a GLIN2 (blue) and a RC (green): Dendrites of the two cells heavily intertwined for localized stretches of dendrite. Since both dendrites were postsynaptic, they did not make synapses. D: Contact site between a ruff (green) and the dendrite of a GLIN2 (blue) without synapse. E: Contact site between a GLIN2 axon (gold) and a ruff (red) without synapse. F: Only contact site between a RC (red) and a GLIN2 dendrite (green) with a synapse from RC to IN. Scale bars overview: 15 µm, details: 1.5 µm.

Interactions With Other Neurons

The GLIN2s projected their dendrite predominantly into the volume defined by a single glomerulus. Yet, the dendrite was not strictly confined to a single glomerulus. In most cells a small, but appreciable part of the dendrite resided in neuropil not occupied by any of the glomeruli. Some GLIN2s innervating glomerulus M67D45A12, for example, projected a dendrite of intermediate size across the entire imaged volume towards the deep left portion of the GL, which did not contain any sensory axons (fig. 26A). These dendrites showed only minor ramification. Such side projections were observed in most large GLIN2s, but often these projected outside the imaged volume. The GLIN2s were considered monoglomerular, but a more detailed investigation is necessary to determine the nature of the inputs to these cells outside of the glomerular volumes.

I examined the connections to PN for three GLIN2s innervating M5D5A12 and two GLIN2s projecting to glomerulus M45D45A1. In M5D5A12 the GLIN2s only projected to the smaller subcompartment and received input from all six MCs that innervated this subcompartment. For two of these INs the number of contacts was remarkably high, and the number of synapses made in these pairs was estimated to exceed ten. The synapses could originate from the thick primary dendrite of MCs, but more often originated from their distal varicosities, and targeted the filiform appendages of the GLIN2 (fig. 26B). Input to the third neuron was less frequent but still exceeded four synapses with five of six MCs. The M45D45A1 did not show compartmentalization. Here, one of the two GLIN2s received input from a large fraction of MCs (6 of 9 (67%)), but with only one or two synapses per pair. The other cell was targeted by a limited number of MCs (3 of 9 (33%)) but received multiple synapses from each. Altogether, these observations indicate that MCs contribute strong input to GLIN2s.

The dendrites of GLIN2s and RCs overlapped substantially, but the interaction was not as intimate as between RCs and MCs, or RCs and GLIN1s. RC dendrites seemed to follow the projection of the GLIN2 dendrites and approach particularly in the vicinity of input synapse from MCs (fig. 26C). A separate pairwise overlay of all 18 GLIN2s with the 17 CR and ICR RCs as well as additional 17 RCs, which were not reconstructed and predominantly represented as a ruff protruding into the imaged volume, yielded seven contact sites between a ruff and GLIN2 dendrites and four contacts between a GLIN2 axon and a ruff (fig. 26D, E), but no contacts between a GLIN2 axon and RC dendrites. Only in one case of contact between ruff and GLIN2 dendrite a synapse was identified (fig. 26F), indicating that RCs provide little input to GLIN2s.

GLIN2s interacted with a variety of local INs. Apart from input to the appendages, frequent inputs to the bigger dendrite shafts, but not the thin dendrites, could be observed. Numerous inputs originated from GLIN3s (see below) that innervated the same glomerulus. The somata of the GLIN2s received input from varicose enlargements containing small granular synaptic vesicles that resided on otherwise very thin neurites, which enter the imaged volume from the deep layers.

None of the axons of the GLIN2s were represented to completion within the imaged volume. A random sampling of axonal varicosities revealed the presence of both reciprocal, as well as unidirectional outbound and inbound synapses. The GLIN2s gave input to a variety of descending neurites of deep layer INs of different morphological classes. In particular the DLIN1s with long-necked spines (see → DLIN CLASS I) were a regularly encountered downstream partner (fig. 25A). Furthermore, synapses from GLIN2s onto the proximal dendrite or somata of GLIN3s innervating different glomeruli were found. Reciprocal and inbound synapses onto axonal enlargements originated from beaded neurites, the somata of which could not be traced back in the imaged volume. These neurites were similar in appearance to the neurites giving input to the somata of the GLIN2s.

GLIN CLASS III

The third morphological class of GLINs (GLIN3) comprised 11 cells characterized by a hairy proximal dendrite and a bushy, beaded distal dendrite (fig. 27A). These neurons differed from the other two GLIN classes by the absence of an axon. Nevertheless, different parts of the dendrite exhibited differential in- and output properties. Most cells were very well preserved in the imaged volume (CD0: 1, CD1: 8, CD2: 1, CD3: 1). The GLIN3 class contains a group of three neurons which stood out from the other eight due to their very small size and their distal dendrites residing very close to the cell body. Otherwise, they exhibited the same morphological features as the larger neurons and did not differ obviously in their interactions with PNs.
The GLIN3s shared morphological similarity with superficial representatives of DLIN3s or PLIN2s, whilst the smaller variant of this class bears resemblance to the axonless PLIN1s. However, GLIN3s are distinguished by the confinement of their dendrite to GL as well as the mostly monoglomerular innervation.

Morphology

The cell bodies were located in the deep GL and superficial PL. All somata were part of small cell clusters with heterogeneous composition of cell types, which could involve other INs, glia or more rarely a MC. The surface of the somata was flattened where it touched other cell bodies, and was otherwise bumpy and uneven, but not ragged. It was populated to varying degrees with filopodial dendritic twigs and a few protrusions that resembled branched or long-necked spines but were commonly not recipients of synaptic input.

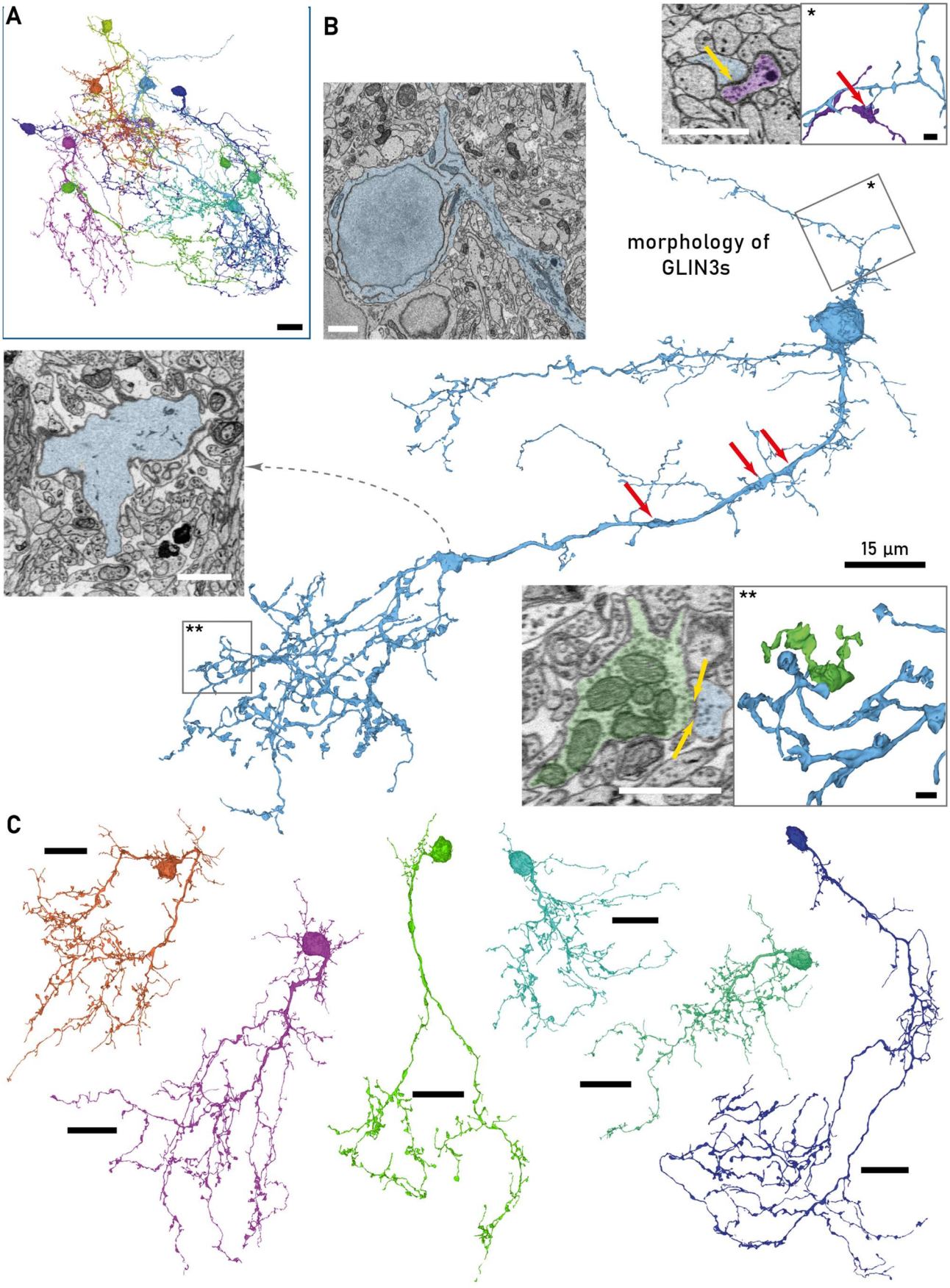
A
B
morphology of
GLIN3s
15 µm
C

Figure 27. Morphology of GLIN3s. A. Overview of the 11 GLIN3. B: A GLIN3 large dendritic projection to glomerulus M67D45A12 and minor projections to glomerulus M456D4A1. Insets: Top: Input to a dendritic spine at the proximal dendrite. Left: Cross section of an enlargement of the dendritic shaft (further dendritic enlargements see red arrows). Bottom: Close up on the distal dendrite showing spine-like varicosities that made reciprocal synapses with MCs (yellow arrows). C: Six GLIN3 displaying the variability in coarse topology and size. All scale bars except insets 15 µm, insets: 1.5 µm

The cell bodies were of small size (ø: 7 - 9 µm, $\bar{x}$ ± σ: 8.3 ± 0.6 µm), roughly ovoid and contained little or moderate amounts of cytosol. The nucleus filled the soma almost completely and followed the outline of the soma in shape (fig. 27B). Except for the base of the biggest primary dendrite, only few short strands of ER and very few slender mitochondria were visible. A primary cilium of medium length arose from each soma (1.8 – 4.5 µm, $\bar{x}$ ± σ: 2.7 ± 0.8 µm). No vesicles and no outbound synapses from the soma were observed. At the base of the biggest dendrites mitochondria in larger numbers and ER accumulated and the single Golgi apparatus usually stretched into the dendrite for a couple of microns.

The dendritic tree was composed of branches that could be classified into two different morphological groups: a larger, superficially projecting type and a delicate type. The latter bore many branched or long-necked spines and ramified predominantly laterally in the deep GL and superficial PL (fig. 27B*). The delicate dendrites could arise from the soma, but also emanated from the proximal parts of the larger dendrites. Their diameter was usually smaller than 500 nm. The number and length of these dendrites varied a lot between cells: Some cells bore multiple shorter branches with a length up to 20 µm. Others had only one or two of these dendrites, which extended for far more than 50 µm and made a few side branches. Few of these longer dendrites were projected towards the superficial GL, where they showed comparable morphological appearance as the distal portions of the large dendrites (see below). The thin dendrites were covered with a multitude of protrusions and small side-branches bearing spines of diverse shapes. This gave rise to the hairy appearance of these neurons (fig. 27B*). Some protrusions had a rather typical morphology of thin spines with a small head, which was often flattened in one axis, and a usually rather long neck (>1.5 µm). Fewer branched and short-necked spines were present, and some rare, filiform spines were found. Filopodial branches without any enlargement were also very frequent. Some side-branches gave rise to a few spines and then terminated in a large spine head. I visited a random number of spine heads, filopodial twigs and side branches in all cells and followed the longer thin dendrite along the entire length in two neurons. All spine heads received an inbound synapse. Input to the filopodial protrusions was less frequent and could occur at all positions along the protrusion. I discovered a considerable number of synapses onto the main dendritic shaft but no presynaptic structures in the thin, deep dendrites.

The soma gave rise to one, sometimes two larger dendrites, which at their base had a diameter between 0.5 and 1.5 µm ($\bar{x}$ ± σ: 1.1 ± 0.4 µm). The outline of the cross section was irregular: It was flattened in one axis, thus, rather oblong, and varied frequently in the ratio of the two principal axes. Short, darkly stained strands of ER stretched throughout the dendrite. Microtubuli were clearly discernible. The proximal portions of the dendrite were covered with spines, filopodial protrusions

and thin branches similar to the proximal dendrites. In the larger representatives these dendrites were projected towards the superficial parts of the GL and could obtain considerable length (> 100 µm), traversing the entire imaged volume in its x dimension. However, shorter stalks were also common. The dendritic stalk made a few, very irregularly shaped dilations that contained lots of ER and sometimes few, small mitochondria immersed in large cytosolic volumes. No synapses could be observed at these locations (fig. 27B). At their distal end the larger dendrites ramified increasingly and formed a besom-like, cone-shaped, or bushy tree. In most cells the frequency of spines and filopodia on the thicker dendrite reduced gradually towards the distal parts. In the smaller representatives the dendritic stalk was much shorter (<10 – ~20 µm) and the transition between the appearances of the proximal to the peripheral dendrite occurred in relatively close proximity to the soma. The dendritic ramifications resulted in a more globular, bushy outline of the cell and the direction of the peripheral dendrites towards the more superficial GL was less apparent in two cells and absent in one.

In the peripheral dendritic tree, spines were absent. Instead, this part of the dendrite bore enlargements and protrusions of a different appearance: irregularly shaped, sometimes voluminous enlargements, which showed indentations and concavities formed by contacting other neurites, emerged at high frequency all over the distal dendrite (fig. 27B**). They could sit on branch points, as dilation of a dendritic shaft, like sessile spines on a branch, or similar to a typical spine at the end of a neck-like branch. Altogether, the dendrites appeared as if they were embroidered with pearls or buttons. Most notably, the vast majority of these structures contained synaptic vesicles and were not only sites of inbound, but also outbound synapses (fig. 27B**), which could be unidirectional or reciprocal (see below). As regularly observed for sites of synaptic release, these enlargements usually contained some of the small, slender mitochondria characteristic for GLIN3s surrounded by ample cytoplasm.
In many neurons the change from proximal/deep and distal/superficial dendritic morphology could be pinpointed to a particular bifurcation, arising at one of the enlargements of the dendritic stalk described above. Yet, two cells did not show such a clear-cut transition, here the distal dendrite appeared more widely spread, the enlargements were less dense and more often sat at the end of a neck. Nevertheless, a qualitative examination suggests presynapses were restricted to the distal dendritic enlargements in these GLIN3s as well.

Interactions With Other Neurons

In GLIN3s, synapse detection was complicated by the vesicles loosely scattered in the cytosol of the enlargements of distal dendrites. Furthermore, output synapses could be rather small, comprising only a few vesicles associated with the membrane. Nevertheless, distinct synapses could be detected. The thin proximal dendrites resided outside the volume in which sensory axons terminated. The emergence of the morphological phenotype of the distal dendrites coincided with the entrance of the dendrite into a glomerulus. The majority of GLIN3s innervated only one glomerulus within the stack boundaries (8/11), while three neurons directed a smaller side branch to a second glomerulus.

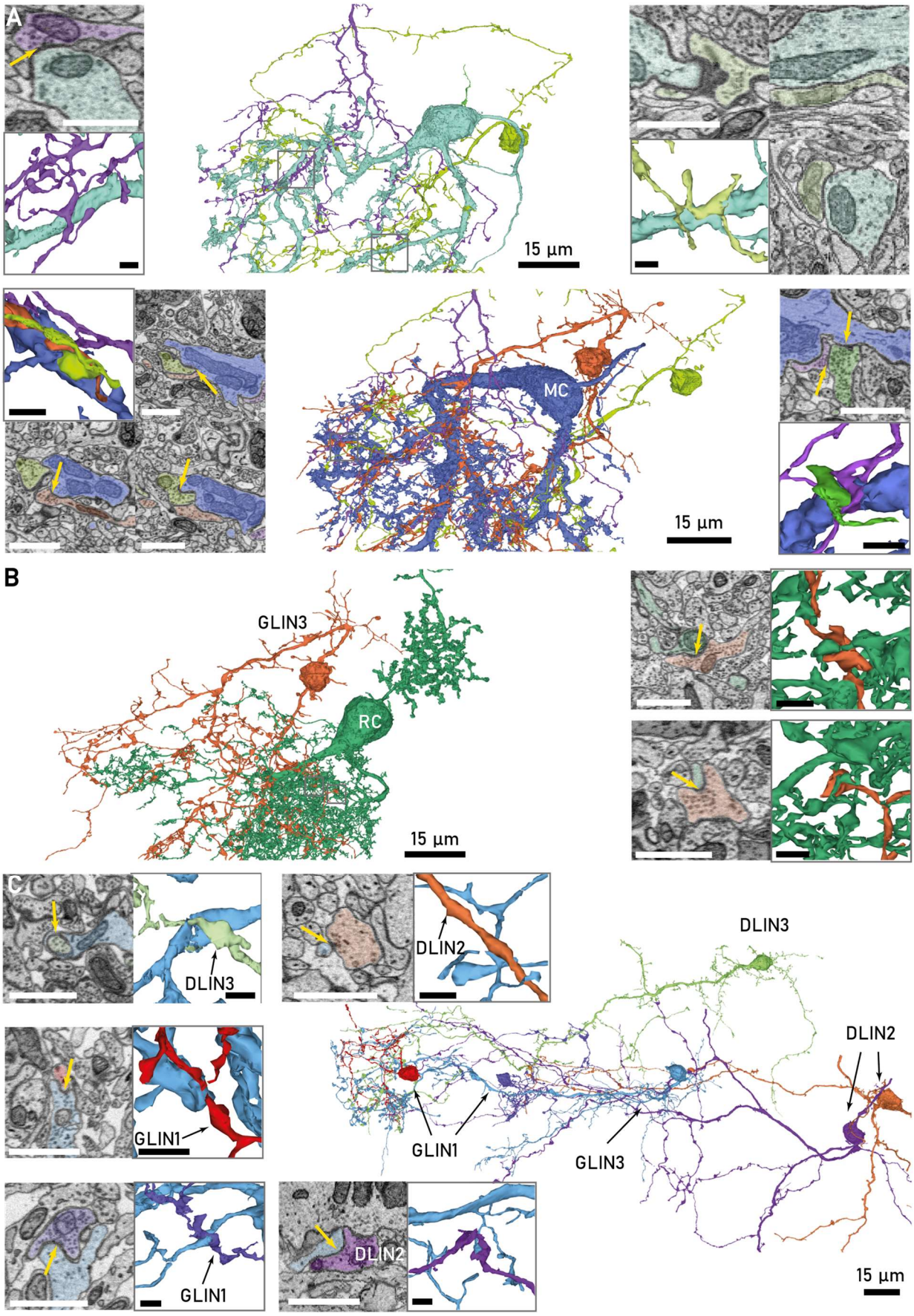
A
15 µm
MC
15 µm
B
GLIN3
RC
15 µm
C
DLIN3
DLIN2
GLIN1
GLIN1
DLIN2
DLIN3
DLIN2
GLIN1
GLIN3
15 µm

Figure 28. Connectivity of GLIN3 with other bulbar neurons. A. GLIN3 innervating glomerulus M45D45A1. Top left: The MC (turquoise) received input from one GLIN3 (purple). Top right: not all contact sides showed synapses. Bottom left: Another MC (blue) made reciprocal interactions with all three GLIN3. Bottom right: The GLIN3 and the MC received shared input in proximity to their reciprocal synapses B: Example of a GLIN3 of glomerulus M45D45A1 giving input to an RC. C: Example of a GLIN3 (blue) interacting with five other reconstructed INs: Top left: Input from a DLIN3 (light green). Top right: Input from a DLIN2 (orange). Middle and bottom left: Input from and to GLIN1s (red, purple). Bottom right: Input from a DLIN2 (violet). All scale bars inset: 1.5 µm, others: 15 µm.

I inspected interactions with the PNs for three GLIN3s in glomerulus M45D45A1, two GLIN3s in glomerulus M67D45A12 and one small GLIN3 in glomerulus M5D5A12. The two GLIN3s of M67D45A12 projected in non-overlapping fashion to different subcompartments. Most GLIN3s broadly innervated MCs of the glomerulus or glomerular subcompartment they projected to (ID414: 4/6 MCs (67 %), ID987: 6/9 MCs (67 %), ID1330: 2/9 MCs (22 %), ID1008: 3/4 MCs (75 %), ID1346: 4/7 MCs (57 %), ID2868: 3/9 MCs (33 %)). Usually each connected MC-IN pair made multiple contact sites, in which an enlargement of the GLIN3 dendrite was either wrapped around or immersed into the MC dendrite (fig. 28A). This interaction occurred predominantly at the thicker MC dendrites and to a lesser extent at their distal varicosities. The number of contact sites between pairs varied from one to far more than ten contact sites and all inspected contact sites contained synapses (fig. 28A). Most pairs were connected through multiple synapses (> 3). Reciprocally connected pairs were most frequent (16/22), but both MC-GLIN3 pairs, in which the GLIN3 provided only input to the MC (2/22) and vice versa (4/22), were found. Most synapses in reciprocally connected pairs were reciprocal, however, additional unidirectional synapses, both in- and outbound, were also commonly observed (13/16). The three GLIN3s innervating M45D45A1 strongly overlapped: They formed localized dendrite bundles, made reciprocal connections with the same MC in close proximity and received shared input with that MC from passing neurites (fig. 28A). One of the GLIN3 projected a smaller dendrite to M456D4A1, where it also connected reciprocally to a MC.
Only one GLIN3 was connected to the RCs examined, giving input to the dendrites of all three RCs of M5D5A12 through one or several synapses (3/16 RC-GLIN3 pairs). Apart from that, I did not find any more contacts between GLIN3s and RCs (fig. 28B).

Connections detected during reconstruction and the inspection of the proximal dendrites provide some insight into the interaction of GLIN3s with the IN network of OB. This showed ample input originating from passing neurites onto somata, spines and proximal dendrites of GLIN3s. These neurites were usually very thin (ø: 100 - 200 nm). Their synapses were located on enlargements, which assumed shapes varying from bulbous to flattened trapezoids, and bore indentations and bulges, where they contacted other neurites. The enlargements were often, but not always, packed with small point-shaped vesicles. These morphological features were characteristic for the distal branches of DLINs but could not be assigned to a particular neuron class. Indeed, one input originated from a reconstructed DLIN2. I further noted in- and outbound connections with other DLIN2s and DLIN3s. In addition, I observed interaction with some of the local GLINs: I found a few GLIN3s gave input to dendrite shafts of the GLIN2s and several GLIN1s make one or two separate synapses onto some GLIN3s. The latter interaction might have been reciprocal (fig. 28C).

III. INTERNEURONS OF THE PLEXIFORM LAYER

The INs of the plexiform layer (PLINs) comprised a group of 36 neurons, all of which were axonless and whose cell bodies resided in the open, neuropil rich PL. These cells were diverse in morphology and topology. The majority of PLINs projected primarily to GL. Yet, compared to GLINs the association to defined glomeruli was less clear and only a subset of PLINs showed a pronounced preference for a single glomerulus.

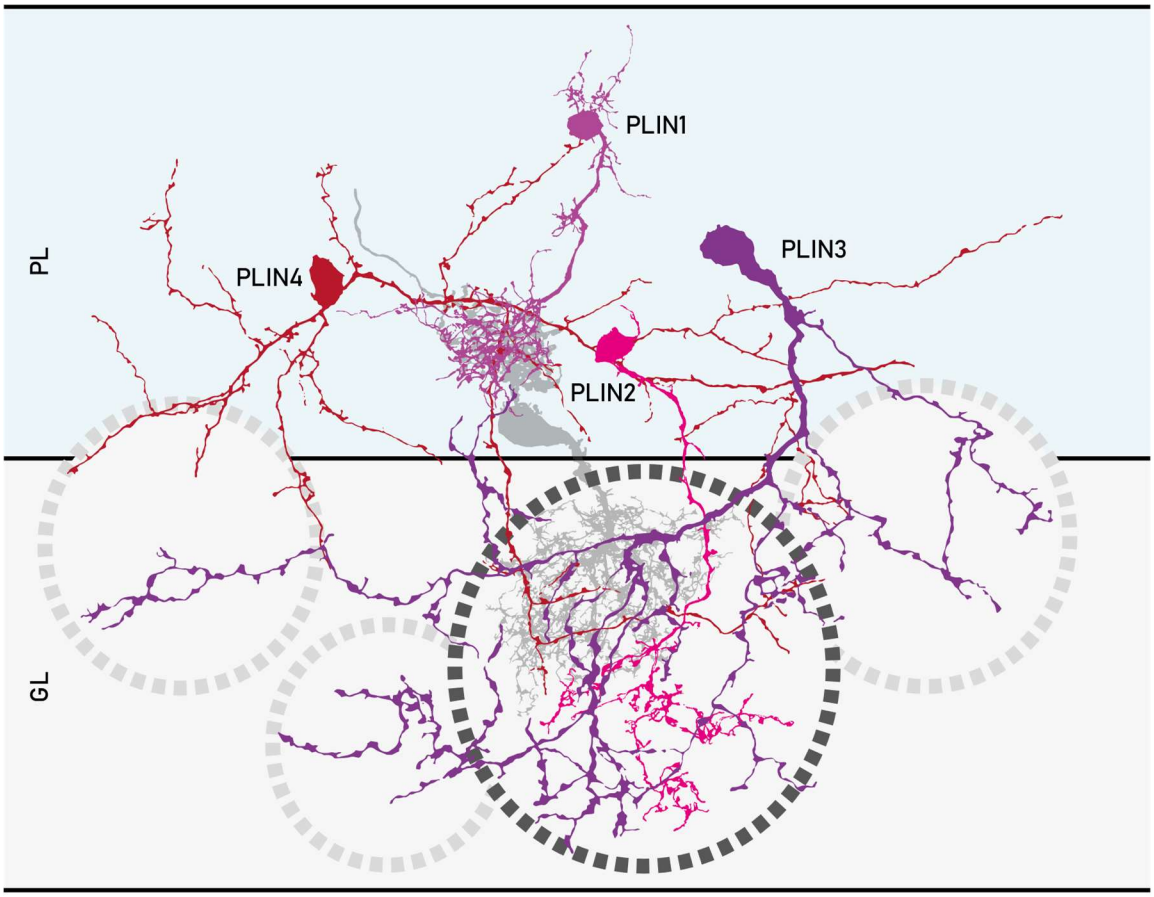

Figure 29.Schematic illustration of PLIN classes and their innervation of glomeruli.

I identified four morphological classes of PLINs (fig 29): The PLIN1s were represented by a small group of six petite neurons, which were almost entirely confined to the PL. These INs were characterized by a bushy distal dendrite, which strongly intertwined with one or several RC ruffs. A characteristic feature of the five PLIN2s were long, straight primary dendrites studded with spines at long but very regular intervals. These neurons ramify their distal dendrite within a single glomerulus. The 13 PLIN3s were large neurons which spread widely through GL, innervating multiple glomeruli. This group was further subdivided into two classes. The PLIN4s comprised 12 neurons of considerable topological heterogeneity. Assuming any orientation within the image volume, these cells ramified their thin, gnarly dendrites broadly through PL and made contacts with varying numbers of glomeruli in GL. Table 6 summarizes the main features of the PLIN classes.

IN class		cell count	axon	spine freq.	cell volume [µm³]	total length [mm]	soma volume [µm³]	soma diam. [µm]	# glomeruli innervated	reciprocal PN connections
PLIN1		6	-	+	230 ± 38	1.4 ± 0.4	75 ± 17	7.8 ± 0.9	1	+
PLIN2		5	-	++	221 ± 38	0.9 ± 0.2	71 ± 9	7.8 ± 0.4	1	+
PLIN3	rlPLIN3	5	-	+	395 ± 164	2.0 ± 0.9	122 ± 41	8.8 ± 0.7	4.6 ± 2.4	+
	vPLIN3	8	-	+	473 ± 93	1.8 ± 0.5	144 ± 29	9.0 ± 0.5	3.8 ± 1.4	+
PLIN4		12	-	+	314 ± 46	1.6 ± 0.6	135 ± 36	9.5 ± 1.0	1.0 ± 1.2	+

Table 6. Features of PLIN classes. Abbreviations: -: absent, +: present, ++: pronounced, +++: very pronounced. Numbers given as mean ± standard deviation.

PLIN CLASS I

The PLIN class I (PLIN1) comprised a group of six small, bushy neurons that were almost entirely confined to the PL and well represented in the stack (CD0:1, CD1:4, CD2:1, fig. 30 E). These neurons stood out by a very tight association with RCs.

Morphology

Embedded in the PL neuropil or part of a deep layer clusters, the somata of these cells are very small (ø: 7 - 9 µm, $\bar{x}$ ± σ: 7.8 ± 0.9 µm) and resemble an unshaped globule or ellipsoid. The somata had a rough surface and bore membrane excrescences that did, however, not resemble spines. The contour of the nucleus roughly followed the soma outline. Only a thin layer of cytosol separated it from the plasma membrane (fig. 30A). Cellular organelles resided in a cytoplasmic protuberance at a pole of the soma. This was not necessarily located at the base of a dendrite: In two cells it was completely externalized from the soma into a bulge, which was connected to the soma via a short bridge and gave rise to the primary dendrite. A single, short primary cilium emerged from either soma or the cytosol bulge at the base of the dendrite (1.5 – 2.5 µm, $\bar{x}$ ± σ: 2.0 ± 0.3 µm)

One or two small to medium-sized dendrites arose from the somata (ø: 0.5 – 1.0 µm, $\bar{x}$ ± σ: 0.6 ± 0.2 µm, fig. 30B). The dendrites were projected towards the deep GL or superficial PL, where they ramified into a bushy dendritic tree with a diameter on the order of 20 to 30 µm. In addition, the PLIN1s bore several thin, proximal branches of variable length, which emanated from the soma or arose from the main dendrite. The proximal branches made small, infrequent, flattened rather than voluminous varicosities, which could occur at any position on the branch (fig. 30C). In one neuron multiple thin branches emanated from the deep anterior pole of its soma, forming a structure similar to a sparse version of the distal, bushy ramification. The distal dendrite exhibited varicosities at a much higher density (fig. 30D). Similar to varicosities in other parts of the dendrite, they were predominantly amorphous and flattened, but bulky voluminous enlargements usually containing mitochondria were also observed.

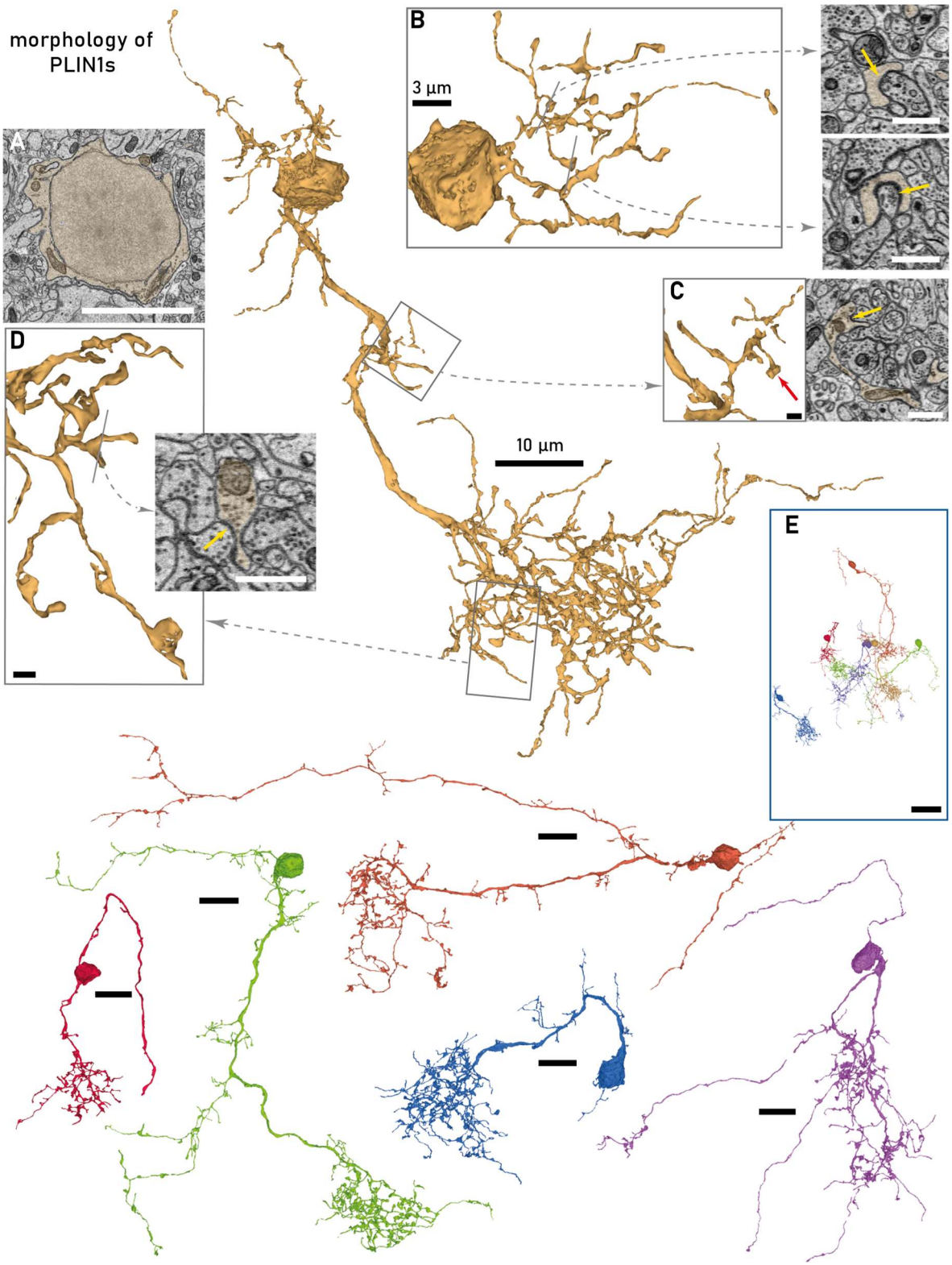

Figure 30. Morphology of PLIN1s. Top: Morphological details at the example of one PLIN1: A. Cross section of the soma surrounded by little cytosol. A small Golgi apparatus was visible at the base of the primary dendrite. B: Close-up on the bushy proximal dendrite receiving input to the spine-like protrusions. C: A dendritic side branch arising from the primary dendrite: A synapse onto a local IN is visible D: Tip branches of the distal dendrite exhibited plenty coin-shaped enlargements with pre- and postsynaptic sites. E: Overview of all six PLIN1s in the bounding box of the imaged volume. Bottom: Individual portraits of five PLIN1s (scale bar: 10 µm). Scale bars: A: 5 µm, E: 30 µm, others: 1 µm.

The distal dendrite made many thin, almost pointy tip branches, reminiscent of a thorn bush. Some of these tip branches spread far outside the main globular dendritic ramification. I visited and browsed along a random subset of proximal and distal branches. I could not determine any clear-cut pre- and post-synaptic compartmentalization in these neurons. Presynapses were small, with vesicle clouds comprising usually only a handful of vesicles. Pre- and postsynaptic structures were most frequent in the distal dendritic varicosities but were not limited to these structures and occurred on shafts as well. Notably, not all varicosities made outbound synapses.

Interactions With Other Neurons

The PLIN1s showed little interaction within glomeruli. Even the most superficially projecting neuron spread its ramification in a cleft between the M56D56A2 and the M5D5A12 glomerulus, which was not innervated by any MCs. Three neurons projected into a glomerulus, but only minor parts of the distal dendrites were immersed into a single glomerular volume. For one cell, I could not find any synaptic contacts to the PNs forming the M5D5A12 glomerulus. The other two PLIN1 projected to M5D4A12 and made connections with one or two out of four MCs, respectively (fig. 31B). These connections were mediated by one or two reciprocal synapses. In one pair I found four additional outbound synapses from the PLIN1 onto the MC.

A striking feature of PLIN1s was their association with RCs. The PLIN1s immersed their dendrite into RC ruffs and made synaptic contacts. In that, they were far more promiscuous in their interaction with RCs than the GLIN1 (see GLIN CLASS I): I could identify up to five different RCs being connected to a single PLIN1 ($\bar{x}$ ± σ: 3.2 ± 1.3 connected RC/PLIN1, fig. 31A). These RCs included reconstructed RCs innervating different glomeruli, but also unreconstructed RCs entering the images volume at the dorsolateral side. The PLIN1s contact the RCs not only via the distal, bushy dendrite, but also any other of their side branches. The fraction of dendrite projected into a given ruff varies significantly: Most PLIN1s immerse their bushy distal dendrite into one or at most two RCs and project only a few subbranches into additional ruffs. Notably, a subset of these smaller projections does not make any connection to the RC. Connections via the bushy distal dendrites involved several reciprocal, but also additional unidirectional in- and outbound synapses, resulting in ca. two to five contacts per pair. In addition to the 13 reciprocally connected RC-PLIN1 pairs, in four of the 19 pairs the RC gives input to the PLIN1 and in two pairs the PLIN provides input to the RC dendrite. The unidirectionally connected pairs encompass only a single, at most two synaptic contacts.

I also noted synapses to other neurites within the volume of a ruff a given PLIN innervates. To further explore their connections to other INs, I searched for contacts between one PLIN1 to all sGLIN1 innervating the same RCs by pairwise overlay of the meshes. Indeed, I found the PLIN1s to give input to the dendrite of five of 10 reconstructed GLIN1s innervating the same three RC ruffs. The number of contact sites varied between one and four synapses but was not necessarily restricted to a single ruff if both pairs innervated the same second ruff. In addition, I found several PLIN1s to provide input to different GLIN2s, these connections consisted of a single synapse each.

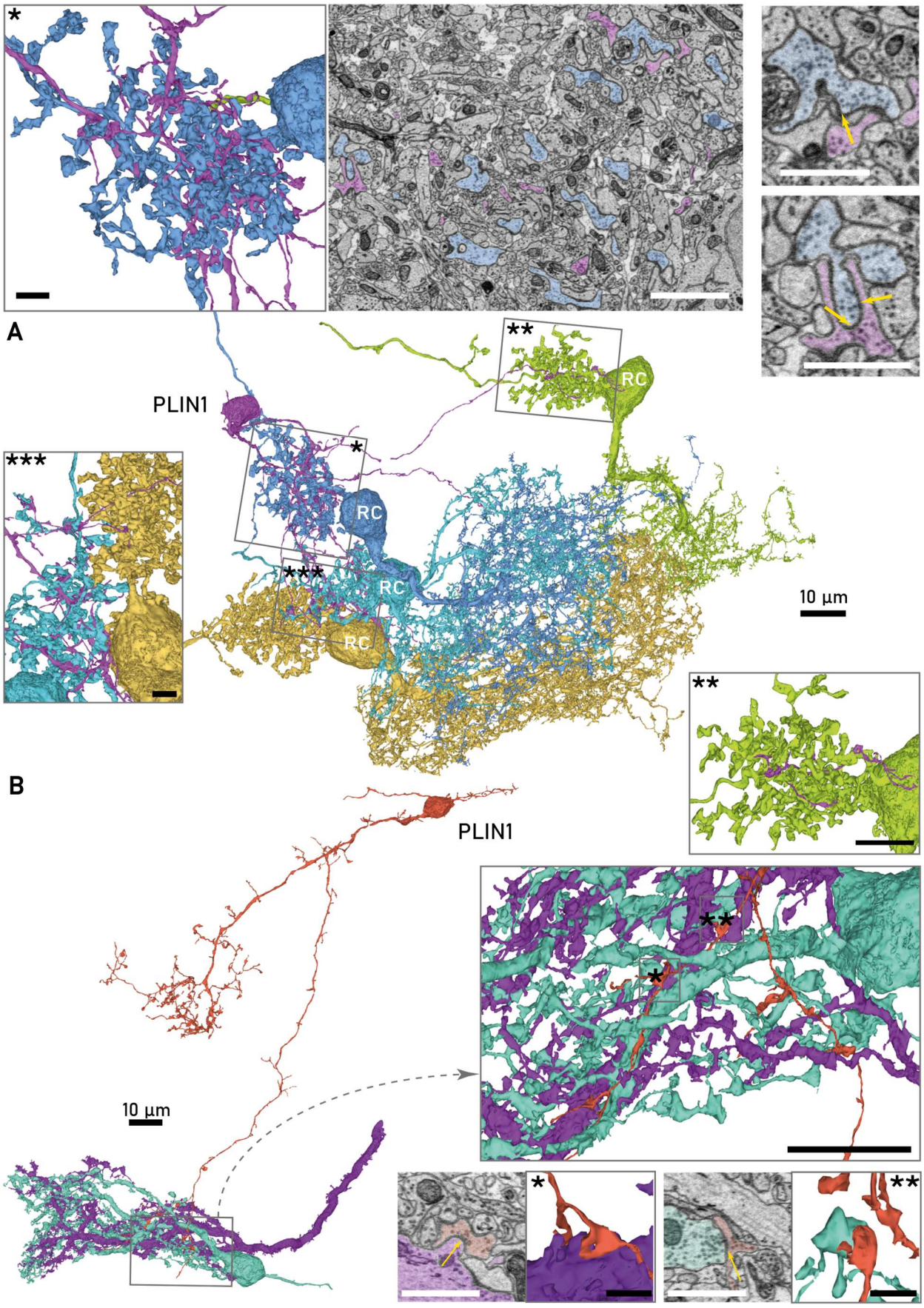
A
PLIN1
RC
RC
RC
10 µm
B
PLIN1
10 µm

Figure 31. Interactions between two exemplary PLIN1s and PNs of OB. A: A PLIN1 (purple) interacts with four RCs of different glomeruli. The amount of dendrite immersed in the individual ruffs varied from a single branch (golden RC) to several branches (green RC) to large bushy trees (light and dark blue). Insets: Cross section at the ruff. The PLIN1 interacted with other INs in the ruff neuropil, right: examples of inbound and reciprocal synapses between the RC and the PLIN1 (arrows). B.: Another PLIN1 (red) made reciprocal synapses with two MCs of glomerulus M5D5A12 (purple, turquoise), but no others. The connection was established from an isolated side branch, remote to the main dendritic tuft, which interacted with RCs of a different glomerulus. Insets: Enlargements of the dendrites and cross section of in and outbound synapses (see arrows). Both synapses were reciprocated in different sections. Scale bars: close-ups on ruff interaction: 3 µm., close-ups on synapses: 1.5 µm.

PLIN CLASS II

A small group of five axonless INs, characterized by a thin, elongated main dendrite, which penetrated the glomerular area, formed the PLIN class 2 (PLIN2, see fig. 32A). These neurons were represented to varying degrees of completeness in the stack. Three neurons had been subjected to only minor cuts (CD1), while in one cell with a second dendrite cut at the main shaft was rated (CD2) and another was rated CD3, because the distal dendrite was largely cut off.
Neurons of this class were morphologically closest to the GLIN3s. They set themselves apart from this group by their lack of proximal dendrites, the regularity of their spine-like protrusions and the sparseness of their distal dendrite.

Morphology

The somata of these INs occurred as members of pairs or small clusters throughout the PL and had a small diameter (ø: 7 - 8 µm, $\bar{x} \pm \sigma$: 7.8 ± 0.4 µm). They were of an approximately ovoid or globular shape with a rough, but non-spiny surface that sometimes bore amorphous membrane excrescences. Typically, they exhibited several indentations made by larger passing neurites or neighboring somata. The perikaryon was only represented by a thin layer of cytosol separating the nucleus from the plasma membrane, and the indentations of the outer membrane were sustained in the nucleus outline (fig 32C). Very few small mitochondria and basically no ER cisternae were found in the cytosol surrounding the nucleus. The majority of cellular organelles were collected in protuberances at the base of the primary dendrite or were fully outsourced to proximal parts of that dendrite (fig 32C). In each PLIN2 a short primary cilium could be identified (1.3 – 2.0 µm, $\bar{x} \pm \sigma$: 1.7 ± 0.3 µm).

The majority of cells gave rise to a single dendrite, only one cell had two dendrites of similar size. The dendrite was small in diameter (ø: 0.8 – 1.3 µm, $\bar{x} \pm \sigma$: 0.9 ± 0.3 µm) and had an irregular outline with varying cross section. Maintaining its circumference, it traversed the PL in a more or less straight fashion without branching. The main shaft was garnished with spines or spine-like protrusions that occurred at quite regular intervals on the order of several microns. The length of this interval as well as the appearance of the protrusions varied between cells. Two cells bore rather branch-like spines, while the other two exhibited rather flat or bulky round headed spines. The last cell showed membrane protrusions of variable shape that resembled sessile spines with a saw-tooth-like appearance. Not all of these received synaptic input. In other cells all randomly picked spines received synaptic input originating from varicosities on thin neurites that contained many small, dark-stained,

dot-like, synaptic vesicles (fig 32B).
When entering the glomerular volume, the dendrite branched and formed a sparse, besom-shaped tree with thin branches (ø: 200-300 nm). As observed for other IN types this distal dendrite did not bear spines but exhibited amorphous varicosities that contained synaptic vesicles. Flattened and bulky varicosities occurred in equal measure in each cell (fig 32D). They could be located along the branch, but more often occurred at tips and, thus, gave an appearance of very bulky headed spines.

Interactions With Other Neurons

The PLIN2s were an exception among the PLINs in that each neuron only innervated a single glomerulus. I examined the interactions with PNs for one PLIN2 each in M45D45A1 and M5D4A12. I did not find any connections to RCs. The PLIN2s did not connect to all MCs of a given glomerulus (5/12 MCs (42 %), 2/4 MCs (50 %)). The number of synapses between connected pairs as well as their direction varied: In two pairs numerous contact sites and synapses could be observed. These pairs were connected through reciprocal or unidirectional synapses (fig. 33A). In other pairs I found only isolated contact sites, making unidirectional synapses (fig. 33B). Both input from PLIN2s to MCs as well as vice versa were observed.
The interaction with other INs of the OB was not explored in detail. Yet, a synapse from a GLIN2 onto the proximal shaft of a PLIN2 was found (see fig. 25A). Conversely, I found several inputs from the PLIN2 onto the dendrite of the GLIN2 for two pairs, and furthermore, input onto GLIN3 and PLIN3 dendrites were observed (fig. 33C).

PLIN CLASS III

The 13 neurons of PLIN class III (PLIN3) were characterized by an ovoid cell-body usually giving rise to a single, long dendrite which spread in a swirl-like fashion throughout the GL. Due to the wide spread of these dendrites, the degree of completeness of their representation was more difficult to assess. All neurons obtained at least minor cuts at their dendrite (CD1: 4, CD2: 6, CD3: 2).
Two subclasses could be distinguished within this morphological class: a varicose (vPLIN3) and a ribbon-like variant (rlPLIN3). These shared an overall coarse morphology, but expressed subtle differences that were largely correlated across several features as summarized in table 7. I will first describe common features and then highlight distinct characteristics for the individual subclasses.

Morphology

The ovoid somata were of medium size (ø: 8 - 9 µm, $\bar{x} \pm \sigma$: 8.8 ± 0.6 µm) and all located in the PL. The nuclei were ovoid and encompassed by little cytosol. The perikaryon contained a few very small mitochondria, or narrow mitochondrial side branches. A few large vesicles, and short strands of ER were observed. At the pole giving rise to the dendrite, a large funnel-shaped bulge formed in which large amounts of cytosol were collected. Here, a primary cilium of medium length emerged (2.0 – 3.0 µm, $\bar{x} \pm \sigma$: 2.4 ± 0.3 µm) and the elements of the endomembrane system accumulated.

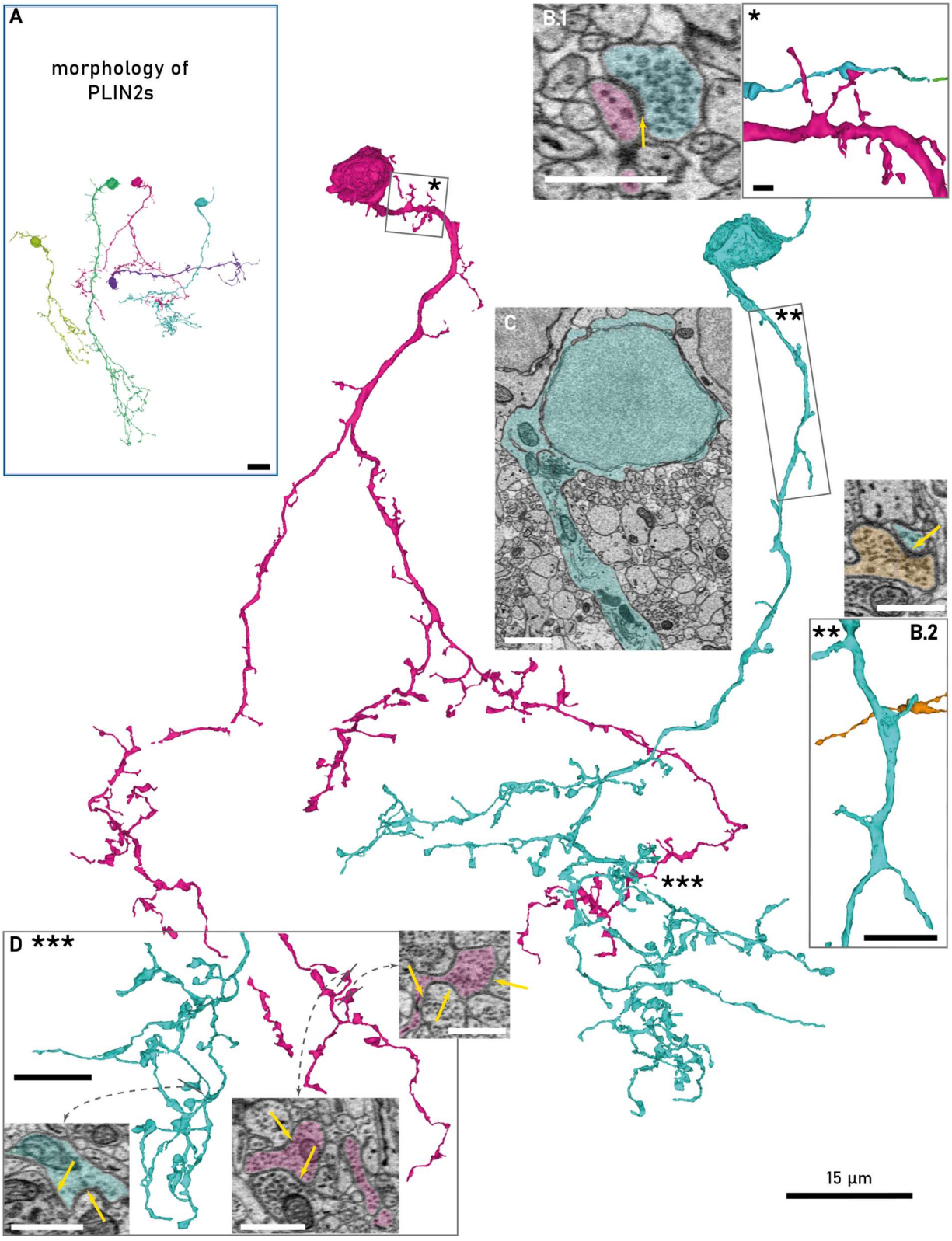

Figure 32. Morphological properties of PLIN2s. A. Overview of all five PLIN2 within the stack boundaries. B: Close up on spines: B.1. example of a branched spine version, input from a varicosity of a thin neurite. B.2 example of round headed spine version. C: Enlargement of the soma showing cellular organelles "outsourced" into the proximal dendrite. D. Close up on the (often spine-like) varicosities at the distal dendrites. These enlargements contained many vesicles and were pre- and postsynaptic to INs and PNs. Scale bars: A: 15 µm, B.2, D: 5 µm, all image views: 1 µm.

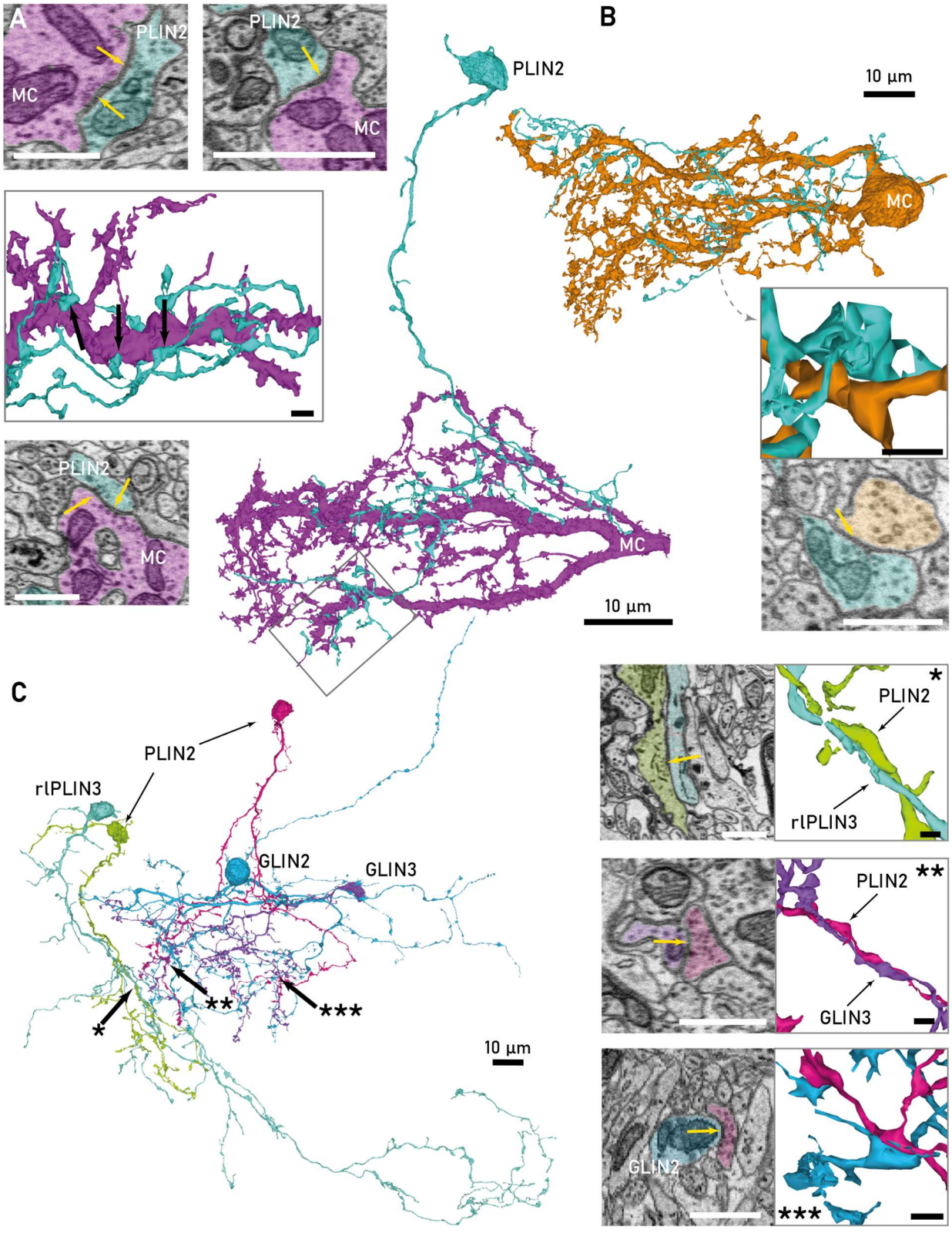

Figure 33. Interaction between PLIN2s and other bulbar neurons. Top: Differential interaction between PLIN2s & MCs. An exemplary PLIN2 made multiple, mostly reciprocal connections in close proximity and across the entire glomerular volume with one large MC (A), but only one input to another MC (B, dendrite of PLIN2 cut) and no other MC of that glomerulus. C: Interaction with local INs. A PLIN2 (lime) gave input to the shaft of a rlPLIN3 (turquoise, *). Another PLIN2 (pink) was presynaptic to a GLIN3 (purple, **) and a GLIN2 (dark blue, *). Scale bars insets: 1 µm.**

The cells usually had one or two Golgi apparatus that stretched far into the dendrite. Mitochondria were larger here, making slender side branches that reached far into the dendrite or extend around the nucleus.

Due to this funnel shaped expansion the dendrite appeared massive at its base (ø: 3-5 µm) before it leveled at a diameter of ~1 µm (ø: 0.5 – 1.5 µm, $\bar{x}$ ± σ: 1.0 ± 0.3 µm) (fig. 34B.1, B.2). The dendrite had an oblong cross section that was occasionally dilated in its long axis by mitochondria. In most cells the dendrite was directed laterally in its initial course and descended towards the superficial layer only at a very shallow angle. The dendrites gave rise to many side branches that projected either laterally or superficially. With some distance to the soma the side branches became thicker and longer and ramified. The branching pattern remained asymmetric though, and the primary dendrite could be retraced over its entire length. By meandering towards the superficial parts, the dendritic processes passed through large portions of the GL volume (fig. 34A).

The proximal portions of the dendrites bore spine-like protrusions at low to moderate density. A qualitative examination by randomly visiting subsets of these excrescences suggests that these were post- and not presynaptic (fig. 34C.1, C.2). However, a considerable fraction did not receive any input. Along the proximal to distal axis of the dendrites the appearance of protrusions rather gradually transitions from a more spine-like aspect to a more varicose aspect. Whilst no not criterion could be made out that would indicate a separation between a pre- and postsynaptic part in these neurons, synaptic vesicles were not abundant in the proximal portions of the dendrites. Presynapses were most reliably found at enlargements of the distal dendrite and with considerable distance to the soma also on the shaft of the primary dendrite. The distal varicosities could arise at every part of the distal dendrite, i.e., shaft, bifurcations or at the terminal end of a branch. They were mainly bulky, amorphous with a rough surface and often bear stubby or pointy excrescences.

The Ribbon-Like PLIN3

The group of ribbon-like PLIN3s (rlPLIN3s) contained five neurons, whose somata were associated with a small cluster of neurons of heterogeneous types. The cell bodies had a smooth surface and sometimes made one or two spine-like protrusions of irregular shape. The nuclei had an even outline without notable indentations (fig. 34B.1). Cytosol was particularly sparse in the perikaryon of these cells. All neurons had a single dendrite with very thin and short branchlets in the proximal portion. Side branches became more substantial and ramified with increasing distance from the soma. Compared to the vPLIN3s, the dendrites spanned a larger volume, but, because of a lower branching frequency, they filled this volume to a lesser extent (fig. 34, overview). The overall appearance of this subset was more delicate, with thinner branches. The dendrite, which was oblong in cross section and predominantly smooth in surface, frequently twirled around its own axis. Some neurons of this subgroup exhibited a unique pattern of curls in their dendrite (fig. 34E). Altogether the aspect of the dendrite was reminiscent of a ribbon. Proximal to the soma the dendrites infrequently bore spine-like excrescences that were mainly of filopodial and short-necked, flat, round headed appearance. At the

distal dendrites varicosities were far less frequent and less pronounced than in the vPLIN3s and in three neurons flattened and smooth enlargements dominated (fig. 34D.1).

neuron id / feature	952	1121	3362	2789	487	1257	1504	1392	1414	1457	1153	1516	893
CD	2	2	1	2	1	3	3	1	2	2	1	2	2
soma surface	sm	sm	sm	sm	sm	ro	sm	ro	ro	ro	ro	sm	sm
nucleus indentations	-	-	-	-	-	-	-	+	++	+	++	-	-
spines	r, fi	r	fr, r	r	r, fi	st, fr	fr	fr	fr	st, fr	st, fr	fr, br	fr
thin dendrites	++	+	+	+	++	-	-	-	-	-	-	-	-
ribbon curls	-	+	++	-	+	-	-	-	-	-	-	-	-
varicosities	+	+	+	+	++	+++	+++	+++	+++	+++	+++	+++	+++
varicosity form	b, ro	b, ro	f, sm	b, s	f, sm	b, ro	b, ro	b, ro	b, ro	b, ro	b, ro	b, ro	b, ro
glomerular projection													
M45D56A1	++	+	++	-	-	-	+	+	+	-	-	-	-
M56D56A2	++	+	+	-	-	-	-	+++	-	-	+	-	++
M45D45A1	-	-	-	++	-	++	-	++	++	+++	-	-	-
M5D5A12	-	++	-	-	+++	++	-	+	+++	++	++	+++	++
M5D4A12	-	-	-	-	-	+	-	-	+	+	-	-	-
M67D45A12	+++	++	+++	-	-	-	+++	+	-	+	+++	-	-
M456D4A1	-	+	+	+	-	-	-	-	+	-	-	-	-
M6D45A1	-	+	++	-	-	-	+	-	-	-	-	-	-
M45D4A2	-	+	+	-	++	-	-	+	-	++	+	++	-
M6D34A12	-	+	++	-	+	-	++	-	-	-	-	-	-
# glomeruli	3	8	7	2	3	3	3	6	5	5	4	2	2

Table 7. Summary of morphological features of ribbon-like (grey shading) and varicose PLIN3s (blue shading). Abbreviations: -: absent, +: present, ++: pronounced, +++: very pronounced, sm: smooth, ro: rough, b: bulky, f: flat, r: round headed spines, fi: filopodial spines, fr: frayed spines, st: stubby spines, br: branched spines,

Figure 34 (next page). Morphology of PLIN3s: A ribbon-like (green, rlPLIN3) and a varicose PLIN3 (red, vPLIN3). The rlPLIN3 had a wider spread but branched at lower frequency. The vPLIN3 was more compact and its bushy distal dendrite bore many varicosities, sites of synapses with local neurons. A: Overview of all PLIN3s within the bounding box of the imaged volume. All somata were located in PL, the dendrites spread extensively on a meandering path through GL. B. Close up of the somata: the rlPLIN3 had a comparably smooth surface (B.1), whereas the surface of the vPLIN3 was more ragged (see undulations in cross section). In both somata the cellular organelles mainly collected in a funnel-shaped bulge at one pole of the soma. C.1 Close up of proximal branch showing several stubby and long-necked, round headed spines on rlPLIN3 dendrites. C.2 The vPLIN3 had rather fringy, stubby spines. D. Close up on the distal dendrite. D.1 the rlPLIN3 made flattened varicosities at low frequency. D.2 the vPLIN3 had a high density of bulgy varicosities. Both neurons made reciprocal interactions with MCs and other neurons. E. Close-up on a ribbon curl. Scale bars: overview & A.: 50 µm, all other insets: 1.5 µm.

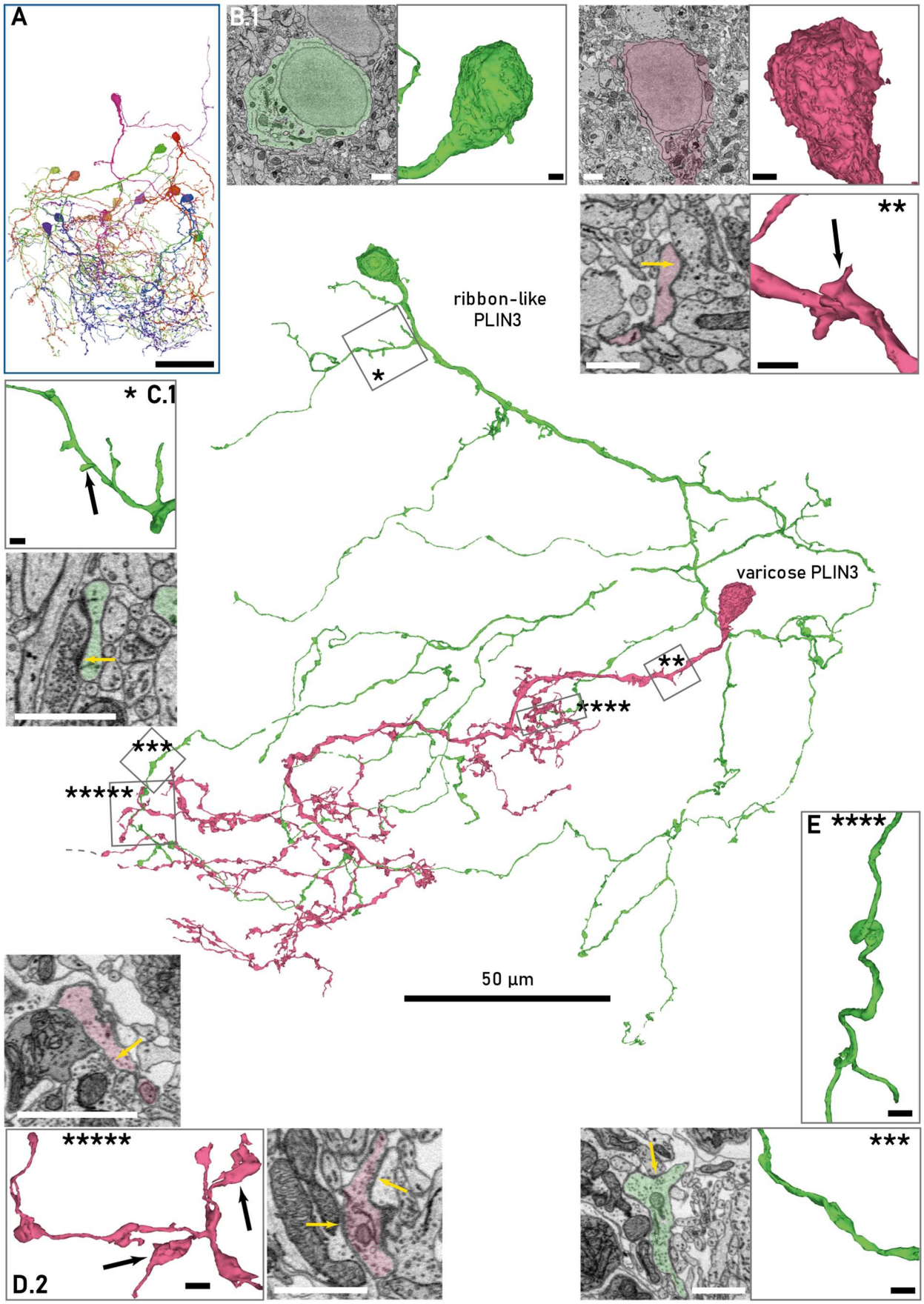
A
B.1
**
ribbon-like
PLIN3
*
* C.1
varicose PLIN3
**
****
***
*****
E ****
50 µm
*****
D.2
***

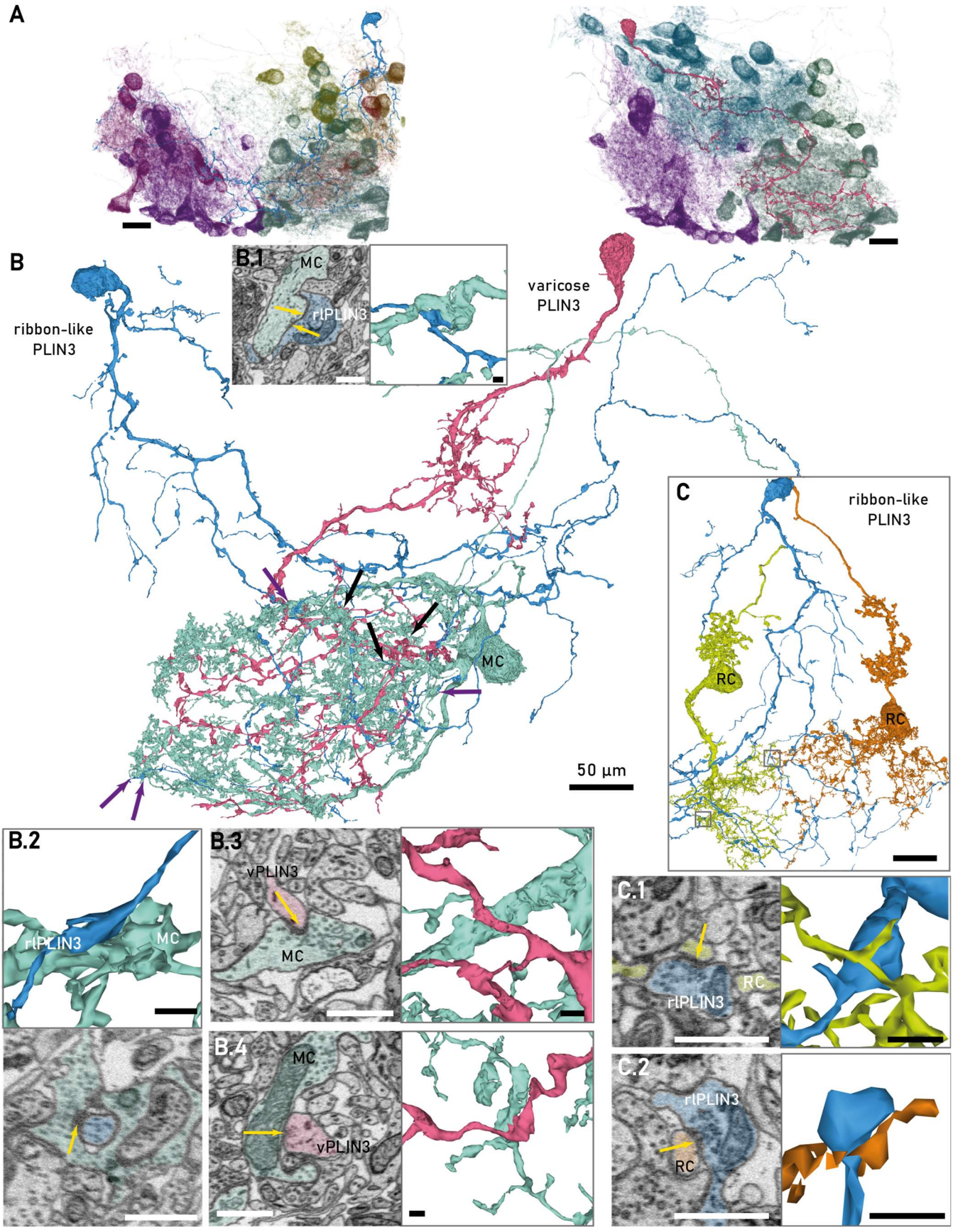
A
B
B.1
MC
rlPLIN3
ribbon-like
PLIN3
varicose
PLIN3
MC
50 µm
C
ribbon-like
PLIN3
RC
RC
B.2
rlPLIN3
MC
B.3
vPLIN3
MC
B.4
MC
vPLIN3
C.1
RC
rlPLIN3
C.2
rlPLIN3
RC

Figure 35. Interactions between PLIN3 and PNs. A: Glomerular innervation by PLIN3s. PNs of a given glomeruli are displayed in one color and at low opacity. The ribbon-like PLIN3 (blue, left) projected to five glomeruli, whereas the varicose PLIN3 (red, right) had projections in four glomeruli. B. Overlay of the same cells with a MC of M67D45A12. The ribbon-like PLIN3 made three reciprocal synapses and an input synapse with the MC (purple arrows, insets B.1 and B.2). The varicose PLin3 made three synapses with the MC (black arrows), two outbound (B.3, B.4) and one inbound synapse. C. Overlay of two RCs of M67D45A12. Scale bars: A.: 15 µm, all other insets: 1 µm.

The Varicose PLIN3

The somata of the eight neurons assigned to the varicose PLIN3s (vPLIN3s) were all loosely immersed in the neuropil of the PL. Five somata exhibit a rather craggy or bumpy surface without spines. Their nuclei showed undulating indentations (fig. 34B.2). In this subclass cytosol was slightly more abundant and often long-stranded ER was arranged as a single concentric circle surrounding the nucleus. Whilst four cells also gave rise to only a single dendrite, three neurons emanated a second, smaller neurite that was directed towards the PL at the dorsal and the lateral anterior side of the imaged volume, respectively. The dendrites of this subclass had a more robust appearance: they were slightly thicker, varied in diameter and possessed an irregular, bumpy surface structure. They lacked the thin, short branches observed in the rlPLIN3s.

Proximally, they exhibited spine-like excrescences that predominantly classify as sessile, stub–like protrusions or had an appearance similar to the frayed spines observed in DLIN2 (see below) (fig. 34C.2). The distal portions of the dendrites were decorated with amorphous, bulky varicosities at a very high frequency (fig. 34D2).

Interactions With Other Neurons

The dendritic morphology suggested that the PLIN3s did not restrict their neurites to a single glomerulus. To get a notion of the breadth of the glomerular interactions, I overlaid each PLIN3 with the PNs forming a glomerulus. I visually estimated the relative proportion of dendrite projected into a particular glomerulus and verified that at least one synaptic connection was made within a given glomerular volume. This examination confirmed that PLIN3s interacted with numerous glomeruli ($\bar{x}$ ± σ: 4.2 ± 1.9 glomeruli, fig. 35A). Differences in the number of innervated glomeruli between the subclasses were not pronounced (see table 7). The fraction of a dendrite innervating individual glomeruli varied between cells. Some PLIN3s projected strongly to few glomeruli, others showed a more distributed glomerular innervation pattern with varying degree of preference for individual glomeruli. Again, no obvious difference between the two subclasses was noted (see table 7).

I inspected the connectivity to PNs within a glomerulus for five vPLIN3s and two rlPLIN3s for the glomeruli M45D45A1, M5D4A12, M67D45A12 and M45D4A2. Only one cell projected into all four glomeruli. In addition, I checked the interaction of a vPLIN3 with the PNs of the central M5D5A12. The PLIN3s were strongly connected to MCs (fig. 35B): On average 53 % vPLIN3-MC pairs and 41 % rlPLIN3-MC pairs were connected (vPLIN3: ID893: 6/13 MC (46 %) ID1153: 10/16 MC (63 %), ID1257: 9/13 MC (62 %), ID1457: 16/36 MC (44 %), ID1504: 5/12 (42 %); rlPLIN3: ID952: 5/16 MC (31 %), ID3362: 5/10 MC (50%)). The majority of pairs were reciprocally connected (vPLIN3: 27/46 pairs, rlPLIN3: 8/10 pairs). Of these, four vPLIN3-MC pairs were not connected by reciprocal

synapses but through spatially separated in- and outbound synapses. Most vPLIN3s-MC pairs connected through reciprocal synapses made additional unidirectional synapses (21/23 pairs). These were mainly outbound (19/21 pairs), but occasional inbound synapses were also observed (8/21 pairs). The reciprocally connected rlPLIN3-MC pairs made only reciprocal synapses. I found additional outbound synapses in two of these pairs. Among the unidirectionally connected pairs, pairs in which a PLIN3 was presynaptic to a MC were more frequent (vPLIN3: 16/46 pairs, rlPLIN3: 2/10 pairs) than the opposite directionality (vPLIN3: 3/46 pairs, rlPLIN3: 0/10 pairs). The number of synapses between a given pair was highly variable for both PLIN3 subclasses, ranging from one to 11 synapses. The majority of pairs made, however, on the order of three – five synapses.

Connectivity with RCs was rather sparse for the vPLIN3s. I found only one of 16 investigated pairs to be connected through an outbound synapse from the PLIN3. In contrast, three of four rlPLIN3-RC pairs were connected, with the PLIN3 giving input to the RC dendrite via one or two synapses.

Interactions with local INs were not examined systematically. During reconstruction I detected reciprocal synapses with a GLIN1 at its axon varicosities and I also found another PLIN3 giving input to the dendrite of a GLIN1. Furthermore, I observed input from and reciprocal interactions with different DLIN.

PLIN CLASS IV

A group of 12 widespread, thin branched neurons formed the fourth PLIN class (PLIN4). These neurons were not associated with only a single glomerulus. The wide-spread nature of the dendritic tree, the overall thin appearance of the branches and the fact that no cell was entirely contained in the volume (fig. 36A) complicated the assessment of the neurons' completeness. Finally, four neurons were rated CD1, five neurons CD2 and three neurons CD3.

Morphology

The majority of the somata was ovoid, but flattened in one axis, while two were more globular. They were mostly part of small clusters, of medium size (ø: 8 - 11 µm, $\bar{x}$ ± σ: 9.5 ± 1.0 µm) and had an uneven surface that did not bear spines but membrane protrusions. The nuclei were roughly ovoid-shaped and displayed mild undulations. The little to moderate amounts of cytoplasm surrounding the nucleus was mostly devoid of cellular organelles with the exception of very few small mitochondria or mitochondrial side branches. The organelles collected in dents in front of the nucleus. These bulges of cytoplasm were usually located at the base of the primary dendrites and in four cells these dents were connected, creating a link between the dendrites (fig. 36B). Here, many mitochondria of varying size were located. These mitochondria could be notably voluminous and exhibited a relatively lightly stained intermembrane space and small cisternae. Most cells contained two Golgi apparatus located at the base of the dendrite without stretching into it. In one cell the cellular organelles accumulate in bulgy enlargements of the biggest dendrite that were located at a distance of several microns from the soma. Particularly in the initial portions the dendrites were pervaded with ample, darkly stained strains of ER. With exception to one cell, which was severely cut at the soma, all PLIN4s possessed a

primary cilium of medium length (1.8 - 3.3 µm, $\bar{x}$ ± σ: 2.4 ± 0.5 µm) that arose from the soma or base of one of the main dendrites (fig. 36B.1*).

The somata gave rise to one or two larger dendritic branches (ø: 0.5 - 1.8 µm, $\bar{x}$ ± σ: 1.0 ± 0.4 µm) and up to four smaller branches (ø: 0.1 - 0.3 µm, $\bar{x}$ ± σ: 0.3 ± 0.1 µm). These dendrites spread widely, and the dendritic tree assumed any orientation on a range from fusiform to stellate. All PLIN4s had considerable ramifications traversing the PL. Two neurons had their soma very deep in the imaged volume. They projected predominantly to the PL neuropil at the dorsal side of the stack. The majority of PLIN4s (10/12) sent parts or even a major portion of their branches through the GL. Dendritic cross sections generally appeared round, but exhibited considerable variability, and the circumference and surface were often irregular, giving them a withered and gnarly aspect. The branching was rather infrequent, and the side-branches are long, thin and of delicate, almost fragile appearance.

The branches bore no or very few spine-like protrusions but made numerous varicose enlargements that sat alongside a branch rather than on a tip or neck (fig. 36C). There was considerable variability in the appearance of these varicosities within and across cells. First, the frequency of these varicosities was notably different between PLIN4s. Their extent along the dendrite could cover from a couple of hundred nanometers up to a few microns. In most cases they were voluminous enlargements of amorphous shape, but some appeared rather flattened. The ratio between flattened and voluminous varicosities differed substantially between cells. Some varicosities were rather small and bulbar. Oftentimes, they made filiform protrusions, which also varied in frequency and length (fig. 36D). I randomly sampled varicosities in a subset of neurons starting on the proximal parts of the dendrites. It appeared that while varicosities were predominantly postsynaptic proximal to the soma, these structures made more outbound synapses with distance from soma. This appeared to be independent of the layer through which the branch projected.

Figure 36 (next page). Morphology of PLIN4s. A: Overview of 12 PLIN4s within the bounding box of the imaged volume. B: The soma. B.1 Close up on the soma showing the cytosol dent connecting the primary dendrites. The proximal dendrites bore several filiform spine-like protrusions (arrow, see C.1). A primary cilium emerges from the bulge at the base of the main dendrite (*). B.2/B.3 Cross section of the somata. C: Close up on proximal dendrites and spines C.1: cross section on a proximal spine receiving input (arrow). C.2: Enlargement of a larger part of the proximal dendrite showing the thin, gnarly branches and the close-up on a spine-like protrusion in cross section (arrows). The head of the protrusion contained several vesicles, but no synapse could be found. D: Close up on the distal dendrite: D1. The distal varicosities were bulbous and made outbound synapses. D.2: Right: The cross section of a large varicosity which made multiple outbound synapses (arrows). Left: Enlargement on a larger portion of the dendrite showing multiple varicosities at moderate density. Scale bars: A, C2, D.2.: 15 µm, all other insets: 1 µm.

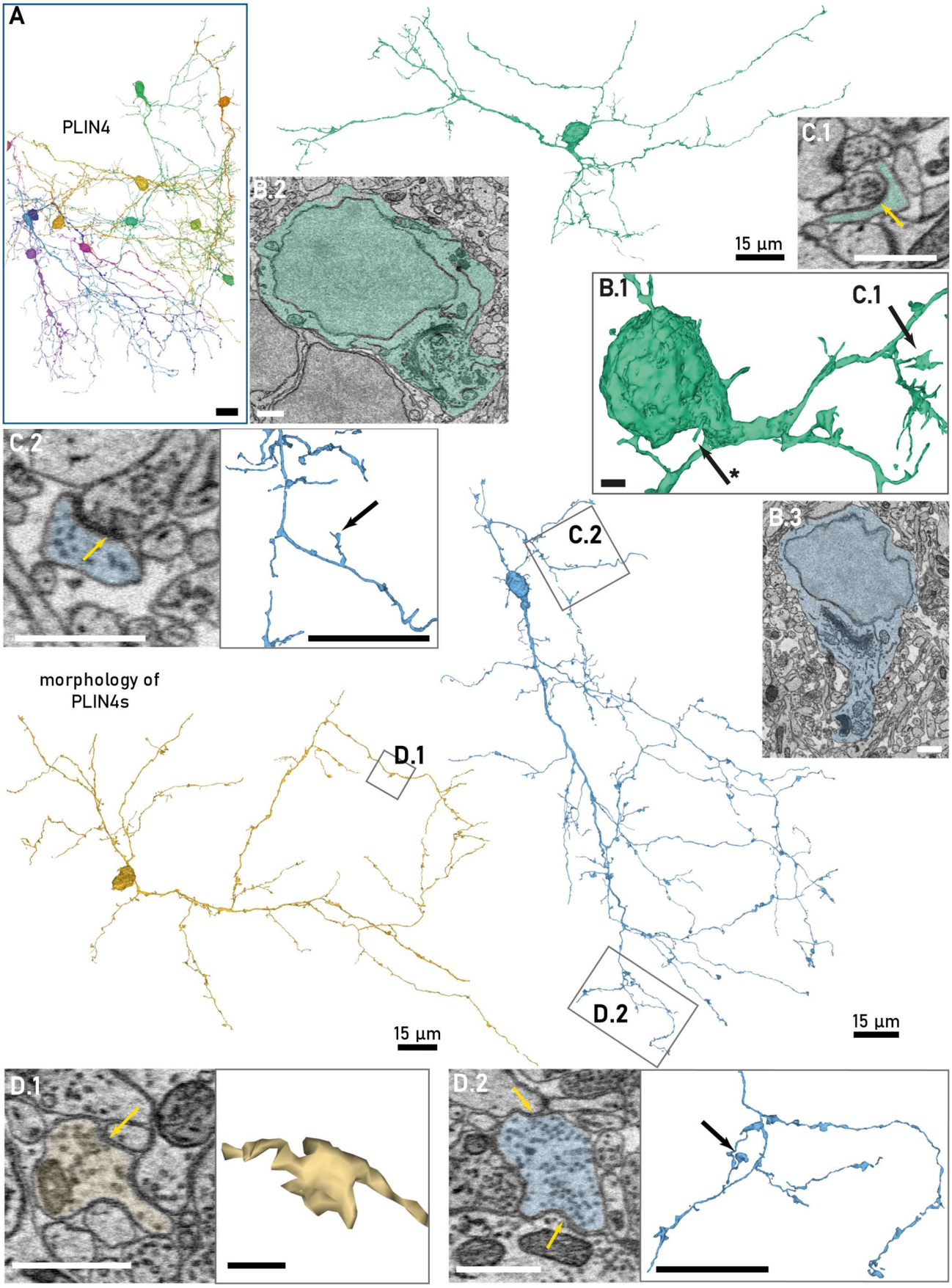
A
PLIN4
B.2
15 µm
C.1
B.1
C.1
*
C.2
B.3
C.2
morphology of
PLIN4s
D.1
15 µm
D.2
15 µm
D.1
D.2

Interactions With Other Neurons

In three PLIN4s no association to any of the glomeruli described above was found. Two of these did not enter the GL within the imaged volume and the third reached the GL with only a single branch that passed between glomeruli. The other nine PLIN4s traversed up to four glomeruli ($\bar{x} \pm \sigma$: 1.0 ± 1.2 glomeruli). In doing so, they commonly immersed only a small portion of their distal branches into the volume of a given glomerulus.

A glomerulus specific PN interaction analysis was conducted for three PLIN4s in the glomeruli M45D45A1, M5D5A12, M67D45A12 and M45D4A2. Each PLIN4 projected to a subset of these glomeruli. Contact sites with MCs were rather infrequent and not all, but the majority of contact sites had synapses. The PLIN4 projecting to three glomeruli had synapses with ten of the 30 MCs (30%), the other two connect to four of nine MCs (44%) and to four of 15 MCs (24%), respectively. A given pair usually connected with one or two, at most three synapses. Most PLIN4-MC pairs were reciprocally connected (42%, fig. 37A). If a second synapse existed in a reciprocally connected pairs, the IN was usually presynaptic to the MC. In 33% of all connected PLIN4-MC pairs the PLIN4 was presynaptic and in 25% it was postsynaptic. The PLIN4 innervating M45D45A1 was an exception: It immersed its proximal part into the glomerulus and in all four connections the MC gave input to the PLIN.

Four of nine potential PLIN4-RC pairs (44%) were connected and in all connected pairs the PLIN4 was presynaptic to the RC. These synapses targeted the RC dendrite. They were very large, and most pairs made multiple (≥ 3) synapses.

In addition, I detected unidirectional input from a MC to a PLIN4 on two occasions during the reconstruction process. Moreover, I encountered connections an additional 23 RC-PLIN4 pairs. These connections were made at the ruff and comprised 10 reciprocally connected pairs, nine pairs with the RC presynaptic to the PLIN4 and in three PLIN4-RC pairs the RC was postsynaptic. Three PLIN4s made connections onto the same ruff, and I detected an additional synapse between a pair of these PLIN4s in close proximity. I did not observe any RC-PLIN4 pair with synaptic connections on both ruff and dendrite of the same RC.

Frequent observations of synapses between PLIN4s and neurites reminiscent of the sGLIN1s inspired a closer investigation of this type of interaction by overlaying meshes. For 29 GLIN1s and 11 PLIN4s, eight connected pairs were found. In seven of these the PLIN4 was presynaptic to the GLIN1 (fig. 37B), in one the PLIN4 was postsynaptic. Furthermore, I observed both in- and outbound synapses with different DLIN classes.

Figure 37 (next page). Interactions of PLIN4s with local neurons. Top: Connections to PNs: The PLIN4s (turquoise) gave input to a RC dendrite (purple, A.1). It was furthermore reciprocally connected to two MCs (A.2, A.3 the outbound synapse is in a different plane). Each connection was made through one synapse. Bottom: Another PLIN4 gave input to the dendrites of three small GLIN1s. The same PLIN4 also received input from or was reciprocally connected to the RCs, in which the GLIN1s immersed their dendrites (not shown). Scale bars: 15 µm, all other insets: 1 µm.

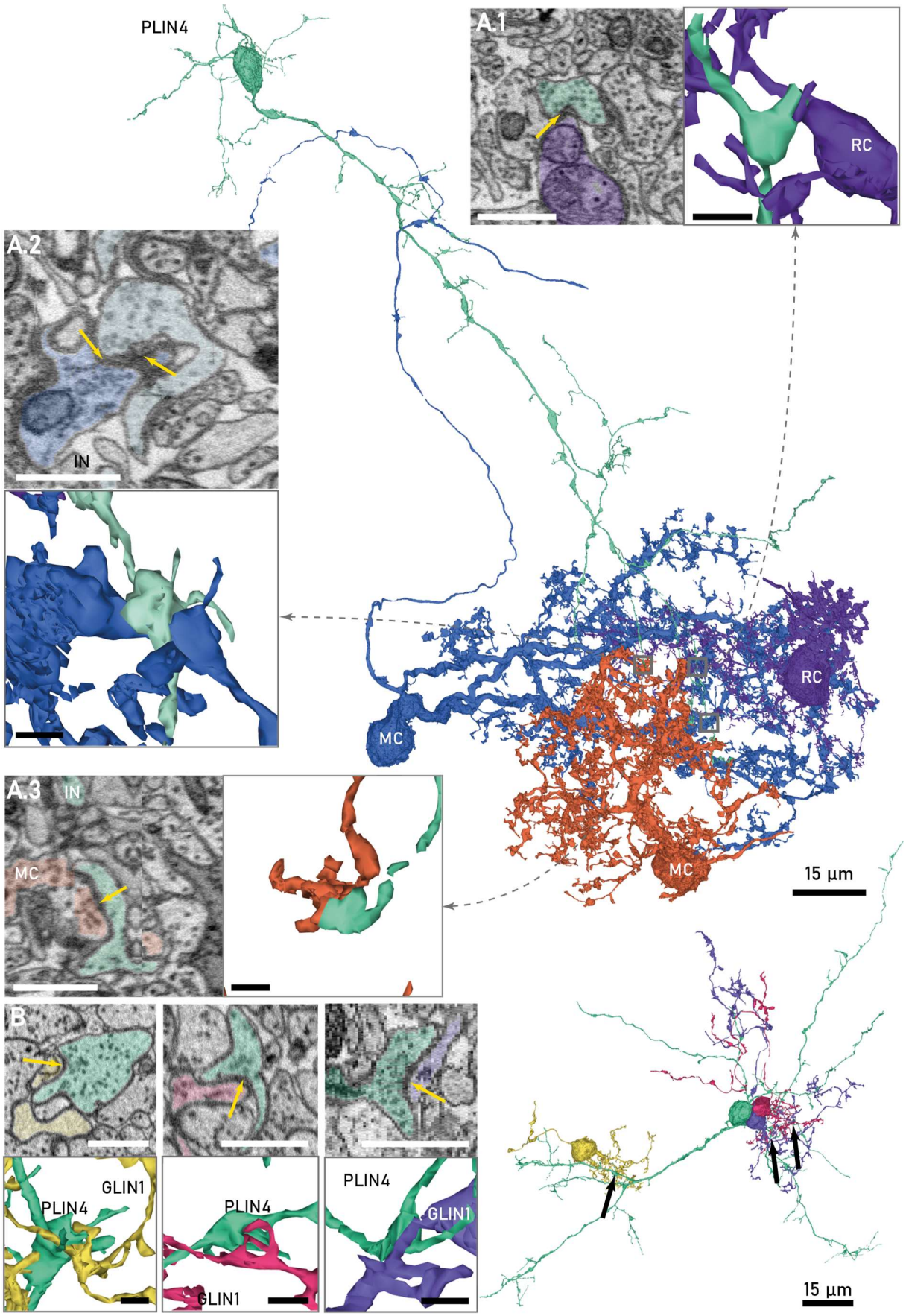
PLIN4
A.1
I
RC
A.2
IN
MC
RC
MC
15 µm
A.3
IN
MC
B
PLIN4
GLIN1
PLIN4
GLIN1
PLIN4
GLIN1
15 µm

IV. INTERNEURONS OF THE DEEP LAYER

I reconstructed 110 INs of the deeper layers. In their coarse appearance these neurons shared many features: Cell bodies were medium-sized and located in the deep PL or GCL. All DLINs were axonless and sent one or more large dendrites towards the GL. In GL the dendrites made dispersed, often besom-like ramifications, which projected through multiple glomeruli. Within the glomeruli DLINs made reciprocal synapses with MCs and local INs. The overall shape varied between fusiform and radial. Due to the overall far-ranging spread of the dendrites, many of the cells were considerably cut and not a single DLIN was completely represented in the stack. Another shared characteristic of DLIN was the differential aspect of the proximal, spiny dendrites versus the distal dendrites bearing varicosities of various appearance.

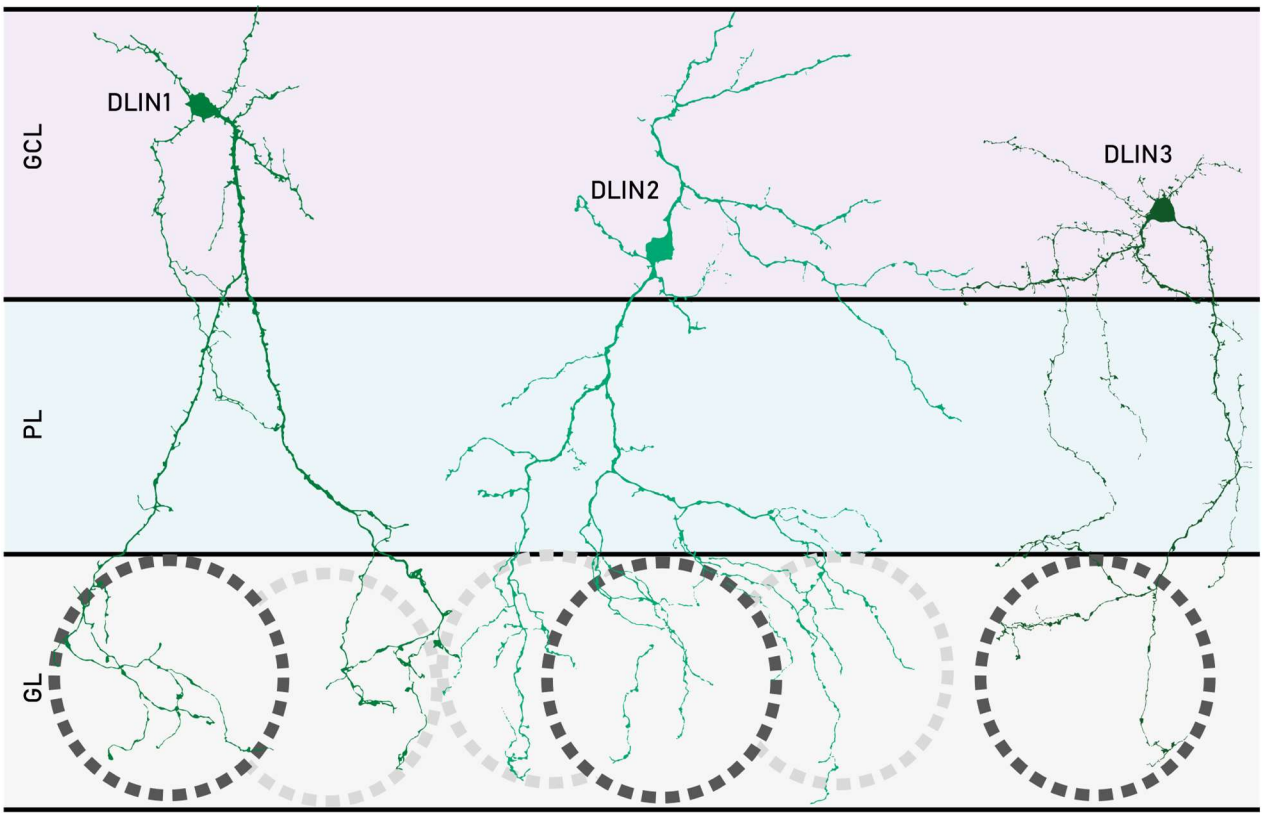

Figure 38. Scheme of the three main classes of INs in the granule cell layer.

By the appearance of the deep, proximal spines and the shape of the distal dendritic varicosities DLINs most conspicuously divide into separate classes. In the following section I describe three morphological classes of DLINs (fig. 38): The DLIN1s contained 42 cells which were primarily characterized by a round, chamfered appearance of their proximal spines and a, for the most part, flattened and stretched aspect of the varicosities at the distal dendrites. The 42 neurons that constituted the DLIN2s were foremost distinguished based on the frayed aspect of their spines. The varicosities of the distal dendrites had a predominantly voluminous and bulky aspect. The 26 neurons of the third class, the DLIN3s, exhibited an overall hairy aspect of the proximal dendrites, resulting

from the high frequency of long and branched spines. Based on additional differences in spine morphology and frequency the DLIN1s and DLIN2s further subdivide into three subclasses each. Table 8 summarizes features of the three DLIN classes.

	IN class	cell count	axon	spine freq.	cell volume [µm³]	total length [mm]	soma volume [µm³]	soma diam. [µm]	n glomeruli innervated	reciprocal PN connections
DLIN1	rDLIN1	18	-	+++	495 ± 127	2.4 ± 0.7	157 ± 43	9.4 ± 0.9	3.2 ± 1.3	+
	lDLIN1	12	-	+++	306 ± 54	1.6 ± 0.7	118 ± 32	8.5 ± 0.7	2.3 ± 1.1	+
	sDLIN1	12	-	+	399 ± 74	2.0 ± 0.7	127 ± 29	8.6 ± 0.7	3.0 ± 1.0	+
DLIN2	cDLIN2	26	-	++	531 ± 139	2.1 ± 0.6	200 ± 55	9.8 ± 0.8	2.6 ± 1.7	+
	fDLIN2	13	-	+++	579 ± 151	3.0 ± 0.7	196 ± 46	9.8 ± 0.8	4.0 ± 1.0	+
	sDLIN2	3	-	+++	596 ± 87	2.6 ± 1.1	174 ± 8	9	4.0 ± 0.8	+
DLIN3		26	-	+++	334 ± 134	1.9 ± 0.7	100 ± 29	8.3 ± 0.5	2.0 ± 1.0	+

Table 8. Features of DLIN classes. Abbreviations: –: absent, +: present, ++: pronounced, +++: very pronounced. Numbers given as mean ± standard deviation.

DLIN CLASS I

The first class of DLIN (DLIN1) comprises 42 cells (CD1: 7, CD2: 23, CD3: 12). The key characteristic identifying representatives of this morphological class, was the predominance of spines, which exhibited a rounded outline of their ending. The shape of the spines could obtain substantially different appearance: both long and short necked spines were present. The spine head could appear as flattened membrane sheath or as bulky enlargement (see fig. 39A-D). Any graduation in between these ends of the scale could occur. Stubby spines in form of flat, enlarged membrane protrusions with rounded endings, which sat directly on the dendritic shaft, were also frequent (see fig. 39E). Thin, filopodial spines without head were regularly observed in this neuron class. Most spines showed cupped indentations, where they wrapped around a connected neurite.

The distal dendrites, meandering through the GL, had an oblate outline, which together with the remarkably smooth and even, aspiny surface created a ribbon-like appearance. Occasionally, curls as described for PLIN3s were observed. The already flattened dendrite made frequent dilations, in which it stretched out and became so thin that in some portions the cytoplasm was no longer discernible. These dilations occurred at branch points, along the branch, and most commonly, when wrapping around connected neurites. Despite obvious similarities these processes could be easily distinguished from glial sheaths by an abundance of synaptic vesicles (fig. 39G). Oftentimes, sites of synaptic

interactions adopted a more complex shape: Wrapping around connected partners, they formed varicosities with cavities holding the connected neurite. Amorphous, complex structures emerged when the neuron enveloped several neurites in close proximity (fig. 39F). However, these varicosities were not only presynaptic, but also postsynaptic, and were targeted not only in reciprocal synapses, but also received unidirectional input.

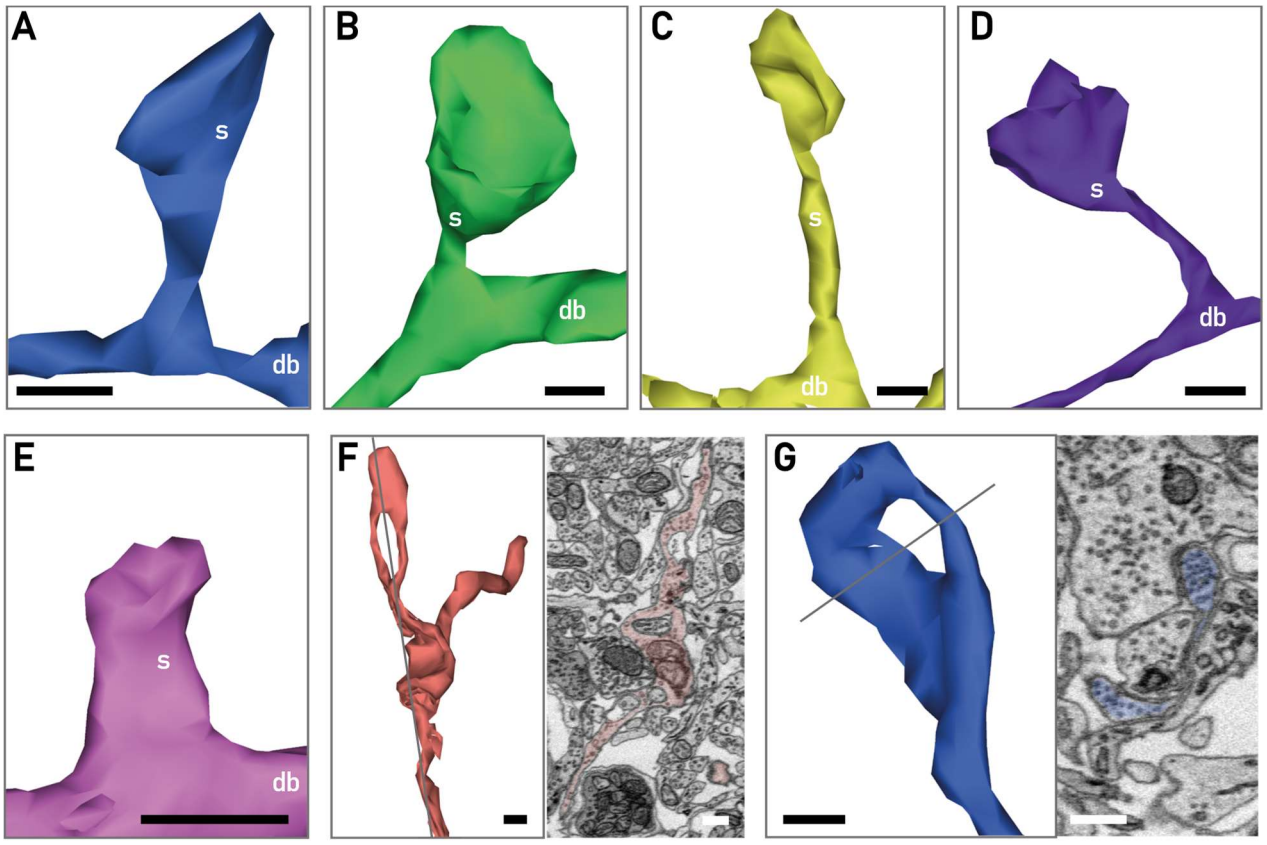

Figure 39. Spines of DLIN1s possessed a predominantly rounded spine head. A. short-necked spine with a flat hat. B. Short-necked spine with a bulky head. The head had a cup-shaped indentation where it contacted the partner neurite. C. long-necked spine with a flat head. D. long-necked spine with a bulky head. E. stubby spine F & G. Close up of varicosities of the distal dendrites. Varicosities made amorphous structures, when wrapping around other neurons (F). The varicosities were at some parts so thin that only their plasma membranes were visible. This produced a stretched, holey appearance in the 3D reconstruction (G). Scale bars 500 nm. Abbreviations: s: spine, db: dendritic branch

Within this neuron class three different subclasses were distinguishable. These differed mainly in the prevailing spine shape and the spine frequency, but also showed other morphological differences. The expression of these differences could be subtle and transitions between subclasses were smooth. Therefore, confusion between subclasses could occur. I will give a detailed morphological description of one subclass and specify differences to the other two subsequently, before discussing their interaction with other OB neurons.

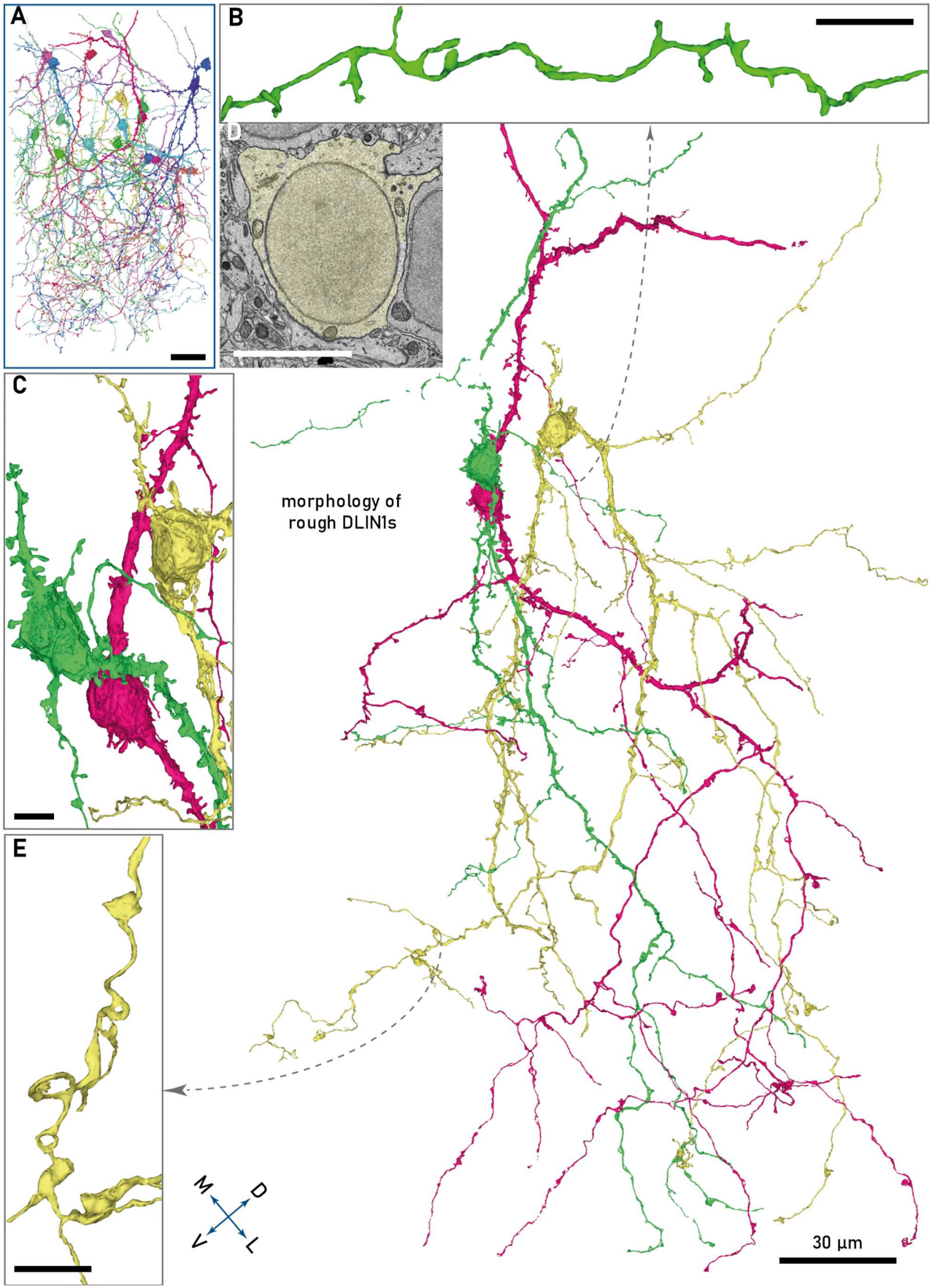
A
B
D
C
E
morphology of
rough DLIN1s
M
D
V
L
30 µm

Figure 40. The morphology of rough DLIN1s. Enlargement of three DLIN1s. While one IN projected two large, primary dendrites towards the GL at the ventro-lateral end, the other two rDLIN1s (green, pink) projected their second primary dendrite medio-dorsally, presumably reaching GLs outside the imaged volume. In GL the distal dendrites spread widely and bore varicosities at low to moderate frequency. A. The 18 rough DLIN1s covered a large part of the imaged volume. B. Close up on a thin, proximal dendrite which spread through GL and PL. It bore short-and long-necked round spines at moderate density. C. Close up on the somata and proximal primary dendrites. The surface of these structures was densely covered with membrane excrescences, stubby and short-necked, round spines. D. Cross section of the soma displaying an ovoid nucleus. E. Close up on a section of distal dendrite: The oblong shaped dendrite made several curls. Scale bars: A: 30 µm, all other insets: 5 µm.

Morphology

The Rough DLIN1s

The first subclass was characterized by a rather rough appearance of the soma and proximal dendrites, which were, often densely, covered with rounded spines. These rough DLIN1s (rDLIN1s) included the largest DLIN1 representatives and comprised 18 neurons. With exception of two cells, the medium-sized somata (ø: 8-11 µm, $\bar{x} \pm \sigma$: 9.4 ± 0.9 µm) lay within or at the border of a big cluster of the GCL. Most somata were approximately ovoid shaped (14/18), while the remaining cell bodies were roughly globular. A striking detail was the smoothly outlined nucleus, which obtained a near-perfect ovoid shape and displayed no undulations or indentations (fig. 40D). This stood in stark contrast to the rough, rugged surface of the cell body. The perikaryon appeared as a thin layer of cytoplasm surrounding the cell body. Only a few, very small, and compact mitochondria were observed. The ER was also remarkably scarce and often had an uncommonly large lumen. Depending on the number of big dendrites emanating from the soma, one or two Golgi apparatus could be found. They were located in a swell at the base of the big dendrites and extended far into them. Here, a few large vesicles and lysosomes could be observed. From each soma a single primary cilium projected into the surrounding extracellular space, usually directed parallel to the cell body's outline (2-4 µm, $\bar{x} \pm \sigma$: 2.9 ± 0.7 µm).

The surface of the somata was of a conspicuously rough, craggy aspect: It was overcast by flat, extensive membrane excrescences and protuberances, and it was covered by many rounded spines (fig. 40C). In addition, somata often showed indentations from passing neurites. They received input that primarily targeted the bulgy excrescences, but also the soma directly. Furthermore, protrusions of neighboring cell bodies regularly penetrated the somata and created extensive cavities. Only a subset of these structures was associated with a synapse. I did not observe any rDLIN1 making such projections into another cell but noticed some somata synapsing onto passing neurites.

Most rDLIN1s (11/18) showed a distinct asymmetry in the size and circumference of their primary dendrites. Usually, they made one or two large dendrites, directed towards the GL, and one or two additional small, basal dendrites that remained in the deep layers. Cells with a single large dendrite (5/18) or several dendrites of equal size (2/18) gave rise to one or more small, basal dendrites from their large, primary branch. The appearance of large and small dendrites differed significantly. Due to copious membrane excrescences on their surface, the large primary dendrites had a similarly rough and craggy appearance as the soma. This aspect was further intensified by the dense coverage with predominantly short-necked and stubbed spines, which could be observed over

several tens of microns on the proximal parts of the dendrite (fig. 40C). The irregular cross section complicated precise measurements of the dendritic diameter, which varied between 1 - 4 µm ($\bar{x}$ ± σ: 2.1 ± 0.7 µm). In all rDLIN1s at least one large branch was directed towards the GL at the ventro-lateral side. Projections towards the dorso-lateral and dorso-medial side were also common, presumably targeting GL areas in other parts of the OB. Due to the diversity in dendritic spread, the coarse morphology could not be reduced to a more stellate vs. fusiform pattern. Single, large dendrites branched at least once symmetrically. Noteworthy was the extent of the dendrite, which spanned the entire imaged volume in its long axis, whilst still being cut in most rDLIN1s.

The spine frequency gradually reduced on the trajectory of the large dendrites towards the GL, and upon entry in the GL spines were absent. Traversing the deep layers, the large dendrites made several side branches of the same make-up as the deep, basal branches (see below). This asymmetric branching scheme was no longer dominant within GL. Here, the dendrites branched heavily, spread widely and extensively, and displayed the varicosities as described above (fig. 40E). Consistent, with sides of strong synaptic interactions, mitochondria were abundant here. The cytosol of the distal dendrites was filled with vesicles. Synapses could be very easily distinguished by a cloud of small vesicles and membrane fusion sites. In addition, the dilated enlargements frequently contained large vesicles with clear lumen. These were abundant in the apical dendrites, but clear signs of a presynaptic site or vesicle fusion were lacking.

The basal dendrites were very thin, with a diameter of 0.3 – 0.75 µm ($\bar{x}$ ± σ: 0.5 ± 0.2 µm). As the apical processes, they were oblong in cross section. They usually projected dorso-laterally and dorso-medially within the deeper layers. Though their length could exceed 50 µm, they did not enter GL. The basal dendrites also bore spines, but at a much lower frequency (fig. 40B). Similar to the large dendrites, spine frequency decreased with distance to soma. Spines were usually long-necked or thin, stubby spines were rare. It was not uncommon to find spine heads receiving more than one input. An inspection of multiple, randomly picked spines on the proximal large dendrites and the basal, deep layer dendrites showed that spine heads were mostly devoid of vesicles. I did not observe presynaptic structures. ER was frequently found in spine heads, however, these structures did not exhibit the stacked structure reported for mammalian spine apparatus.

Before entry into the GL, mitochondria were sparse and rather small in the thinner branches. Microtubuli were clearly visible in the cytosol throughout the dendrite, even in thinner ones. The cytosol often contained larger vacuoles, and very dark, threadlike ER was abundant. Few vesicles were observed in the basal and proximal portions of the large dendrite. I found few presynaptic sites on the dendrite shafts. The small dendrites in the deep layer received a lot of synaptic inputs. In the basal dendrites and the proximal portions of the big dendrites, this input was mostly directed to the spines. With larger distance from the soma these dendrites also received frequent input to the shaft.

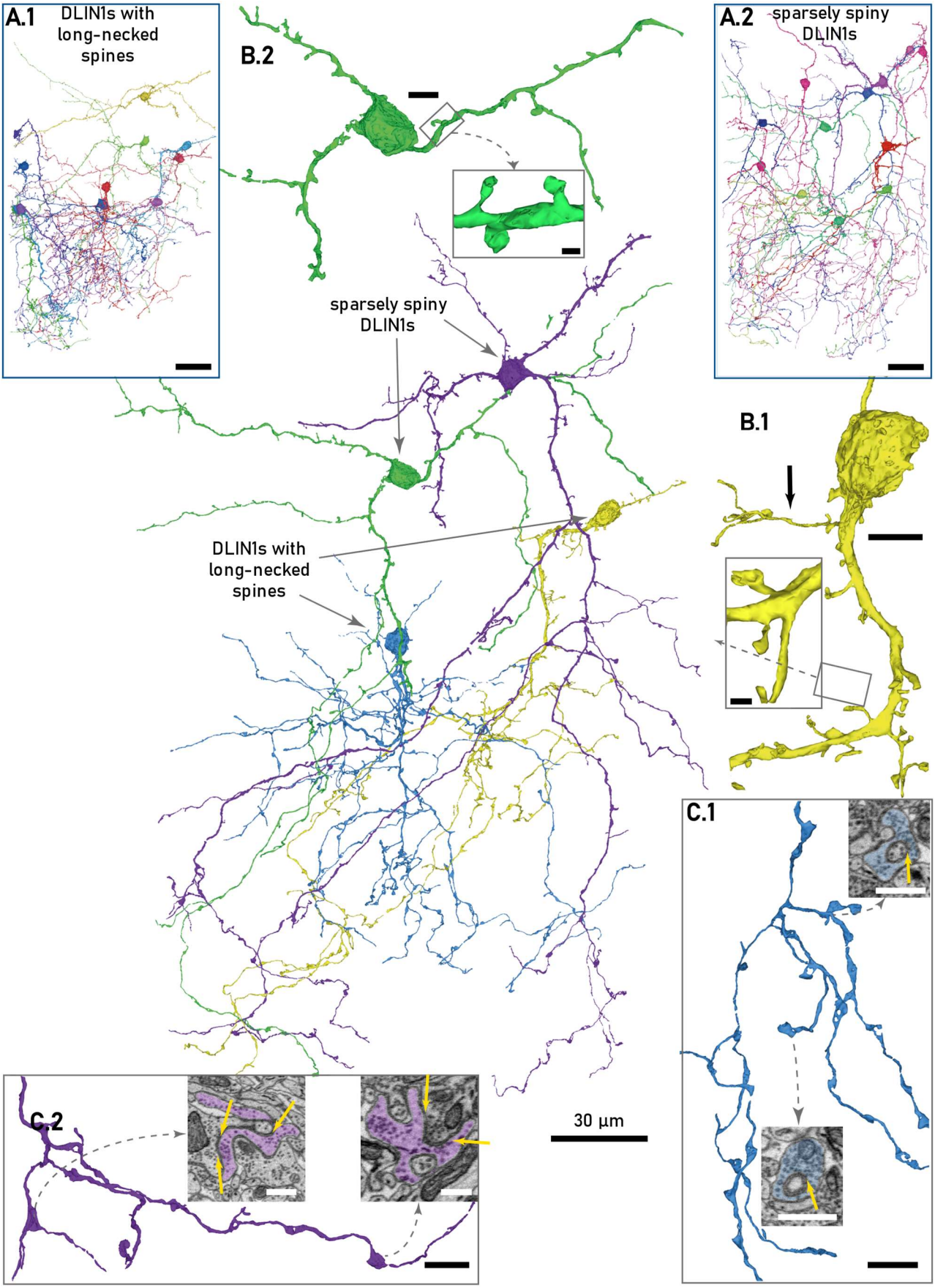
A.1
DLIN1s with long-necked spines
B.2
A.2
sparsely spiny DLIN1s
sparsely spiny DLIN1s
DLIN1s with long-necked spines
B.1
C.1
C.2
30 µm

Figure 41. The morphology of sparsely spiny DLIN1s (sDLIN1) and DLIN1s with long-necked spines (lDLIN1). Large: Two lDLIN1s (blue, yellow) and two sDLIN1s (green, purple). A. Overview on the entire set of reconstructed neurons per subclass. The 12 lDLIN1s (A.1) were located more superficially and their dendrite spanned a smaller volume than 12 sDLIN1s (A.2). B. Close up on the soma and the proximal dendrites. B.1. The lDLIN1 bore long spines at moderate frequency (see inset) and made thin, basal dendrites (arrow). B.2. Few sDLIN1s made basal dendrites. These dendrites bore predominantly stubby and short necked spines at low to moderate frequency (see inset). C. Close up on the distal dendrites. In both subclasses varicosities were densely filled with synaptic vesicles and often made (and receive) multiple synapses. C.1. Varicosities were frequent in lDLIN1s and by trend smaller than in rDLIN1s. C.2. sDLIN1 varicosities were larger and quite similar to rDLIN1s. Scale bars: A: 30 µm, 3D insets: 5 µm, image insets: 1 µm.

The DLIN1s with Long-Necked Spines

The second DLIN1s subclass was characterized by the predominance of long-necked spines. At a glance, long-necked spined DLIN1s (lDLIN1s) showed obvious differences to the rDLIN1s because they were smaller, and both the location of their soma and the extent of their neurite tree were more superficial. The lDLIN1s comprised a group of 12 neurons (fig. 41A.1).

The somata were only slightly smaller in terms of their largest diameter (ø: 8-10 µm, $\bar{x}$ ± σ: 8.5 ± 0.7 µm), but more so in volume (table 8). An irregular, roughly globular somatic outline (6/12) was found slightly more frequent than an ovoid shape (4/12). All nuclei displayed mild undulations. Except for two neurons with somata in a big GCL cluster, lDLIN1s were located in the PL, either as part of a small cluster (7/10) or freely in the neuropil (2/10). Their surface was slightly uneven and bumpy, and spines were infrequent. Somata did not bear membranous excrescences like the rDLIN1s. A single primary cilium was found in all lDLIN1s (1.5 - 3.3 µm, $\bar{x}$ ± σ: 2.3 ± 0.5 µm). Two neurons were cut at the soma.

The somata gave rise to one to four dendrites projecting to GL ($\bar{x}$ ± σ: 1.6 ± 0.8). The separation between small, basal and the large, distally projecting neurites was far less pronounced than in rDLIN1s. One cell completely lacked basal dendrites. Others gave rise to only a few basal dendrites of variable length (≤ 15 µm or > 50 µm, ø: 0.3 - 0.8 µm, $\bar{x}$ ± σ: 0.5 ± 0.1 µm), which projected through the deeper layers (fig. 41B.1). They made thin and long-necked spines at long, but regular intervals. Synaptic vesicles were absent in the basal dendrites as well. Hence presynaptic structures were not found, but many postsynaptic sites at which input from thin neurites of remote cells seemed to dominate. The distally directed dendrites emerged with relatively small diameter (ø: 0.5 – 2.0 µm, $\bar{x}$ ± σ: 1.1 ± 0.4 µm). Neurons with a soma position deep in PL or GCL tended to expand their dendritic trees more radially, spreading widely, before projecting towards the ventro-lateral GL. The dendritic orientation of the other cells followed the long axis of the imaged volume. Their ramification in the GL was strongest and represented the larger fraction of their dendritic tree.

The larger dendrites sometimes bore stubby and short-necked spines in their proximal parts. The predominant spine form was, however, the long-necked variant with a flat or a bulky rounded head. These covered the dendrites at moderate frequency, which only slightly decreased towards the GL. The apical dendrite was characterized by sheath-like expansions that could be platelet-like, cupped or obtain more complex shapes enveloping other neurites. The distal varicosities occurred at a higher frequency than in the rDLIN1s. Also, they were by trend smaller in diameter, more circular. A noteworthy fraction took on a spine-like appearance, resting on neck-like protrusions. The presence of synaptic vesicles distinguished them from deep layer spines (fig. 41C.1).

The Sparsely Spiny DLIN1s

The sparsely spiny DLIN1s (sDLIN1s) comprised a group of 12 thin-branched, delicate DLINs (fig. 41A.2). Their cell bodies were located in big clusters of the GCL (8/12), in small PL clusters or immersed in the PL neuropil (4/12). Somata were of medium size (ø: 8 - 10 µm, $\bar{x}$ ± σ: 8.6 ± 0.7 µm) and predominantly of irregular, roughly globular shape. The surface was coarse, bore isolated short-necked spines and membrane excrescences were found in seven sDLIN1s (fig 41B.2). These were, however, far smaller, and less pronounced than in the rDLIN1s. As in the other DLIN1 subclasses, primary cilia were of medium length (1.8 - 3.0 µm, $\bar{x}$ ± σ: 2.5 ± 0.4 µm). The somata gave rise to two to four slender dendrites (ø: 0.3 – 2.0 µm, $\bar{x}$ ± σ: 1.0 ± 0.4 µm). Only four neurons showed a clear difference of dendrite size. Yet, small, thin dendrites, which restricted their projection to the deep layers, could be found in other sDLIN1s as well. But, apart from the small diameter, differences to the other dendrites were not obvious (fig. 41B.2). The dendrites were sparsely spiny, with stubby and short-necked spines dominating. Only in two sDLIN1s the long-necked variant seemed to prevail. As in the other subclasses, the dendrite branched more frequently in the GL and displayed varicosities of medium frequency (fig. 41C.2).

Interactions With Other Neurons

The overlap of the dendritic tree with identified glomeruli in the imaged volume was inspected for all neurons, but the presence of synapses within the glomerular volume was only confirmed for a subset (see below). All cells sending a dendrite into the GL within the imaged volume projected through the volume of at least one glomerulus (fig. 42A). The projections of the rDLIN1s and sDLIN1s passed on average through slightly more glomeruli than the projections made by the lDLIN1s (rDLIN1s: 3.2 ± 1.3, lDLIN1s: 2.3 ± 1.1, sDLIN1s: 3.0 ± 1.0 glomeruli). The fraction of distal dendrites immersed in individual glomeruli was highly variable within and across cells but appeared to be by trend lower in the larger rDLIN1s.

The glomerulus specific PN interactions were investigated for two rDLIN1s, one sDLIN1 and one lDLIN1 for the glomeruli M56D56A2, M45D45A1 and M67D45A12. This analysis suggested a complex and individual pattern of interaction between PNs and DLIN1s. All examined cells made synapses with at least one MC within each of the glomerular subcompartments to which they projected. The tworDLIN1s and the sDLIN1 connected to a similar fraction of MCs within the glomeruli they innervate (4/19 MCs (21%), 10/34 MCs (29%) and 7/25 MCs (28%), respectively). The rDLIN1s rarely made more than a single synaptic contact with a given MC and if so at least one of these synapses was reciprocal. I observed a higher fraction of connected MCs for the lDLIN1, which made synapses with 11/19 MCs (58%) in the glomeruli innervated. Thus, DLIN1s showed both selective and broad connectivity to MCs of a given glomerulus. The number of synapses between connected pairs was low. Reciprocal connections dominated over DLIN1 output and MC input connectivity in all subclasses (rDLIN1s: reciprocal: 62%, output: 31%, input: 8%, sDLIN1: reciprocal: 83%, output: 17%, input: 0%; lDLIN1: reciprocal: 64%, output: 18%, input: 18%). Noteworthy was the size of some of the synapses from the rDLIN1 onto MCs, which could become gigantic (fig. 42B).

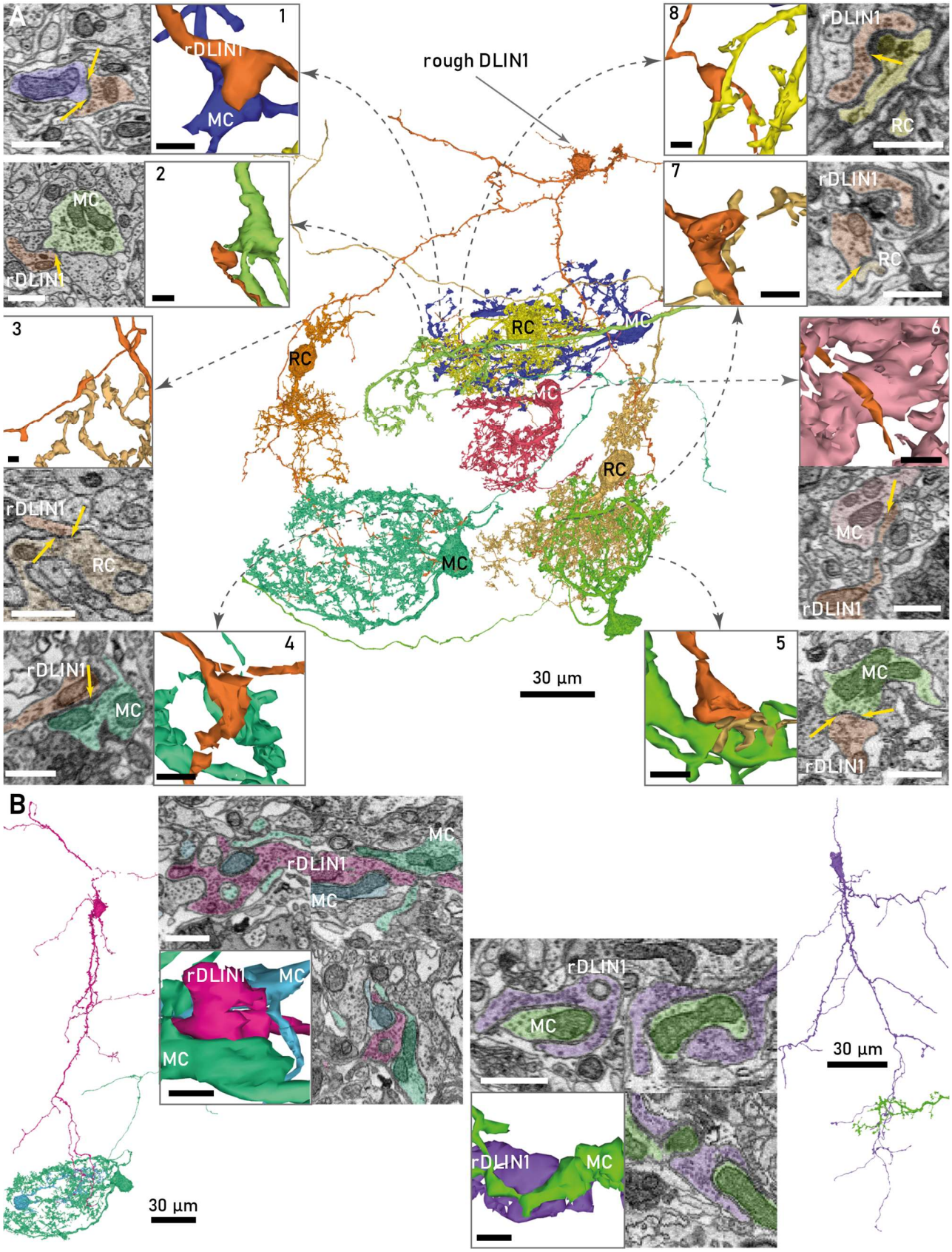
A
1
rDLIN1
MC
rough DLIN1
8
rDLIN1
RC
2
MC
rDLIN1
7
rDLIN1
RC
3
RC
RC
MC
MC
6
rDLIN1
RC
MC
rDLIN1
4
rDLIN1
MC
30 µm
5
MC
rDLIN1
B
MC
rDLIN1
MC
rDLIN1
MC
MC
rDLIN1
MC
rDLIN1
MC
30 µm
30 µm

Figure 42. Connectivity of rough DLIN1s to PNs. A: A rDLIN1 with a subset of connected PNs from six different glomeruli. The rDLIN1 was reciprocally connected to intermediate (1) and large MCs (2, 4, 5) and a RC (3). The rDLIN1 gave input to a small MC (6) and two RCs. B. Examples of large synapses: The distal dendrite of the rDLIN1 formed large sheaths that wrapped intensely around MC dendrites. Synapses onto the MC could comprise several active zones or zones extending over several hundred nm (see insets). Scale bars: overviews.: 30 µm, insets: 1 µm.

The two rDLIN1s and the lDLIN1 gave input to the dendrites of the majority of RCs in the glomeruli examined via one to four synapses (rDLIN1s: 4/7 (57%), 3/5 (60%); lDLIN1: 4/5 (80%)). I did not find any connections between the sDLIN1 and the four RCs in the glomeruli it innervated. During reconstruction and morphological classification, I found additional synapses between all of the DLIN1s examined here and RCs of other glomeruli. Noteworthy was the interaction of sDLIN1s with RCs, of which I found 23 connected pairs. Reciprocally connected pairs and pairs in which a sDLIN1 provided input to an RC dendrite made up the vast majority of these connections (ten pairs each, fig. 43A, B).

All synapses to PNs in the GL originated from the varicose enlargements on distal dendrites. Both the proximal portions of the apical dendrite and basal dendrites received many synapses onto shaft and spines. The somata received input from neighboring cell bodies and from thin dendrites with dark staining full of small, granular vesicles. Most of the input terminating on the proximal parts of the DLIN1s originated from neurites coming from deep sources. During proofreading I observed diverse interactions of DLIN1s with the local IN network. I found connections between DLIN1s, as well as to representatives of other DLINs, not only in the deep layers, but also in GL (fig. 43C). These synapses were located on the varicosities of distal dendrites, often in vicinity to MC dendrites, to which both DLINs connected. I detected both reciprocal, as well as unidirectional in- or output connectivity. Further inspection suggested that such DLIN pairs were connected through a single synapse. Additionally, I found isolated synapses with representatives from all three classes of GLINs, as well as PLIN3s, and the PLIN4s (fig. 43C).

Figure 43 (next page). Connectivity of sDLIN1s and lDLIN1s with other bulbar neurons. A. This sDLIN1 (violet) made reciprocal synapses with six RC of different glomeruli. Inset: Each connection involved multiple synapses at the ruff. Scale bars image: 1 µm. B. Another sDLIN1 (red) connected to five RCs of three different glomeruli. The sDLIN1 gave input to the dendrites of four RCs through multiple synapses. One connection was reciprocal. *: A close up shows the overlap of the sDLIN1 dendrite with the RC. This pair was connected through three synapses (see inset **). Scale bar image: 1 µm. Enlargement 3D (*). C: This lDLIN1 (blue) was found to give input to a sGLIN1 (orange, 3), a lGLIN1 (green, 1), three GLIN2 (one example in pink, 2) and a cDLIN2 (red) in GL. Scale bars Insets: 3D in C1, C2, C4: 5 µm, all images and 3D of C3: 1 µm.

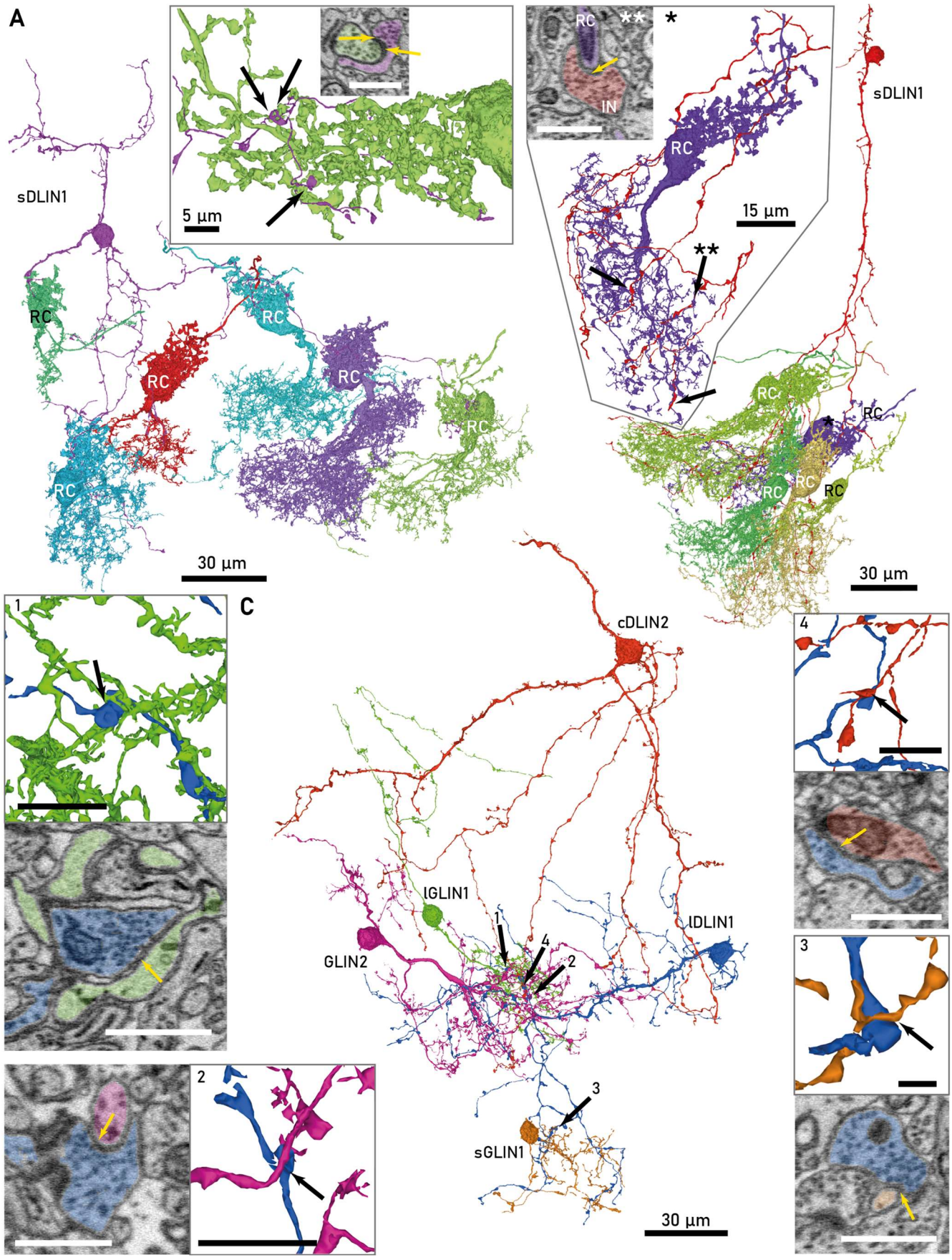
A
sDLIN1
5 µm
RC
IC
RC
RC
RC
RC
RC
RC
30 µm
RC
**
*
IN
15 µm
**
sDLIN1
RC
RC
RC
RC
RC
RC
30 µm
1
C
cDLIN2
lGLIN1
GLIN2
1
4
2
lDLIN1
3
sGLIN1
30 µm
4
3
2

DLIN CLASS II

A group of 42 neurons (CD1: 11, CD2: 20, CD3: 11) formed a morphological class which was characterized by the presence of spines of unique aspect. The common characteristic of these spines was a bulgy and frayed appearance, which involved, however, a significant variability in the overall spine shape.

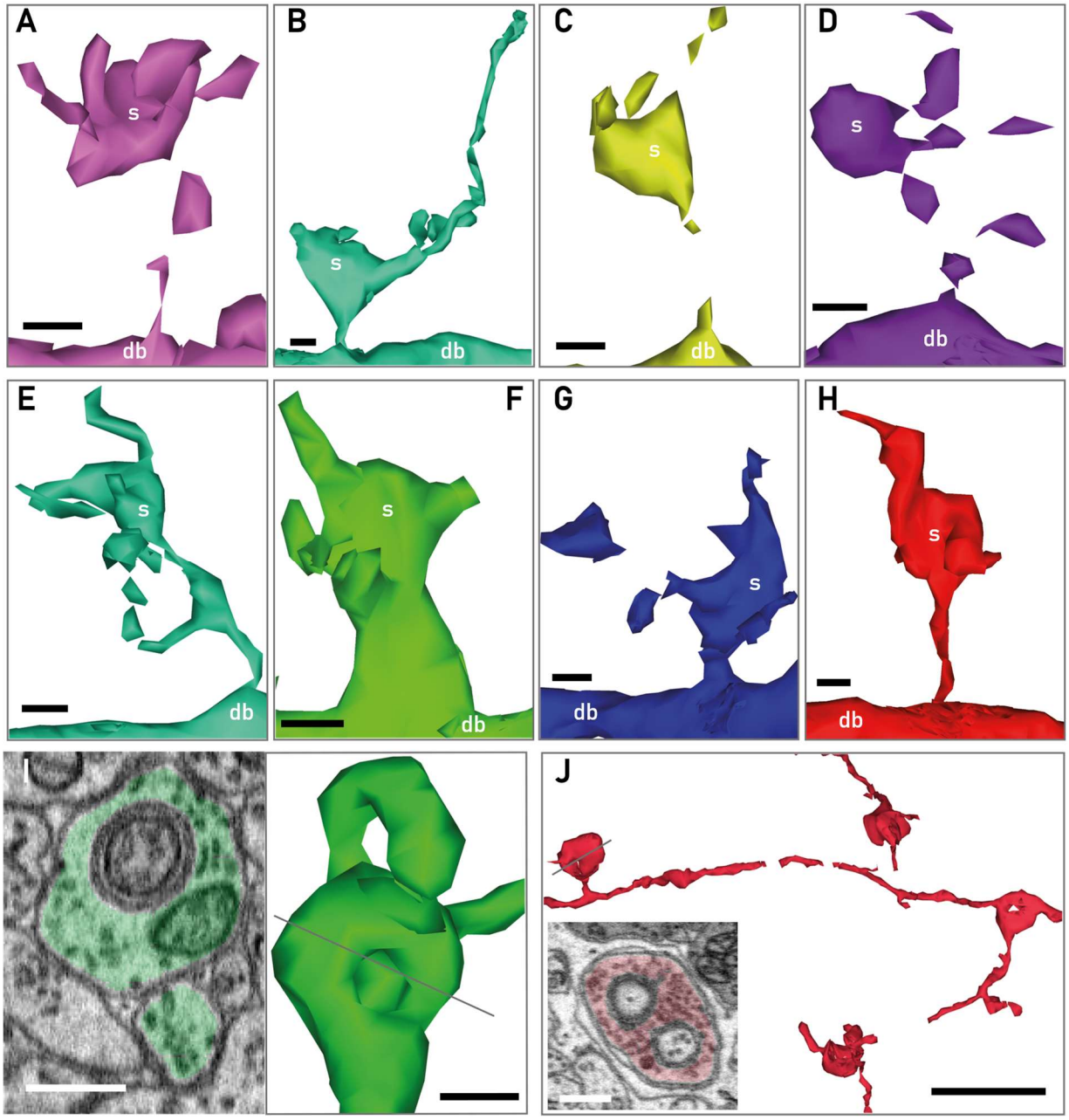

Figure 44. Spine aspect of DLIN2s. A-H: variation of frayed spines. I-J: Close up on distal varicosities. Scale bars A-I: 500 nm, J: 5 µm, inset 500 nm, Abbreviations: s: spine, db: dendritic branch.

Short necked spines were the dominating spine type (fig. 44A, B, D, G). The less frequent, long necked spines could assume a length of several microns, and sometimes had side branches, that terminated

in a spine head or often a pointy tip (fig. 44E, H). I did not aim for a clear distinction between spines and small dendritic side branches but considered any studded, deep layer protrusion below a visually judged length of five microns as a spine. The spine necks could become very narrow (≤ 100 nm), which was challenging to segment, and, thus, contributed to the overall tattered appearance of the spines (fig. 44ACD). In their simplest form, spine heads resembled bulky rods or bulbar enlargements. In most cases, they were completely amorphous and studded with several protrusions. These protrusions could be short pointy tips, more filopodial, or of beaded appearance, due to repeated bulbar dilations followed by constrictions (fig. 44C-E). Stubby spines were the second most common spine type (fig. 44F). They often sat on dendritic varicosities, had a large base, and bore many short, filopodial protrusions. The spine heads seemed to be mainly postsynaptic to a single contact. Rarely, multiple synapses onto the same spine were observed. In addition, a small, but notable fraction did not receive any synaptic input. I did not observe synapses onto the filopodial protrusions. The spine heads often contained vesicles and ER strands, that did however, not form layers of stacked discs as commonly described for spine apparatus.

At first glance, the aspect of the distal dendrite was very similar to the distal dendrites in DLIN1s. These dendrites were very thin (ø: ~ 150 - 500 nm). Pre- and postsynaptic interaction mainly occurred at bulky or flattened varicosities, which could assume a complex, amorphous shape, when coiling around connected neurites. Taking a closer look, subtle, but distinct differences became apparent. I observed some flattened enlargements, which were stretched so much, that they appeared perforated. However, these were not very frequent. More often, the varicosities were bulky, but elongated along the branch, resulting in a roughly spindle-shaped structure, sometimes indented by connected neurites (fig. 44J). Furthermore, the varicosities frequently bore filopodial, pointy protrusions, extending into the neuropil without synapses. The cross section of the dendrites had a roundish outline, which varied a lot in diameter, giving rise to a rather bumpy, irregular surface. This contrasted with the smooth ribbon-like appearance of the distal dendrites in DLIN1s. Moreover, dendrites exhibiting the aspect of distal dendrites appeared already in the PL. Both small synaptic vesicles, as well as larger vesicles with clear lumen, were abundant in the varicosities and branches of the distal dendrites.

I divided this group into three subclasses based on the predominant spine form and frequency, as well as additional morphological characteristics. I will describe one group in detail and highlight differences for the other two subclasses.

Morphology

The Common DLIN2s

The common DLIN2s (cDLIN2s) comprised 26 neurons whose somata were predominantly located in big clusters of the GCL (21/26). Five neurons had their cell bodies located in the small cluster or freely in the neuropil of the PL. There appeared to be a gradual reduction in overall size, i.e., soma size, neurite perimeter and length from deep to superficially located cells. The somata were among the

largest observed for INs of the OB (ø: 8 - 12 µm, $\bar{x}$ ± σ: 9.8 ± 0.8 µm) and were mainly pyramidal to globular-shaped (16/26) or rather ovoid (10/26). Their surface was mostly even and without dents made by passing neurites but with impressions of neighboring somata. They had isolated spines or membrane excrescences. The nuclei were embedded in moderate amounts of cytosol and displayed only minor undulations, but only three of them exhibited the perfect ovoid shape observed in many rDLIN1s. Their perikaryon contained little to moderate amounts of long stranded ER. The mitochondria were slender and often elongated. Many multi-vesicular bodies and darkly stained endosomes were observed in vicinity to the Golgi apparatus. These varied strongly in size; they were mostly located at the base of primary dendrites and sometimes stretched into them. Primary cilia could be found in all neurons (fig 45A*). These cilia could obtain considerable length (2.0 – 7.5 µm, $\bar{x}$ ± σ: 3.8 ± 1.2 µm) and projected into the surrounding extracellular space without any obvious common direction.

Two to four dendrites of small to moderate diameter emerged from the soma. About half of the cells (12/26) exhibited a distinct size difference between their primary dendrites ($ø_{WIDE}$: 0.8 - 3 µm, $\bar{x}$ ± σ: 1.5 ± 0.5 µm, $ø_{THIN}$: 0.2 - 0.75 µm, $\bar{x}$ ± σ: 0.5 ± 0.2 µm, equal sized: ø: 0.5 – 2.0 µm, $\bar{x}$ ± σ: 1.0 ± 0.4 µm), but apart from diameter the wider and narrower branches did not differ morphologically. The dendrites branched regularly, making both symmetric and asymmetric bifurcations. This resulted in a predominantly stellate orientation, with branches spreading widely through the deep and superficial portions of the imaged volume. In contrast to DLIN1s, the branching frequency increased already within the PL. The dendritic cross section was round. Thin, elongated mitochondria and ER strands with wide lumen stretched through the proximal dendrites in GCL. Disregarding spines, the surface structure of the proximal branches was mainly even and smooth. At more or less regular intervals the dendrites of the deep layers expanded in diameter and formed varicosities, often, but not always, associated with an accumulation of mitochondria (fig. 45C). In most cases, these enlargements result formed a regular expansion of the dendrite to all sites, but they could also obtain more irregular shapes e.g., stubby, or cone-like. On the proximal dendrites a large fraction of the varicosities was associated with spine-like protrusions (fig. 45A). I did not find these varicosities associated with synaptic vesicles. In the more superficially positioned cDLIN2s, varicosities on proximal dendrites were less pronounced or absent. Spines were not restricted to varicosities and could emerge directly from the shaft as well. In this subclass the spines were predominantly stubby or short-necked, with only a few representatives showing some long-necked spines. The density of spines varied from sparse to moderate. Following along proximal dendrites of several neurons, I noticed several outbound synapses from the dendritic shaft.

Figure 45 (next page). Morphology of the common DLIN2. A. Somata had a smooth surface. The proximal dendrites made regular bulbar dilation that bore frayed spines. The primary cilium projected from the soma (*). A.1. Superficial neurons had a smaller soma with less cytosol. B. Beaded dendrites spread through the PL: The dendrites made frequent bulbar dilations that were separated by very thin strips of dendrite, giving the neurites the appearance of a pearl-necklace. C. With some distance to the soma the dendrites in the deep layer became less spiny, but still exhibited bulbar dilations that usually contained one or more mitochondria. D. Varicosities in PL could make in- and outbound synapses. E. Varicosities of the distal dendrite were usually voluminous (left) but could also be coin-shaped. F. Overview of all 26 cDLIN2 Scale bars: Overview: 30 µm, insets 3D: 5 µm, insets image: 1 µm.

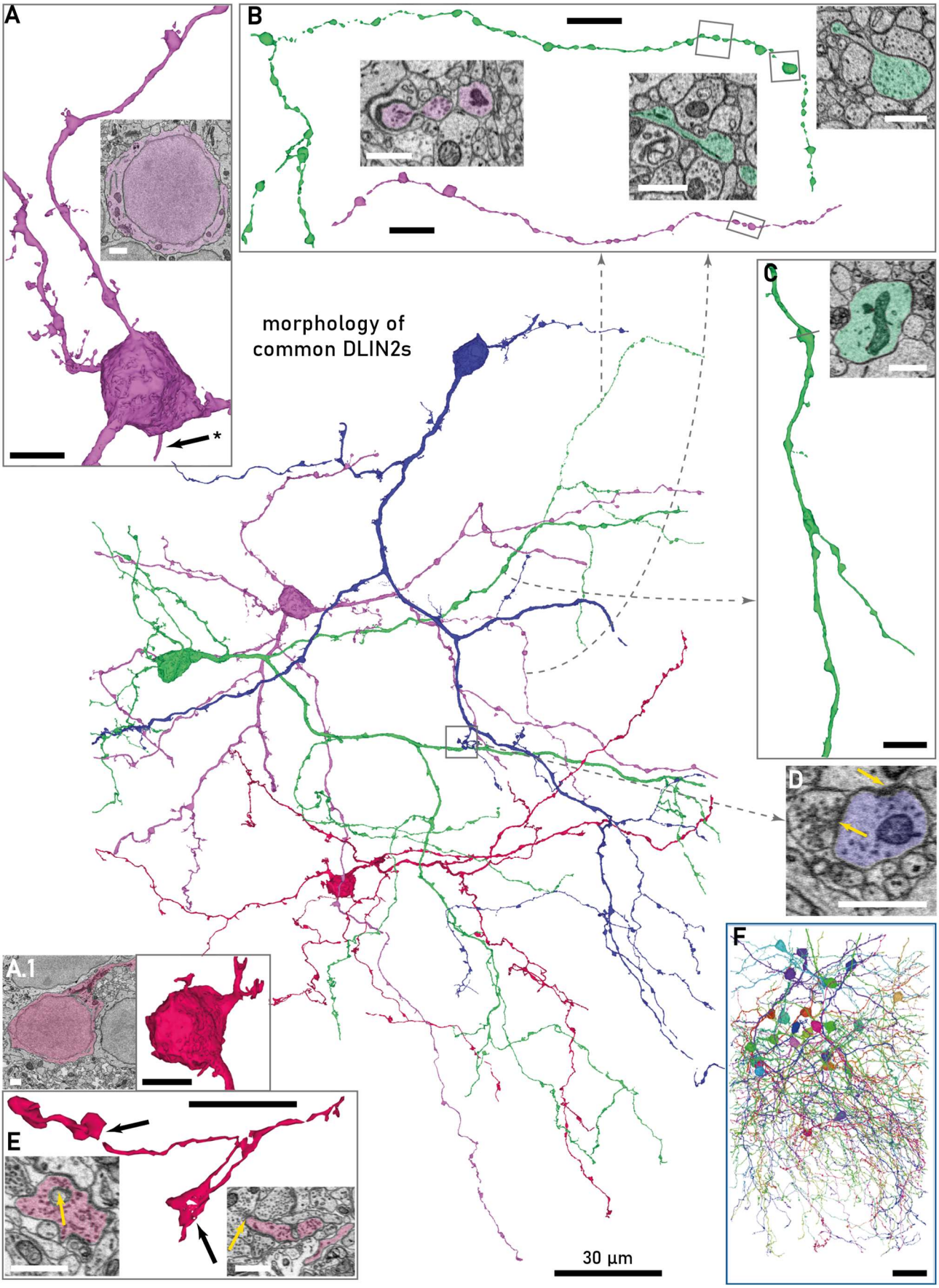
A
B
C
D
E
F
A.1
morphology of
common DLIN2s
30 µm

The transition from proximal, deep dendrite to distal dendrite was gradual. With distance from the soma spine frequency decreased, while many times the frequency of the varicosities increased. They became smaller in diameter and were no longer associated with spines. At these varicosities, in- and outbound, as well as reciprocal, synapses were found already in PL (fig. 45D). Upon entrance into the GL varicosities became larger, bore pointy protrusions, and more often adopted a flattened appearance as described above.

In most cDLIN2s (19/26) I observed one or more branches that stood out through a beaded appearance: These dendrites were completely aspiny. They exhibited roundish enlargements, which were much smaller than the other varicosities (0.5 – 1.0 µm) and also much more frequent. These were separated by very thin, short stripes of dendrite, giving the dendrite a pearl neckless-like appearance (fig. 45B). The varicosities did not contain mitochondria, but the dendrites were rich in ER. In contrast to what was common in thinner neurites, microtubules were very clearly visible in these dendrites. At a low frequency, both pre- and post-synapses were found at the varicosities. These beaded dendrites were guided through neuropil rich regions of the GCL or the PL.

The Rough, Fringy DLIN2s

The DLIN2s with fringy spines (fDLIN2s) comprised a group of 13 neurons. This subclass shared strong morphological similarities to cDLIN2s with respect to the cursory topology: Up to four dendrites of small to moderate size (equal size (9/13): ø: 0.5 – 1.5 µm, $\bar{x}$ ± σ: 1.0 ± 0.3 µm; unequal size (4/13): $ø_{WIDE}$: 1.0 – 2.5 µm, $\bar{x}$ ± σ: 1.8 ± 0.6 µm, $ø_{THIN}$: 0.3 - 0.8 µm, $\bar{x}$ ± σ: 0.5 ± 0.2 µm) emanated from the soma, branched regularly and spread in all direction through the imaged volume. The appearance of the distal dendrites was indistinguishable from those of cDLIN2s. The identifying characteristic of this subclass was the aspect of the soma and the dominating spine appearance. All somata (ø: 9 – 11 µm, $\bar{x}$ ± σ: 9.8 ± 0.5 µm) were located in a big cluster or neuropil rich regions of the GCL, with a globular soma outline dominating (11/13) and a near perfect ovoid shaped nucleus in six fDLIN2s. The somata had a very rugged surface (fig. 46A). They were studded with filopodial protrusions and many long-necked frayed spines, which produced a very rough, frazzled, sometimes spiky appearance. This aspect extended to the proximal part of the dendrites. Primary cilia were long (2.3 – 6.0 µm, $\bar{x}$ ± σ: 3.4 ± 1.0 µm).

At moderate to very high density, dendrites were covered with long-necked frayed spines. Many spines terminated in an elongated, frayed spine head (fig. 46A), made side branches, and bore long filopodial protrusions. Such protrusions were also found on the rarer, short-necked spines. Altogether, this resulted in a hairy aspect. The bulbar varicosities on the proximal dendrites associated with spines, observed in cDLIN2s, were either absent or far less pronounced (fig. 46B). However, the beaded side branches, traversing the PL and neuropil rich parts of GCL, were also present in this subclass (fig. 46C).

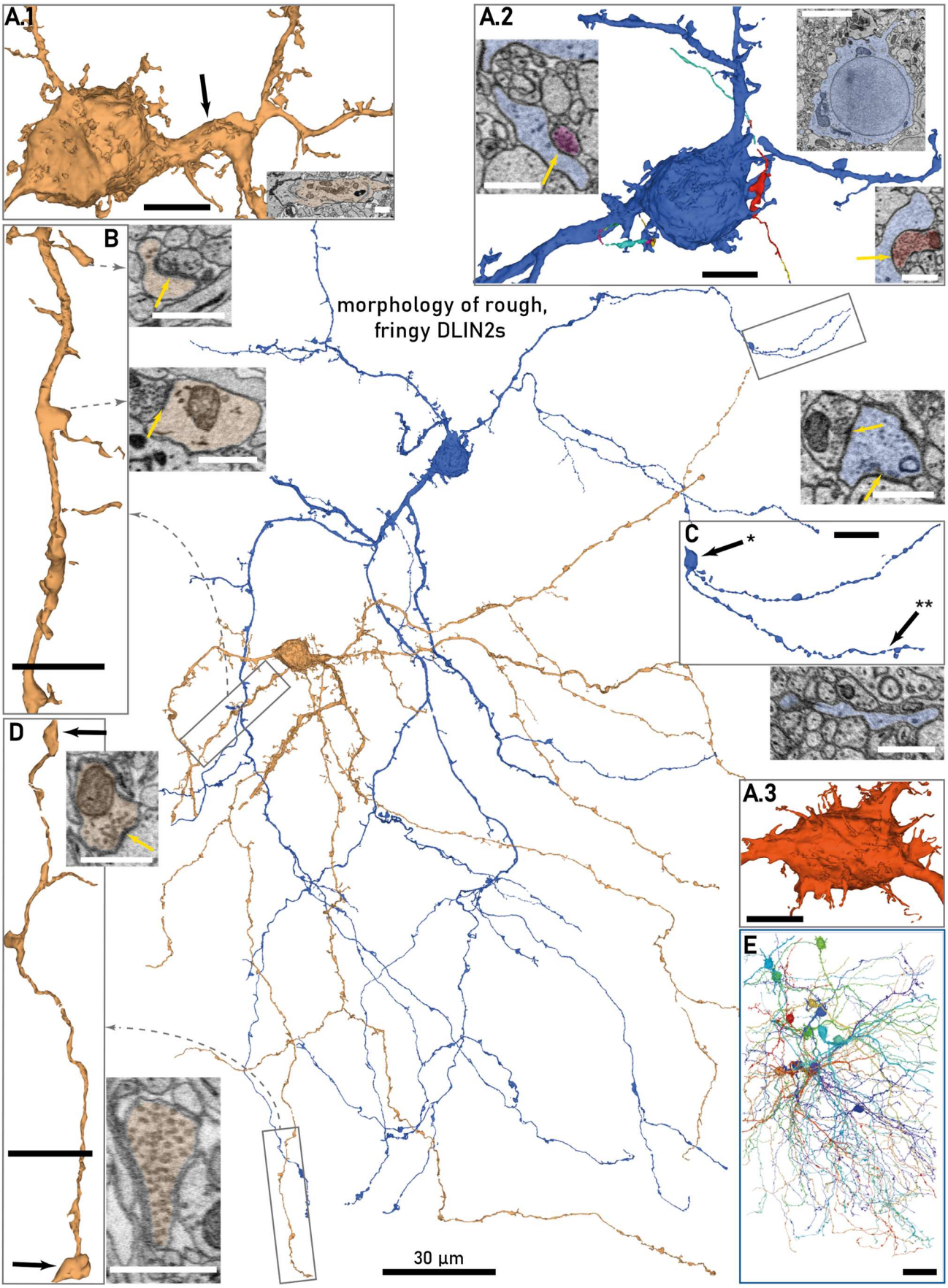
A.1
A.2
B
morphology of rough,
fringy DLIN2s
C
*
**
D
A.3
E
30 µm

Figure 46. Morphology of fringy DLIN2s (fDLIN2) at the example of two INs with stellate topology. A.1. Somata had a rough appearance covered with multiple long-necked, frayed spines and membrane excrescences. Inset: The Golgi apparatus spread well into the primary dendrite. A.2. Thin neurites with varicosities packed with small vesicles gave input to fDLIN2 spines. A.3. Some somata displayed a very spiky appearance. B. The proximal dendrites made regular dilations. These contained mitochondria and that usually bore spines receiving input. C. Like the cDLIN2s these neurons had beaded dendrite branches in PL that were pre- and postsynaptic sites. D. Close up on voluminous varicosities in GL. E. Overview on all 11 neurons of this subclass in the boundaries of the imaged volume. Scale bar: insets 3D: 5 μm, insets image: 1 μm.

The DLIN2s with Stubby Spines

The DLIN2s with stubby spines (sDLIN2s) comprised only three neurons, which showed notable morphological differences to representatives of the other two subclasses. All cell bodies were part of a big cluster in GCL and had a diameter of 9 µm. The surface was rough, rugged, and covered with stubby, frayed spines and large, elongated membrane excrescences (fig. 47C, D). The three sDLIN2 bore a single primary cilium (3 – 4 µm, $\bar{x} \pm \sigma$: 3.7 ± 0.6 µm, fig. 47D*). The soma gave rise to one or two large dendrites (ø: 1 – 2 µm, $\bar{x} \pm \sigma$: 1.7 ± 0.4 µm) that were directed towards the superficial OB layers on the dorso-lateral and ventro-lateral end of the imaged volume. The proximal dendrites were densely covered with stubbed and short-necked frayed spines but did not exhibit any varicosities (fig. 47A). In two cells thin dendrites emerge, which bore thin or long-necked spines at low frequency or were completely aspiny (fig. 47B, D). The thin dendrites ramified in the deep layers, one eventually reaching the GL. All three cells had beaded side branches, projecting through the deeper layers. The aspect of the distal dendrite was similar to the other subclasses, however, with a tendency towards flattened, stretched varicosities (fig. 47F). Altogether the sDLIN2s had a strong resemblance to the rDLIN1s, however, spine type and the aspect of the distal dendrite clearly placed them with the other DLIN2s.

Interactions With Other Neurons

I checked the overlap of all neurons of this class with the glomeruli. The presence of synapses within these volumes, however, was only confirmed for a subset of DLIN2s. Almost all cells with projections in the GL immersed their neurites in at least one glomerulus (40/42). On average the cDLIN2s appeared to pass their dendrites through fewer glomeruli than the other two subclasses (cDLIN2s: 2.6 ± 1.7, fDLIN2s: 4 ± 1, sDLIN2s: 4.0 ± 0.8 glomeruli).

I investigated the glomerulus-specific PN interaction for a superficial cDLIN2, one sDLIN2 and one fDLIN2 in the glomeruli M67D45A12, M56D56A2 and M45D4A2. Each investigated cell projected to a different subset of these glomeruli. All DLIN2s showed a selective MC innervation pattern and made primarily few synapses per connection: The superficial cDLIN1 was presynaptic to two of 19 (11%) MCs via a single synapse each. This neuron did not make any connections to RCs of these glomeruli, but I found inbound and reciprocal synapses with RCs of other glomeruli. The fDLIN2 was connected to four of 25 MCs (16%). These connections were mediated through single contacts (75% outbound, 25% reciprocal). The fDLIN2 made no connections to RCs of the glomeruli investigated but received input from an additional RC.

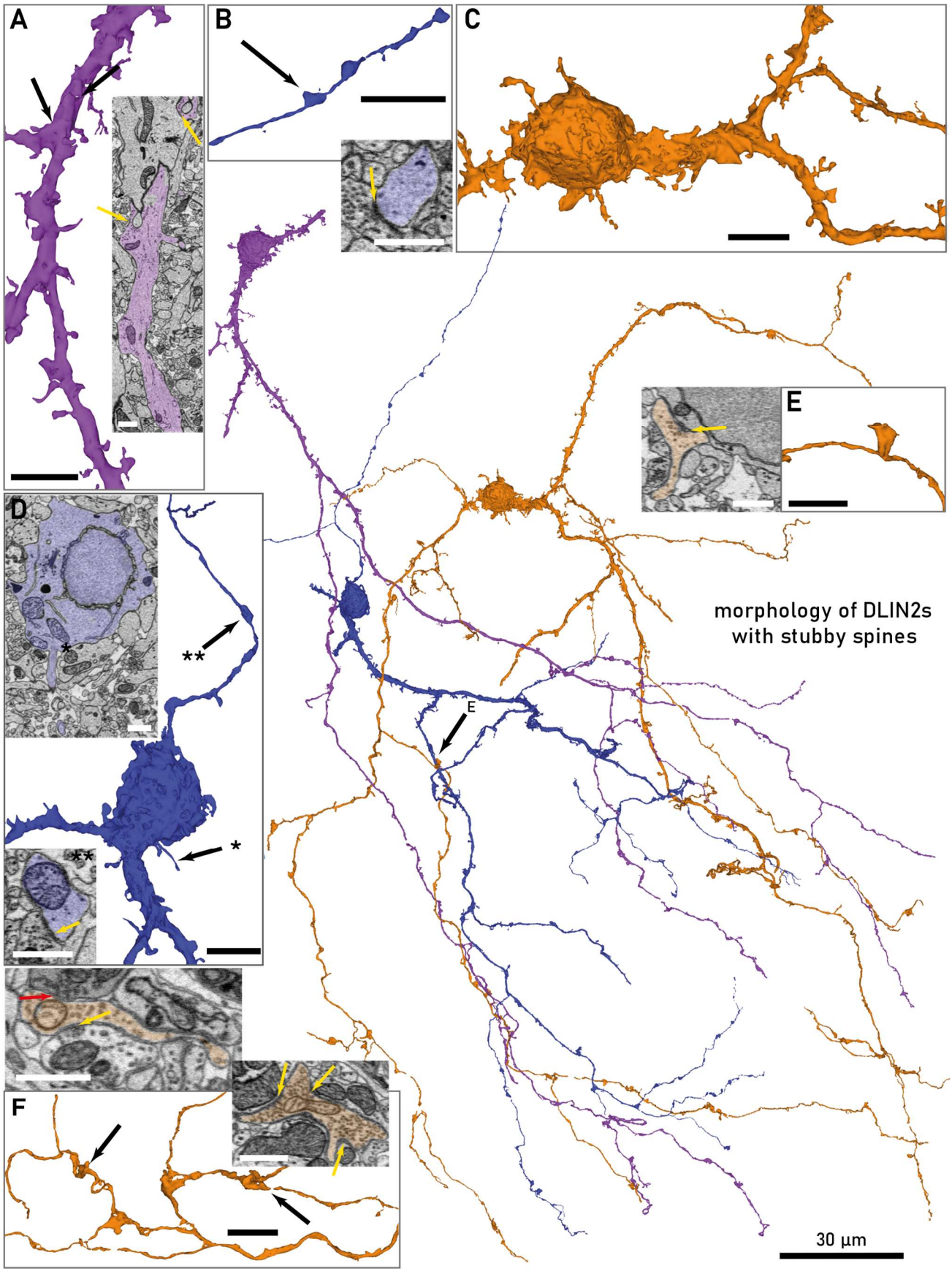
A
B
C
D
E
F
morphology of DLIN2s
with stubby spines
30 µm

Figure 47. The three DLIN2 with stubby spines. A: The proximal part of the primary dendrite was densely covered with short-necked and stubby, frayed spines. Inset: Synapses onto a neighboring DLIN soma (arrows). B: Tip of an aspiny, basal dendrite in GL with several varicosities, that received input. C: The somata were covered with ragged membrane excrescences and spines. D: Closeup on another soma from which a primary cilium emerged (*). A thin basal dendrite arose from the soma and received input to varicosities (**). E: A varicosity or stubby spine in PL containing a synapse onto a soma. F. Distal dendrite varicosities were rather flattened. Insets: top: Some varicosities received sensory input (red arrow). Others made multiple outbound synapses. Scale bar: insets 3D: 5 µm, insets image: 1 µm.

I investigated the glomerulus-specific PN interaction for a superficial cDLIN2, one sDLIN2 and one fDLIN2 in the glomeruli M67D45A12, M56D56A2 and M45D4A2. Each investigated cell projected to a different subset of these glomeruli. All DLIN2s showed a selective MC innervation pattern and made primarily few synapses per connection: The superficial cDLIN1 was presynaptic to two of 19 (11%) MCs via a single synapse each. This neuron did not make any connections to RCs of these glomeruli, but I found inbound and reciprocal synapses with RCs of other glomeruli. The fDLIN2 was connected to four of 25 MCs (16%). These connections were mediated through single contacts (75% outbound, 25% reciprocal). The fDLIN2 made no connections to RCs of the glomeruli investigated but received input from an additional RC. The sDLIN2 connected to eight in 25 (32%) MCs, showing a strong bias for the M67D45A12 glomerulus, where it made 7 connections. The output onto MCs clearly dominated over reciprocal connections, making up 75% of these connections. The number of synapses also varied, with predominantly one or two synapses per pair. One sDLIN2-MC pair was connected through six very large outbound synapses. This sDLIN2 also gave input to the dendrite of a RC (1/4 RCs (25%)).

In addition, I inspected the connections between a large, deep cDLIN2 and the PNs of all nine glomeruli it projected to (fig. 48). This IN connected to 16 of the 68 MCs within these glomeruli (24%), each connection was usually mediated by a single, sometimes two synapses. The majority of pairs are connected by reciprocal synapses (69% reciprocal, 25% outbound and 6% inbound connections). The cDLIN2 also connected to eight of the 12 RCs (67%) in these glomeruli. Only one of these pairs made reciprocal synapses at the ruff. In another pair the RC was presynaptic to the cDLIN2 and in turn receives input from the cDLIN2 to the dendrite. In four pairs the cDLIN2 provided input to either ruff or dendrite of the RC, whereas it received input from two other RCs.
During the reconstruction process I discovered further connections with both PNs and local INs. I found outbound synapses from shafts of the proximal dendrites and soma onto DLINs of all classes. Interactions with other DLINs were not restricted to the deep layers: I observed several instances of synapses from DLIN1s giving input from the distal dendrites of DLIN2s. These synapses were in proximity to synapses with PNs to which both DLINs connected. Furthermore, instances of both in- and outbound connections with all classes of GLINs were found, as well as input to PLIN4s.

Figure 48 (next page). Example of a large, deep cDLIN2, which connected to 16 MCs and nine RCs in nine different glomeruli. Eleven of the connections with MCs were reciprocal (e.g., 2, 8, 9), whereas only one connection to a RC was reciprocal (not shown). The cDLIN2 provided input to four MCs (5, 6, 10) and five RCs (1, 3). Only one connection to a MC was inbound (4), but the cDLIN1 received input from three RCs (7) without directly reciprocating it. Notably, with exception to the outbound connections to RCs, the majority of connections involved only a single or sometimes two synaptic contacts. Scale bars: insets 3D: 5 µm, insets image: 1 µm.

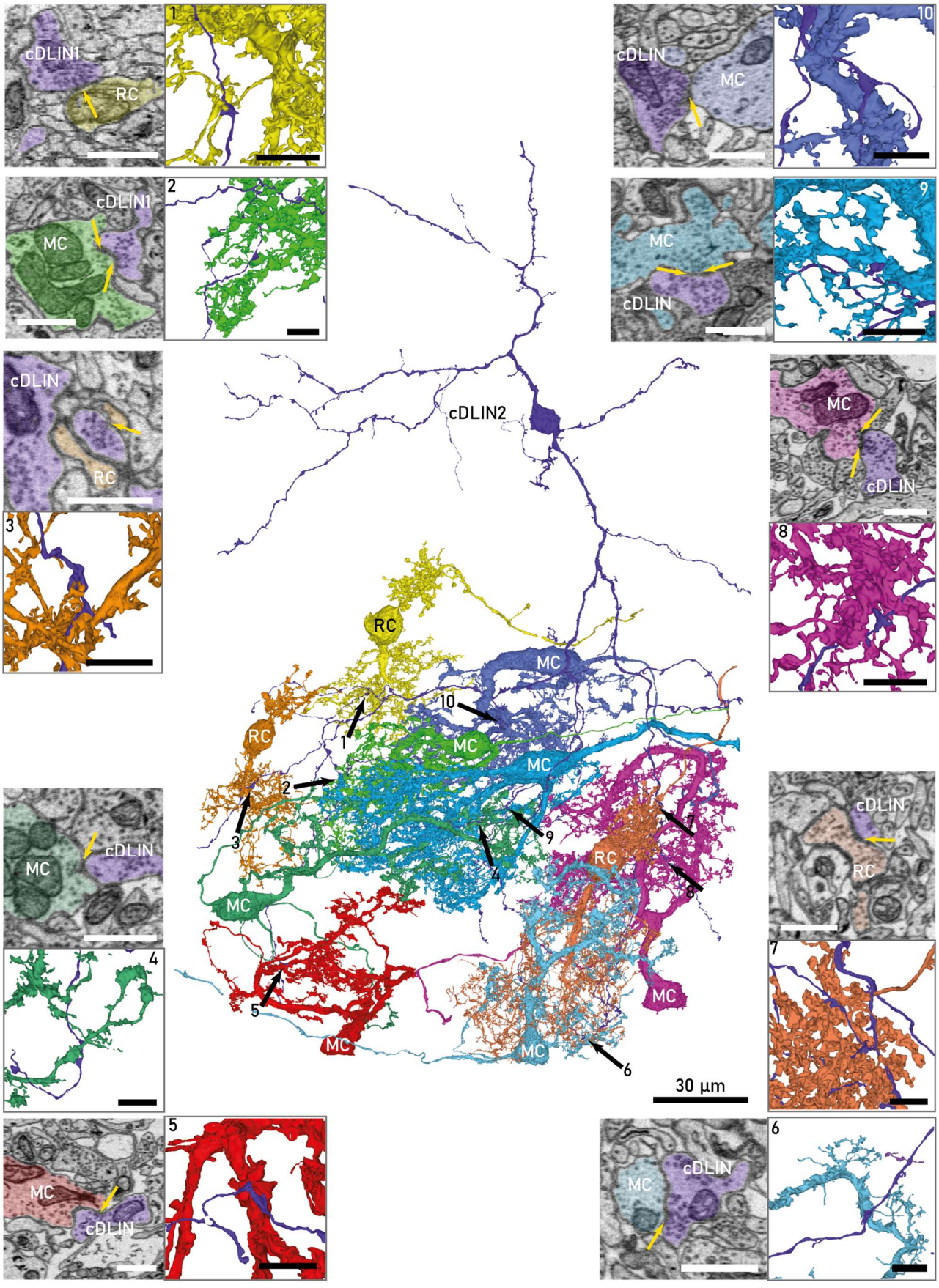
cDLIN1
RC
1
cDLIN1
MC
2
cDLIN
RC
3
cDLIN2
RC
MC
10
RC
MC
MC
1
2
3
4
5
6
7
8
9
MC
MC
MC
MC
RC
30 µm
MC
cDLIN
4
MC
cDLIN
5
cDLIN
MC
10
MC
cDLIN
9
MC
cDLIN
8
cDLIN
RC
7
MC
cDLIN
6

DLIN CLASS III

The third class of DLINs comprised a group of 26 neurons (CD1: 5 (19%), CD2: 12 (46%), CD3: 9 (35%)). These cells stood out by their hairy appearance. Numerous spines and fine basal branches, as well as the relatively slender appearance of the superficially projecting dendrites, gave these neurons an almost delicate aspect.

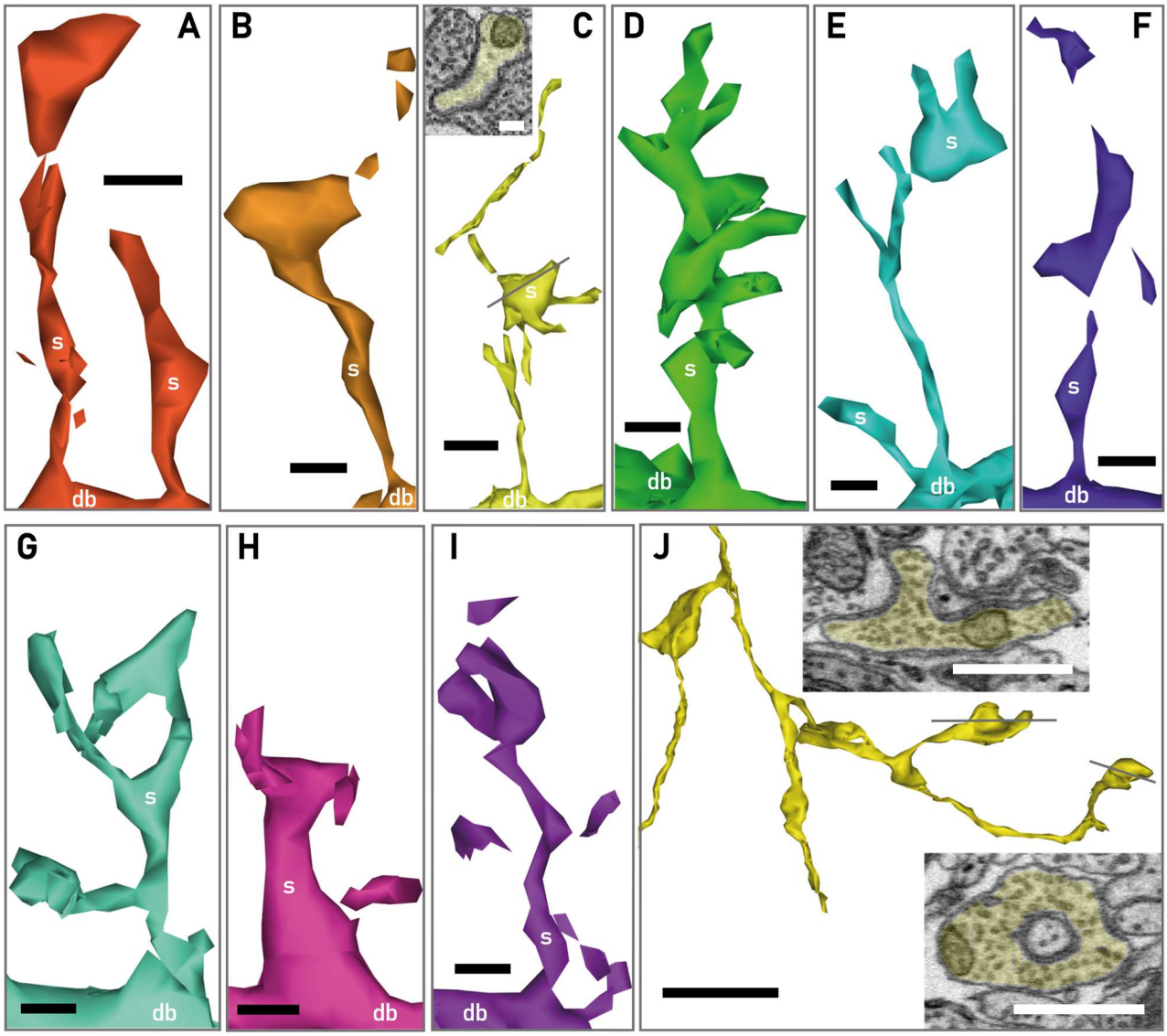

Figure 49. Aspect of DLIN3 spines. A-I: variations of the hairy spines of DLIN3. J: Close up on distal dendrite varicosities. Scale bars A-G: 500 nm, H: 3D: 3 µm, inset 1 µm, Abbreviations: s: spine, db: dendritic branch.

All neurites in the deeper layers were densely covered with thin, elongated protrusions of several microns' length. The appearance of spines was quite diverse. The largest fraction of spines could be characterized as long-necked, branched, or both. Filopodial, as well as mushroom-like branches could arise in the middle of a spine neck, as well as the distal end of a spine (fig. 49B-G). Many spines also exhibited amorphous dilations along the spine neck, which were usually targeted by synapses, and

which continued with a filopodium (fig. 49C). Given this appearance, spines were often undistinguishable from side branches of basal dendrites, which were also very thin and delicate.
The spine heads expressed a considerable variability; bulky heads dominated over flattened ones. They could be amorphous and associated with additional filopodia, pointy tips or beaded branches that tapered off similar as in frayed spines. The presence of long beaded protrusions on spine heads separated the DLIN3s into a group with a frizzly appearance (fig. 49B, F, I) and a non-frizzly variant, in which these kinds of protrusions were absent, and spines were more compact (fig. 49A, D, E, G, H). However, these groups were highly similar in other respects. I regularly observed spine heads, which sat like elongated long, amorphous rods on thinner spine necks (fig. 49A). Short-necked spines associated with these types of spine heads, as well as long, filopodial headless spines were also common (fig. 49A) while stubby spines were rare (fig. 49H).

The appearance of the distal dendrites was very similar to those described for DLIN2s. The neurites were round in cross section and with frequent, irregular modulations of the diameter. Compact and bulky varicosities associated with pointy tips dominated. In contrast to DLIN2s, varicosities stuck out more from a branch, resembling sessile spines and often sat on the end of a short branch (fig. 49J). Stretched out flattened enlargements were rare. However, altogether, considering only distal dendrite morphology, the two classes could not be set apart.

Morphology

The majority of cell bodies (19/26) lay in the big clusters of the GCL with the remaining cells located in the neuropil of the PL. Similar as in other classes of DLINs, there was a gradual reduction in terms of soma size and dendrite perimeter with soma position along the deep – superficial axis. The somata were globular or droplet-shaped and of a medium diameter (ø: 8 – 10 µm, $\bar{x}$ ± σ: 8.3 ± 0.5 µm). They stood out for their mostly very smooth surface, which was yet studded with many elongated spines and delicate basal dendrites (fig. 50A1-2). The nuclei displayed mild undulations and were embedded in rather little, sometimes moderate amount of cytosol. The cytosol was very clear and lightly stained, containing only a few short strands of ER with wide lumen, few slender mitochondria and scarcely any vesicles. A single compact Golgi apparatus was usually located at the base of one of the larger dendrites without stretching into it (fig. 50A1). Here, other components of the endomembrane system were identified. All neurons had one primary cilium of medium length (2 – 5 µm, $\bar{x}$ ± σ: 3.3 ± 0.7 µm).

Figure 50 (next page). The morphology of DLIN3s at the example of four neurons. The topology could obtain any shape from fusiform to stellate. The somata were positioned throughout PL and GCL. A. Somata and proximal dendrites were densely covered with hairy spines (see also fig. 49), these could take on a smooth (A.1) or frizzly aspect (A.2). A.2 insets: Left: A spine receiving input, right: Some spines contained large vesicular structures that resembled synapses. B1–3. Other spines in the deep layers made obvious synapses, which could be distinguished by clouds of small vesicles fusing to the membrane. These target neurites of presumed DLINs. C: Varicosities of the distal dendrites were voluminous but compact and often bore pointy tips (red arrows). D. Overview of all 26 DLIN3 within the stack boundaries. Scale bars: insets 3D: 5 µm, insets image: 1 µm.

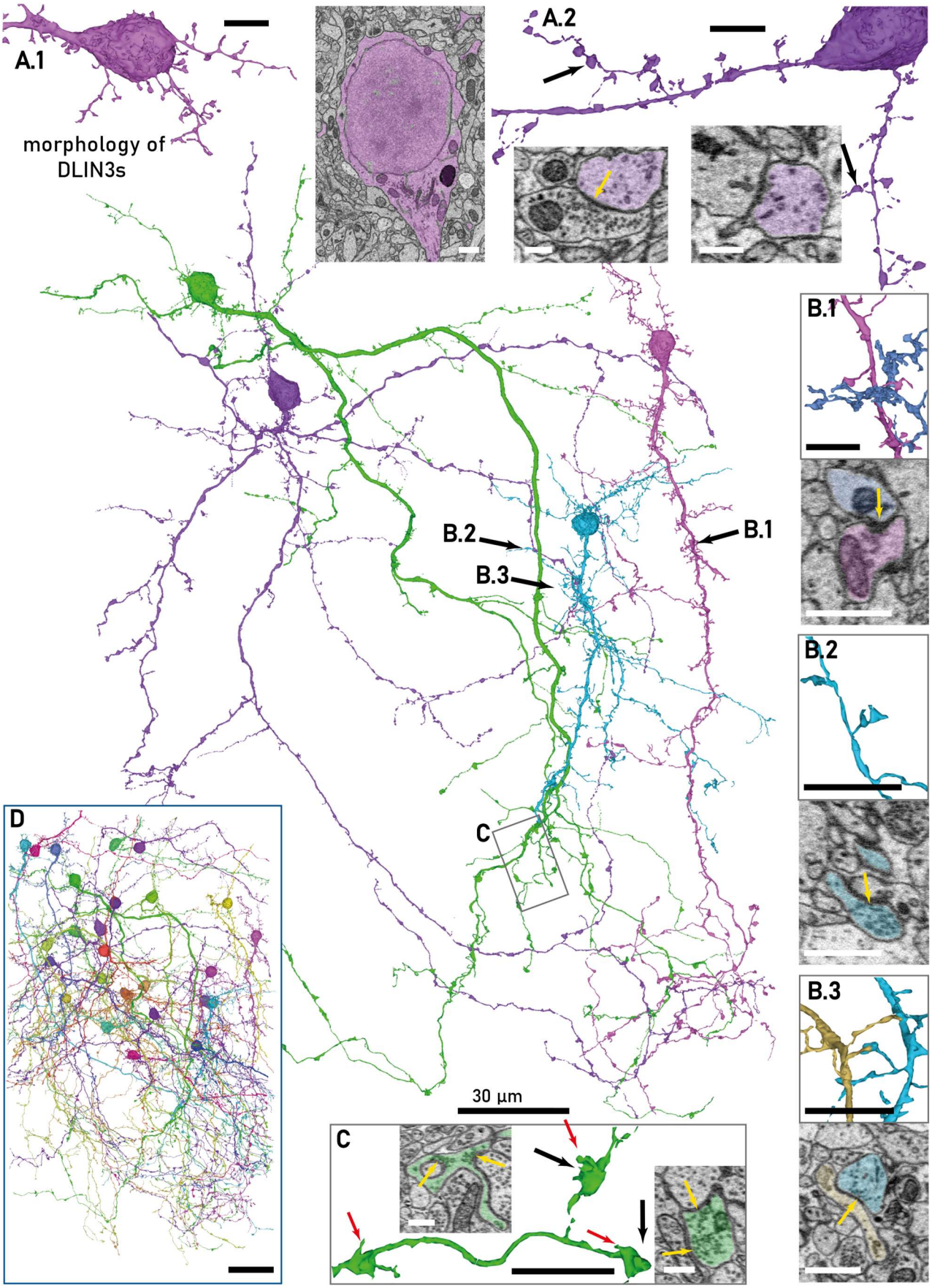
A.1
morphology of
DLIN3s
A.2
B.1
B.2
B.3
C
D
30 µm

Several dendrites emanated from the soma. Most cells (23/26) gave rise to one or two large dendrites (ø: 0.5 - 1.8 µm, $\bar{x}$: 1.1 ± 0.4 µm) and up to three fine, basal dendrites (ø: 0.1 - 0.5 µm, $\bar{x}$: 0.4 ± 0.2 µm). The larger dendrites were directed laterally and superficially towards the GL. On this path, some branched once or twice symmetrically within PL. The overall orientation of the dendritic tree varied between DLIN31s. A more stellate and a besom-like shape were equally frequent.
Elongated spines covered the dendrites at a very high frequency. Their occurrence was highest at the proximal dendrites and gradually reduced with distance from soma. In between spines the dendrites generally exhibited an even, smooth surface and were round in cross section. The large, proximal dendrites of 12 DLIN3s made noticeable bulbar dilations which often contained mitochondria. These dilations were of low frequency. In a subset of ten DLIN3s, I observed the aspiny, beaded neurites traversing PL noted in DLIN2s. Within the deep layers, the large, superficially projecting dendrites gave rise to many delicate basal dendrites. These were equally densely covered with elongated spines and extended usually around 10 – 30 µm but may occasionally spread well beyond 50 µm.

I visited 10 – 15 randomly picked spines on deep layer dendrites of 8 cells. The majority of spines received input at least at one site. Branched spines often received more than one synapse. Most spine heads were free of vesicles, but contained ER, which was not arranged in stacked discs as reported for spine apparatus. I also observed one to three spines that made outbound synapses onto deep layer neurites in four DLIN3s. These spines were quite proximal to the soma, showed no obvious differences to neighboring spines and could also be postsynaptic to additional neurites. I detected further spines containing many small vesicles, which resembled synaptic vesicles. However, I could not find sites of vesicle fusion, which are sufficiently distinct to be identified as a synapse (fig. 50B1-3). I also noted outbound synapses on dendrites and varicosities in the deep layers at low frequency.

Interactions With Other Neurons

DLIN3s projected to fewer glomeruli than other DLINs (2 ± 1 glomeruli, fig. 51, center). This excludes four DLIN3s, which did not reach the ventro-lateral GL and one DIN3, which passed its distal dendrite through neuropil between the identified glomeruli.

The glomerulus specific PN interaction was assessed for 5 DLIN3 in the glomeruli M56D56A2, M67D45A12 and M5D5A12. Only one DLIN3 projected to all glomeruli. With one exception the DLIN3s connected to only few of the MCs or RCs: On average, they made connections to 20% of the MCs and 13% of the RCs within the glomerular subcompartments they projected to (ID0111: 0/23 MCs, 2/4 RCs (50%), ID1084: 4/25 MCs (16%), 1/6 RCs (17%), ID1496: 6/10 MCs (60%), 0/2 RCs, ID2519: 3/27 MCs (11%), 0/4 RCs, ID2711: 2/13 MCs (15%), 0/2 RCs).

Figure 51 (next page). Connectivity between DLIN3s and PNs. Center: The DLIN3 (pink) was connected to four MCs (blue, yellow, purple, mint) and an RC (green). A. With one MC it made 11 synapses distributed across the MC dendrite (arrows). A.1. The DLIN3 made reciprocal synapses onto the shaft and varicosities in close proximity. Scale bar: 1.5 µm. B. The connection to the RC was established through a single synapse onto the RC dendrite. Scale bar: 1 µm. C. Example of the interaction of another DLIN3 with a RC. This pair made three reciprocal synapses at the ruff. Scale bars: 3D: 5 µm, insets image: 1 µm.

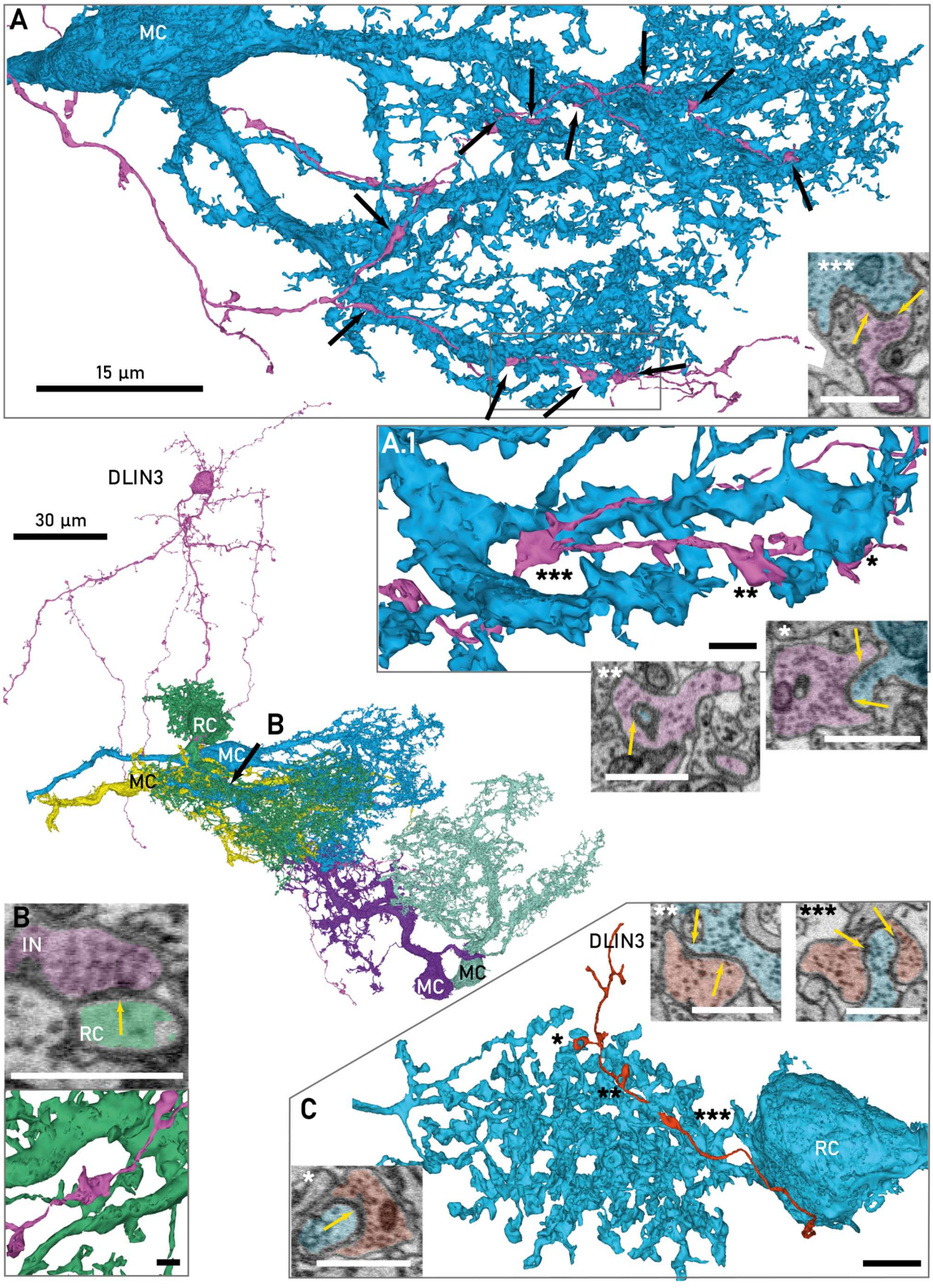
A
MC
15 µm
***
A.1
***
**
*
**
*
DLIN3
30 µm
RC
B
MC
MC
MC
MC
B
IN
RC
DLIN3
**
***
*
**
***
C
RC
*

Most DLIN3 - MC pairs (14/15) were connected through reciprocal synapses, but in one pair the DLIN3 gave input to the MC through a single synapse. In some reciprocally connected pairs, I found additional unidirectional, outbound synapses from the DLIN3. The number of synapses per connection was remarkably variable: About half of the connected pairs made only 1 or 2 synapses (8/15), while the other seven pairs were connected through up to 11 synapses ($\bar{x} \pm \sigma$: 6.7 ± 2.7 synapses/pair, fig. 51A). Each DLIN3 connected to MCs made at least one connection with many synapses. Furthermore, the synapses onto the MCs were notably large, mainly with respect to the associated vesicle cloud, but sometimes also with respect to the size of the active zone.
Synapses with RCs involved both reciprocal synapses at the ruff (fig. 51C), as well as outbound synapses onto the RC dendrite (fig. 51B). These could co-occur within a given connected RC-DLIN3 pair. Few additional synapses to RCs were found during the reconstruction process.
I identified the partners receiving input from proximal spines of DLIN3s (see above) as sDLIN1s and neurites belonging to other INs of the deeper layers e.g., PLIN4s. During reconstruction few connections to DLINs of the other classes, as well as some connections to GLIN1s and GLIN3s were noted.

V. UNCLASSIFIED NEURONS

UNCLASSIFIED GLIN

One IN could not be classified into any of the identified morphological classes. The soma was medium-sized (ø: 10 µm) with a flattened, ovoid shape and was located at the very surface of the ventro-lateral GL. A single dendrite (ø 1.5 µm) arose and extended towards the ventral, anterior side, where it left the imaged volume. Close to the soma it gave rise to 2 thin side branches, but otherwise branched only infrequently. The main dendrite had a very flat, oblong cross section. Throughout the entire length the dendrite was pervaded with dark ER structures and made occasional dilations in which slender mitochondria were found. These enlargements bore stubby and pointy protrusions and received input from MCs. The side branches had similar excrescences, which in contrast to those at the main dendrite, could contain synaptic vesicles. I identified a few synapses targeting MC dendrites and neurites resembling the distal dendrites of DLINs.
The dendrite traversed both M56D56A2 and M45D56A1. The IN did not make synapses with any of the 9 PNs of M45D56A1 and did not connect to any of the RCs in M56D56A2. However, I found the IN to connect to 6 of the 15 MCs in M56D56A2, with both reciprocal (3/6) as well as inbound (2/6) and outbound (1/6) connections relative to the IN. These connections were made by one or at most two synapses.

2.4.6 NEURON CLASSIFICATION CONTROLS

HUMAN CLASSIFICATION OF NEURONS

To confirm the existence of subclasses in the population of reconstructed neurons, four neuroscientists with deep general knowledge of the olfactory system, but unfamiliar with the reconstructed morphologies, were asked to assign 125 fully reconstructed cells into up to 12 classes (see section 2.2). These assignments, as well as my own assignment based on only these 125 cells, were pooled into a graph, and resulted in an adjacency matrix which is shown ordered by the final classification in (fig. 52A).

Whilst discrepancies occurred at the assignment of individual cells, the analysis clearly confirmed the existence of defined morphological neuron classes as described above: With exception of one RC with a truncated ruff, MCs and RCs were faithfully distinguished. The class assignments of superficial INs showed a strong overlap among classifiers: The first two morphological classes of GLINs were reliably identified. The lGLIN1s were often confused with the smaller and more superficial representatives of GLIN3s, PLIN1s and PLIN2s, which are only represented by one and two cells, respectively. The PLIN3s were reliably recognized as an independent morphological class. Deep GLIN3s and PLINs, particularly the PLIN4, were sometimes misclassified as DLINs. These neurons can share coarse topological features, especially with regard to their position along the y-axis of the imaged volume. Aside from that, DLINs were faithfully differentiated from other INs, but a more fine-grained distinction was only made by a subset of classifiers and the assignment was more variable.

Thus, whereas the details of the class assignment varied slightly, the main classes of PNs and INs were reliable identified by all human classifiers.

SEMI-AUTOMATED CLASSIFICATION OF NEURONS

In order to complement human cell type classifications with a more objective and unbiased approach, morphological features of the neurite tree were extracted from the skeletonized representation of the volumetric neuron reconstruction (see section 2.2.1). This feature space was further extended by measures obtained from the volumetric representation, namely the volume, the surface area of both neuron and soma, and two manually extracted features, axon and spine presence.

The extracted morphological features were used to identify morphological classes in 196 neurons with CD < 3. For dimensionality reduction before clustering both principal component analysis (PCA) and uniform manifold projection (UMAP) [138] was explored (see section 2.2). UMAP projections were used for visualization. Both partitioning (KMeans) and clustering (HDBSCAN) on either the original or the dimensionality reduced feature space yielded results that were qualitatively similar to the assessment obtained by visual inspection of the UMAP projections in 2D. Fig. 52B shows the UMAP projection of the 40 features space for all neurons in 2D. The analysis separated PNs from INs with high reliability, however, it allowed limited prospects to identify subclasses. A separate analysis of INs

distinguished between superficial and deep layer INs (fig. 52C.1). Visual inspection of neurons in the individual clusters showed that the automatic classification indeed captured morphological similarities well.

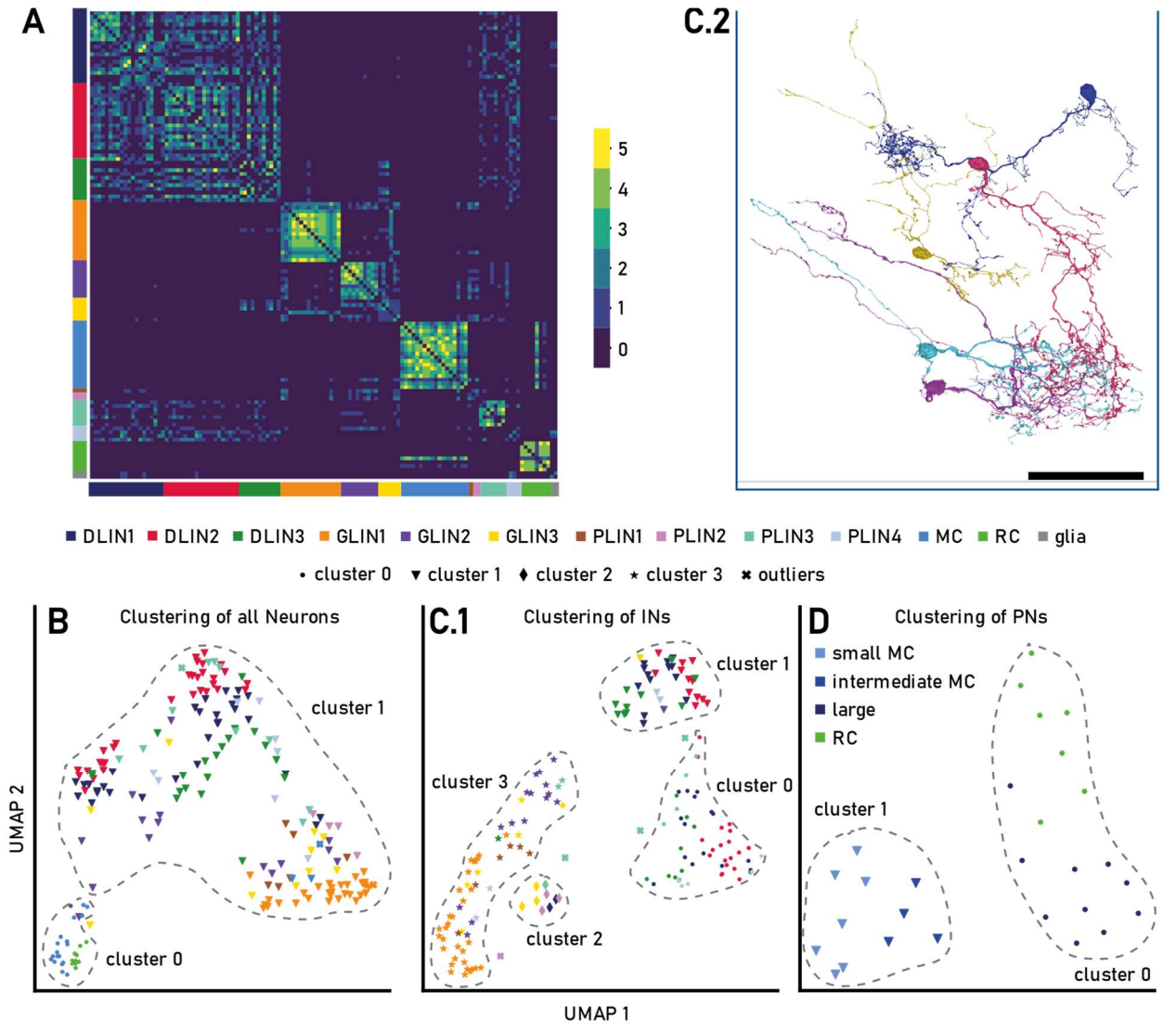

Figure 52. Human and semi-automated classification control. A: Adjacency matrix of the joint classification graph derived from five human classifications. The order of neurons reflects their assignment according to the manual classification described in section 2.4.4. The two classes of PNs, RCs and MCs, as well as the GLIN1s, GLIN2s and PLIN3s were identified reliably by all human classifiers. Color bar: edge weight. B: UMAP embeddings of 40 morphological features for all 196 neurons with CD < 3. Clustering with HDBSCAN on the 40 features: With exception of a GLIN2 and two small MCs, PNs and INs got well separated. C: Analysis of only the IN population. C.1: HDBSCAN clustering on UMAP projections (20 components) of the 63 morphological features discovered four clusters: Two clusters (cluster 0, cluster 1) comprised DLINs and large PLINs, another small cluster contained large GLINs and small PLINs (cluster 2), cluster 3 comprises all of the GLINs and small PLINs. C.2: Five randomly picked examples from cluster 3 in C.1 illustrate the morphological diversity of this cluster. Three axonal GLINs, a lGLIN1 (yellow) and two GLIN2s (purple, light blue), and two axonless PLINs, a PLIN1 (dark blue) and a vPLIN3 (pink) had been clustered together (scale bar 50 µm). D: Analysis of only the PN population: HDBSCAN clustering on UMAP projections of 40 features (20 components) identified two clusters containing small and intermediate MCs (cluster 1) and large MCs and RCs (cluster 0), respectively. Color code in figures A, B, C.1. and D reflects the class assignment as described in section 2.4.4.

The neurons in cluster 2 (fig. 52C.1), which emerged across a large range of parameters tested, were similar in size, position and spread, but differed on fine morphological features, e.g., spine distribution and existence of proximal dendrite. However, the analysis also resulted in some seemingly unnatural decisions, for example it mixed axonal and axonless GLINs (fig. 52C.2). The evaluation of only PNs revealed two subgroups (fig. 52D). One subgroup encompasses the small and intermediate subclasses of MCs. The second subclass comprises RCs and representatives of large MCs.
In summary, the semi-automated classification revealed that the PNs and INs can be reliably distinguished by clustering of computable features and confirmed the morphological differences between GLINs and more superficial PLINs on the one hand and deeper PLINs and DLINs on the other. However, the analysis yielded some decisions that human experts did not make and could not provide a more fine-grained classification of INs.

2.4.7 SENSORY INPUT TO OB-INS

In mammals superficial INs, the ETCs, as well as small subpopulations of PGCs and sSACs, receive direct sensory input [55, 154]. To investigate the input to INs in the zebrafish OB, I searched for and inspected contact sites by overlaying each cell individually with the mesh of sensory axons created from the semantic tissue segmentation (see section 2.2.1), carefully screening each cell by following individual neurites in GL. From each morphological class of INs I inspected at least three representatives. In addition, I tracked sensory input to INs encountered during the reconstruction process. The findings are summarized in table 9:

	sGLIN1	lGLIN1	GLIN2	GLIN3	PLIN1	PLIN2	rtPLIN3	vPLIN3	PLIN4	rDLIN1	lDLIN1	sDLIN1	cDLIN2	fDLIN2	sDLIN2	DLIN3
# neurons inspected	11	2	8	7	6	4	3	2	3	4	3	3	4	5	1	4
# receiving sensory input	0	0	1	2	0	0	2	0	0	4	2	2	0	5	1	3
# giving input to sensory axon	0	0	0	1*	0	0	0	0	0	0	0	0	0	0	0	1**

Table 9. Summary of observed connections between subsets of INs and OSNs. *IN gave input to two sensory axons; one synapse was reciprocal. **IN received input from an axon terminal remote from the one it provided input to.

I did not find any sensory input to GLIN1s, PLIN1s, PLIN2s or any of the PLIN4s. In all other GLINs and the PLIN3s, I found at least one neuron to receive sensory input. These inputs were mediated by a single synapse, most of which were distinct and unambiguous, but a few were small and of lower confidence (see fig 53). Like sensory input to RCs, these synapses were on average much smaller than the sensory synapses onto MCs. In the DLIN classes sensory input was more frequent (19/26 cells).

With the exception of the cDLIN2s, I found sensory input to all subclasses of DLINs. In more than half of these I found more than one input synapse (11/19) and these synapses could overlap with different glomeruli.

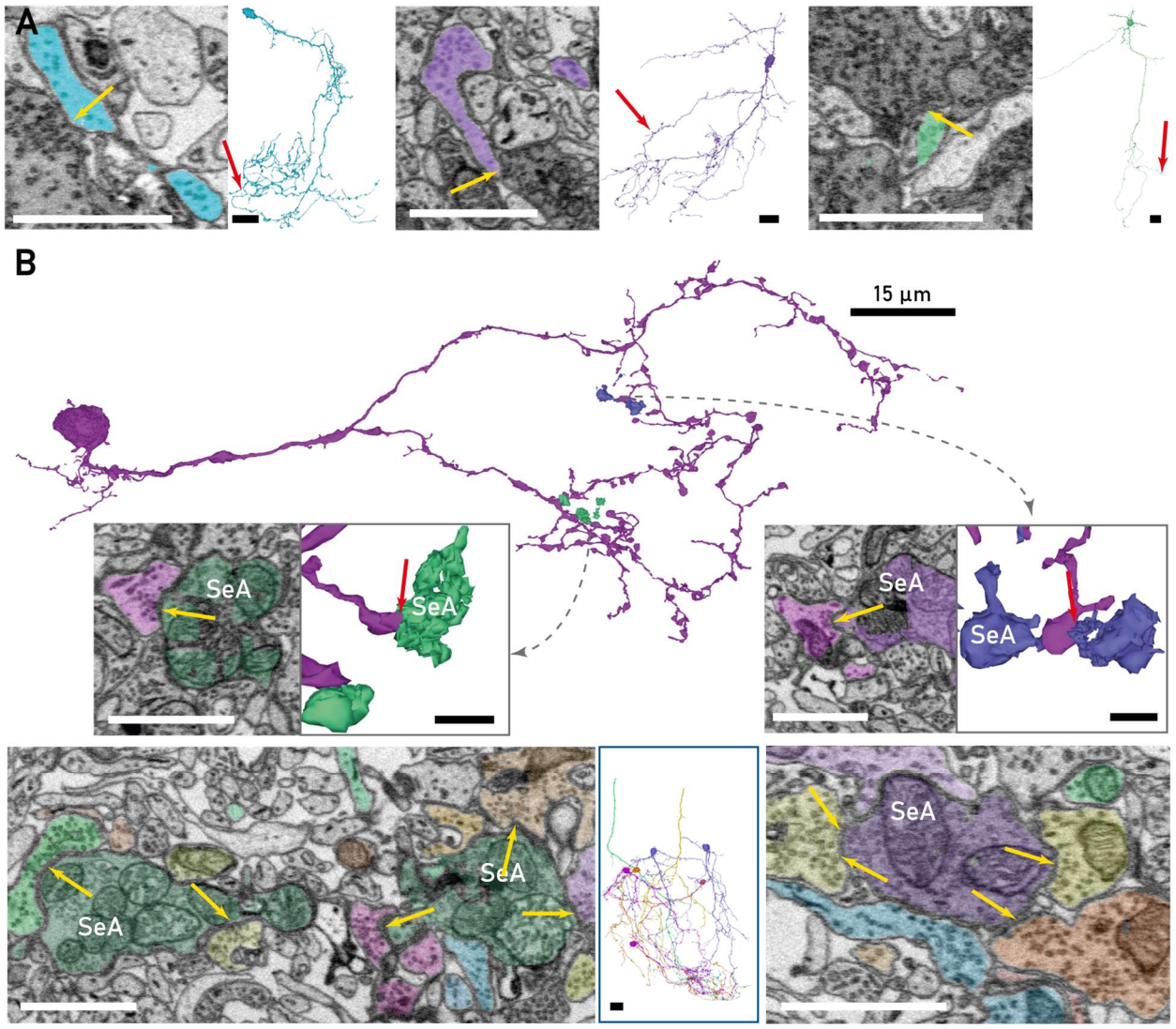

Figure 53. Connectivity between OSNs and bulbar INs. A: Examples of sensory synapses onto fully reconstructed INs: Left: sensory synapse onto a PLIN3. Middle: sensory synapse onto a DLIN3. Right: sensory synapse onto a fDLIN2. B: IN synapses onto OSNs. Top: A GLIN3 gave input to two sensory axons (SeA). Insets: Closeup of synapses (see arrows). Bottom: Closeup of two SeA boutons that received input from multiple INs. All highlighted neurites gave input to the SeAs. Synapses are indicated by arrows; some synapses are out plane. Left: several neurites were connected to the SeA in green. Middle: Overview of neurons connected to the SeA (green) shows the high diversity of INs that gave input to SeAs. Right: A reciprocal synapse between an IN and a SeA can be seen. Scale bars raw image: 1.5 µm, 3D insets: 1.5 µm, 3D view overview: 15 µm.

Some sensory axons also received input from local neurons (see fig 53). Among the fully reconstructed neurons I found one GLIN3 and a DLIN3 to give input to separate axon terminals. These axon boutons received input from many other neurites. Many of these synapses were reciprocal. Remarkably, these boutons did not make apparent output synapses onto MCs in vicinity of the IN input.

I could trace some unreconstructed IN neurites, reciprocally connected to OSNs, back to a vPLIN3s, several DLIN2s and a DLIN3. The morphology and projection patterns of the other neurites suggests that these inputs might also originate from PLINs or DLINs. However, their soma could not be found in the stack.

2.4.8 PN-IN INTERACTION

The interactions between MCs and RCs with different IN classes are summarized in a connectivity scheme (fig. 54) that considers the glomerulus-specific examination of PN-IN connectivity as well as the additional observations described in the specific sections for the IN classes. I assessed connections as weak, moderate, and strong based on the fraction of connected pairs and based on the number of contacts between pairs.

There were only two IN classes to which MCs were not reciprocally connected: The lGLIN1s, which received only very sparse MC input (1/92 pairs) and the GLIN2s. The latter received strong MC input. Given the postsynaptic nature of the dendrite and the trajectory of the GLIN2 axon through deep layers, I consider local, reciprocal connections between MCs and GLIN2s unlikely. No connections between MCs and sGLIN1s were found. MCs made moderate to strong reciprocal connections with the axonless GLIN3s and the PLIN2s, PLIN3s and PLIN4s. Many of these connections were characterized by a remarkably large number of synapses (see GLIN3s, PLIN3s). Connections between DLINs and MCs were also reciprocal. These connections were mediated by fewer synapses per pair and in many morphological classes the IN input to the MC appeared stronger in terms of synapse number and size.

Interactions between RCs and INs give a more diverse picture. RCs were presynaptic to both subclasses of GLIN1s. However, whereas input to lGLINs was infrequent, the interaction with the sGLIN1 were particularly outstanding (see section 2.4.4 → GLIN Class I). RC input onto GLIN2s was very sparse (1/612 pairs, see section 2.4.4 → GLIN Class II). Strong reciprocal connections to PLIN1s and PLIN4s were present, but no connection to PLIN2s was found. Moderate to strong input to the RC dendrite originated from PLIN3 and DLIN1. Interestingly, subclasses of PLIN3s showed differences in the connectivity to RCs: All examined rlPLIN3-RC pairs were connected, whereas only 1 of 16 possible vPLIN3-RC pairs was connected. Strong input to the RC dendrite came from all DLIN1 classes. However, I found only sparse input to the RC dendrite to originate from GLIN3s, sDLIN2s and DLIN3s. Reciprocal connections between RC and DLINs were infrequent to moderate. However, the RCs output was likely underestimated, because the glomerulus-specific examination of PN-IN connectivity did not consider the ruff, the primary, local, RC output structure, which resided outside the glomerular volume.

IN class	glomerular innervation	MC selectivity	# synapses/ IN-MC pair	% IN ⇄ MC pairs	% IN ↦ MC pairs	% MC ↦ IN pairs
sGLIN1	mono	-	-	-	-	-
lGLIN1	mono	selective	low	0	0	100
GLIN2	mono	broad	high	0	0	100
GLIN3	mono	broad	high	73	9	18
PLIN1	mono	variable	low	100	0	0
PLIN2	mono	broad	low	57	29	14
rlPLIN3	multi	broad	high	80	20	0
vPLIN3	multi	broad	low	59	35	7
PLIN4	multi	variable	low	42	33	25
rDLIN1	multi	selective	low	62	31	8
lDLIN1	multi	broad	low	64	18	18
sDLIN1	multi	variable	low	83	17	0
cDLIN2	multi	selective	low	65	29	6
fDLIN2	multi	selective	low	25	75	0
sDLIN2	multi	variable	low	25	75	0
DLIN3	multi	selective	variable	93	7	0

Table 10. Features of connectivity between different IN subclasses and MCs. MC selectivity of a IN class was rated broad, if most INs connected to ≥ 40% of the MCs, selective, if the majority connected to < 40% of MCs of a glomerulus and variable, if both broad and selective representatives were present. The number of synapses per IN-MC pair was considered high, if it involved ≥ 3 synapses and low otherwise.

Local IN-MC interactions can be assumed to occur primarily in the glomerular volume. Table 10 gives an overview of the nature of connectivity to MCs for the individual IN subclasses. This shows systematic differences in MC connectivity between superficial and deeper INs. The INs of GL and the smaller PLINs all had monoglomerular innervation pattern, whereas all DLINs and larger PLINs made projections into several glomeruli. Both GLINs and PLINs connected broadly to many MCs within a glomerulus. GLIN2s, GLIN3s and rlPLIN3s typically made high numbers of synapses with individual MCs. In contrast, almost all DLINs exhibited a selective connectivity with MCs of a given glomerulus and these connections were usually mediated by a low number of synapses. The DLIN3s represented an exception here, as they connected to at least one MC through a large number of synapses. With the exception of lGLIN1s and GLIN2s, which were uniquely postsynaptic to MCs, all OB-INs made reciprocal synapses with MCs. Indeed, most connections between MCs and INs of nearly all classes were reciprocal. The second most frequent connection type was input from the INs onto the MC, whereas pairs in which only the MC was presynaptic to INs were rare.

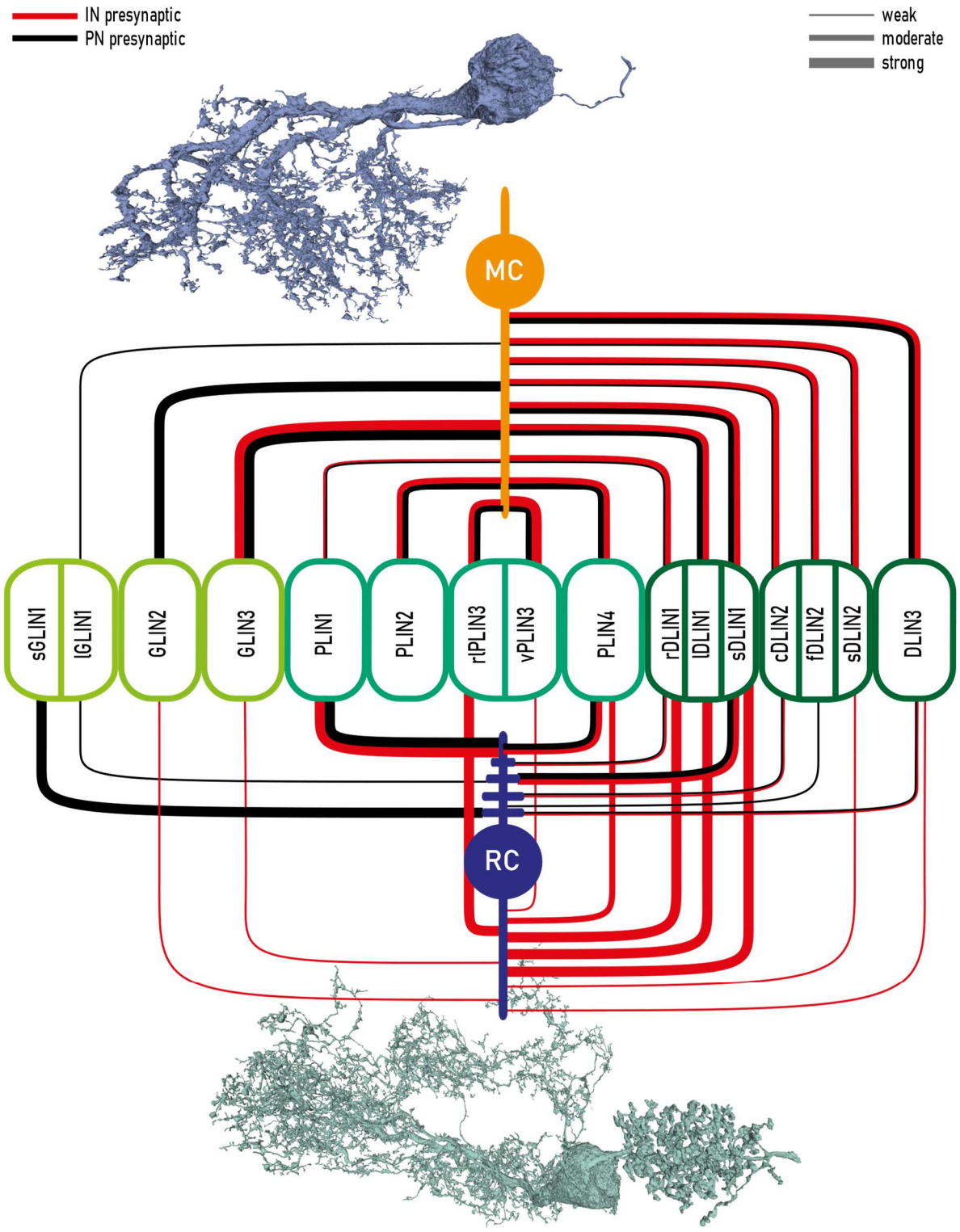

Figure 54. Scheme of the connectivity between PNs and INs. Top: The MC-IN connectivity was predominated reciprocal mediated by dendro-dendritic, reciprocal synapses. Only the GLIN2s and - to a very limited extent - the small GLIN1s received unrequited MC input. With most DLIN subclasses input to the MC was stronger than output onto the IN. Bottom: The interaction between RCs and IN was more diverse: Originating from the ruff, RC gave prominent input to both subclasses of GLIN1s. Strong reciprocal connections to PLIN1s and PLIN4s could be observed. Additional reciprocal connections to the majority of DLIN subclasses were found. Pronounced input to the dendrite originated from the ribbon-like PLIN3s, the PLIN4s and DLIN1s.

2.4.9 THE GLOMERULAR COLUMN IN ADULT ZEBRAFISH OB

To give an overview of the neuronal components that can connect to a given glomerulus, a summarizing scheme of the glomerular column in zebrafish OB is shown (fig. 55). This scheme is based on my manual classification described in section 2.4.4. The main morphological and connectivity of neuron classes and subclasses described in that section are summarized in table 11.

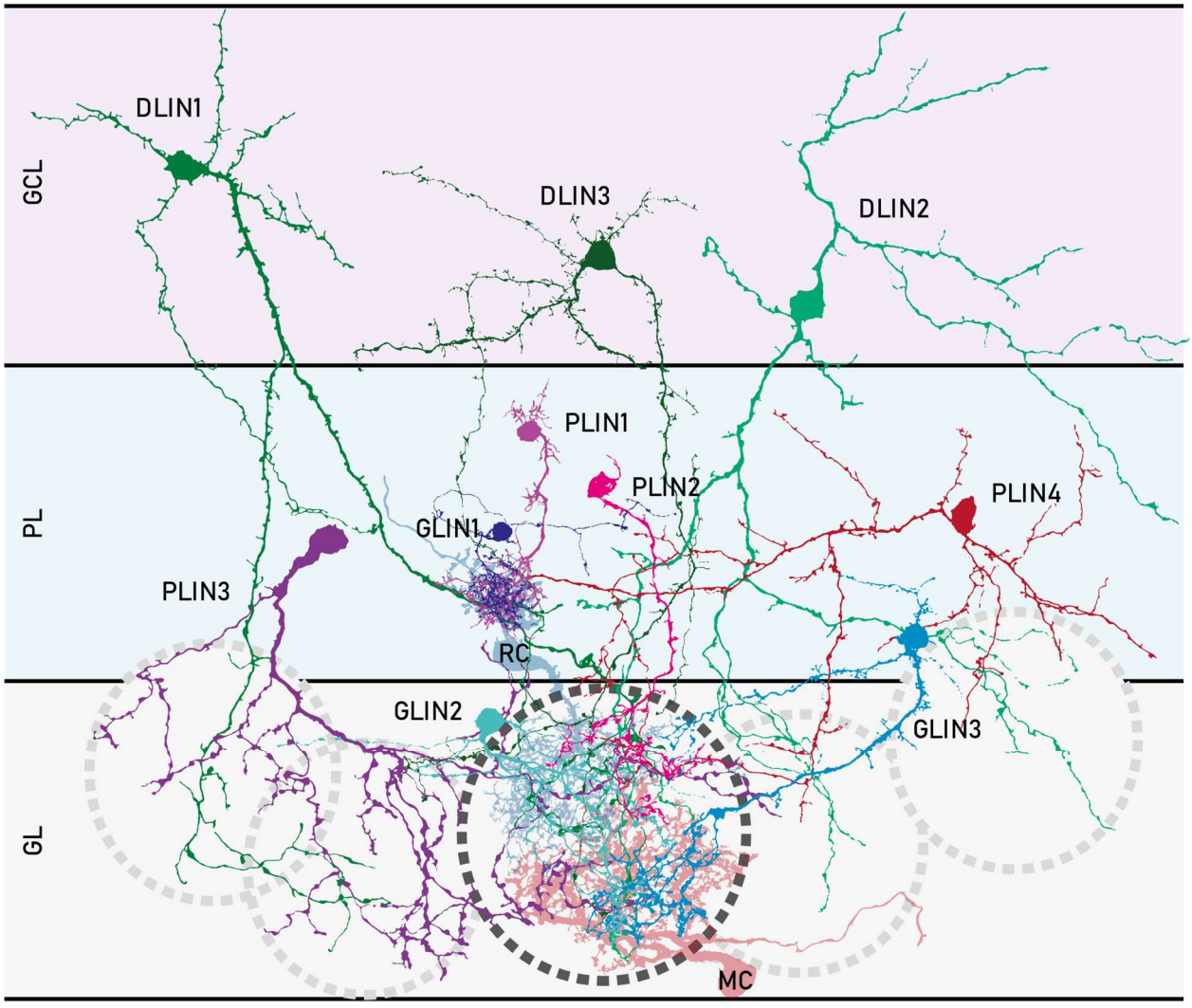

Figure 55. Scheme of a conceptual glomerular column in adult zebrafish. Each neuron class is depicted by a single representative independent of the number of cells per subclass. Abbreviations: DLIN: interneuron of the deep layers, GCL: granule cell layer, GL: glomerular layer, GLIN: interneuron of GL, MC: mitral cell, PL: plexiform layer, PLIN: interneuron of PL, RC: ruffed cell.

In adult zebrafish, a glomerulus contains multiple MCs of all subclasses. The number of MCs (>4-15) varied significantly with the size of the glomerulus. MC were predominantly monoglomerular, received strong sensory input and connected to the majority of bulbar INs reciprocally. Subclasses of

MCs differed mainly in overall size. Each glomerulus or glomerular subcompartment contained at least one RC, but up to three were observed. These PNs distinguish by the name-giving local output structure, the ruff, where reciprocal synapses with many IN classes are formed [117]. RCs were found to receive small to moderate amounts of sensory input. Each RC was associated with several sGLIN1s, usually positioned deep to the glomerular volume. These small INs did not connect to MCs and were not immersed in the glomerular neuropil. Through association to RCs they were mainly monoglomerular. It is not yet determined whether all glomeruli are associated with lGLIN1s. Within GL multiple monoglomerular GLIN2s and GLIN3s were associated with a given glomerulus.

	neuron type	cell count	cell volume [µm³]	total length [µm]	soma volume [µm³]	axon	spine frequency	glomerular innervation	sensory input	MC selectivity	synapses/ IN-MC pair	RC connections	dendro-dendritic synapses	reciprocal synapses
MC	small MC	8	542±221	2.0±0.8	217±68	+	-	mono	+++	-	-	+	+	+
MC	intermed. MC	4	1116±350	4.1±0.7	394±69	+	-	mono	+++	-	-	+	+	+
MC	large MC	12	1958±522	7.0±1.5	667±244	+	-	mono	+++	-	-	+	+	+
RC		8	1186±318	6.3±2.0	633±109	+	-	mono	++	/	l	-	-	+
GLIN	sGLIN1	23	161±40	0.8±0.3	58±17	+	-	mono	-	-	-	+	-	+
GLIN	lGLIN1	8	192±49	1.2±0.3	65±17	+	-	mono	-	s	l	+	-	+
GLIN2		18	428±185	2.1±0.9	152±61	+	+++	mono	-	b	h	-	-	+
GLIN3		11	274±101	1.7±0.8	97±34	-	++	mono	+	b	h	+	+	+
PLIN1		6	230±38	1.4±0.4	75±17	-	+	mono	-	v	l	+	+	+
PLIN2		5	221±38	0.9±0.2	71±9	-	++	mono	-	b	l	-	+	+
PLIN3	rlPLIN3	5	395±164	2.0±0.9	122±41	-	+	multi	+	b	h	+	+	+
PLIN3	vPLIN3	8	473±93	1.8±0.5	144±29	-	+	multi	-	b	l	+	+	+
PLIN4		12	314±46	1.6±0.6	135±36	-	+	multi	+	v	l	+	+	+
DLIN1	rDLIN1	18	495±127	2.4±0.7	157±43	-	+++	multi	+	s	l	+	+	+
DLIN1	lDLIN1	12	306±54	1.6±0.7	118±32	-	+++	multi	+	b	l	+	+	+
DLIN1	sDLIN1	12	399±74	2.0±0,7	127±29	-	+	multi	+	v	l	+	+	+
DLIN2	cDLIN2	26	531±139	2.1±0.6	200±55	-	++	multi	-	s	l	+	+	+
DLIN2	fDLIN2	13	579±151	3.0±0.7	196±46	-	+++	multi	+	s	l	+	+	+
DLIN2	sDLIN2	3	596±87	2.6±1.1	174±8	-	+++	multi	+	v	l	+	+	+
DLIN3		26	334±134	1.9±0.7	100±29	-	+++	multi	+	s	v	+	+	+

Table 11. Summary of main morphological and connectional features of all neuron classes and subclasses in adult zebrafish OB described in section 2.4.4. Abbreviations: b: broad, h: high, l: low, s: selective, v: variable, -: absent/not applicable, +: present, ++: pronounced, +++: very pronounced, /: not assessed

Both classes of INs made synapses with MCs, the GLIN2s received MC input and the GLIN3s made reciprocal connections. However, synaptic connections with RCs were very sparse. Whether all RCs are associated with PLIN1s remains to be established. Only a subset of these INs was connected reciprocally with MCs. Several monoglomerular PLIN2s, as well as the multiglomerular PLIN3s and PLIN4s, innervate parts of the glomerular volume. Multiple multiglomerular DLINs of all subclasses are associated with a zebrafish glomerulus. All DLIN classes made reciprocal connections with both classes of PNs as well as multiple different IN classes.

Several observations bring out particularities of the zebrafish OB circuit. Sensory input to INs was rare and more consistently observed for DLINs. Remarkably, all neuron classes of zebrafish OB were found to make reciprocal synapses, either on their dendrite or their axon. Further, with the exception of RCs, GLIN1s and GLIN2s, dendro-dendritic synapses were found in all neuron classes.

Together, the findings summarized in fig. 55 and table 11 demonstrate adult zebrafish OB is rich in diversity of both principal and interneurons, that are characterized by connectivity features, e.g. the abundance of reciprocal synapses.

2.5 DISCUSSION

The following section recapitulates the main findings of the neuronal composition of zebrafish OB. I aim at embedding these findings into knowledge that emerged from previous neuroanatomical investigations of teleost OB. In addition, I review potential homologies of individual neuron classes to classes described in mammalian OB but also point out fundamental differences. Taking into consideration the interactions observed between particular IN classes and PNs, I discuss potential functional implications.

Odorants evoke distributed and overlapping activity patterns across glomeruli in the olfactory bulb (OB), where these patterns get transformed through normalization and decorrelation to optimize computation in downstream networks [155, 25, 35]. These transformations crucially depend on diverse interactions between projection neurons (PNs) and various types of interneurons (INs), which outnumber the former many times [37, 78, 20, 21, 27]. However, a detailed picture of the diversity and composition of neurons, particularly IN types in zebrafish OB has so far been lacking.
Here, we use of one of the most advanced approaches for large scale neuron reconstruction at ultrastructural resolution to explore the neuroanatomy and neuron composition of the adult zebrafish OB. Provided with a SBEM volume of zebrafish OB, which was recorded previously in the lab, as well as an automated, volumetric segmentation by our collaborators, I created a software tool, which enabled me to efficiently reconstruct and proofread entire neurons in this dataset. The volumetric reconstruction of 239 neurons, 32 PNs and 207 INs, from all layers of OB, allowed me to explore and analyze the cellular topology and morphology of multiple neurons in the same individual at unprecedented detail. I describe ten morphological classes of INs, which can be subdivided into further subclasses, and find that the main group of OB principal neurons, the MCs, encompass three morphological subclasses. Analysis of synaptic and non-synaptic contacts between neurons revealed specialized interactions between MCs and INs with prominent dendro-dendritic reciprocal synaptic connectivity.

2.5.1 NEURON RECONSTRUCTION

The development of software to correct agglomeration errors enabled me to proofread and reconstruct many neurons at a fast rate. Generally, neurons were volumetrically reconstructed in a non-redundant fashion and reconstruction completeness was not quantified. In principle, assessment and reduction of reconstruction errors could be achieved through multiple redundant reconstructions or a dense reconstruction, but this approach is very labor-intensive and beyond the scope of this current project. Instead, I compared the volume and skeleton length of redundantly skeletonized and non-redundantly reconstructed in some exemplars (DLINs). This comparison did not reveal major differences, indicating that completeness of volumetric reconstructions was not reduced substantially by missing branches (see fig. 8).

In general, the completeness of neuron reconstructions may be affected by numerous factors: First, a considerable number of neurons (115/239) was estimated to be only represented to less than 75 % within the imaged volume. The resulting incompleteness is expected to exceed the error arising from manual reconstruction manifold. Second, it is conceivable that due to the convoluted neurite path of complex, tufted cells, their reconstruction benefits less from the additional information of the 3D volumetric representation, resulting in more over-looked segmentation errors than in the reconstruction of simpler cells. Furthermore, neuron properties, like the extreme thinning of the neck of the spine-like protrusions in GLIN2s, could result in systematic differences in the reconstruction

completeness between cell types, particularly in a sparse reconstruction. Importantly, while such biases are likely to affect connectomic analysis, I do not expect this to impair the morphological classification of neurons notably.

2.5.2 NEURON CLASSIFICATION

Substantial research has been dedicated to elucidate the diversity of cell types in the early olfactory system of mammals in morphological, structural, molecular and physiological studies [61, 72, 60, 156, 53, 157] and the circuitry of the mammalian OB has been revisited and reviewed many times [62, 63, 59, 158, 67, 51, 159]. The literature in teleost fish and zebrafish in particular is much sparser and has predominantly focused on the description of principal neurons [94, 84, 117, 95, 85, 81], which allowed me to reliable identify PNs among the reconstructed neurons. The diversity of INs, in contrast, is not well understood. A few studies analyzed physiological functions of INs in the zebrafish OB [20, 37] but anatomical descriptions are rare [87]. Hence, I described the morphological features of the reconstructed neurons of the OB in detail as a basis for a systematic classification of neurons. The volumetric reconstruction allowed me to analyze morphological aspects across all layers of the OB and across different levels of resolution, from coarse topology to ultrastructural features, within the same neurons.

To corroborate the existence of different morphological neuron classes and substantiate my classification, I conducted two controls. First, I asked trained neuroscientists ("human classifiers") to classify a subset of the reconstructed cells. This analysis showed a strong agreement among humans in the classification of PNs, as well as many INs. GLIN1s, GLIN2s and PLIN3s, were reliably recognized as distinct groups. Other PLIN groups were not recognized unanimously, which may be partly due to their underrepresentation in this dataset. While DLINs were faithfully distinguished from INs of the superficial layers, there was a large variation with respect to the subgroups to which DLINs were assigned. DLINs shared strong resemblance in their coarse topology and my own classification was based on systematic differences across classes of DLINs in features a microscale resolution. An inspection of discrepancies between the individual assignments suggested that, when the human classifier was less familiar with the dataset, classifications were predominantly guided by similarities in geometry and location, whereas other systematic differences between cells on a higher level of detail were ignored. An obvious example is a RC with a missing ruff, which all human classifiers misclassified as MC. At a glance, RC and MC dendrites are very similar in size, extent and location within OB and they have a tufty outline and branch extensively. However, upon closer inspection, MC and RC dendrites can be unambiguously differentiated by numerous morphological features, e.g., the variability in diameter, the size and fraction of tip branches, the frequency of sensory input, and many more.

As a second control, I ran an automatic clustering analysis based on features extracted from the skeletal neuron representation and some additional volumetric features. This analysis found a reliable

and clear separability of PNs and INs and further subgroups. Namely, it managed to separate the sparser MC subclasses, the small and the intermediate MCs, from the dense MC classes, and faithfully distinguished DLINs from superficial INs. However, the clustering failed to serve as an independent, alternative classification method, as it could not make a more fine-grained distinction between neuron classes that showed obvious differences (see e.g., the clustering of axonal and axonless INs in one group in fig. 52C.1/C.2). The method can likely be further improved by increasing the number of reconstructions, better skeleton representations, feature selection or a meaningful expansion of the feature space, for example with further volumetric measures or measures of spine shape and distribution. Alternatively, unsupervised deep learning approaches are likely to provide further insight. However, even an improved automated classification method requires solid evaluation, for which ground truth was so far missing.

In conclusion, both controls independently confirmed the existence of main the neuron classes described in my manual classification, i.e., different PN classes and a differentiation of INs beyond a categorization in superficial and deep layer INs. Variations affected only the detailed assignments of some neurons to some of the classes. A fine-grained classification relies on the integration of morphological features across a wide range of resolutions. On this note, it must be also pointed out, that I not only considered structural and morphological features for neuron classification, but also integrated knowledge about interactions between neurons, which was obtained through the deep exploration of the dataset during reconstruction. For example, the tight interaction between PLIN1s and RCs, which (among other features) allowed me to immediately set these INs apart from the morphologically similar GLIN3s. To give another example, the knowledge of extent and position of glomeruli, to which GLIN2s projected their dendrite, enabled me to disregard the considerable difference in their coarse geometrical structure and identify them as neurons of the same subclass. Equally important for a solid classification, was a thorough understanding of the structural organization of OB, namely the layering, in the imaged volume and the reconstruction of a substantial number of cells, particularly considering the subtle differences between some neuron classes.
Eventually, the classification controls conducted could not fully dissolve subjectivity underlying my manual classification. In particular, the identification of DLIN classes was based on subtle features and alternative ways of grouping these neurons are imaginable. Yet, the classification represents an elaborate study based on detailed morphological description, which can serve as foundation of subsequent studies.

2.5.3 SENSORY INNERVATION

GLOMERULAR ORGANIZATION

The anatomical organization of glomeruli in the adult zebrafish OB has been described previously [46, 86, 160, 161]. Based on the position of the recording site within the animal's body axis and based on

a comparison of the trajectories of the sensory axon tracts with anatomical images and descriptions in [46] and [86], I assume the imaged volume was obtained posterior to the lateral glomeruli (lG) group, likely coinciding with the lateral plexus (LP). This region is innervated by microvillous OSNs [160], responsive to amino acids [16, 155], and anatomically differs from other regions of the OB. Here, OSN axon terminals do not aggregate to defined glomeruli distinguishable across animals, but are loosely organized and diffuse, forming multiple microglomerular structures small in diameter [46, 86]. Yet, odor responses in this region are localized in larger, discrete regions suggesting a glomerular organization [16]. A light-microscopy study showed MC dendrites occasionally form compartments resembling glomeruli in LP [86].

Here, I extensively reconstructed PNs and found all their dendrites to organize into discrete, spherical to ellipsoid glomeruli, suggesting this organization to be the rule for ventro-lateral OB. These glomeruli were composed of MCs of all subclasses and always contained 1-3 RCs. Only MCs were observed to project to different glomerular subcompartments, but not RCs. MCs of LP were previously described as almost exclusively multiglomerular [86]. With the exception of 7 MCs that project large neurites outside the imaged volume and potentially target remote glomeruli with secondary dendrite tufts, I find almost exclusive evidence for monoglomerular MCs. Several aspects may contribute to this discrepancy. First, Braubach & Croll, report the number of MCs in a full OB in the low hundreds [86], which is likely an underestimation as others estimate ~1500 MCs in an adult OB [89]. Braubach & Croll could thus have missed smaller, monoglomerular MCs.

Another important aspect is the definition of a glomerulus which is more difficult in teleost OB, where glomeruli are not as clearly delineated by glial elements and periglomerular cells as in mammalian OB [82]. Previous studies used labelling of OSN axons to outline the presynaptic component of glomeruli [161, 46, 86], whereas I describe glomeruli as units formed by the postsynaptic PNs. The glomeruli described here have been reconstructed to varying degrees of completeness with respect to the number of PNs, which formed them, and none is fully completed. Still, it is obvious that the size of glomeruli varied substantially, both with regard to spatial extent and PN number (see table 3). Yet, even the smallest glomerulus, M5D4A12, clearly exceeded the extent of a single OSN microglomerulus, whose maximal extent was reported as 4.8 ± 3.9 µm [86]. Given that MCs receive sensory input throughout their dendrite with preference to the distal compartments, it is likely, that the glomeruli formed by the postsynaptic PN dendrites comprise multiple afferent microglomeruli. Thus, PNs of LP form more complex, but self-contained, postsynaptic glomerular structures in which MCs might be multiglomerular with respect to microglomeruli. These structures could only be uncovered by overlaying the dendritic arbors of multiple PNs from the same OB. Importantly, this portrayal of glomeruli on the basis of the postsynaptic PN neuropil reconciles the disagreement between the microglomerular organization of sensory input described previously and the large-area odor response pattern observed in this region [46, 16].

Across diverse taxa, olfactory systems have been found to be organized following the principles of "*one sensory neuron-one receptor*" and "*one glomerulus–one receptor*" [10, 41, 3]. However, alternative

wiring principles supporting efficient olfactory coding can be imagined. Indeed, in the mammalian accessory olfactory bulb (AOB) axons from OSNs expressing different, but related OLFRs converge onto the same glomeruli was observed [162]. This wiring has been proposed to optimize the detection of pheromonal blends [162]. It remains to be determined whether the glomeruli described here are homo- or heterotypic with respect to their OSN innervation. However, the glomeruli of LP were homogeneous with respect to their innervation by PNs and can thus be considered discrete functional units. A more detailed reconstruction of OSN axons could contribute to a better understanding of the organization of afferent input to glomeruli. Insight into the presynaptic OSN composition is of particular interest, when investigating and comparing the local OB circuitry between MCs of a given glomerulus innervating different or multiple compartments of a specific glomerulus.

SENSORY INPUT TO INS

Sensory input to INs has not been investigated exhaustively, but some interesting observations could be made. In zebrafish OB sensory input appears to be sparse: In most cases, INs do not receive more than one sensory synapse, and if a given morphological class was found to receive input, usually not all of the inspected representatives were innervated by OSNs. Among the superficial INs cogent evidence for OSN input was only found for the monoglomerular GLIN3s. Solid OSN input targets the PLIN3s, but even more so the DLINs, in which all but the cDLIN2s were found to receive sensory input. Often DLINs received OSN input through multiple, separate contacts in different glomeruli.

This picture contrasts the findings of OSN input to INs in the mammalian OB where OSN input targets three types of superficial INs, two of which are monoglomerular. A prominent target of OSN inputs in the mammalian OB are the glutamatergic ETCs [154], which mediate feed-forward excitation and have not been described in teleosts so far. As none of the IN types observed here match the characteristics of ETCs, it appears likely that this cell type does not exist in zebrafish and possibly other teleosts (see also section 2.5.5). Other OSN input to the mammalian OB targets monoglomerular PGCs and multiglomerular sSACs [51, 55, 21], which mediate gain control and possibly shape odor representations through specific inhibitory interactions within and across glomeruli [51]. My results indicate that feed-forward inhibition in the zebrafish is mediated exclusively by multiglomerular INs of the inner OB layers (PLIN3s and DLINs). This observation does not contradict the hypothesis that these INs mediate gain control and shape odor representations. More detailed insights into the functions of these cell types could be obtained by the reconstruction of axons and comprehensive mapping of sensory inputs by IN type. It would also be interesting to map the reciprocal interactions more precisely between INs and some OSN boutons, which occur spatially separated from synapses onto MCs.

2.5.4 PROJECTION NEURONS OF ADULT ZEBRAFISH OB

Beyond the broad classification into tufted cells (TCs) and mitral cells (MCs) diverse subclasses of PNs in mammalian OB have been described based on morphological and physiological properties, projection targets, gene expression and odor response [64, 65, 66, 163, 164, 157]. In mammals, the depth of the soma within OB correlates with the length and the depth of the secondary dendrites and, in consequence, the type of GC, with which they interact [64, 65, 165]. Moreover, odor tuning becomes narrower with increasing soma depth [163]. These differences led to the proposition that MCs and TCs form parallel odor processing pathways with different function: The more sensitive, fast-responding, heterogeneous group of TCs, projecting to the anterior olfactory nucleus (AON) and olfactory tubercle (OT), may play a role for olfactory functions requiring speed as well as motivational aspects of olfactory behavior and odor source localization [165, 67]. The more narrowly tuned MCs, projecting to multiple brain regions, most prominently piriform cortex, are expected to convey information necessary for odor encoding and identification, odor learning, discrimination and perception of complex mixtures [166, 167, 168, 67].

In teleosts, two types of PNs have been described, the mitral cell (MC) and the ruffed cell (RC). Whereas targets of OB PNs have been investigated [169, 170], it is unknown whether these regions are targeted by both MCs and RCs or whether a differential projection pattern exists. Besides the genetic identification of some distinct PN subpopulations little is known about the heterogeneity of PNs in the zebrafish OB [169, 91, 170].

2.5.5 DIVERSITY OF MITRAL CELLS

Previously, MCs have been classified into mono- or multidendritic [84] and uni- and multiglomerular [86]. Subgroups of MCs differing in cholinergic responsiveness were reported [171] and genetically identifiable PN subtypes were found to differentially target OB output regions [170]. More detailed information on subclasses of MCs in zebrafish has been so far lacking. Here, I have described three morphologically distinct subclasses of MCs, which were almost exclusively monoglomerular (see section 2.4.4. → I. PROJECTION NEURONS). These three groups varied predominantly in size, but also differed in other morphological features and with respect to the local axonal output. Only the small subclass of MCs was found to give input to diverse, nearby INs via axo-dendritic synapses outside the glomerulus, from which the MC received OSN input. Only in one intermediate and none of the large MCs local collaterals could be identified. It cannot be excluded that these MCs make axonal output outside the volume covered by the stack, but there was no evidence for axon collaterals remote from the soma.

Within the boundaries of the imaged volume none of the small MC axons were myelinated. It is

possible that these MCs do not project out of the OB, and teleost MCs may, thus, be a neuron class comprising both PNs and local INs. In mammalian OB, the external tufted cells (ETCs) represent a heterogeneous group of glutamatergic neurons receiving direct OSN input, of which the majority make axonal projections restricted to OB [60, 156, 54, 172, 173]. These ETCs convey the afferent input to a wide range of partners, namely MCs and TCs, PGs and other ETCs and represent an important excitatory driving force within a glomerulus [50, 54, 173]. Unlike local ETCs, however, small MCs do not make inputs to other PNs. Other ETCs have long-range projections within the OB that terminate near the location of the mirror glomerulus associated with the same odorant receptor [174]. However, this mirror-symmetrical organization of glomeruli is absent in teleosts, and it remains unclear where axons of small MCs terminate. Small MCs are therefore not equivalent to any of the known types of ETCs in mammals. However, it is possible that small MCs and ETCs are related but their synaptic connectivity is not identical. Alternatively, small MCs may correspond to other PN types in the mammalian OB, such as subtypes of TCs, or they may not have a direct equivalent in mammals.

2.5.6 THE RUFFED CELL

Ruffed cells (RCs) were first described in detail in correlative Golgi and EM studies in goldfish by Kosaka & Hama [117, 153, 95]. Many of the morphological and ultrastructural features described here as characteristic for RCs are conserved across teleost species [150, 151, 152, 94]. In the publications of Kosaka & Hama [117, 153, 95] one can observe the light appearance of the mitochondria, the high density of cell organelles at the soma especially with the intricate maze of sER cisternae or the vesicle free cytosol in the dendritic tip branches, which contrasts the higher frequency of ER and vacuoles at the dendritic shaft described here as well.

In zebrafish, MCs and RCs were characterized by retrograde labeling with a lipophilic fluorescent dye [84]. RCs were described as larger than MCs and making up less than 5% of the PNs in OB [84]. Here, I found RCs to be larger in soma size and dendrite length than the small and intermediate MCs, but not the large MCs. The fraction of RCs among zebrafish OB PNs could not be assessed here. However, RCs were found to be part of every glomerulus described. This suggests that RCs represent an integral component of the glomerular column. The fact that there were two types of local INs, which tightly, intensely and (almost) exclusively interacted with RCs, but not MCs, corroborates the idea that RCs play a specific role in the early olfactory processing in zebrafish.

The reconstruction of entire neurons allowed to revisit some findings and proposals on the in- and output characteristics of RCs made in [117, 153, 95]. While these authors observed sparse outputs onto INs, which originated from the dendritic shaft and involved very few vesicles and a postsynaptic density, I could not identify a single presynaptic site on a RC dendrite. Based on my analysis, it seems likely that the RC dendrite is purely or predominantly postsynaptic.

In contrast to MCs, RCs did not make reciprocal synapses within a glomerulus, their local output appeared restricted to the ruff, which was always extraglomerular. In [117, 153, 95], RCs are

described to make both reciprocal and unidirectional synapses with INs, which were thought to be GCs, because these INs were also found to make reciprocal synapses with MCs. Here, RCs were found to make synapses with a large variety of local INs at their ruff. Examining the connectivity at the RC dendrite with 3D reconstructions of several partial branches, Kosaka & Hama concluded that RCs receive only little synaptic input mostly from presumed GCs. My results suggest that synaptic input to RC dendrites is less frequent than input to MC dendrites but nevertheless substantial, and that it originates from a broad variety of IN classes. Furthermore, while Kosaka & Hama suggested that RCs do not receive input from OSNs [95], I found OSN input of low to moderate density in all RCs. OSN synapses onto RCs were smaller in size than those onto MCs and comparable to those onto INs. In compartmentalized glomeruli, RC dendrites were always restricted to a single compartment, which may indicate a more restricted OSN input range for RCs compared to MCs.

2.5.7 INTERACTIONS BETWEEN MITRAL AND RUFFED CELLS

The ultrastructural description and the partial 3D reconstructions of MC and RC dendrites by Kosaka & Hama demonstrated that RC dendrites tightly entwine around MC dendrites, but they did not find evidence for RCs receiving MC input. I found that dendrites of MCs and RCs were often closely apposed with a large contact area, but synapses were rare and small. Dendrites of RCs and MCs were intertwined along defined stretches, sometimes occurring at multiple locations within the dendritic trees of a given RC-MC pair. A given RC could interact in such a manner with multiple, but not all MCs of a given glomerulus or glomerular compartment without an obvious preference for any MC subclass.

Kosaka & Hama proposed MCs inhibit RCs via GCs [95]. Indeed, physiological recordings from PNs in goldfish OB suggest MCs inhibit RCs, because (odor-induced) MC suppression correlated with an increase in RC activity [175, 176]. Further evidence substantiating the notion of antagonistic activity between MCs and RCs comes from concomitant whole-cell patch recordings in MCs and Ca^{2+}-imaging, showing Ca^{2+}-traces in connected follower PNs anticorrelated with the MC membrane potential [177]. These follower PNs showed anticorrelated odor responses and paired recordings in these neurons showed that the follower could be inhibited in a unidirectional manner by the MC. This inhibition could not be shut down pharmacologically by blocking AMPA and NMDA receptors, arguing against a di-synaptic inhibitory circuitry, but only with antagonists of metabotropic glutamate receptors (mGLURs) [177]. Separate studies using intracellular recordings and dye labeling suggested that the inhibited follower PNs are indeed RCs (Rainer Friedrich, unpublished observation). More recently, the metabotropic glutamate receptor mGluR6, which mediates inhibitory postsynaptic glutamate activity, was found to be expressed in RCs [178]. The tight intertwining of RCs with MCs and their glia-like ensheathing of synapses from MCs to INs are suggestive of and consistent with paracrine volume

transmission as mode of interaction between RCs and MCs [179, 180, 181]. Particularly intriguing is the protrusion of the RC filopodial terminal dendrites into surroundings of MC-IN synapses, since mGluR6 has been reported to be localized exclusively on dendritic tips [182]. Tracking the MC activity through the intense entanglement, RCs could be activated in a paracrine fashion by in the extracellular space. Such a circuitry could serve to expand the dynamic range of odor representations in OB: MCs are spontaneously active at a frequency of around 5-10 Hz [26, 183] and respond to many odors with suppression [26]. MC suppression would result in a gradual release of the inhibition of RCs (see also [175]), which would transmit information contained in inhibitory responses of MCs to higher brain areas. This hypothesis may be tested by experiments combining targeted pharmacological interventions with functional recordings in identified RCs, e.g., paired MC-RC activity recordings using manipulators of the mGLUR6 activity. Given sufficient accuracy and precision of the mGLUR6 for RCs, expression of Ca2+ indicators under its promoter should allow to directly investigate RC response properties across larger range of odors through calcium imaging. The effect of RCs on odor representations in OB could be studied further by direct optogenetic manipulation of RC activity. In addition, another important piece of information necessary for the identification of RC function is their projection target which could be identified using transgenic lines.

In mammals separate IN circuits formed by MCs and TCs have been proposed for INs across different layers of OB: In GL, differential inhibition of MCs and TCs by periglomerular cells (PGCs) causes differences in concentration sensitivity and odor response latency between the two PNs, exerting stronger impact onto MCs [184]. Conversely, tuning, magnitude, and temporal dynamics of odor responses in TCs appear to be more strongly modulated by EPL-INs than in MCs [185]. Parallel pathways to distinct subclasses of GCs and EPL-INs have been proposed based on the distribution of secondary dendrites [64, 65] and synapses [186] of MCs and TCs in EPL. My examination provides preliminary evidence for separate IN subnetworks in the connectivity of MCs and RCs with superficial INs: The GLIN1s and PLIN1s strongly connected to RCs but did not make any or only exceptional connections with MCs. Conversely, the GLIN2s, GLIN3s and the PLIN2s were strongly connected to MCs, but not RCs. Remarkably, each PN type gave unreciprocated input to one IN type (RC ↦ GLIN1, MC ↦ GLIN2), which in turn did not make output synapses within the glomerular volume. The other classes of superficial INs, which were differentially innervated by MCs and RCs, made reciprocal connections with the respective PNs (RC ↦ PLIN1, MC ↦ GLIN3 & PLIN2). In contrast, MCs and RCs were found to connect to the same DLINs (see e.g., fig. 19A.2). Thus, the connectivity to the more deeply positioned PLINs and DLINs appeared to be more similar between the two PN types, thus potentially linking the two PN-IN subnetworks.

The presence of RCs in each glomerulus suggests they play an integral role in olfactory processing of teleosts. In mammals, the two different PNs differ in projection target [66], odor response [163] and possibly form separate local circuits [184]. Antagonistic responses of MC-TC pairs in mammals, as observed for MC-RC pairs in zebrafish, have not been reported. While no final conclusion can be drawn, it is very well possible that there is no equivalent to the teleostean RCs in mammalian OB.

2.5.8 INTERNEURONS OF ADULT ZEBRAFISH OB

Early investigations into the architectural organization of teleost OB in goldfish report the presence of short axon cells and granules cells in the internal layers [80] and the existence of a perinest (PNC) and a mixed-synapse cell (MSC) in GL [87, 153]. Notably, in these early EM studies all INs connected through reciprocal synapses with PNs were collectively considered as one cell type corresponding to the mammalian PGCs and GCs [85, 87]. Since then, anatomical and functional data gave rise to a multitude of IN classes and subclasses in the different layers of the mammalian OB (reviewed in [51, 63, 59, 62]). However, a systematic picture of IN classes and their function in mammalian systems is still lacking [59] and evidence for more fine-grained distinctions continues to surface [53, 68]. While extensive research of IN diversity in teleost OB is lacking, immunohistochemical and functional studies in zebrafish suggests homologies across the different taxa (e.g., [83, 20]). The present study is likely to represent the most comprehensive description of morphological classes of INs in the OB of a vertebrate species and is expected to be a useful resource for comparative studies.

Because the postsynaptic density was not distinctly stained, asymmetrical and symmetrical appearance of synapses could not be used to distinguish excitatory and inhibitory synapses [187]. However, previous EM studies in the teleost OB report reciprocal synapses of MCs and RCs always as a combination of an asymmetrical and a symmetrical synapse, (e.g., [80, 117, 85, 88]). In the mammalian OB only one class of INs, the ETCs, is considered glutamatergic, whereas all others are GABAergic, but may co-release dopamine (DA) (reviewed in [63, 62, 59]). Therefore, I assume all IN classes, which make reciprocal synapses with PNs, to be GABAergic, potentially co-releasing DA [20]. This excludes only the GLIN1s and the GLIN2s. These two classes of INs differed from the others not only through the lack of reciprocal synapses to PNs, but also by the existence of an axon-like output structure, which did make reciprocal synapses with local INs. I do not make any assumptions on their chemotype.
In the following I discuss the IN classes individually or in conjunction, potential functional implications derived from the observed local circuit interactions and where applicable use these observations to reference to described types of INs in mammalian OB.

2.5.9 THE GLIN1S

The GLIN1s constitute a group of neurons that clearly stood out from all other INs by the small, compact dendritic tree, which apparently lacked outbound chemical synapses, by the distinct, locally arborizing axonal process, and by the fact that they did not make reciprocal synapses with PNs. These INs were classified into a small (sGLIN1) and large variant (lGLIN1) based on size as well as position and extent of the dendritic tree. Substantiating the definition of the two subclasses, these morphological characteristics largely correlated with the glomerular and RC interactions observed.

Namely the sGLIN1s immersed their dendrite into the RC ruff, whereas the lGLIN1s dendrite showed tight association with the RC dendrite. However, for 3 of 23 INs, defined as sGLIN1s defined as sGLIN1s based on morphological aspects, no connected RCs could be identified. These cells were located superficially. RC ruffs are generally located deep to the glomerulus innervated by the RC dendrite (see fig. 18), accordingly undiscovered interactions between a ruff and these exceptional sGLIN1s are unlikely. Rather, it is possible that these cells would be best classified as lGLIN1s. A dense neuron reconstruction or a complete description of the connectivity of the two classes is expected to help determine the subclass assignment more confidently in such ambiguous cases.

Kosaka & Hama described a type of IN, which is closely associated to the neuropil region occupied by RC ruffs, which they referred to as nest. They therefore named this IN the perinest cell (PNC) [87]. The PNC matches the features characterizing sGLIN1s very well: One to three PNCs, sometimes in a cluster attached to the RC soma, surrounded the ruff. PNCs were characterized by an arborizing axon and a tufty, spherical dendrites, whose branches were described to "wedge themselves between" RC and GC [87]. PNCs received frequent input from INs, Kosaka & Hama considered GCs, but not from RCs. The latter were found to make infrequent gap junctions onto the PNC dendrite. In light of these similarities, I propose that sGLIN1s are PNCs. I reliably found three to six sGLIN1s surrounding each ruff, thus these small neurons are rather numerous in OB. Kosaka & Hama, who were able to detect postsynaptic densities, did not describe synapses from RCs onto sGLIN1s. In contrast, I identified contacts that I classified as synapses. However, these involved few vesicles with apparent membrane contact sites, and it cannot be excluded that these include false positives. An explanation for the lack of an obvious synaptic density at these locations could be a metabotropic interaction between RC and sGLIN1. Metabotropic glutamate receptors are often expressed extrasynaptically and more diffusely distributed in dendritic shafts [188, 189].

Fewer lGLIN1s were found than sGLINs and it remains to be determined whether representatives of this subclass are present in all glomeruli. The localized, tight dendritic intertwinement between RCs and the lGLIN1s within the glomerulus could be reflective of paracrine transmission between these two cell types. However, given that RC dendrites make at most scarce outbound synapses [95] and that the lGLIN1 dendrites were found to be only postsynaptic, this seems unlikely. Rather it is more likely that the two cells are electrically connected. Alternatively or additionally, the lGLIN1s could be tracking inputs to the RC via metabotropic reception. Glasauer et al. report expression of *mglur6b* in superficial neurons of OB that lack a ruff structure [178]. Based on position and morphology, it was proposed these cells were MCs. It may, however, be possible that this subpopulation of *mglur6b* expressing OB neurons contains GLIN1s as well. Notably, I did not observe a tight dendritic intertwinement between lGLIN1s and MCs.

At this stage, the nature of inputs to both subclasses of GLIN1s remains enigmatic. Their interaction with RCs is of particular interest given the intense physical contact, but also because they seem to lack connections to MCs, which may indicate the existence of parallel OB circuits in teleosts. When a larger number of reconstructions becomes available it would be interesting to perform a detailed investigation of connections to local INs shared with the respective associated RCs. Axons of both

subclasses collateralized locally and made outbound and reciprocal synapses with different PLINs and DLINs, as well as with monoglomerular, superficial INs associated to other glomeruli. This suggests that they locally forward RC activity, however, it remains to be determined whether this action is excitatory or inhibitory.

2.5.10 THE GLIN2S

The GLIN2s were the only other IN class that also had an axon and that did not make reciprocal synapses with PNs. GLIN2s are characterized by a widespread, but slender dendrite, which extends through a single glomerulus and bears delicate filiform spine-like appendages. In their review of the organization of teleost OB Kosaka and Hama, 1982, report another type of IN localized in the glomerular area, the mixed-synapse cell (MSC), which receives input from MCs via chemical synapses and additionally connects to MCs via gap junctions [87]. The MSC neurites are described as fine and cylindrical, bearing cup shaped appendages at high frequency. These make interdigitated contacts with MCs and may contain both chemical and electrical contacts. These neurites also receive input from INs, to which they refer to as granule cells, but do not contain any presynaptic sites. The camera lucida drawing of a Golgi staining, which they present, also depicts an axon, which makes some collaterals and bears bulbar varicosities [87]. The coarse geometrical structure of this neuron is consistent with many examples of the more superficially located GLIN2s. I therefore suggest that the MSCs are equivalent to the GLIN2s.

GLIN2s were connected to many sister MCs associated with a given glomerulus through numerous contacts and may thus track the mean MC activity within this glomerulus. The connection through gap junctions could function to synchronize MCs of a glomerulus and maybe distribute or amplify weaker inputs among them. The axons of GLIN2s project outside the glomerular volume, thus forwarding MC activity, and can connect to numerous types of INs. The current study provides only limited insight into the nature of their targets, but I encountered inputs to several GLIN3s of other glomeruli and lDLIN1s. Without knowledge of the sign of GLIN2 outputs possible functions of this circuitry remain highly speculative.

2.5.11 THE GLIN3S & THE PLIN2S

The GLIN3s and the PLIN2s are discussed in conjunction as they shared similarity in morphology and connectivity. Both IN classes were axonless and characterized by a bushy, varicose dendrite innervating mainly a single glomerulus and made broad connections to the MCs therein. GLIN3 dendrites covered larger parts of the glomerular volume than the PLIN2s and made more synapses with individual MCs. Such a circuitry may provide efficient inhibition to the MCs of a glomerulus. This could have several potential functions, e.g., feedback or recurrent inhibition and competitive

suppression of homotypic MCs [28]. Given that synaptic contacts were numerous, but nevertheless variable, it would be interesting to investigate a complete wiring diagram between all GLIN3s/PLIN2s and all MCs of a glomerulus to probe for potential differential connectivity and cohorts of connected neurons. Activated externally, e.g., by neighboring glomeruli or top-down inputs, GLIN3s/PLIN2s could represent a substrate for interglomerular inhibition or odor evoked suppression. Importantly, while PLIN2s have a single, sparsely spiny, dendritic stalk traversing PL, GLIN3s have an elaborate, hairy, proximal dendrite, presumably integrating inputs of a broader spectrum of local and potentially top-down inputs.

With regard to the MC connectivity and the monoglomerular innervation pattern, GLIN3s and PLIN2s resemble mammalian PGCs. The PGCs, especially the calbindin-expressing subgroup, were also described to make reciprocal connections to MCs/TCs [60, 190] and have been shown to provide strong intraglomerular inhibition [58]. PGCs are also known to receive centrifugal input [191]. Functional investigations are required to further assess the role of GLIN3s and PLIN2s for olfactory computations.

2.5.12 THE PLIN1S

Morphologically the PLIN1s shared some similarity with the GLIN3s given their tufty distal dendrites and the somewhat hairy aspect of the proximal parts of the dendrite. Morphological differences were nevertheless apparent, e.g., the pointy tips protruding out of the tuft, the flat aspect of the varicosities, the overall size and the near complete confinement to the PL. Most conspicuous difference was, however, the interaction with RCs: Connections to up to five different RCs innervating different glomeruli were observed. These showed a clear preference for one or two RCs innervated by the bushy distal PLIN1 dendrite. In contrast to GLIN1s, the PLIN1s dendrite did not tightly intertwine with the RC and made reciprocal connections at the ruff. Given the limited number of reconstructed PLIN1s, no statement can be made about the number of PLIN1s innervating a RC or whether all RCs are connected to PLIN1s. Even more obscure was the connection between PLIN1s and MCs. In only two PLIN1s, I found reciprocal and several outbound synapses with MCs. These connections were located on a separate, thin dendrite, remote from the RC connections. One PLIN1, completely represented in the imaged volume, did not make synapses with MCs. The other PLIN1s were contained in the stack presumably to a large extent and did not enter the GL. However, it cannot be excluded that MC connections outside the imaged volume had been cut. Nevertheless, it can be concluded that PLIN1s are more strongly connected to RCs than to MCs.

2.5.13 THE PLIN3S

Based on subtle morphological differences, e.g., the frequency of thin proximal branches or distal varicosities, two subclasses of PLIN3s can be distinguished. The preliminary, qualitative analysis of connectivity to PNs suggests that this grouping is reflected here as well, e.g., the interactions with RCs were much stronger in the rlPLIN3s than in the vPLIN3s. An extended, more quantitative analysis of connectivity between PLIN3s and PNs, but also INs, ideally including a higher number of PLIN3s reconstructions, is required to confirm this observation. Given the subtlety of the morphological differences between rlPLIN3s and vPLIN3s, requiring resolution of fine processes for distinction, it might be challenging to distinguish these cell types in functional studies in the absence of molecular markers.

Neurons of both subclasses are widespread, oligo- or multiglomerular INs, which projected essentially the entire dendrite in GL, encompassing large portions of the imaged volume. Even the sparse neuron reconstruction performed here revealed that each glomerulus was innervated by multiple PLIN3s that broadly innervated MCs. This circuitry could coordinate inhibition across a wide range of glomeruli. Previous studies examined a heterogeneous group of INs that was labeled by transgene expression driven by a dlx4/6 enhancer. A subset of these neurons mediates dense and widespread inhibition of MCs [20]. In combination with an equally dense and widespread electric coupling, these INs were found to support concentration invariance by equalizing the MC output. This is achieved by boosting weak inputs through gap junctions and attenuating strong inputs via chemical synapses. Further, the subset of neurons targeted by the dlx4/6 enhancer differentially modulated the sensitivity of individual MCs to odor stimulation, which was attributed to varying connection strengths between dlx4/6 neurons and MCs [20]. PLIN3s are potentially corresponding to these neurons as they connected to many, but not all MCs within a glomerulus and because the number of synapses per connected pair varied substantially.

About 50% of the neurons targeted by the dlx4/6 promoter co-expressed tyrosine hydroxylase, a marker for DA neurons in the OB, suggesting that these neurons are homologs of the mammalian sSACs [20]. Consistent with this hypothesis, PLIN3s share morphological similarity with mammalian sSACs with regard to their multiglomerular innervation pattern [55]; however, they do not have an extensive axon as described for some sSACs [61].

2.5.14 THE PLIN4S

The PLIN4s set themselves apart from other INs by their fine, delicate, wide-spread dendrites. Within the group, PLIN4s were relatively heterogeneous regarding their topology and geometry, but also with respect to aspect and distribution of spine-like appendages and varicosities. Additional reconstructions of PLIN4s could reveal the presence of subclasses in this morphological class.

PLIN4s projected to fewer glomeruli than PLIN3s, but this number is likely underestimated here,

because most PLIN4s extended radially through the PL and were cut at the stack boundaries before presumably reaching remote glomeruli. It appears that PLIN4s have the potential to link activity across large spatial scales of the OB. Both broad and selective innervation of MCs was observed. Most connections were reciprocal and mediated by few synapses, however, the fraction of reciprocally connected MC-PLIN4 pairs was lower than for most other IN classes. Reminiscent through morphological similarity, the mammalian, axonless EPL-INs extend their wide-ranging dendrites laterally through EPL. EPL-INs make dense, reciprocal connections with multiple MCs/TCs from a large range of locations in the OB [68, 69], and these connections showed little plasticity during associative odor learning [192]. These neurons are broadly tuned and mediate divisive gain control [70].

PLIN4s also exhibited a pronounced connectivity to RCs, they gave input to the dendrite and made reciprocal synapses at the ruff. With that, the PLIN4s may present the most superficial INs, at which in- and outputs of both MCs and RCs converge. Altogether the preliminary examination of connectivity to PNs yields a rather diverse picture and it is difficult to make predictions about functional roles of these neurons.

2.5.15 THE DLINS

The DLINs were subdivided into three separate morphological classes. This classification has been based on several subtle but correlated morphological features. A striking feature turned out to be the appearance of the proximal dendritic spines. Conventionally, spines are classified based on the shape of spine head and neck into mushroom, filopodial, stubby or branched spines. The appearance of spines described here rather refers to an aspect that governed all spines within a certain DLIN class, independent of the conventional class a given spine belonged to. Namely spines of DLIN1s exhibited a rounded, chamfered aspect independent of their shape. DLIN2 spines had a frayed and tattered appearance, whereas those of the DLIN3s were elongated and hairy. These differences in spine morphology were reliable morphological markers of DLIN types as they had been noted independently by different human experts. While spine frequency is commonly used to characterize neurons, spine aspect has, to my knowledge, not yet been used to classify neurons. Given that the differences in spine appearance observed here were subtle, it is likely that most image datasets do not provide sufficiently high resolution for systematic assessments of spine shape. Dendritic spines are highly dynamic [193] and their morphology has been linked to functional characteristics [194, 195] and to the maturity of synaptic connections [196, 197]. However, it remains unclear how the observed differences in spine morphology may translate into functional differences between DLIN types.

Alternative schemes to classify DLINs morphologically are possible, for example based on the depth of the soma, which appeared to correlate with overall cell size and by trend, the number of connected glomeruli. However, systematic differences in dendritic spine appearance remain undeniable. They correlated with other morphological features and were used for subgrouping DLINs by experienced

neuroscientists in the human classification control as well (personal communication with human classifiers, data not shown).

Because of parallels to mammals, e.g., the large cell numbers in the central, deep OB layers [38] and their late developmental emergence [198], the INs of the central, deep layer in teleost OB are usually referred to as GCs (e.g. [87, 81, 91]). This was intentionally avoided here. The mammalian GCL contains multiple different types of GCs (e.g. [159, 64, 63]) and deep SACs (dSACs) [71, 73]. Currently, homologies or analogies between these IN classes and the DLINs in the zebrafish OB cannot be established with certainty.

The zebrafish DLINs shared several morphological characteristics with mammalian GCs. Pioneering anatomical studies in mammals [74, 75] report that GCs make multiple, fine, proximal dendrites, which arise from soma or the superficially directed, main dendrite. These proximal dendrites remain in the deep layer and bear spines reducing in frequency with distance to soma [74]. This description fits the appearance of proximal dendrites in DLIN1s, especially the deeply located DLIN1s, the sDLIN2s and also in the vast majority of DLIN3s. The deep, proximal dendrites of mammalian GCs are reported to make regular, varicose swellings of the dendritic shaft, often associated with a spine [74], a phenomenon also found in the proximal portions of DLIN2 dendrites. As observed in the most DLINs, proximal dendrites of mammalian GCs receive synapses onto spines and shafts, and spines are described as only postsynaptic [74, 75].

In their proximal portion dendrites of DLINs and mammalian GCs are studded with spines which gradually reduce in frequency with distance to soma. While mammalian GCs typically have one primary dendrite that terminates in the EPL, DLINs often gave rise to more than one large dendrite, which could reach the glomerular layer at multiple distant locations. Branching of the large DLIN dendrites on the course to GL resulted in a wide-spread dendritic field, which encompassed multiple glomeruli. In particular, cDLIN2s exhibited a rather radial structure. Within the glomerular neuropil DLINs made few side branches. Mammalian GCs possess a localized apical dendrite and viral tracings found inputs to be organized in a columnar fashion, consistent with the notion of the glomerular column [199, 92, 69]. Nevertheless, GCs are more broadly tuned than MCs and are presumed to connect with PNs from multiple glomeruli [200], first due of the anatomical organization of the long-range, secondary MC/TC dendrites in EPL, second through direct, proximal input from MC onto axon collaterals in GCL [64, 65].

Notable morphological differences between GCs and DLINs exist at the level interaction with PNs: In mammalian GCs the majority of reciprocal synapses to PNs are located in so called gemmules, appendages similar to spines, but usually larger, and only rarely in dendritic varicosities [74, 75, 201]. These specialized compartments are considered the basis for localized, action potential independent recurrent inhibition of MCs [201, 202]. GABA release from the GC synapse requires substantial Ca^{2+} influx mediated by NMDA receptors and high-voltage-gated-Ca^{2+} channels into the gemmule [202, 203, 204]. Previous models proposed that gemmules electrically isolate the PN-GC interaction to coordinate lateral inhibition selectively between co-active PNs [205, 203]. However, electron

microscopically studies show a substantial portion of gemmules possessed a wide neck [75, 159, 201], suggesting low neck resistance, which is inconsistent with efficient electrical compartmentalization [206]. An alternative hypothesis proposes gemmules could rather serve as chemical compartments to confine second messengers like Ca^{2+} and thereby restrict reciprocal inhibition to single synapses with the co-active MC [206, 207]. In contrast to the gemmules formed by mammalian GCs, the DLINs of zebrafish did not connect to PNs via distinct spine-like appendages. Rather, the distal dendrite formed flattened, glial sheath-like expansions or bulky varicosities that envelop the MC dendrite. The diameter of distal dendrites of DLINs (< 500 nm, see section 2.4.4 → IV. INTERNEURONS OF THE DEEP LAYER) is similar to the diameter of mammalian gemmule necks [201]. Therefore, it is possible that gemmules might not be necessary to achieve compartmentalization of second messenger signaling in DLIN dendrites.

Despite much attention the role of GCs in olfactory computations remains enigmatic. The extent of their contribution to decorrelation of odor representations and lateral inhibition is controversial [69, 70, 59], particularly in light of their low inhibitory drive onto PNs in vivo [208]. Yet, GC activity has been shown to impact performance in olfactory memory tasks [78, 209] and is considered to be strongly modulated by centrifugal input [210]. Viral tracings and paired recordings suggest that connectivity rates between PNs and GCs are low [69, 70], but a comprehensive picture of the connectivity between these cell classes is still missing. A preliminary analysis of the connectivity between DLINs and MCs reveals a very individualized innervation of MCs by DLINs. Most DLINs selectively innervated MCs of a given glomerulus and the majority of connections were mediated by few (1-2) synapses. These synapses could be very large, possibly involving several active zones (see fig. 42), which suggests that despite the low number of contact sites DLIN inputs should significantly impact the MC at least locally on the dendrite. The dataset at hand provides the opportunity to gain detailed insight into the nature of connections between MCs and DLINs. In this context, it would be of particular interest to determine communalities and differences in DLIN partners for MCs of a given glomerulus. In contrast to DLINs, more superficial INs are by trend broadly connected to MCs, making many synapses per pair. Comparing PN connectivity patterns between superficial and deep INs across different glomeruli could further elucidate their potentially differential function in odor processing.

Mammalian GCs and DLINs show some obvious dissimilarities with respect to their embedding in the local OB circuitry: First, whereas GCs do not extend to GL, with exception to the cDLIN2, weak to moderate OSN input could be observed to representatives of all DLIN subclasses. Second, though a systematic investigation of the DLIN connectivity to other INs has not been conducted, many presynaptic neurites giving input to the proximal dendrites of various superficial INs, could be traced back to identifiable DLINs. Furthermore, I observed several synapses between DLINs of the same and different classes, both in the deep layers as somato-dendritic synapses as well as dendro-dendritic synapses in GL. This suggests that DLINs are strongly embedded in the local IN network. Whereas gap junction coupling between mammalian GCs of the same cluster has been reported [211], information on input from GCs onto other bulbar INs is lacking [92, 63, 72, 212] and it has been proposed that the

reciprocal synapses to MC are the only efferent synapses of mammalian GCs [74]. The deep SACs (dSACs), on the other hand, are considered to provide input selectively to INs of the mammalian OB [71], and being primary target of top-down projections, to relay centrifugal input [71, 72]. Morphologically, these axon-bearing cells differ substantially from DLINs. Dendrites of dSACs spread widely but are entirely confined to the inner OB layers, i.e., MCL, ICL and GCL. Subtypes of dSACs have been defined based on the layer their wide-spreading axon targets [71]. In zebrafish OB individual subclasses of DLINs differed in the layer depth, in which they started making outbound synapses: output of DLIN1s appeared to be restricted to GL, DLIN2s made many outbound synapses already in PL, whereas in DLIN3s at least a few outbound synapses were located on dendritic spines in the deep layer. In summary, different functions mediated by dSACs and GCs in mammals might be realized in the DLINs in combined fashion. Comparative immunohistochemical or transcriptomic approaches, using selective markers, as well as a more detailed analysis of the DLIN connectome and identification of centrifugal input, is expected provide further insight into homologies or analogies between DLINs and IN types of the mammalian GCL.

2.5.16 COMPARISON TO MAMMALIAN OB

With the peripheral glomeruli and the densely populated, central GCL, separated by a neuropil rich PL, mammalian and teleost OB share coarse similarities in architectural organization. However, teleost OB is much smaller, and the layering is less stringent. Nevertheless, the findings of this study demonstrate that many organizational principles are preserved at higher level of detail as well. As such, despite the diffuse OSN innervation of the lateral portions of zebrafish OB [161, 46, 86], discrete glomerular units are formed by the postsynaptic OB network. The extensive spread of secondary dendrites in mammalian MCs and TCs within EPL is thought to enable lateral interactions between GCs and PNs from a wide range of glomeruli [159, 203]. In zebrafish, MCs lack secondary dendrites and the reciprocal contacts between PNs and DLINs are intermingled with OSN inputs and other inputs and restricted to the glomerular volume, implying that lateral interactions between a DLIN and different MCs of distant glomeruli are precluded. My findings demonstrate that DLINs make contacts with MCs from numerous glomeruli (see e.g., fig. 48) and make projections across far-reaching areas of OB, suggesting principles of lateral connectivity are preserved. Further, similar to mammalian OB, zebrafish OB contains a rich diversity of IN classes within all layers. These INs show a tighter association to individual glomeruli in the superficial layers compared to the inner layers, where multiglomerular INs prevail. A striking feature of both mammalian and teleost olfactory systems is the prevalence of reciprocal synaptic connection and the widespread occurrence of dendro-dendritic synapses [59].

In mammalian OB, neither a morphological counterpart to the teleostean RC nor a functional equivalent of the proposed sign inversion of MC activity have been described so far. Conversely, this study could not identify any equivalent to the mammalian ETCs, which relay OSN input thereby

exerting excitatory drive onto PNs and INs. Therefore, such a cell type may be absent in zebrafish (see 2.5.5 DIVERSITY OF MITRAL CELLS). In zebrafish OB the majority of INs made dendro-dendritic synapses and while they seemed to maintain some form of separation with regard to inputs and outputs, namely mainly postsynaptic deep and proximal dendrites vs. pre- and postsynaptic distal dendrites, this separation was gradual and vague. Only two classes of superficial IN made axons. In contrast, in mammalian OB, more IN classes have been reported to contain axon-bearing subpopulations, namely ETCs, PGCs, sSACs, internal SACs and dSACs.
To determine to what extent the equivalent challenges in transforming and relaying olfactory sensory information have been solved through similar or different circuit implementation, requires a more detailed reconstruction of the circuity in the two taxa and a link to functional data.

2.5.17 FUTURE DIRECTIONS

COVERAGE NEURON DIVERSITY OF ZEBRAFISH OB

Despite the large number of neuron reconstructions in this study, it is conceivable that the morphological classes described here does not reflect the diversity of neurons in zebrafish OB in its entirety. Rare neuron types could have been missed and the unclassified IN (see section 2.4.4. → V. UNCLASSIFIED NEURONS) could reflect such an instance.
Additional neuron reconstructions could improve the definition and delineation of neuron classes and subclasses, especially in groups of small sample size, and lead to a more accurate account of relative neuron numbers per class. This could support, for example, a better distinction of the lGLIN1s from the sGLIN1s. It could help determine for both lGLIN1s as well as the PLIN2s whether these INs are present in all glomeruli, which would indicate an integral role of these neurons in the glomerular column of zebrafish. Moreover, some IN classes like the PLIN4s or the DLINs are more heterogeneous and might not be sufficiently well captured by the set of reconstructed neurons. Here, extending the number of reconstructions could uncover the existence of additional subclasses.

Targeted interrogation of the functional role of a particular IN type in the computations performed in OB requires the identification of selective transcriptomic markers. The lack of such targets has impeded functional dissection of mammalian OB circuitry [59]. Assuming morphological characteristics of the IN classes described here can be captured at light microscopical resolution, the inspection of fish lines expressing different transgenes in bulbar INs could reveal markers selective for a specific morphological class. Especially many of the GLIN and PLIN classes reported in this study exhibit a rather distinct morphotype, which is likely identifiable through three-dimensional light microscopy imaging even without ultrastructural resolution. An obvious first step in that direction could be an examination of the dlx4/6 neurons, which has been demonstrated to mediate concentration invariance [20], and screen for overlap to morphotypes of the INs described here. With this it could be possible to determine whether PLIN3s contribute to the effects mediated by dlx4/6

neurons.
Alternatively, whole cell recordings targeting e.g., GABAergic OB neurons with consecutive filling and reconstruction would allow to map morphological characteristics on physiological properties. Though laborious, ideally, patch sequencing experiments could provide means to define neuron classes based on morphology, physiology and molecular expression [213, 214, 215] and could help to identify genetic targets to selectively probe the function of neuron types, when embedded into the circuitry. Combined immunohistochemistry and SBEM approaches [216] or other correlative light and EM approaches [217] may be best suited to appraise distinctness in the expression of selected markers between INs, which differ in ultrastructural features.

FROM STRUCTURE TO FUNCTION…

Whereas the interactions between individual IN classes and PNs described provide first indications supporting the idea that these classes reflect functional neuron types as well, the functional relevance of the morphological classification remains to be established.

A different approach to assess the concreteness of neuron classes, obvious for the dataset at hand, is to extend the morphological characterization by a description of the synaptome, i.e., the distribution of in- and outbound synapses, concomitant, for example, with the identification of the partner neuron type or the classification of synapse types [218]. The connectivity information derived from this analysis can itself serve to define neuron types [219]. With this information the purely morphological classification of neuron types can be revisited, fine-tuned, diversified, or corrected accordingly.

Incorporating knowledge about circuit computation with the connectome may allow predictions of potential functional roles of a particular neuron type and to verify or constrain network configurations for modelling studies [220, 221, 222, 223]. The analysis of network motifs is a well-established method for characterizing circuits. Adopted to early olfactory processing, this analysis revealed that contrast enhancement and decorrelation depended on input patterns in larval OB depends on reciprocal connectivity between similarly tuned MCs [28]. In adult OB the landscape of IN types is highly different. Assuming glomerular association is a proxy for MC tuning, a similar analysis utilized for the dataset at hand would allow to determine, whether equivalent network properties can be identified in the adult zebrafish OB, and whether these properties differentially involve classes of INs described here.

3. OLFACTORY BEHAVIOR IN ZEBRAFISH

“Danio rerio”, Ulrich Mönig, 2022

3.1 INTRODUCTION

If the main task of the brain is to adapt an organism's capabilities to optimally interact with its environment, understanding the function of a particular neural circuit (element) requires ultimately to probe its impact on behavior. Pioneered as a vertebrate model organism in the 1970s for developmental and genetic research [224, 225], the zebrafish is a widely used vertebrate model organism and particularly for the larval fish and increasingly the adult many well-established behavioral essays have been developed [226, 227, 228, 229, 230, 231, 232]. In the olfactory system of zebrafish neuroanatomical studies, functional imaging and electrophysiological experiments have uncovered brain regions and computational mechanisms that are expected to support the formation of odor percepts and olfactory memory, e.g., [233, 35, 19, 170, 20]. However, confirmation of their relevance for olfactory perception on a behavioral level is missing due to the lack of easily reproducible, scalable experimental protocols to explore olfactory behavior.

To lay some groundwork for such studies, we developed an appetitive, associative odor discrimination task for adult zebrafish. In this behavioral experiment both training procedure and analysis are largely automated and return a measure of performance for individual fish. Using this paradigm, we demonstrated that adult zebrafish quickly learn reward association and discrimination of odors and can overcome innate preferences through training. This study has been published [11].

3.2 PUBLICATION: RAPID OLFACTORY DISCRIMINATION LEARNING IN ADULT ZEBRAFISH

The following section comprises the peer-reviewed publication:

I. NAMEKAWA*, N. R. MOENIG* AND R. W. FRIEDRICH, "Rapid olfactory discrimination learning in adult zebrafish," *Experimental Brain Research,* vol. 236, p. 2959–2969, 2018.

* equal contribution

Experimental Brain Research (2018) 236:2959–2969
https://doi.org/10.1007/s00221-018-5352-x

RESEARCH ARTICLE

Rapid olfactory discrimination learning in adult zebrafish

Iori Namekawa[1] · **Nila R. Moenig**[1,2] · **Rainer W. Friedrich**[1,2]

Received: 4 May 2018 / Accepted: 2 August 2018 / Published online: 7 August 2018

Abstract
The zebrafish is a model organism to study olfactory information processing, but efficient behavioral procedures to analyze olfactory discrimination and memory are lacking. We devised an automated odor discrimination task for adult zebrafish based on olfactory conditioning of feeding behavior. Presentation of a conditioned odor (CS+), but not a neutral odor (CS−) was followed by food delivery at a specific location. Fish developed differential behavioral responses to CS+ and CS− within a few trials. The behavioral response to the CS+ was complex and included components reminiscent of food search such as increased swimming speed and water surface sampling. Appetitive behavior was therefore quantified by a composite score that combined measurements of multiple behavioral parameters. Robust discrimination behavior was observed in different strains, even when odors were chemically similar, and learned preferences could overcome innate odor preferences. These results confirm that zebrafish can rapidly learn to make fine odor discriminations. The procedure is efficient and provides novel opportunities to dissect the neural mechanisms underlying olfactory discrimination and memory.

Keywords Zebrafish · Olfaction · Behavior · Discrimination · Learning

Introduction

The zebrafish is an important vertebrate model to study neuronal circuit structure and function (Sumbre and de Polavieja 2014). Zebrafish larvae are small and relatively transparent, allowing for high-resolution optical measurements of neuronal activity throughout most of the brain. Even in juvenile and adult fish, activity patterns throughout major brain areas can be measured and manipulated by optical methods (Aoki et al. 2013; Fajardo et al. 2013; Jetti et al. 2014; Portugues et al. 2013; Rupprecht et al. 2016; Zhu et al. 2012). The small size of the zebrafish brain is also advantageous for dense reconstructions of neuronal connectivity (Friedrich et al. 2013; Wanner et al. 2016) and for genetic or chemical screens (MacRae and Peterson 2015). Zebrafish thus provide unique opportunities for quantitative analyses of brain function in wild-type animals and in genetic disease models.

To understand the neural basis of behavior, it is important to quantify behaviors of interest. At embryonic and early larval stages, zebrafish show primarily reflex-like sensory-motor behaviors with a limited potential for plasticity. Social behaviors and an increasing potential for associative learning emerge at later larval and juvenile stages (Buske and Gerlai 2011; Dreosti et al. 2015; Valente et al. 2012). Adult zebrafish and other teleosts show complex innate and cognitive behaviors (Abril-de-Abreu et al. 2015; Arganda et al. 2012; Brown et al. 2006; Buske and Gerlai 2011; Chou et al. 2016; Kalueff et al. 2013; Saverino and Gerlai 2008; Yabuki et al. 2016) including place preference and associative learning in different sensory modalities (Agetsuma et al. 2010; Aoki et al. 2013; Braubach et al. 2009; Darland and Dowling 2001; Doyle et al. 2017; Eddins et al. 2009; Lau et al. 2006; Mueller and Neuhauss 2012; Sison and Gerlai 2010; Xu et al. 2007). While various quantitative procedures have been established to analyze sensory–motor behaviors of zebrafish larvae, there is an increasing demand for methods to study complex behaviors and learning in juvenile or adult zebrafish.

Adult zebrafish have been used to study principles of information processing in olfaction (Friedrich 2013).

Iori Namekawa and Nila R. Moenig contributed equally to this work.

✉ Rainer W. Friedrich
Rainer.Friedrich@fmi.ch

[1] Friedrich Miescher Institute for Biomedical Research, Maulbeerstrasse 66, 4058 Basel, Switzerland

[2] University of Basel, 4003 Basel, Switzerland

Imaging experiments demonstrated that odors evoke scattered but non-random spatial patterns of activity across the olfactory glomeruli, the input channels of the olfactory bulb (Friedrich and Korsching 1997). Neuronal circuits within the olfactory bulb decrease the overlap between activity patterns representing similar odors and stabilize odor representations against variations in stimulus intensity (Friedrich 2013; Friedrich and Laurent 2001; Niessing and Friedrich 2010; Zhu et al. 2013). Hence, processing of odor-evoked activity patterns in the olfactory bulb may support the classification of odor representations in higher brain areas. Further studies provide insights into transformations of spatio-temporal activity patterns between the output neurons of the olfactory bulb, the mitral cells, and telencephalic area Dp, the homolog of olfactory cortex (Blumhagen et al. 2011; Jacobson et al. 2018; Yaksi et al. 2009). To explore the impact of these computations on behavior, quantitative procedures are desired to analyze odor discrimination behavior and associative learning in adult fish. Ideally, such procedures should be automated and simple to implement in a standard fish facility.

Adult zebrafish can learn to associate different sensory stimuli with reward or punishment (Agetsuma et al. 2010; Aoki et al. 2013; Braubach et al. 2009; Darland and Dowling 2001; Doyle et al. 2017; Eddins et al. 2009; Lau et al. 2006; Mueller and Neuhauss 2012; Sison and Gerlai 2010; Xu et al. 2007). Two procedures have been described for olfactory conditioning of appetitive behaviors in adult zebrafish. Based on a procedure developed for catfish (Valentinčič et al. 2000), Valentinčič and colleagues paired the infusion of an odor into a home tank with food delivery 90 s later (Miklavc and Valentinčič 2012). After approximately 30 training trials, the frequency of large-angle turns during the 90 s period after odor onset was significantly higher than the turn rate evoked by non-trained odors. Braubach et al. developed an appetitive olfactory conditioning procedure that follows a similar rationale (Braubach et al. 2009, 2011). The results obtained using these approaches showed that zebrafish can learn olfactory associations and discriminations. However, both approaches require substantial technical resources that are not available in a standard zebrafish facility. Moreover, most experiments did not analyze odor discrimination. We therefore sought to develop a procedure for olfactory discrimination learning that is simple to implement and automate.

To minimize stress, we chose an appetitive rather than an aversive conditioning paradigm. Odor discrimination tasks for rodents often involve unfamiliar behavioral components such as nose pokes or lever presses (Bodyak and Slotnick 1999; Frederick et al. 2009; Kay and Laurent 1999; Rinberg et al. 2006). We avoided such unfamiliar components and conditioned a familiar feeding behavior on an olfactory cue in an environment similar to the home tank. One odor stimulus (CS+) was followed by a food reward while another stimulus (CS−) had no consequence. A closely related strategy has recently been successful in auditory and visual conditioning of adult zebrafish without discrimination training (Doyle et al. 2017). Our behavioral paradigm includes the analysis of multiple behavioral components and resulted in rapid and robust olfactory discrimination learning, thus providing a basis for mechanistic analyses of olfactory processing and associative learning in zebrafish.

Methods

Animals

Zebrafish (Danio rerio) were raised and kept as groups in a standard facility at 26.5–27.5 °C on a 14/10 h light/dark cycle. Fish were 7–10 months old and not selected for sex. Different wild-type strains and transgenic lines were used in separate cohorts. Experiments 1 and 3 were performed using wild-type fish (Abek × WIK). Experiments 2 and 4 were performed using fish that expressed halorhodopsin fused to YFP [eNpHR3.0YFP; (Gradinaru et al. 2010)] in GABAergic neurons. Experiment 5 was performed using a mixture of different wild-type and transgenic fish. All experimental protocols were approved by the Veterinary Department of the Kanton Basel-Stadt (Switzerland).

Experimental setup and odor application

Throughout the experiment, fish were kept individually in tanks that were usually custom-made from flat transparent polystyrole to avoid optical distortions by curved surfaces (typical dimensions: 29 × 9.5 × 7 cm; height of the water column: ca. 6 cm). The tank was divided by a mesh into a front compartment containing the fish (~ 10 × 20 cm) and a rear compartment containing the suction tube for water removal (~ 9 × 10 cm). A feeding ring with a diameter of ~ 4.5 cm was made of silicon tubing and floated in a front corner (Fig. 1a). Food was delivered into the feeding ring from a remote location through a feeding tube. In most experiments, food was pushed down the tube into the feeding ring by a custom device that applied computer-controlled pulses of pressurized air to the food delivery tube. In a subset of experiments, food was manually blown into the feeding ring using a plastic Pasteur pipette. Visual contact between the fish and the experimenter was avoided. Food was either a mixture of Gemma Micro 300 (Skretting) and crushed food flakes (Tetramin, Tetra) or powder food (SDS100). Food was delivered in small portions that were usually consumed within < 30 s.

Tanks were perfused with water from the fish facility using a peristaltic pump at a flow rate of 25 ml/min. The flow

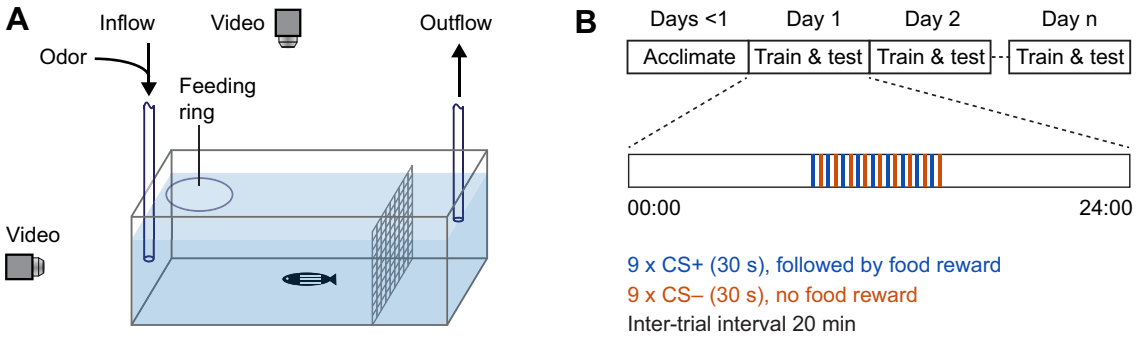

Fig. 1 Experimental setup and protocol. **a** Schematic of experimental setup. **b** Experimental schedule

was constantly on for approximately 7 h on each day during the period when odor and food stimuli were delivered. Outside this time window and during the acclimation period the flow was off. Water entered the tank through an inflow tube (inner diameter, 1.6 mm) in the front approximately at half-height in the water column. Water was removed from the tank by suction through an outflow tube at the rear of the tank and discarded. To minimize fluctuations of the water level, a pipette tip (200 µl) was attached to the tip of suction tube and positioned at the desired height.

Olfactory stimuli were amino acids (Ala, Trp or Cys; Sigma Aldrich, ≥98% purity), which are natural odorants for aquatic animals (Carr 1988). Odors were prepared freshly on each day by diluting a stock solution (6×10^{-3} M) in fish water to a concentration of 6×10^{-5} M. Odors were delivered into the tank by switching the perfusion for 30 s from a reservoir-containing fish water to a reservoir-containing odor solution. Switching was achieved using computer-controlled, motorized valves (WTA-2K-3MFE-3, Takasago Electric, Inc.) and valve controllers (ValveLink8.2® Controller, Automate Scientific). Video analyses using a dye showed that the stimulus distribution during the first 30 s of application was inhomogeneous and discontinuous with highest concentrations near the inflow tube. Subsequently, the stimulus distribution equilibrated throughout the tank. The nominal odor concentration assuming even dilution in the tank was ~4.5×10^{-8} M, which is at or below the detection threshold of adult zebrafish for amino acids (Michel and Lubomudrov 1995; Miklavc and Valentinčič 2012). Hence, stimulus concentration was reduced to levels below threshold by dilution and water exchange (Miklavc and Valentinčič 2012).

Experiments were performed in up to four tanks in parallel, each containing a single fish. Tanks were separated by opaque screens, illuminated from below by infrared light, and filmed simultaneously by two orthogonal cameras (Fig. 1a). Sufficient video quality was achieved using standard web cameras at video rate (30 frames per second). Simple devices such as tennis balls or shock absorbers were used to partially isolate the tabletop from vibrations. The setup was placed inside an opaque enclosure which was lined with sound-absorbing foam in most experiments.

Experimental schedule

Fish remained in the experimental tanks after transfer from the facility for the duration of the experiment. During an initial acclimatization period of 1–3 days, fish received neither food nor odor stimuli. When training started, odors were applied at inter-trial intervals (ITIs) of 20 min. No specific cue was given to signal trial onset. One odor (conditioned stimulus, CS+) was followed by food application (unconditioned stimulus, US) 30 s after stimulus onset while a second odor (CS−) was not followed by food application. Usually, a total of nine CS+ and nine CS− were delivered per day in alternating fashion (Fig. 1b). Hence, training extended over a period of 6 h/day, usually starting at approximately 09:00 h. Fish were trained for a total of 2–9 days. During training, behavior was quantified in each trial during the 30 s period between odor onset and food delivery. Four fish of the same strain and age were usually trained in parallel on the same two odors A and B. Training was balanced such that two fish received odor A as CS+ and B as CS− while assignments were reversed for the other two fish.

Quantitative analysis of behavior

Orthogonal video recordings were analyzed to track the 3D position of each fish as a function of time (Fig. 2a). In each frame, the fish was segmented and represented by a point at the center of gravity. The following behavioral parameters were then extracted from the 3D trajectories: (1) Swimming speed. Instantaneous swimming speed was calculated as the displacement of fish between successive video frames. (2) Relative z-position. This parameter quantifies the relative position in the water column along the z-direction. 0 represents the bottom of the tank; 1 represents the water surface. (3) Residence in the reward zone. This binary parameter is 1 when the fish is located

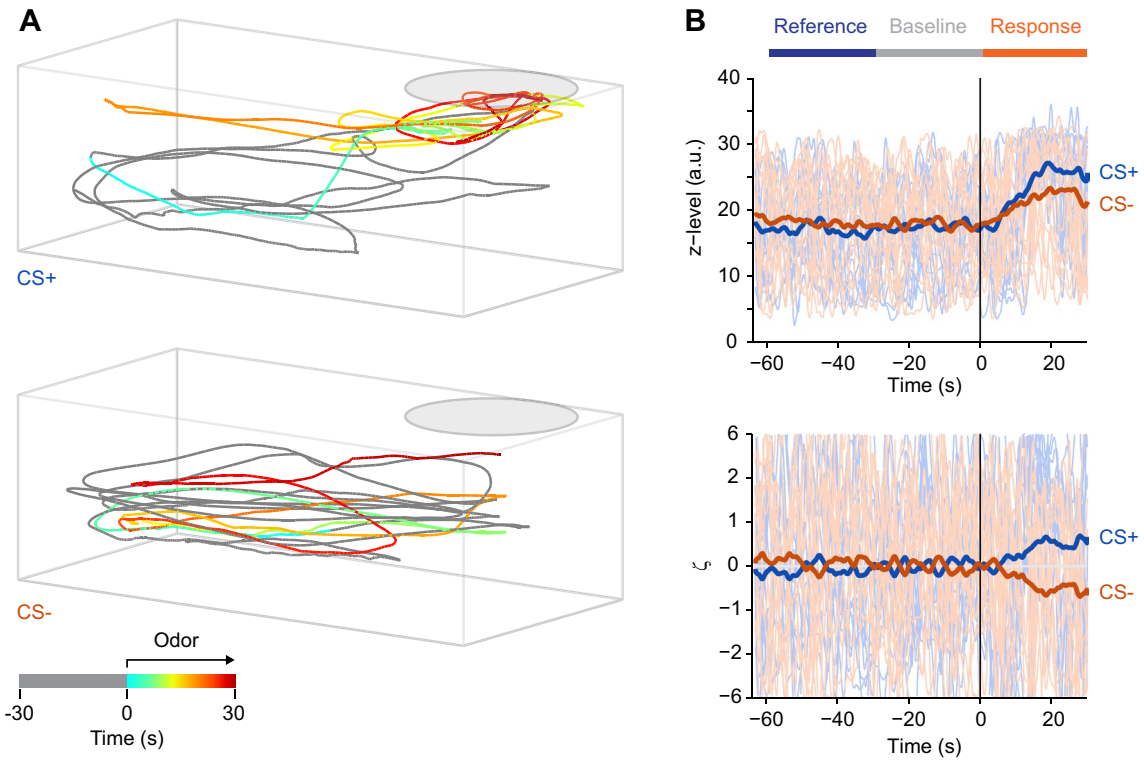

Fig. 2 Analysis of behavior. **a** Examples of swimming trajectories prior to and during presentation of CS+ (top; Trp) and CS− (bottom; Ala) on day 5 of training. Each trajectory is 60 s long, comprising 30 s before and 30 s after odor onset, prior to food delivery. Time is color coded; pre-odor time is gray. **b** Top: time series showing one behavioral variable (z-level) as a function of time for all trials in an experiment; thick lines show averages. Odor was delivered at $t=0$. Bottom: Same time series after transformation to ζ scores. Horizontal bars indicate reference, baseline and response time windows

in the reward zone and 0 otherwise. The reward zone is defined as a rectangular area bounding the feeding ring and spanning the shorter axis of the experiment tank, covering approximately one-third of the tank's footprint. (4) Surface sampling events. A surface sampling event is defined as the crossing of a threshold in the z dimension below the center of the feeding ring. The threshold was set at approximately 70% of the height of the water column. Surface sampling events are usually discrete and occur when fish collect food from the water surface but are rare otherwise. (5) Distance to inflow. This is the 3D distance between the fish and the opening of the inflow tube. (6) Circling. This behavior refers to stereotyped circular swimming along the walls of the tank. We observed that such a swimming pattern is sometimes maintained for extended periods of time when fish are undisturbed but the behavior is interrupted by salient sensory input. To quantify circling, we computed power spectra from measurements of the position along the long axis of the tank using a 30 s Tukey window and quantified the relative power in a low-frequency regime that corresponded to the frequency of circular swimming (0.029–0.146 Hz) in 1-s time bins. Python-based software for automated video analysis is available at https://github.com/i-namekawa/TopSideMonitor. Because the analysis of behavior was fully automated, it was not performed blindly.

Measurements of each behavioral parameter in each video frame yielded one time series of values per parameter and trial. We defined three time windows for analysis: (1) Baseline time window: This window comprised the 30 s prior to odor onset and served as a baseline in each trial. (2) Response time window: This window was defined as the time between odor onset and the time of food delivery in CS + trials or the equivalent time in CS− trials. This time window was usually 30 s long and used to assess behavioral responses to odor stimulation. (3) Reference time window. This time window was defined as a time window immediately prior to the baseline window with a length equal to the response window. This window served to assess trial-to-trial variability of behavior in the absence of stimulation. Note that the response window and the reference window were equidistant in time from the baseline window.

Because spontaneous behavior can fluctuate between trials, we quantified the change in parameter values relative to a baseline in each trial. The baseline was defined as the mean value of a parameter during the baseline time window

and subtracted from the time series. Time series were then averaged over all CS+ and over all CS− trials, and the mean of these averages was subtracted from each individual time series. To quantify trial-to-trial variability in the absence of stimulation, the standard deviation of the time-averaged values during the reference window across trials was calculated. To normalize mean-subtracted time series to this variability measure in each fish, all time series from a given fish were divided by this standard deviation. As a consequence, the family of time series for each behavioral parameter was centered on zero and normalized by a measure of pre-stimulus variability (Fig. 2b). We refer to these transformed time series values as ζ scores because they are closely related to z-scores: positive values represent behavioral responses larger than the mean response to all stimuli, negative values represent behavioral responses smaller than the mean, and the absolute value reflects response magnitude relative to a variability measure. ζ scores differ from z-scores because they are normalized to the variability during a fixed pre-stimulus time window. As a consequence, ζ scores reflect the change in behavior relative to a baseline but they cannot be interpreted quantitatively as a z-score.

To obtain a single measure per trial, ζ scores were time-averaged over the response time window. The sequence of these averaged ζ scores over successive trials is referred to as a trial series of ζ scores.

Results

Olfactory discrimination learning: method and basic observations

We developed an experimental paradigm to establish associations between odors and food. Individual zebrafish were trained in tanks with continuous water perfusion and a feeding ring floating in one corner (Fig. 1a). Fish were acclimated to the training tanks for at least 24 h prior to training and kept in the training tank throughout the experiment. Every 20 min, one of two amino acid odors (CS+, CS−; 6×10^{-5} M) was introduced into the perfusion for 30 s (Fig. 1b) and slowly removed thereafter by dilution and water exchange (Methods). Thirty seconds after the onset of the CS+, a few small food pellets were delivered into the feeding ring while the CS− was not rewarded. Usually, nine trials with each stimulus were alternated on each day. We hypothesized that fish learn to respond to the CS+, but not to the CS−, with anticipatory food search behavior.

Fish were tracked in 3D using two orthogonal video cameras and custom software. In trained fish, swimming trajectories showed obvious differences after delivery of the CS+ or CS− (Fig. 2a). Upon presentation of the CS+, fish often increased their swimming speed and spent more time near the feeding ring, consistent with previous observations in other olfactory conditioning paradigms (Braubach et al. 2009; Miklavc and Valentinčič 2012). In addition, fish often elevated their position in the water column, sampled the water surface as during feeding, and sometimes approached the inflow tube. Stereotyped cyclic swimming along the wall of the experiment tank, which usually occurred during inter-stimulus intervals, was often interrupted. These behavioral changes were less pronounced or absent upon presentation of the CS−.

To quantify these observations, we analyzed parameters of the 3D swimming trajectory that reflect different behavioral components. Analysis tools were developed to automatically quantify (1) the instantaneous swimming speed ("Speed"), (2) the relative height of the fish in the water column ("z-level"), (3) the distance of the fish to the water inflow ("Distance"), (4) the frequency of surface sampling events ("Surface"), (5) the probability that the fish is located in a rectangular area around the feeding ring ("Area"), and (6) the amount of stereotyped, cyclic swimming ("Circling"). For each parameter and trial, time series of measurements were obtained. To transform measurements into values related to z-scores, we defined three time windows, each usually 30 s long: a "baseline time window" immediately before stimulus onset, a "response time window" immediately following the baseline time window, and a "reference time window" immediately preceding the baseline time window (Fig. 2b). Measured values were transformed by (1) subtraction of the mean value during the baseline time window, (2) subtraction of the time series averaged over all trials, and (3) normalization to the inter-trial variability in the reference time window (Methods). This transformation results in a dimensionless measure that is normalized to pre-stimulus variability and centered on the mean at each time point (Fig. 2b). Because this measure is closely related to a z-score, we refer to it as ζ score (Methods). The signs of ζ scores for "Distance" and "Circling" were inverted so that positive (negative) ζ values always reflected responses that were more (less) appetitive than the mean for all parameters. To analyze learning curves over trials, ζ scores were time-averaged during the 30 s between odor onset and food delivery ("response time window") to obtain one value per trial. Medians were then calculated over the trials of each day to obtain one value per day.

Experiment 1: extended discrimination training

We initially trained 12 fish using Ala and Trp as odor stimuli (experiment 1; 9 CS+ trials and 9 CS− trials per day). Fish were trained for a total of nine days (81 trials for each stimulus). Assignments of odors as CS+ or CS− were balanced over fish. ζ scores of all parameters were significantly

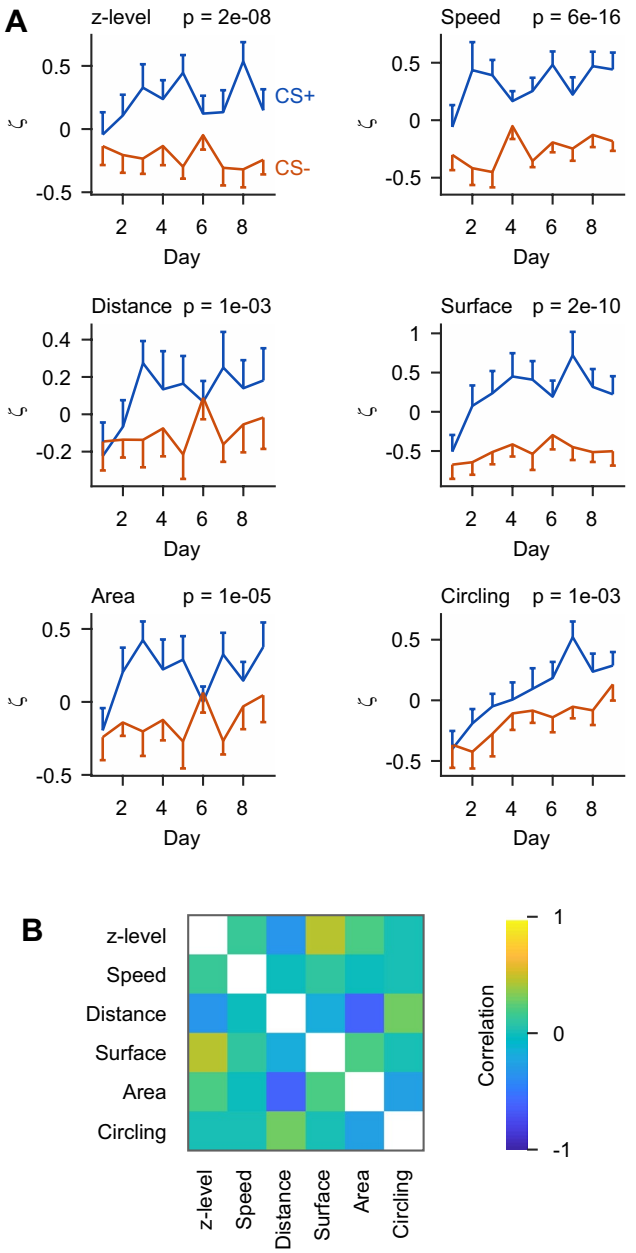

Fig. 3 Analysis of discrimination learning. **a** ζ scores for the six behavioral parameters as a function of time, binned per day (medians) and averaged over fish ($n = 12$ fish). P values show that responses to CS+ and CS− were significantly different (Wilcoxon rank-sum test comparing all individual trials). Assignment of odor stimuli (Ala and Trp) as CS+ and CS− was varied between individuals. **b** Mean correlation between time series of ζ scores for different behavioral parameters ($n = 62$ fish from experiments 1–3). Correlations were calculated on a trial-by-trial basis for each fish and averaged over fish

different between CS+ and CS− trials (Fig. 3a). Hence, fish learned to discriminate between the CS+ and the CS−.

Visual observations of behaving fish further suggested that the contribution of different components to the overall behavioral response varied substantially between trials and individuals. For example, a fish may respond to the CS+ primarily with fast swimming in one trial but with surface sampling in the next trial. Consistent with this observation, trial-by-trial correlations between most parameters were relatively low (Fig. 3b; mean correlation coefficient ± SD: 0.00 ± 0.27). Hence, combining multiple behavioral measurements may improve the detection of learned behavior because different parameters convey non-redundant information. Alternatively, combining measurements may increase noise. To explore these possibilities, we computed a composite measure of behavior, ζ_{comp}, based on Stouffer's method for the combination of z-scores (Stouffer et al. 1949). As in Stouffer's method, ζ_{comp} is the sum over all ζ scores normalized by the square root of the number of ζ scores ($n = 6$). This procedure enhanced, rather than decreased, the statistical significance (Fig. 4a). Hence, the combined analysis of multiple behavioral parameters enhanced the detection of learning-induced changes in behavior, presumably because the conditioned behavior comprises multiple components.

The detection of learned behaviors may be further optimized by taking the covariances between behavioral parameters into account. To test this hypothesis, we weighted each parameter by the ratio of its auto-covariance to the sum of its auto- and cross-covariances (Stouffer et al. 1949). Covariances were determined using all fish in experiments 1–3 ($n = 62$). The resulting combined score $\zeta_{comp,weighted}$ is thus corrected for redundant information in individual parameters. This approach further enhanced the separation of behavioral scores for the CS+ and CS− (Fig. 4b). However, the enhancement was minor, consistent with the modest cross-correlation between behavioral response components (Fig. 3b). The non-weighted ζ_{comp} therefore offers the opportunity to obtain a highly informative combined behavioral score without the need to determine a behavioral covariance matrix, which is labor-intensive. As this approach is likely to be chosen in future applications, further analyses used the non-weighted measure ζ_{comp}.

Odor discrimination at the end of training was quantified by the difference d between ζ_{comp} for the CS+ and CS−, averaged over the last 12 trials. After 9 days of training, d was significantly different from zero ($d = 0.98 \pm 0.28$; mean ± SEM; $n = 12$ fish; $P = 0.005$; Wilcoxon signed rank test), confirming that fish discriminated between the CS+ and CS−.

Behavioral responses to the CS + and CS− deviated already during the first day of training and approached saturation after approximately 3 days (Fig. 4a). Differences between behavioral scores for the CS+ and the CS− were statistically significant already on day 2, and the discrimination score d was statistically significant already when all data after day 2 were omitted ($d = 0.66 \pm 0.26$; mean ± SEM; $n = 12$ fish; $P = 0.03$; Wilcoxon signed rank test). Hence,

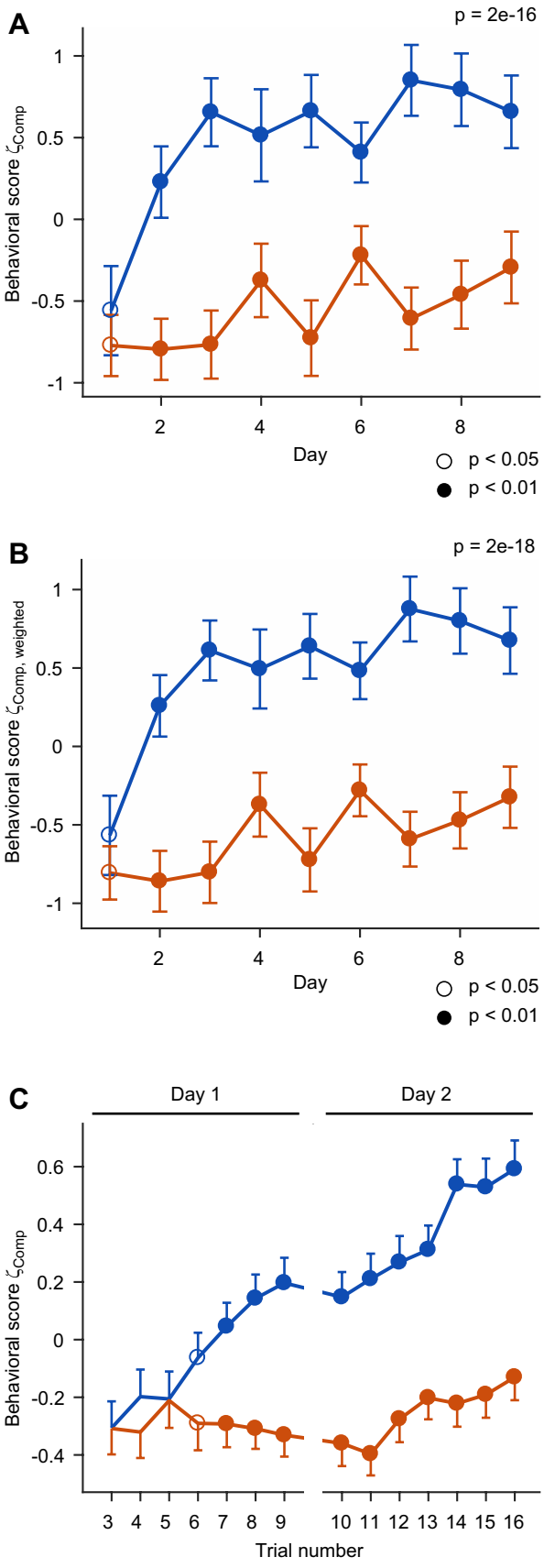

Fig. 4 Discrimination learning curve. **a** Mean composite behavioral scores ζ_{comp} for responses to the CS+ and CS− as a function of training days (experiment 1). Data points for each day show the median of nine trials, averaged over $n = 12$ fish. Error bars show SEM over fish. *P* value: Wilcoxon rank-sum test comparing all individual CS+ and CS− trials, pooled over all days. Circles depict significant differences between behavioral responses to the CS+ and CS− on each day (Wilcoxon rank-sum test comparing all individual trials on a given day). Open circles: $0.01 \le P < 0.05$; filled circles: $P < 0.01$. Assignment of odor stimuli (Ala and Trp) as CS+ and CS− was varied between individuals. **b** Same as above for the combined behavioral score $\zeta_{comp,weighted}$, which weights individual ζ scores by their auto/cross-covariances. **c** Quantification of behavioral responses to the CS+ and CS− in successive trials during the first 2 days of training, averaged over all fish in experiments 1–3 ($n = 62$ fish; mean ± SEM). The first two trials and the last two trials were omitted because individual trial series of ζ scores were median filtered with window size five to minimize the potential impact of outliers. Open and filled circles depict significant differences between behavioral responses to the CS+ and CS− as in **a**. Assignment of odor stimuli (Ala and Trp) as CS+ and CS− was varied between individuals

fish learned to discriminate between odors after few training trials.

Experiments 2 and 3: shorter discrimination training

To corroborate these results, we trained 36 additional fish on the discrimination of Ala and Trp for 27–36 trials (experiment 2). Again, fish showed significantly different behavioral responses to the CS+ and CS− at the end of training, with a discrimination score similar to that observed in experiment 1 ($d = 1.14 \pm 0.17$; mean ± SEM; $n = 36$ fish; $P = 3e{-}7$, Wilcoxon signed rank test; Fig. 5).

In addition, another 14 fish were trained on the discrimination of Ala and Trp for a total of 18 trials each (experiment 3) and showed significant discrimination behavior at the end of training ($d = 0.51 \pm 0.15$; mean ± SEM; $n = 14$ fish; $P = 0.002$, Wilcoxon signed rank test). These results were pooled with the first 18 CS+ and 18 CS− trials from experiments 1 and 2 to obtain a large sample ($n = 62$ fish). The mean discrimination score in this sample was ($d = 0.76 \pm 0.12$; mean ± SEM; $p = 2e{-}7$, Wilcoxon signed rank test; Fig. 5). The large sample size was exploited to analyze the initial phase of the learning curve at single-trial resolution. To minimize the impact of outliers, trial series of ζ_{comp} scores were median-filtered using a window size of five trials. The mean behavioral scores ζ_{comp} of responses to the CS+ and CS− gradually diverged and became statistically different at trial six (median-filtered data from trials 4–8; Fig. 4c). Hence, significant discrimination behavior emerged already during the first day of training.

Behavioral scores in experiments 1–3 were similar although fish were from different strains and included transgenics (see "Methods"). Hence, behavioral results are unlikely to be sensitive to the genetic background. No

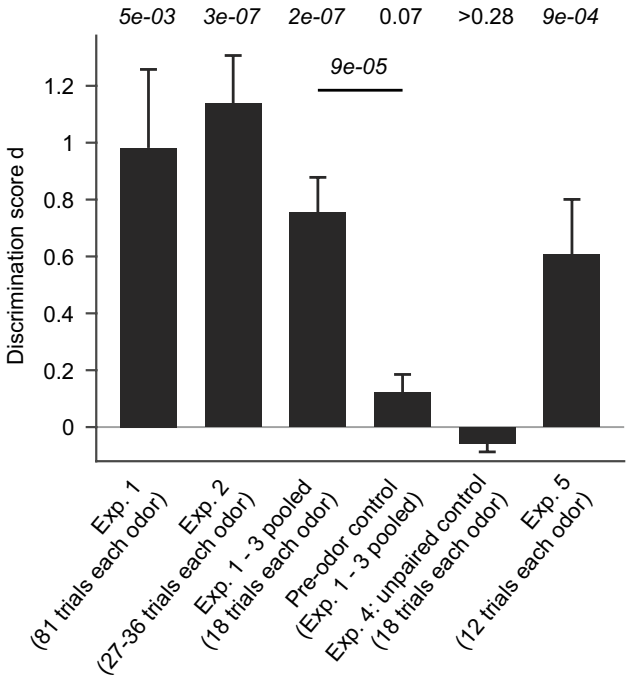

Fig. 5 Quantification of discrimination behavior. Bars show the discrimination score d (mean ± SEM) obtained in different experiments. *P* values are from a Wilcoxon signed rank test comparing the observed discrimination score d against the null hypothesis that $d = 0$. Horizontal line shows statistical comparison between the discrimination score d obtained in pooled experiments 1–3 (first 18 trials only) and the d value of the corresponding pre-odor control (Wilcoxon rank-sum test)

significant differences were observed between males and females in any experimental group.

Experiment 4: unpaired control

Differential responses to the CS+ and CS− in experiments 1 and 2 cannot be explained by innate odor preferences because amino acid stimuli were balanced across fish, implying that the observed behavior reflects associative learning. To confirm this conclusion, we performed two controls. First, we analyzed behavior in the absence of a conditioned stimulus by re-analyzing swimming trajectories from experiments 1–3 using the time window 60–30 s before odor application as the response time window. The baseline and reference time windows were shifted accordingly. The resulting value of d was not significantly different from zero ($d = 0.12 \pm 0.07$; mean ± SEM; $n = 62$ fish; $P = 0.07$, Wilcoxon signed rank test) and significantly different from the discrimination score of stimulus-induced behavior in the same fish ($P = 9e{-}5$; Fig. 5). Hence, the observed discrimination behavior cannot be explained by a bias in the training or analysis procedure.

Second, we exposed an additional 16 fish to 18 presentations of Ala and 18 presentations of Trp as before (9 trials each per day; 2 days total). However, food was delivered 15 min after application of both odors with a probability of 50%. Hence, fish were exposed to the same number of odor stimuli and food deliveries as before but odors did not predict food. We then randomly assigned Ala or Trp as CS+ and CS− in different fish in a balanced fashion and analyzed behavioral responses as before. The procedure was repeated 10 times for different random stimulus assignments. No significant discrimination score was obtained in any of these assignments ($P > 0.28$ in all cases; mean ± SD: $P = 0.64 \pm 0.22$; range 0.28–0.87) and the discrimination score remained close to zero ($d = -0.06 \pm 0.10$; mean ± SD; Fig. 5). These results support the conclusion that the differential behavioral responses in experiments 1–3 reflect associative learning.

Experiment 5: conditioning can overcome innate preferences

We further examined whether the learned association between an odor stimulus and a food reward can overcome innate odor responses. A previous study reported that naïve zebrafish are attracted to Ala but repelled by Cys (Vitebsky et al. 2005). We tested whether the aversive response to Cys can be overcome when zebrafish are trained in the odor discrimination paradigm with Cys as CS+ and Ala as CS− (6 fish) or the opposite assignment (8 fish). Each fish received only 12 trials with each stimulus, distributed over 3–5 days. Nevertheless, training resulted in the emergence of positive behavioral responses to Cys and odor discrimination was statistically significant ($d = 0.61$; $n = 14$ fish; $P = 9e{-}4$; Fig. 5). Hence, associative appetitive conditioning can also be performed using aversive odors.

Discussion

We developed efficient methods to analyze olfactory discrimination learning in adult zebrafish. Fish learned to respond selectively to one of two odor stimuli with anticipatory appetitive behavior. Training and analysis procedures are automated and can be performed in a standard laboratory environment. This paradigm is well-suited to analyze odor discrimination behavior and the underlying neuronal mechanisms in zebrafish.

Odor discrimination paradigm

Olfactory conditioning resulted in complex modifications of behavioral responses to odors. Learned responses to the CS+ included an increase in swimming velocity, an

approach of the reward zone, and sampling of the water surface, reminiscent of the behavior that fish display in their home tanks when caretakers approach for feeding. Hence, fish appeared to learn the association between an olfactory cue and a familiar set of feeding-related behaviors. We therefore assume that our training procedure resulted primarily in classical conditioning.

Previous procedures for olfactory conditioning of adult zebrafish are difficult to implement in a standard laboratory setting because they require enormous amounts of water (Braubach et al. 2009) or very large tanks (Miklavc and Valentinčič 2012). Moreover, training and analysis were time-consuming because procedures are not automated. Importantly, previous procedures did not involve differential conditioning to two odors (CS+ and CS−), with few exceptions (Miklavc and Valentinčič 2012). We therefore developed a procedure that is fully automated, requires only standard resources, and includes discrimination training. We expect that this procedure will be valuable to analyze the neural basis of discrimination learning.

A recent study by Doyle and colleagues described automated procedures for auditory and visual conditioning of adult zebrafish that also rely on the conditioning of feeding behavior (Doyle et al. 2017). The tasks follow a similar rationale as ours but exhibit differences in experimental procedures. First, we did not maintain fish in the fish facility during training, mainly to facilitate odor application and to avoid contamination of the circulating water with odors. Second, we trained fish individually rather than in groups. Training one fish per tank decreases throughput but facilitates quantitative analyses of multiple behavioral components and enables comparisons between individuals. Third, we trained fish to discriminate between two sensory cues (CS+ and CS−), rather than to associate a single cue with a behavioral output, because differential conditioning is desired to analyze the neural basis of sensory discrimination. Despite the differences in task design and sensory modalities, fish rapidly learned associations between the CS and US in both studies (Doyle et al. 2017). An appetitive paradigm for operant visual discrimination learning, in contrast, required more extensive training (Mueller and Neuhauss 2012), possibly because fish needed to learn a novel behavioral sequence to collect rewards. Hence, classical conditioning of feeding behavior appears to be an effective strategy for the design of appetitive learning tasks in zebrafish.

Based on observations of behaving fish, we hypothesized that the conditioned behavior consists of multiple behavioral components, and that the contribution of different behavioral components varies between trials and individuals. Consistent with this observation, the combined analysis of multiple behavioral components improved the detection of learned behavioral responses. Hence, the overt behavior was complex even though the conditioning paradigm is conceptually simple.

Olfactory discrimination learning

Zebrafish developed differential behavioral responses to related amino acid odors when and only when they differed in their prediction of food. Hence, fish discriminated between odors and learned specific associations between odors and behaviors, consistent with previous findings (Braubach et al. 2009; Miklavc and Valentinčič 2012). Appetitive olfactory conditioning could be achieved even using an odor that is innately aversive. Hence, olfactory conditioning is a robust phenomenon that can overcome innate odor preferences. This approach may be exploited to dissect neural pathways that mediate innate and learned behavioral responses to odors.

The 30 s delay between the onset of the CS and US provided the opportunity to quantify behavioral responses in each trial. Continuous learning curves could therefore be acquired without the need to introduce separate probe trials, which may result in extinction. As the acquisition of memory can be sensitive to the precise temporal relationship between the CS and the US, experimental conditions may be further improved by optimizing the delay between odor and food application. However, we did not attempt this because the chosen protocol already resulted in robust conditioning.

Statistically different behavioral responses to the CS+ and CS− were detected already after few training trials. Zebrafish can therefore establish specific olfactory memories based on a small amount of experience. Odor discrimination tasks that are widely used in rodents, in contrast, often require hundreds of training trials to reach asymptotic performance (Abraham et al. 2004; Bodyak and Slotnick 1999; Rinberg et al. 2006). The reason for this difference in training requirement remains unclear. One possibility is that the tasks for rodents include unnatural behavioral components such as nose pokes, whereas the task for fish is based on the conditioning of familiar food search behavior.

The ability of animals to discriminate odors is usually assessed by a behavioral readout that is based on odor discrimination learning. However, because learning itself modifies odor representations (Abraham et al. 2014; Chapuis and Wilson 2011; Chu et al. 2016; Li et al. 2008; Yamada et al. 2017), mechanisms of odor discrimination in naïve or nearly naïve animals remain difficult to analyze. A rapid conditioning procedure may open new opportunities to address this issue. We anticipate that the combination of behavioral and physiological analyses in zebrafish will provide new insights into the neuronal basis of olfactory processing and memory.

Acknowledgements We thank G. Jacobson for helpful input and support and the Friedrich lab for stimulating discussions. This work

was supported by the Novartis Research Foundation, by the Deutsche Forschungsgemeinschaft (DFG; FR 1667/2–2), by the Swiss National Science Foundation (SNF; 31003A_135196 and 310030B_1528331), and by the European Research Council (ERC) under the European Union's Horizon 2020 research and innovation programme (Grant Agreement No 742576).

References

Abraham NM, Spors H, Carleton A, Margrie TW, Kuner T, Schaefer AT (2004) Maintaining accuracy at the expense of speed: stimulus similarity defines odor discrimination time in mice. Neuron 44:865–876

Abraham NM, Vincis R, Lagier S, Rodriguez I, Carleton A (2014) Long term functional plasticity of sensory inputs mediated by olfactory learning. eLife 3:e02109 https://doi.org/10.7554/eLife.02109

Abril-de-Abreu R, Cruz AS, Oliveira RF (2015) Social dominance modulates eavesdropping in zebrafish. R Soc Open Sci 2:150220. https://doi.org/10.1098/rsos.150220

Agetsuma M et al (2010) The habenula is crucial for experience-dependent modification of fear responses in zebrafish. Nat Neurosci 13:1354–1356. https://doi.org/10.1038/nn.2654

Aoki T et al (2013) Imaging of neural ensemble for the retrieval of a learned behavioral program. Neuron 78:881–894. https://doi.org/10.1016/j.neuron.2013.04.009

Arganda S, Perez-Escudero A, de Polavieja GG (2012) A common rule for decision making in animal collectives across species. Proc Natl Acad Sci USA 109:20508–20513. https://doi.org/10.1073/pnas.1210664109

Blumhagen F, Zhu P, Shum J, Zhang Schärer Y-P, Yaksi E, Deisseroth K, Friedrich RW (2011) Neuronal filtering of multiplexed odour representations. Nature 479:493–498. https://doi.org/10.1038/nature10633

Bodyak N, Slotnick B (1999) Performance of mice in an automated olfactometer: odor detection, discrimination and odor memory. Chem Senses 24:637–645

Braubach OR, Wood HD, Gadbois S, Fine A, Croll RP (2009) Olfactory conditioning in the zebrafish (Danio rerio). Behav Brain Res 198:190–198

Braubach OR, Wyeth RC, Murray A, Fine A, Croll RP (2011) A simple and effective method to condition olfactory behaviors in groups of zebrafish. In: Kalueff AV, Cachat JM (eds) Zebrafish neurobehavioral protocols. Humana Press, New York City, pp 85–98

Brown C, Laland K, Krause J (eds) (2006) Fish cognition and behavior. Blackwell Publishing, Oxford

Buske C, Gerlai R (2011) Shoaling develops with age in Zebrafish (*Danio rerio*). Prog Neuro-psychopharmacol Biol Psychiatry 35:1409–1415. https://doi.org/10.1016/j.pnpbp.2010.09.003

Carr WES (1988) The molecular nature of chemical stimuli in the aquatic environment. In: Atema J, Fay RR, Popper AN, Tavolga WN (eds) Sensory biology of aquatic animals. Springer, New York, pp 3–27

Chapuis J, Wilson DA (2011) Bidirectional plasticity of cortical pattern recognition and behavioral sensory acuity. Nat Neurosci 15:155–161. https://doi.org/10.1038/nn.2966

Chou MY et al (2016) Social conflict resolution regulated by two dorsal habenular subregions in zebrafish. Science 352:87–90. https://doi.org/10.1126/science.aac9508

Chu MW, Li WL, Komiyama T (2016) Balancing the robustness and efficiency of odor representations during learning. Neuron 92:174–186. https://doi.org/10.1016/j.neuron.2016.09.004

Darland T, Dowling JE (2001) Behavioral screening for cocaine sensitivity in mutagenized zebrafish. Proc Natl Acad Sci USA 98:11691–11696

Doyle JM et al (2017) A simple automated system for appetitive conditioning of zebrafish in their home tanks. Behav Brain Res 317:444–452. https://doi.org/10.1016/j.bbr.2016.09.044

Dreosti E, Lopes G, Kampff AR, Wilson SW (2015) Development of social behavior in young zebrafish. Front Neural Circuits 9:39. https://doi.org/10.3389/fncir.2015.00039

Eddins D, Petro A, Williams P, Cerutti DT, Levin ED (2009) Nicotine effects on learning in zebrafish: the role of dopaminergic systems. Psychopharmacology 202:103–109. https://doi.org/10.1007/s00213-008-1287-4

Fajardo O, Zhu P, Friedrich RW (2013) Control of a specific motor program by a small brain area in zebrafish. Front Neural Circuits 7:67

Frederick DE, Barlas L, Ievins A, Kay LM (2009) A critical test of the overlap hypothesis for odor mixture perception. Behav Neurosci 123:430–437

Friedrich RW (2013) Information processing in the olfactory system of zebrafish. Annu Rev Neurosci 36:383–402

Friedrich RW, Korsching SI (1997) Combinatorial and chemotopic odorant coding in the zebrafish olfactory bulb visualized by optical imaging. Neuron 18:737–752

Friedrich RW, Laurent G (2001) Dynamic optimization of odor representations in the olfactory bulb by slow temporal patterning of mitral cell activity. Science 291:889–894

Friedrich RW, Genoud C, Wanner AA (2013) Analyzing the structure and function of neuronal circuits in zebrafish. Front Neural Circuits 7:71

Gradinaru V et al (2010) Molecular and cellular approaches for diversifying and extending optogenetics. Cell 141:154–165

Jacobson GA, Rupprecht P, Friedrich RW (2018) Experience-dependent plasticity of odor representations in the telencephalon of Zebrafish. Curr Biol 28:1–14 e13. https://doi.org/10.1016/j.cub.2017.11.007

Jetti SK, Vendrell-Llopis N, Yaksi E (2014) Spontaneous activity governs olfactory representations in spatially organized habenular microcircuits. Curr Biol 24:434–439. https://doi.org/10.1016/j.cub.2014.01.015

Kalueff AV et al (2013) Towards a comprehensive catalog of zebrafish behavior 1.0 and beyond Zebrafish 10:70–86 https://doi.org/10.1089/zeb.2012.0861

Kay LM, Laurent G (1999) Odor- and context-dependent modulation of mitral cell activity in behaving rats. Nat Neurosci 2:1003–1009

Lau B, Bretaud S, Huang Y, Lin E, Guo S (2006) Dissociation of food and opiate preference by a genetic mutation in zebrafish. Genes Brain Behav 5:497–505. https://doi.org/10.1111/j.1601-183X.2005.00185.x

Li W, Howard JD, Parrish TB, Gottfried JA (2008) Aversive learning enhances perceptual and cortical discrimination of indiscriminable odor cues. Science 319:1842–1845

MacRae CA, Peterson RT (2015) Zebrafish as tools for drug discovery. Nat Rev Drug Discov 14:721–731. https://doi.org/10.1038/nrd4627

Michel WC, Lubomudrov LM (1995) Specificity and sensitivity of the olfactory organ of the zebrafish, *Danio rerio*. J Comp Physiol A 177:191–199

Miklavc P, Valentinčič T (2012) Chemotopy of amino acids on the olfactory bulb predicts olfactory discrimination capabilities of zebrafish *Danio rerio*. Chem Senses 37:65–75. https://doi.org/10.1093/chemse/bjr066

Mueller KP, Neuhauss SCF (2012) Automated visual choice discrimination learning in zebrafish (*Danio rerio*). J Integr Neurosci 11:73–85. https://doi.org/10.1142/S0219635212500057

Niessing J, Friedrich RW (2010) Olfactory pattern classification by discrete neuronal network states. Nature 465:47–52

Portugues R, Severi KE, Wyart C, Ahrens MB (2013) Optogenetics in a transparent animal: circuit function in the larval zebrafish. Curr Opin Neurobiol 23:119–126. https://doi.org/10.1016/j.conb.2012.11.001

Rinberg D, Koulakov A, Gelperin A (2006) Speed-accuracy tradeoff in olfaction. Neuron 51:351–358

Rupprecht P, Prendergast A, Wyart C, Friedrich RW (2016) Remote z-scanning with a macroscopic voice coil motor for fast 3D multiphoton laser scanning microscopy. Biomed Opt Express 7:1656–1671

Saverino C, Gerlai R (2008) The social zebrafish: behavioral responses to conspecific, heterospecific, and computer animated fish. Behav Brain Res 191:77–87. https://doi.org/10.1016/j.bbr.2008.03.013

Sison M, Gerlai R (2010) Associative learning in zebrafish (*Danio rerio*) in the plus maze. Behav Brain Res 207:99–104. https://doi.org/10.1016/j.bbr.2009.09.043

Stouffer SA, Suchman EA, DeVinney LC, Star SA, Williams RMJ (1949) The American soldier, vol.1: adjustment during army life. Princeton University Press, Princeton

Sumbre G, de Polavieja GG (2014) The world according to zebrafish: how neural circuits generate behavior. Front Neural Circuits 8:91. https://doi.org/10.3389/fncir.2014.00091

Valente A, Huang KH, Portugues R, Engert F (2012) Ontogeny of classical and operant learning behaviors in zebrafish. Learn Mem 19:170–177. https://doi.org/10.1101/lm.025668.112

Valentinčič T, Metelko J, Ota D, Pirc V, Blejec A (2000) Olfactory discrimination of amino acids in brown bullhead catfish. Chem Senses 25:21–29

Vitebsky A, Reyes R, Sanderson MJ, Michel WC, Whitlock KE (2005) Isolation and characterization of the laure olfactory behavioral mutant in the zebrafish, *Danio rerio*. Dev Dyn 234:229–242

Wanner AA, Genoud C, Masudi T, Siksou L, Friedrich RW (2016) Dense EM-based reconstruction of the interglomerular projectome in the zebrafish olfactory bulb. Nat Neurosci 19:816–825. https://doi.org/10.1038/nn.4290

Xu X, Scott-Scheiern T, Kempker L, Simons K (2007) Active avoidance conditioning in zebrafish (*Danio rerio*). Neurobiol Learn Mem 87:72–77

Yabuki Y et al (2016) Olfactory receptor for prostaglandin F2alpha mediates male fish courtship behavior. Nat Neurosci 19:897–904. https://doi.org/10.1038/nn.4314

Yaksi E, von Saint Paul F, Niessing J, Bundschuh ST, Friedrich RW (2009) Transformation of odor representations in target areas of the olfactory bulb. Nat Neurosci 12:474–482

Yamada Y, Bhaukaurally K, Madarasz TJ, Pouget A, Rodriguez I, Carleton A (2017) Context- and output layer-dependent long-term ensemble plasticity in a sensory circuit. Neuron 93:1198–1212 e1195. https://doi.org/10.1016/j.neuron.2017.02.006

Zhu P, Fajardo O, Shum J, Zhang Schärer Y-P, Friedrich RW (2012) High-resolution optical control of spatiotemporal neuronal activity patterns in zebrafish using a digital micromirror device. Nat Protoc 7:1410–1425. https://doi.org/10.1038/nprot.2012.072

Zhu P, Frank T, Friedrich RW (2013) Equalization of odor representations by a network of electrically coupled inhibitory interneurons. Nat Neurosci 16:1678–1686. https://doi.org/10.1038/nn.3528

3.3 DISCUSSION

A comprehensive dissection of any given neural circuit in order to understand its function requires researchers to examine the outcome of specific manipulations on a behavioral level. For this purpose, robust, efficient, scalable, and replicable behavioral assays are required. To this aim, we developed an associative olfactory discrimination task.

This experimental design has several important aspects. First, the automation of the experimental procedure makes it time efficient and allows to separate the experimenter from the subject. The experimental setup consists of simple and affordable components, can be easily reproduced, and conveniently extended and upscaled. Indeed, the initial behavioral setup has been reproduced several times within the Friedrich lab and the experiments have been successfully reproduced by other experimenters. As the extraction of behavioral features from videos is automated and the feature postprocessing standardized, experimenters save time and remain ignorant to experimental subgroups during analysis. The quantification of an individual fish's discrimination performance allows to correlate e.g., functional measurements or effects of targeted manipulation of neural systems with behavioral performance. Using this behavioral score in a study led by Thomas Frank, we could show that the odor preference measured in behavior was represented in the population activity of Dp, the teleost homolog to piriform cortex [12], and that this mapping involved experience-dependent changes in inhibitory IN activity. Moreover, training fish using this olfactory discrimination paradigm, Chie Satou could show that a particular brain region afferent to OB selectively responds upon presentation of odors that had been associated with a reward, but not other odors [234].

The learning of odor-food reward association is a robust phenomenon. We demonstrated odor discrimination in different strains and since then it has been replicated in different experimental conditions, e.g., adult zebrafish after virus injection [234] and juvenile fish (Nesibe Temiz-Karayol, personal communication). We also showed that zebrafish can discriminate between rewarded and unrewarded odors within the first day of training after only a few trials. The agreeable experimental conditions, i.e., training in a home tank environment at a low to moderate flow rate may have contributed to this. Furthermore, the conditioning did not have an operant component, instead we measured odor response based on looking at various parameters of natural food search und feeding behavior, thus capturing multiple aspects in which fish could express food expectation.

The experiment offers a tool to study basic odor discrimination behavior in zebrafish under different conditions. This paradigm can be used as a basis to modify the training protocol in order to explore further aspects of zebrafish olfactory behavior, for example, the resilience of the memory against extinction or an individual fish's capability to discriminate conditioned odors from similar odors.

4. GLOSSARY

AOB = accessory olfactory bulb
AON = anterior olfactory nucleus
CD = cutting degree
CNN = convolutional neuronal networks
CP = cibriform plate
CR = completely reconstructed
DA = dopamine
DL = deep layer
DLIN = deep layer interneuron
cDLIN2 = common DLIN2
fDLIN2 = fringy DLIN2
lDLIN1 = DLIN1 with long-necked spines
rDLIN1 = rough DLIN1
sDLIN1 = sparsely spiny DLIN1
sDLIN2 = DLIN2 with stubby spines
ER = endoplasmatic reticulum
EPL = external plexiform layer
EPL-IN = external plexiform layer interneuron
ERL = expected run length
ETC = external tufted cell
FFN = flood filling networks
GC = granule cell
GCL = granule cell layer
GL = glomerular layer
GLIN = glomerular layer interneuron
sGLIN1 = small GLIN1
lGLIN1 = large GLIN1
GT = ground truth
ICR = incompletely reconstructed
IN = interneuron
IPL = internal plexiform layer
LOT = lateral olfactory tract
MC = mitral cell
MCL = mitral cell layer
MSC = mixed synapse cell
MOT = medial olfactory tract
OB = olfactory bulb
OE = olfactory epithelium
OLFR = olfactory receptor
ONL = olfactory nerve layer
OSN = olfactory sensory neuron
OT = olfactory tubercle
PCA = principal component analysis
PGC = periglomerular cell
PL = plexiform layer
PLIN = plexiform layer interneuron
rlPLIN3 = ribbon-like PLIN3
vPLIN3 = varicose PLIN3
PN = projection neuron
PNC = perinest cell
PV = parvalbumin
RC = ruffed cell
SAC = short axon cell
dSAC = deep short axon cell
sSAC = superficial short axon cell
SBEM = serial blockface electron microscopy
TC = tufted cell
UMAP = uniform manifold projection

5. REFERENCES

[1] P. CISEK, "BEYOND THE COMPUTER METAPHOR: BEHAVIOR AS INTERACTION," *JOURNAL OF CONSCIOUSNESS STUDIES,* VOL. 6, P. 125–142, 1999.

[2] G. F. STRIEDTER AND R. G. NORTHCUTT, BRAINS THROUGH TIME: A NATURAL HISTORY OF VERTEBRATES., OXFORD UNIVERSITY PRESS, 2020.

[3] B. W. ACHE AND J. M. YOUNG, "OLFACTION: DIVERSE SPECIES, CONSERVED PRINCIPLES," *NEURON,* VOL. 48, P. 417–430, 2005.

[4] P. SHI AND J. ZHANG, "EXTRAORDINARY DIVERSITY OF CHEMOSENSORY RECEPTOR GENE REPERTOIRES AMONG VERTEBRATES.," *RESULTS AND PROBLEMS IN CELL DIFFERENTIATION,* VOL. 47, PP. 1-23, 2009.

[5] G. MAJOR, M. E. LARKUM AND J. SCHILLER, "ACTIVE PROPERTIES OF NEOCORTICAL PYRAMIDAL NEURON DENDRITES," *ANNU. REV. NEUROSCI.,* VOL. 36, P. 1–24, 7 2013.

[6] J. ARU, M. SUZUKI AND M. E. LARKUM, "CELLULAR MECHANISMS OF CONSCIOUS PROCESSING," *TRENDS IN COGNITIVE SCIENCES,* VOL. 24, P. 814–825, 2020.

[7] S. PIKA, M. J. SIMA, C. R. BLUM, E. HERRMANN AND R. MUNDRY, "RAVENS PARALLEL GREAT APES IN PHYSICAL AND SOCIAL COGNITIVE SKILLS," *SCIENTIFIC REPORTS,* VOL. 10, P. 20617, 2020.

[8] A. K. SCHNELL, P. AMODIO, M. BOECKLE AND N. S. CLAYTON, "HOW INTELLIGENT IS A CEPHALOPOD? LESSONS FROM COMPARATIVE COGNITION," *BIOL REV,* VOL. 96, P. 162–178, 2 2021.

[9] N. J. STRAUSFELD AND J. G. HILDEBRAND, "OLFACTORY SYSTEMS: COMMON DESIGN, UNCOMMON ORIGINS?," *CURRENT OPINION IN NEUROBIOLOGY,* VOL. 9, P. 634–639, 1999.

[10] L. M. KAY AND M. STOPFER, "INFORMATION PROCESSING IN THE OLFACTORY SYSTEMS OF INSECTS AND VERTEBRATES," *SEMINARS IN CELL & DEVELOPMENTAL BIOLOGY,* VOL. 17, P. 433–442, 2006.

[11] I. NAMEKAWA, N. R. MOENIG AND R. W. FRIEDRICH, "RAPID OLFACTORY DISCRIMINATION LEARNING IN ADULT ZEBRAFISH," *EXPERIMENTAL BRAIN RESEARCH,* VOL. 236, P. 2959–2969, 2018.

[12] T. FRANK, N. R. MÖNIG, C. SATOU, S.-I. HIGASHIJIMA AND R. W. FRIEDRICH, "ASSOCIATIVE CONDITIONING REMAPS ODOR REPRESENTATIONS AND MODIFIES INHIBITION IN A HIGHER OLFACTORY BRAIN AREA," *NATURE NEUROSCIENCE,* VOL. 22, P. 1844–1856, 2019.

[13] M. F. WULLIMANN, B. RUPP AND H. & REICHERT, NEUROANATOMY OF THE ZEBRAFISH BRAIN: A TOPOLOGICAL ATLAS., BASEL: BIRKHÄUSER VERLAG, 1996.

[14] L. BUCK AND R. AXEL, "A NOVEL MULTIGENE FAMILY MAY ENCODE ODORANT RECEPTORS: A MOLECULAR BASIS FOR ODOR RECOGNITION," *CELL,* VOL. 65, P. 175–187, 1991.

[15] L. B. BUCK, "THE MOLECULAR ARCHITECTURE OF ODOR AND PHEROMONE SENSING IN MAMMALS," *CELL,* VOL. 100, P. 611–618, 2000.

[16] R. W. FRIEDRICH AND S. I. KORSCHING, "COMBINATORIAL AND CHEMOTOPIC ODORANT CODING IN THE ZEBRAFISH OLFACTORY BULB VISUALIZED BY OPTICAL IMAGING," *NEURON,* VOL. 18, P. 737–752, 5 1997.

[17] R. C. ARANEDA, A. D. KINI AND S. FIRESTEIN, "THE MOLECULAR RECEPTIVE RANGE OF AN ODORANT RECEPTOR," *NATURE NEUROSCIENCE,* VOL. 3, P. 1248–1255, 2000.

[18] H. U. FRIED, S. H. FUSS AND S. I. KORSCHING, "SELECTIVE IMAGING OF PRESYNAPTIC ACTIVITY IN THE MOUSE OLFACTORY BULB SHOWS CONCENTRATION AND STRUCTURE DEPENDENCE OF ODOR RESPONSES IN IDENTIFIED GLOMERULI," *PROC NATL ACAD SCI USA,* VOL. 99, P. 3222, 3 2002.

[19] J. NIESSING AND R. W. FRIEDRICH, "OLFACTORY PATTERN CLASSIFICATION BY DISCRETE NEURONAL NETWORK STATES," *NATURE,* VOL. 465, P. 47–52, 5 2010.

[20] P. ZHU, T. FRANK AND R. W. FRIEDRICH, "EQUALIZATION OF ODOR REPRESENTATIONS BY A NETWORK OF ELECTRICALLY COUPLED INHIBITORY INTERNEURONS," *NAT NEUROSCI,* VOL. 16, P. 1678–1686, 11 2013.

[21] A. BANERJEE, F. MARBACH, F. ANSELMI, M. KOH, M. DAVIS, P. GARCIAÂ DAÂ SILVA, K. DELEVICH, H. OYIBO, P. GUPTA, B. LI AND D. ALBEANU, "AN INTERGLOMERULAR CIRCUIT GATES GLOMERULAR OUTPUT AND IMPLEMENTS GAIN CONTROL IN THE MOUSE OLFACTORY BULB," *NEURON,* VOL. 87, P. 193–207, 2015.

[22] D. A. STORACE AND L. B. COHEN, "MEASURING THE OLFACTORY BULB INPUT-OUTPUT TRANSFORMATION REVEALS A CONTRIBUTION TO THE PERCEPTION OF ODORANT CONCENTRATION INVARIANCE," *NATURE COMMUNICATIONS,* VOL. 8, P. 81, 2017.

[23] N. UCHIDA AND Z. MAINEN, "ODOR CONCENTRATION INVARIANCE BY CHEMICAL RATIO CODING," *FRONTIERS IN SYSTEMS NEUROSCIENCE,* VOL. 2, P. 3, 2008.

[24] R. HOMMA, L. B. COHEN, E. K. KOSMIDIS AND S. L. YOUNGENTOB, "PERCEPTUAL STABILITY DURING DRAMATIC CHANGES IN OLFACTORY BULB ACTIVATION MAPS AND DRAMATIC DECLINES IN ACTIVATION AMPLITUDES," *EUROPEAN JOURNAL OF NEUROSCIENCE,* VOL. 29, P. 1027–1034, 3 2009.

[25] R. W. FRIEDRICH AND G. LAURENT, "DYNAMIC OPTIMIZATION OF ODOR REPRESENTATIONS BY SLOW TEMPORAL PATTERNING OF MITRAL CELL ACTIVITY," *SCIENCE,* VOL. 291, P. 889–894, 2 2001.

[26] R. W. FRIEDRICH AND G. LAURENT, "DYNAMICS OF OLFACTORY BULB INPUT AND OUTPUT ACTIVITY DURING ODOR STIMULATION IN ZEBRAFISH," *JOURNAL OF NEUROPHYSIOLOGY,* VOL. 91, P. 2658–2669, 6 2004.

[27] O. GSCHWEND, N. M. ABRAHAM, S. LAGIER, F. BEGNAUD, I. RODRIGUEZ AND A. CARLETON, "NEURONAL PATTERN SEPARATION IN THE OLFACTORY BULB IMPROVES ODOR DISCRIMINATION LEARNING," *NAT NEUROSCI,* VOL. 18, P. 1474–1482, 10 2015.

[28] A. A. WANNER AND R. W. FRIEDRICH, "WHITENING OF ODOR REPRESENTATIONS BY THE WIRING DIAGRAM OF THE OLFACTORY BULB," *NATURE NEUROSCIENCE,* 1 2020.

[29] M. CHU, W. LI AND T. KOMIYAMA, "BALANCING THE ROBUSTNESS AND EFFICIENCY OF ODOR REPRESENTATIONS DURING LEARNING," *NEURON,* VOL. 92, P. 174–186, 10 2016.

[30] Y. YAMADA, K. BHAUKAURALLY, T. J. MADARÁSZ, A. POUGET, I. RODRIGUEZ AND A. CARLETON, "CONTEXT- AND OUTPUT LAYER-DEPENDENT LONG-TERM ENSEMBLE PLASTICITY IN A SENSORY CIRCUIT," *NEURON,* VOL. 93, P. 1198–1212.E5, 3 2017.

[31] R. TABOR, E. YAKSI, J.-M. WEISLOGEL AND R. W. FRIEDRICH, "PROCESSING OF ODOR MIXTURES IN THE ZEBRAFISH OLFACTORY BULB," *THE JOURNAL OF NEUROSCIENCE,* VOL. 24, P. 6611–6620, 7 2004.

[32] L. B. HABERLY AND J. M. BOWER, "OLFACTORY CORTEX: MODEL CIRCUIT FOR STUDY OF ASSOCIATIVE MEMORY?," *TRENDS IN NEUROSCIENCES,* VOL. 12, NO. 7, PP. 258-64, 7 1989.

[33] L. B. HABERLY, "PARALLEL-DISTRIBUTED PROCESSING IN OLFACTORY CORTEX: NEW INSIGHTS FROM MORPHOLOGICAL AND PHYSIOLOGICAL ANALYSIS OF NEURONAL CIRCUITRY.," *CHEMICAL SENSES,* VOL. 26, NO. 5, PP. 551-76, 6 2001.

[34] D. WILSON AND R. SULLIVAN, "CORTICAL PROCESSING OF ODOR OBJECTS," *NEURON,* VOL. 72, P. 506–519, 11 2011.

[35] E. YAKSI, F. VON SAINT PAUL, J. NIESSING, S. T. BUNDSCHUH AND R. W. FRIEDRICH, "TRANSFORMATION OF ODOR REPRESENTATIONS IN TARGET AREAS OF THE OLFACTORY BULB," *NAT NEUROSCI,* VOL. 12, P. 474–482, 4 2009.

[36] A. C. AREVIAN, V. KAPOOR AND N. N. URBAN, "ACTIVITY-DEPENDENT GATING OF LATERAL INHIBITION IN THE MOUSE OLFACTORY BULB," *NATURE NEUROSCIENCE,* VOL. 11, P. 80–87, 2008.

[37] R. TABOR, E. YAKSI AND R. W. FRIEDRICH, "MULTIPLE FUNCTIONS OF GABAA AND GABAB RECEPTORS DURING PATTERN PROCESSING IN THE ZEBRAFISH OLFACTORY BULB," *EUROPEAN JOURNAL OF NEUROSCIENCE,* VOL. 28, P. 117–127, 2008.

[38] M. T. WIECHERT, B. JUDKEWITZ, H. RIECKE AND R. W. FRIEDRICH, "MECHANISMS OF PATTERN DECORRELATION BY RECURRENT NEURONAL CIRCUITS," *NAT NEUROSCI,* VOL. 13, P. 1003–1010, 8 2010.

[39] A. KOULAKOV AND D. RINBERG, "SPARSE INCOMPLETE REPRESENTATIONS: A POTENTIAL ROLE OF OLFACTORY GRANULE CELLS," *NEURON,* VOL. 72, P. 124–136, 10 2011.

[40] R. W. FRIEDRICH AND M. T. WIECHERT, "NEURONAL CIRCUITS AND COMPUTATIONS: PATTERN DECORRELATION IN THE OLFACTORY BULB," *FEBS LETTERS,* VOL. 588, P. 2504–2513, 8 2014.

[41] Y. YOSHIHARA, "MOLECULAR GENETIC DISSECTION OF THE ZEBRAFISH OLFACTORY SYSTEM," IN *CHEMOSENSORY SYSTEMS IN MAMMALS, FISHES, AND INSECTS*, S. KORSCHING AND W. MEYERHOF, EDS., BERLIN, HEIDELBERG: SPRINGER BERLIN HEIDELBERG, 2009, P. 1–19.

[42] K. MORI AND H. SAKANO, "HOW IS THE OLFACTORY MAP FORMED AND INTERPRETED IN THE MAMMALIAN BRAIN?," *ANNU. REV. NEUROSCI.,* VOL. 34, P. 467–499, 6 2011.

[43] M. FIGUERES-OÑATE, Y. GUTIÉRREZ AND L. LÓPEZ-MASCARAQUE, "UNRAVELING CAJAL'S VIEW OF THE OLFACTORY SYSTEM," *FRONTIERS IN NEUROANATOMY,* VOL. 8, P. 55, 2014.

[44] J. P. ROYET, C. SOUCHIER, F. JOURDAN AND H. PLOYE, "MORPHOMETRIC STUDY OF THE GLOMERULAR POPULATION IN THE MOUSE OLFACTORY BULB: NUMERICAL DENSITY AND SIZE DISTRIBUTION ALONG THE ROSTROCAUDAL AXIS," *J. COMP. NEUROL.,* VOL. 270, P. 559–568, 1988.

[45] E. MEISAMI, "A NEW MORPHOMETRIC METHOD TO ESTIMATE THE TOTAL NUMBER OF GLOMERULI IN THE OLFACTORY BULB," *CHEMICAL SENSES,* VOL. 15, P. 407–418, 1990.

[46] O. R. BRAUBACH, A. FINE AND R. P. CROLL, "DISTRIBUTION AND FUNCTIONAL ORGANIZATION OF GLOMERULI IN THE OLFACTORY BULBS OF ZEBRAFISH (DANIO RERIO)," *J. COMP. NEUROL.,* VOL. 520, P. 2317–2339, 8 2012.

[47] K. L. SIMPSON AND R. D. SWEAZEY, "CHAPTER 23 - OLFACTION AND TASTE," IN *FUNDAMENTAL NEUROSCIENCE FOR BASIC AND CLINICAL APPLICATIONS (FIFTH EDITION)*, D. E. HAINES AND G. A. MIHAILOFF, EDS., ELSEVIER, 2018, P. 334–345.E1.

[48] C. LEVINE AND A. MARCILLO, "REGARDING SEVERAL POINTS OF DOUBT OF THE STRUCTURE OF THE OLFACTORY BULB: AS DESCRIBED BY T. BLANES," *ANAT REC,* VOL. 291, P. 751–762, 7 2008.

[49] A. J. PINCHING AND T. P. S. POWELL, "THE NEUROPIL OF THE PERIGLOMERULAR REGION OF THE OLFACTORY BULB," *J. CELL SCI.,* VOL. 9, P. 379, 9 1971.

[50] A. HAYAR, S. KARNUP, M. ENNIS AND M. T. SHIPLEY, "EXTERNAL TUFTED CELLS: A MAJOR EXCITATORY ELEMENT THAT COORDINATES GLOMERULAR ACTIVITY," *J. NEUROSCI.,* VOL. 24, P. 6676, 7 2004.

[51] M. WACHOWIAK AND M. T. SHIPLEY, "CODING AND SYNAPTIC PROCESSING OF SENSORY INFORMATION IN THE GLOMERULAR LAYER OF THE OLFACTORY BULB," *SEMINARS IN CELL & DEVELOPMENTAL BIOLOGY,* VOL. 17, P. 411–423, 8 2006.

[52] D. DE SAINT JAN, D. HIRNET, G. L. WESTBROOK AND S. CHARPAK, "EXTERNAL TUFTED CELLS DRIVE THE OUTPUT OF OLFACTORY BULB GLOMERULI," *J. NEUROSCI.,* VOL. 29, P. 2043, 2 2009.

[53] A. TAVAKOLI, A. SCHMALTZ, D. SCHWARZ, T. W. MARGRIE, A. T. SCHAEFER AND M. KOLLO, "QUANTITATIVE ASSOCIATION OF ANATOMICAL AND FUNCTIONAL CLASSES OF OLFACTORY BULB NEURONS," *J. NEUROSCI.,* VOL. 38, P. 7204, 8 2018.

[54] M. ANTAL, M. EYRE, B. FINKLEA AND Z. NUSSER, "EXTERNAL TUFTED CELLS IN THE MAIN OLFACTORY BULB FORM TWO DISTINCT SUBPOPULATIONS," *EUROPEAN JOURNAL OF NEUROSCIENCE,* VOL. 24, P. 1124–1136, 8 2006.

[55] E. KIYOKAGE, Y.-Z. PAN, Z. SHAO, K. KOBAYASHI, G. SZABO, Y. YANAGAWA, K. OBATA, H. OKANO, K. TOIDA, A. C. PUCHE AND M. T. SHIPLEY, "MOLECULAR IDENTITY OF PERIGLOMERULAR AND SHORT AXON CELLS," *J. NEUROSCI.,* VOL. 30, P. 1185, 1 2010.

[56] J. TAN, A. SAVIGNER, M. MA AND M. LUO, "ODOR INFORMATION PROCESSING BY THE OLFACTORY BULB ANALYZED IN GENE-TARGETED MICE," *NEURON,* VOL. 65, P. 912–926, 3 2010.

[57] K. KOSAKA AND T. KOSAKA, "SYNAPTIC ORGANIZATION OF THE GLOMERULUS IN THE MAIN OLFACTORY BULB: COMPARTMENTS OF THE GLOMERULUS AND HETEROGENEITY OF THE PERIGLOMERULAR CELLS.," *ANATOMICAL SCIENCE INTERNATIONAL,* VOL. 80, NO. 2, PP. 80-90, 6 2005.

[58] M. NAJAC, D. DE SAINT JAN, L. REGUERO, P. GRANDES AND S. CHARPAK, "MONOSYNAPTIC AND POLYSYNAPTIC FEED-FORWARD INPUTS TO MITRAL CELLS FROM OLFACTORY SENSORY NEURONS," *J. NEUROSCI.,* VOL. 31, P. 8722, 6 2011.

[59] S. D. BURTON, "INHIBITORY CIRCUITS OF THE MAMMALIAN MAIN OLFACTORY BULB," *JOURNAL OF NEUROPHYSIOLOGY,* VOL. 118, P. 2034–2051, 10 2017.

[60] A. J. PINCHING AND T. P. S. POWELL, "THE NEURON TYPES OF THE GLOMERULAR LAYER OF THE OLFACTORY BULB," *J. CELL SCI.,* VOL. 9, P. 305, 9 1971.

[61] J. L. AUNGST, P. M. HEYWARD, A. C. PUCHE, S. V. KARNUP, A. HAYAR, G. SZABO AND M. T. SHIPLEY, "CENTRE-SURROUND INHIBITION AMONG OLFACTORY BULB GLOMERULI," *NATURE,* VOL. 426, P. 623, 12 2003.

[62] T. KOSAKA AND K. KOSAKA, "NEURONAL ORGANIZATION OF THE MAIN OLFACTORY BULB REVISITED," *ANATOMICAL SCIENCE INTERNATIONAL,* VOL. 91, P. 115–127, 3 2016.

[63] S. NAGAYAMA, R. HOMMA AND F. IMAMURA, "NEURONAL ORGANIZATION OF OLFACTORY BULB CIRCUITS," *FRONTIERS IN NEURAL CIRCUITS,* VOL. 8, P. –, 2014.

[64] K. MORI, K. KISHI AND H. OJIMA, "DISTRIBUTION OF DENDRITES OF MITRAL, DISPLACED MITRAL, TUFTED, AND GRANULE CELLS IN THE RABBIT OLFACTORY BULB," *J. COMP. NEUROL.,* VOL. 219, P. 339–355, 9 1983.

[65] E. ORONA, E. C. RAINER AND J. W. SCOTT, "DENDRITIC AND AXONAL ORGANIZATION OF MITRAL AND TUFTED CELLS IN THE RAT OLFACTORY BULB," *J. COMP. NEUROL.,* VOL. 226, P. 346–356, 7 1984.

[66] K. M. IGARASHI, N. IEKI, M. AN, Y. YAMAGUCHI, S. NAGAYAMA, K. KOBAYAKAWA, R. KOBAYAKAWA, M. TANIFUJI, H. SAKANO, W. R. CHEN AND K. MORI, "PARALLEL MITRAL AND TUFTED CELL PATHWAYS ROUTE DISTINCT ODOR INFORMATION TO DIFFERENT TARGETS IN THE OLFACTORY CORTEX," *THE JOURNAL OF NEUROSCIENCE,* VOL. 32, P. 7970–7985, 6 2012.

[67] F. IMAMURA, A. ITO AND B. J. LAFEVER, "SUBPOPULATIONS OF PROJECTION NEURONS IN THE OLFACTORY BULB," *FRONTIERS IN NEURAL CIRCUITS,* VOL. 14, P. 561822–561822, 8 2020.

[68] L. HUANG, I. GARCIA, H.-I. JEN AND B. ARENKIEL, "RECIPROCAL CONNECTIVITY BETWEEN MITRAL CELLS AND EXTERNAL PLEXIFORM LAYER INTERNEURONS IN THE MOUSE OLFACTORY BULB," *FRONTIERS IN NEURAL CIRCUITS,* VOL. 7, P. 32, 2013.

[69] K. MIYAMICHI, Y. SHLOMAI-FUCHS, M. SHU, B. WEISSBOURD, L. LUO AND A. MIZRAHI, "DISSECTING LOCAL CIRCUITS: PARVALBUMIN INTERNEURONS UNDERLIE BROAD FEEDBACK CONTROL OF OLFACTORY BULB OUTPUT," *NEURON,* VOL. 80, P. 1232–1245, 12 2013.

[70] H. KATO, S. GILLET, A. PETERS, J. ISAACSON AND T. KOMIYAMA, "PARVALBUMIN-EXPRESSING INTERNEURONS LINEARLY CONTROL OLFACTORY BULB OUTPUT," *NEURON,* VOL. 80, P. 1218–1231, 2013.

[71] M. D. EYRE, M. ANTAL AND Z. NUSSER, "DISTINCT DEEP SHORT-AXON CELL SUBTYPES OF THE MAIN OLFACTORY BULB PROVIDE NOVEL INTRABULBAR AND EXTRABULBAR GABAERGIC CONNECTIONS," *J. NEUROSCI.,* VOL. 28, P. 8217, 8 2008.

[72] S. D. BURTON, G. LAROCCA, A. LIU, C. E. J. CHEETHAM AND N. N. URBAN, "OLFACTORY BULB DEEP SHORT-AXON CELLS MEDIATE WIDESPREAD INHIBITION OF TUFTED CELL APICAL DENDRITES," *J. NEUROSCI.,* VOL. 37, P. 1117, 2 2017.

[73] M. D. EYRE, K. KERTI AND Z. NUSSER, "MOLECULAR DIVERSITY OF DEEP SHORT-AXON CELLS OF THE RAT MAIN OLFACTORY BULB," *EUROPEAN JOURNAL OF NEUROSCIENCE,* VOL. 29, P. 1397–1407, 4 2009.

[74] J. L. PRICE AND T. P. S. POWELL, "THE MORPHOLOGY OF THE GRANULE CELLS OF THE OLFACTORY BULB," *J. CELL SCI.,* VOL. 7, P. 91, 7 1970.

[75] J. L. PRICE AND T. P. S. POWELL, "THE SYNAPTOLOGY OF THE GRANULE CELLS OF THE OLFACTORY BULB," *J. CELL SCI.,* VOL. 7, P. 125, 7 1970.

[76] A. CARLETON, L. T. PETREANU, R. LANSFORD, A. ALVAREZ-BUYLLA AND P.-M. LLEDO, "BECOMING A NEW NEURON IN THE ADULT OLFACTORY BULB," *NATURE NEUROSCIENCE,* VOL. 6, P. 507–518, 2003.

[77] J. L. PRICE AND T. P. S. POWELL, "AN ELECTRON-MICROSCOPIC STUDY OF THE TERMINATION OF THE AFFERENT FIBRES TO THE OLFACTORY BULB FROM THE CEREBRAL HEMISPHERE," *J. CELL SCI.,* VOL. 7, P. 157, 7 1970.

[78] N. M. ABRAHAM, V. EGGER, D. R. SHIMSHEK, R. RENDEN, I. FUKUNAGA, R. SPRENGEL, P. H. SEEBURG, M. KLUGMANN, T. W. MARGRIE, A. T. SCHAEFER AND T. KUNER, "SYNAPTIC INHIBITION IN THE OLFACTORY BULB ACCELERATES ODOR DISCRIMINATION IN MICE," *NEURON,* VOL. 65, P. 399–411, 2 2010.

[79] L. WEISS, L. D. JUNGBLUT, A. G. POZZI, B. S. ZIELINSKI, L. A. O'CONNELL, T. HASSENKLÖVER AND I. MANZINI, "MULTI-GLOMERULAR PROJECTION OF SINGLE OLFACTORY RECEPTOR NEURONS IS CONSERVED AMONG AMPHIBIANS," *J COMP NEUROL,* VOL. 528, P. 2239–2253, 9 2020.

[80] M. ICHIKAWA, "FINE STRUCTURE OF THE OLFACTORY BULB IN THE GOLDFISH, CARASSIUS AURATUS," *BRAIN RESEARCH,* VOL. 115, P. 43–56, 1976.

[81] M. SATOU, "SYNAPTIC ORGANIZATION, LOCAL NEURONAL CIRCUITRY, AND FUNCTIONAL SEGREGATION OF THE TELEOST OLFACTORY BULB," *PROGRESS IN NEUROBIOLOGY,* VOL. 34, P. 115–142, 1990.

[82] C. A. BYRD AND P. C. BRUNJES, "ORGANIZATION OF THE OLFACTORY SYSTEM IN THE ADULT ZEBRAFISH: HISTOLOGICAL, IMMUNOHISTOCHEMICAL, AND QUANTITATIVE ANALYSIS," *J. COMP. NEUROL.,* VOL. 358, P. 247–259, 7 1995.

[83] J. G. EDWARDS AND W. C. MICHEL, "ODOR-STIMULATED GLUTAMATERGIC NEUROTRANSMISSION IN THE ZEBRAFISH OLFACTORY BULB," *J. COMP. NEUROL.,* VOL. 454, P. 294–309, 12 2002.

[84] C. L. FULLER, H. K. YETTAW AND C. A. BYRD, "MITRAL CELLS IN THE OLFACTORY BULB OF ADULT ZEBRAFISH (DANIO RERIO): MORPHOLOGY AND DISTRIBUTION," *J. COMP. NEUROL.,* VOL. 499, P. 218–230, 11 2006.

[85] T. KOSAKA AND K. HAMA, "STRUCTURE OF THE MITRAL CELL IN THE OLFACTORY BULB OF THE GOLDFISH (CARASSIUS AURATUS)," *J. COMP. NEUROL.,* VOL. 212, P. 365–384, 12 1982.

[86] O. BRAUBACH AND R. P. CROLL, "THE GLOMERULAR NETWORK OF THE ZEBRAFISH OLFACTORY BULB," *CELL AND TISSUE RESEARCH,* VOL. 383, P. 255–271, 2021.

[87] T. KOSAKA AND K. HAMA, "SYNAPTIC ORGANIZATION IN THE TELEOST OLFACTORY BULB," *JOURNAL DE PHYSIOLOGIE,* VOL. 78, P. 707—719, 1982.

[88] Y. OKA, M. ICHIKAWA AND K. UEDA, "SYNAPTIC ORGANIZATION OF THE OLFACTORY BULB AND CENTRAL PROJECTION OF THE OLFACTORY TRACT," *CHEMORECEPTION IN FISHES,* P. 61–75, 1 1982.

[89] E. YAKSI, B. JUDKEWITZ AND R. W. FRIEDRICH, "TOPOLOGICAL REORGANIZATION OF ODOR REPRESENTATIONS IN THE OLFACTORY BULB," *PLOS BIOL,* VOL. 5, P. E178–, 7 2007.

[90] T. MASUDI, "CONNECTIVITY MOTIFS UNDERLYING NEURONAL COMPUTATIONS IN THE ADULT OB," 2016.

[91] F. KERMEN, L. M. FRANCO, C. WYATT AND E. YAKSI, "NEURAL CIRCUITS MEDIATING OLFACTORY-DRIVEN BEHAVIOR IN FISH," *FRONTIERS IN NEURAL CIRCUITS,* VOL. 7, P. –, 2013.

[92] G. M. SHEPHERD, W. R. CHEN, D. WILLHITE, M. MIGLIORE AND C. A. GREER, "THE OLFACTORY GRANULE CELL: FROM CLASSICAL ENIGMA TO CENTRAL ROLE IN OLFACTORY PROCESSING," *BRAIN RESEARCH REVIEWS,* VOL. 55, P. 373–382, 2007.

[93] A. A. WANNER, "RECONSTRUCTION OF NEURONAL ACTIVITY AND CONNECTIVITY PATTERNS IN THE ZEBRAFISH OLFACTORY BULB," 2016.

[94] C. L. FULLER AND C. A. BYRD, "RUFFED CELLS IDENTIFIED IN THE ADULT ZEBRAFISH OLFACTORY BULB," *NEUROSCIENCE LETTERS,* VOL. 379, P. 190–194, 5 2005.

[95] T. KOSAKA AND K. HAMA, "RUFFED CELL: A NEW TYPE OF NEURON WITH A DISTINCTIVE INITIAL UNMYELINATED PORTION OF THE AXON IN THE OLFACTORY BULB OF THE GOLDFISH (CARASSIUS AURATUS). III. THREE-DIMENSIONAL STRUCTURE OF THE RUFFED CELL DENDRITE," *J. COMP. NEUROL.,* VOL. 201, P. 571–587, 10 1981.

[96] A. WILLS, "HEROPHILUS, ERASISTRATUS, AND THE BIRTH OF NEUROSCIENCE," *THE LANCET,* VOL. 354, P. 1719–1720, 1999.

[97] R. S. TUBBS, M. LOUKAS, M. M. SHOJA, M. M. MORTAZAVI AND A. A. COHEN-GADOL, "FÉLIX VICQ D'AZYR (1746-1794): EARLY FOUNDER OF NEUROANATOMY AND ROYAL FRENCH PHYSICIAN," *CHILD'S NERVOUS SYSTEM,* VOL. 27, P. 1031–1034, 2011.

[98] L. W. SWANSON AND J. W. LICHTMAN, "FROM CAJAL TO CONNECTOME AND BEYOND.," *ANNUAL REVIEW OF NEUROSCIENCE,* VOL. 39, PP. 197-216, 7 2016.

[99] E. D. P. DE ROBERTIS AND H. S. BENNETT, "SOME FEATURES OF THE SUBMICROSCOPIC MORPHOLOGY OF SYNAPSES IN FROG AND EARTHWORM," *J BIOPHYS AND BIOCHEM CYTOL,* VOL. 1, P. 47–58, 1 1955.

[100] M. JANUSZEWSKI, J. KORNFELD, P. H. LI, A. POPE, T. BLAKELY, L. LINDSEY, J. MAITIN-SHEPARD, M. TYKA, W. DENK AND V. JAIN, "HIGH-PRECISION AUTOMATED RECONSTRUCTION OF NEURONS WITH FLOOD-FILLING NETWORKS," *NATURE METHODS,* VOL. 15, P. 605–610, 8 2018.

[101] L. K. SCHEFFER, C. S. XU, M. JANUSZEWSKI, Z. LU, S.-Y. TAKEMURA, K. J. HAYWORTH, G. B. HUANG, K. SHINOMIYA, J. MAITLIN-SHEPARD, S. BERG, J. CLEMENTS, P. M. HUBBARD, W. T. KATZ, L. UMAYAM, T. ZHAO, D. ACKERMAN, T. BLAKELY, J. BOGOVIC, T. DOLAFI, D. KAINMUELLER, T. KAWASE, K. A. KHAIRY, L. LEAVITT, P. H. LI, L. LINDSEY, N. NEUBARTH, D. J. OLBRIS, H. OTSUNA, E. T. TRAUTMAN, M. ITO, A. S. BATES, J. GOLDAMMER, T. WOLFF, R. SVIRSKAS, P. SCHLEGEL, E. NEACE, C. J. KNECHT, C. X. ALVARADO, D. A. BAILEY, S. BALLINGER, J. A. BORYCZ, B. S. CANINO, N. CHEATHAM, M. COOK, M. DREHER, O. DUCLOS, B. EUBANKS, K. FAIRBANKS, S. FINLEY, N. FORKNALL, A. FRANCIS, G. P. HOPKINS, E. M. JOYCE, S. KIM, N. A. KIRK, J. KOVALYAK, S. A. LAUCHIE, A. LOHFF, C. MALDONADO, E. A. MANLEY, S. MCLIN, C. MOONEY, M. NDAMA, O. OGUNDEYI, N. OKEOMA, C. ORDISH, N. PADILLA, C. M. PATRICK, T. PATERSON, E. E. PHILLIPS, E. M. PHILLIPS, N. RAMPALLY, C. RIBEIRO, M. K. ROBERTSON, J. T. RYMER, S. M. RYAN, M. SAMMONS, A. K. SCOTT, A. L. SCOTT, A. SHINOMIYA, C. SMITH, K. SMITH, N. L. SMITH, M. A. SOBESKI, A. SULEIMAN, J. SWIFT, S. TAKEMURA, I. TALEBI, D. TARNOGORSKA, E. TENSHAW, T. TOKHI, J. J. WALSH, T. YANG, J. A. HORNE, F. LI, R. PAREKH, P. K. RIVLIN, V. JAYARAMAN, M. COSTA, G. S. X. E. JEFFERIS, K. ITO, S. SAALFELD, R. GEORGE, I. A. MEINERTZHAGEN, G. M. RUBIN, H. F. HESS, V. JAIN, S. M. PLAZA, E. MARDER, M. B. EISEN, J. PIPKIN AND C. Q. DOE, "A CONNECTOME AND ANALYSIS OF THE ADULT DROSOPHILA CENTRAL BRAIN," *ELIFE,* VOL. 9, P. E57443, 2020.

[102] C. S. XU, M. JANUSZEWSKI, Z. LU, S.-Y. TAKEMURA, K. J. HAYWORTH, G. HUANG, K. SHINOMIYA, J. MAITIN-SHEPARD, D. ACKERMAN, S. BERG, T. BLAKELY, J. BOGOVIC, J. CLEMENTS, T. DOLAFI, P. HUBBARD, D. KAINMUELLER, W. KATZ, T. KAWASE, K. A. KHAIRY, L. LEAVITT, P. H. LI, L. LINDSEY, N. NEUBARTH, D. J. OLBRIS, H. OTSUNA, E. T. TROUTMAN, L. UMAYAM, T. ZHAO, M. ITO, J. GOLDAMMER, T. WOLFF, R. SVIRSKAS, P. SCHLEGEL, E. R. NEACE, C. J. KNECHT, C. X. ALVARADO, D. A. BAILEY, S. BALLINGER, J. A. BORYCZ, B. S. CANINO, N. CHEATHAM, M. COOK, M. DREHER, O. DUCLOS, B. EUBANKS, K. FAIRBANKS, S. FINLEY, N. FORKNALL, A. FRANCIS, G. P. HOPKINS, E. M. JOYCE, S. KIM, N. A. KIRK, J. KOVALYAK, S. A. LAUCHIE, A. LOHFF, C. MALDONADO, E. A. MANLEY, S. MCLIN, C. MOONEY, M. NDAMA, O. OGUNDEYI, N. OKEOMA, C. ORDISH, N. PADILLA, C. PATRICK, T. PATERSON, E. E. PHILLIPS, E. M. PHILLIPS, N. RAMPALLY, C. RIBEIRO, M. K. ROBERTSON, J. T. RYMER, S. M. RYAN, M. SAMMONS, A. K. SCOTT, A. L. SCOTT, A. SHINOMIYA, C. SMITH, K. SMITH, N. L. SMITH, M. A. SOBESKI, A. SULEIMAN, J. SWIFT, S. TAKEMURA, I. TALEBI, D. TARNOGORSKA, E. TENSHAW, T. TOKHI, J. J. WALSH, T. YANG, J. A. HORNE, F. LI, R. PAREKH, P. K. RIVLIN, V. JAYARAMAN, K. ITO, S. SAALFELD, R. GEORGE, I. MEINERTZHAGEN, G. M. RUBIN, H. F. HESS, L. K. SCHEFFER, V. JAIN AND S. M. PLAZA, "A CONNECTOME OF THE ADULT DROSOPHILA CENTRAL BRAIN," *BIORXIV,* P. 2020.01.21.911859, 1 2020.

[103] J. KORNFELD, M. JANUSZEWSKI, P. SCHUBERT, V. JAIN, W. DENK AND M. S. FEE, "AN ANATOMICAL SUBSTRATE OF CREDIT ASSIGNMENT IN REINFORCEMENT LEARNING," *BIORXIV,* P. 2020.02.18.954354, 1 2020.

[104] C. MICRONS, J. A. BAE, M. BAPTISTE, A. L. BODOR, D. BRITTAIN, J. BUCHANAN, D. J. BUMBARGER, M. A. CASTRO, B. CELII, E. COBOS, F. COLLMAN, N. M. DA COSTA, S. DORKENWALD, L. ELABBADY, P. G. FAHEY, T. FLISS, E. FROUDARAKIS, J. GAGER, C. GAMLIN, A. HALAGERI, J. HEBDITCH, Z. JIA, C. JORDAN, D. KAPNER, N. KEMNITZ, S. KINN, S. KOOLMAN, K. KUEHNER, K. LEE, K. LI, R. LU, T. MACRINA, G. MAHALINGAM, S. MCREYNOLDS, E. MIRANDA, E. MITCHELL, S. S. MONDAL, M. MOORE, S. MU, T. MUHAMMAD, B. NEHORAN, O. OGEDENGBE, C. PAPADOPOULOS, S. PAPADOPOULOS, S. PATEL, X. PITKOW, S. POPOVYCH, A. RAMOS, R. C. REID, J. REIMER, C. M. SCHNEIDER-MIZELL, H. S. SEUNG, B. SILVERMAN, W. SILVERSMITH, A. STERLING, F. H. SINZ, C. L. SMITH, S. SUCKOW, M. TAKENO, Z. H. TAN, A. S. TOLIAS, R. TORRES, N. L. TURNER, E. Y. WALKER, T. WANG, G. WILLIAMS, S. WILLIAMS, K. WILLIE, R. WILLIE, W. WONG, J. WU, C. XU, R. YANG, D. YATSENKO, F. YE, W. YIN AND S.-C. YU, "FUNCTIONAL CONNECTOMICS SPANNING MULTIPLE AREAS OF MOUSE VISUAL CORTEX," *BIORXIV,* P. 2021.07.28.454025, 1 2021.

[105] A. SHAPSON-COE, M. JANUSZEWSKI, D. R. BERGER, A. POPE, Y. WU, T. BLAKELY, R. L. SCHALEK, P. H. LI, S. WANG, J. MAITIN-SHEPARD, N. KARLUPIA, S. DORKENWALD, E. SJOSTEDT, L. LEAVITT, D. LEE, L. BAILEY, A. FITZMAURICE, R. KAR, B. FIELD, H. WU, J. WAGNER-CARENA, D. ALEY, J. LAU, Z. LIN, D. WEI, H. PFISTER, A. PELEG, V. JAIN AND J. W. LICHTMAN, "A CONNECTOMIC STUDY OF A PETASCALE FRAGMENT OF HUMAN CEREBRAL CORTEX," *BIORXIV,* P. 2021.05.29.446289, 1 2021.

[106] L. F. ABBOTT, D. D. BOCK, E. M. CALLAWAY, W. DENK, C. DULAC, A. L. FAIRHALL, I. FIETE, K. M. HARRIS, M. HELMSTAEDTER, V. JAIN, N. KASTHURI, Y. LECUN, J. W. LICHTMAN, P. B. LITTLEWOOD, L. LUO, J. H. R. MAUNSELL, R. C. REID, B. R. ROSEN, G. M. RUBIN, T. J.

SEJNOWSKI, H. S. SEUNG, K. SVOBODA, D. W. TANK, D. TSAO AND D. C. VAN ESSEN, "THE MIND OF A MOUSE," *CELL,* VOL. 182, P. 1372–1376, 2020.

[107] B. TITZE AND C. GENOUD, "VOLUME SCANNING ELECTRON MICROSCOPY FOR IMAGING BIOLOGICAL ULTRASTRUCTURE," *BIOL. CELL,* VOL. 108, P. 307–323, 11 2016.

[108] M. BERNING, K. BOERGENS AND M. HELMSTAEDTER, "SEGEM: EFFICIENT IMAGE ANALYSIS FOR HIGH-RESOLUTION CONNECTOMICS," *NEURON,* VOL. 87, P. 1193–1206, 9 2015.

[109] N. L. TURNER, T. MACRINA, J. A. BAE, R. YANG, A. M. WILSON, C. SCHNEIDER-MIZELL, K. LEE, R. LU, J. WU, A. L. BODOR, A. A. BLECKERT, D. BRITTAIN, E. FROUDARAKIS, S. DORKENWALD, F. COLLMAN, N. KEMNITZ, D. IH, W. M. SILVERSMITH, J. ZUNG, A. ZLATESKI, I. TARTAVULL, S.-C. YU, S. POPOVYCH, S. MU, W. WONG, C. S. JORDAN, M. CASTRO, J. BUCHANAN, D. J. BUMBARGER, M. TAKENO, R. TORRES, G. MAHALINGAM, L. ELABBADY, Y. LI, E. COBOS, P. ZHOU, S. SUCKOW, L. BECKER, L. PANINSKI, F. POLLEUX, J. REIMER, A. S. TOLIAS, R. C. REID, N. MAÇARICO DA COSTA AND H. S. SEUNG, "MULTISCALE AND MULTIMODAL RECONSTRUCTION OF CORTICAL STRUCTURE AND FUNCTION," *BIORXIV,* P. 2020.10.14.338681, 1 2020.

[110] A. SHERIDAN, T. NGUYEN, D. DEB, W.-C. A. LEE, S. SAALFELD, S. TURAGA, U. MANOR AND J. FUNKE, "LOCAL SHAPE DESCRIPTORS FOR NEURON SEGMENTATION," *BIORXIV,* P. 2021.01.18.427039, 1 2021.

[111] D. R. BERGER, H. S. SEUNG AND J. W. LICHTMAN, "VAST (VOLUME ANNOTATION AND SEGMENTATION TOOL): EFFICIENT MANUAL AND SEMI-AUTOMATIC LABELING OF LARGE 3D IMAGE STACKS," *FRONTIERS IN NEURAL CIRCUITS,* VOL. 12, P. 88, 2018.

[112] S. DORKENWALD, C. MCKELLAR, T. MACRINA, N. KEMNITZ, K. LEE, R. LU, J. WU, S. POPOVYCH, E. MITCHELL, B. NEHORAN, Z. JIA, J. A. BAE, S. MU, D. IH, M. CASTRO, O. OGEDENGBE, A. HALAGERI, Z. ASHWOOD, J. ZUNG, D. BRITTAIN, F. COLLMAN, C. SCHNEIDER-MIZELL, C. JORDAN, W. SILVERSMITH, C. BAKER, D. DEUTSCH, L. ENCARNACION-RIVERA, S. KUMAR, A. BURKE, J. GAGER, J. HEBDITCH, S. KOOLMAN, M. MOORE, S. MOREJOHN, B. SILVERMAN, K. WILLIE, R. WILLIE, S.-C. YU, M. MURTHY AND H. S. SEUNG, "FLYWIRE: ONLINE COMMUNITY FOR WHOLE-BRAIN CONNECTOMICS," *BIORXIV,* P. 2020.08.30.274225, 1 2020.

[113] B. STAFFLER, M. BERNING, K. M. BOERGENS, A. GOUR, P. VAN DER SMAGT AND M. HELMSTAEDTER, "SYNEM: AUTOMATED SYNAPSE DETECTION FOR CONNECTOMICS," *BIORXIV,* 1 2017.

[114] S. DORKENWALD, P. J. SCHUBERT, M. F. KILLINGER, G. URBAN, S. MIKULA, F. SVARA AND J. KORNFELD, "AUTOMATED SYNAPTIC CONNECTIVITY INFERENCE FOR VOLUME ELECTRON MICROSCOPY," *NAT METH,* VOL. 14, P. 435–442, 4 2017.

[115] L. HEINRICH, J. FUNKE, C. PAPE, J. NUNEZ-IGLESIAS AND S. SAALFELD, "SYNAPTIC CLEFT SEGMENTATION IN NON-ISOTROPIC VOLUME ELECTRON MICROSCOPY OF THE COMPLETE DROSOPHILA BRAIN," IN *MEDICAL IMAGE COMPUTING AND COMPUTER ASSISTED INTERVENTION - MICCAI 2018*, CHAM, 2018.

[116] J. BUHMANN, A. SHERIDAN, C. MALIN-MAYOR, P. SCHLEGEL, S. GERHARD, T. KAZIMIERS, R. KRAUSE, T. M. NGUYEN, L. HEINRICH, W.-C. A. LEE, R. WILSON, S. SAALFELD, G. S. X. E. JEFFERIS, D. D. BOCK, S. C. TURAGA, M. COOK AND J. FUNKE, "AUTOMATIC DETECTION OF SYNAPTIC PARTNERS IN A WHOLE-BRAIN DROSOPHILA ELECTRON MICROSCOPY DATA SET," *NATURE METHODS,* VOL. 18, P. 771–774, 2021.

[117] T. KOSAKA AND K. HAMA, "RUFFED CELL: A NEW TYPE OF NEURON WITH A DISTINCTIVE INITIAL UNMYELINATED PORTION OF THE AXON IN THE OLFACTORY BULB OF THE GOLDFISH (CARASSIUS AURATUS). I. GOLGI IMPREGNATION AND SERIAL THIN SECTIONING STUDIES," *J. COMP. NEUROL.,* VOL. 186, P. 301–319, 8 1979.

[118] A. A. WANNER, C. GENOUD, T. MASUDI, L. SIKSOU AND R. W. FRIEDRICH, "DENSE EM-BASED RECONSTRUCTION OF THE INTERGLOMERULAR PROJECTOME IN THE ZEBRAFISH OLFACTORY BULB," *NAT NEUROSCI,* VOL. ADVANCE ONLINE PUBLICATION, P. –, 4 2016.

[119] S. GERHARD, N. R. MÖNIG, B. TITZE, A. A. WANNER, T. MASUDI, C. GENOUD, M. JANUSZEWSKI AND R. W. FRIEDRICH, "KEYFRAME-BASED IMAGE ALIGNMENT OF VOLUME ELECTRON MICROSCOPY DATA IMPROVES AUTOMATED SEGMENTATION," *(IN PREPARATION).*

[120] P. H. LI, L. F. LINDSEY, M. JANUSZEWSKI, Z. ZHENG, A. S. BATES, I. TAISZ, M. TYKA, M. NICHOLS, F. LI, E. PERLMAN, J. MAITIN-SHEPARD, T. BLAKELY, L. LEAVITT, G. S. X. E. JEFFERIS, D. BOCK AND V. JAIN, "AUTOMATED RECONSTRUCTION OF A SERIAL-SECTION EM <EM>DROSOPHILA</EM> BRAIN WITH FLOOD-FILLING NETWORKS AND LOCAL REALIGNMENT," *BIORXIV,* P. 605634, 1 2020.

[121] M. SATO, I. BITTER, M. A. BENDER, A. E. KAUFMAN AND M. NAKAJIMA, "TEASAR: TREE-STRUCTURE EXTRACTION ALGORITHM FOR ACCURATE AND ROBUST SKELETONS.," PP. 281-, 2000.

[122] J. YELNIK, G. PERCHERON, C. FRANÇOIS AND Y. BURNOD, "PRINCIPAL COMPONENT ANALYSIS: A SUITABLE METHOD FOR THE 3-DIMENSIONAL STUDY OF THE SHAPE, DIMENSIONS AND ORIENTATION OF DENDRITIC ARBORIZATIONS," *JOURNAL OF NEUROSCIENCE METHODS,* VOL. 9, NO. 2, PP. 115-125, 10 1983.

[123] H. F. JELINEK AND E. FERNANDEZ, "NEURONS AND FRACTALS: HOW RELIABLE AND USEFUL ARE CALCULATIONS OF FRACTAL DIMENSIONS?," *JOURNAL OF NEUROSCIENCE METHODS,* VOL. 81, P. 9–18, 6 1998.

[124] G. A. ASCOLI, L. ALONSO-NANCLARES, S. A. ANDERSON, G. BARRIONUEVO, R. BENAVIDES-PICCIONE, A. BURKHALTER, G. BUZSÁKI, B. CAULI, J. DEFELIPE, A. FAIRÉN, D. FELDMEYER, G. FISHELL, Y. FREGNAC, T. F. FREUND, D. GARDNER, E. P. GARDNER, J. H. GOLDBERG, M. HELMSTAEDTER, S. HESTRIN, F. KARUBE, Z. F. KISVÁRDAY, B. LAMBOLEZ, D. A. LEWIS, O. MARIN, H. MARKRAM, A. MUÑOZ, A. PACKER, C. C. H. PETERSEN, K. S. ROCKLAND, J. ROSSIER, B. RUDY, P. SOMOGYI, J. F. STAIGER, G. TAMAS, A. M. THOMSON, M. TOLEDO-RODRIGUEZ, Y. WANG AND D. C. W. &. R. YUSTE, "PETILLA TERMINOLOGY: NOMENCLATURE OF FEATURES OF GABAERGIC INTERNEURONS OF THE CEREBRAL CORTEX," *NAT REV NEUROSCI,* VOL. 9, P. 557–568, 7 2008.

[125] F. PEDREGOSA, G. VAROQUAUX, A. GRAMFORT, V. MICHEL, B. THIRION, O. GRISEL, M. BLONDEL, P. PRETTENHOFER, R. WEISS, V. DUBOURG, J. VANDERPLAS, A. PASSOS, D. COURNAPEAU, M. BRUCHER, M. PERROT AND É. DUCHESNAY, "SCIKIT-LEARN: MACHINE LEARNING IN PYTHON," *JOURNAL OF MACHINE LEARNING RESEARCH,* VOL. 12, PP. 2825-2830, 2011.

[126] L. MCINNES, J. HEALY AND S. ASTELS, "HDBSCAN: HIERARCHICAL DENSITY BASED CLUSTERING," *JOURNAL OF OPEN SOURCE SOFTWARE,* VOL. 2, P. 205, 2017.

[127] P. CIGNONI, M. CALLIERI, M. CORSINI, M. DELLEPIANE, F. GANOVELLI AND G. RANZUGLIA, "MESHLAB: AN OPEN-SOURCE MESH PROCESSING TOOL," IN *EUROGRAPHICS ITALIAN CHAPTER CONFERENCE*, 2008.

[128] N. R. MOENIG, *BRAINMAPS_API_FCN,* 2020.

[129] *PYTHON SOFTWARE FOUNDATION. PYTHON LANGUAGE REFERENCE, VERSION 3.8. AVAILABLE AT HTTP://WWW.PYTHON.ORG.*

[130] C. R. HARRIS, K. J. MILLMAN, S. J. VAN DER WALT, R. GOMMERS, P. VIRTANEN, D. COURNAPEAU, E. WIESER, J. TAYLOR, S. BERG, N. J. SMITH, R. KERN, M. PICUS, S. HOYER, M. H. VAN KERKWIJK, M. BRETT, A. HALDANE, J. FERNÁNDEZ DEL RÍO, M. WIEBE, P. PETERSON, P. GÉRARD-MARCHANT, K. SHEPPARD, T. REDDY, W. WECKESSER, H. ABBASI, C. GOHLKE AND T. E. OLIPHANT, "ARRAY PROGRAMMING WITH NUMPY," *NATURE,* VOL. 585, P. 357–362, 2020.

[131] W. MCKINNEY, "DATA STRUCTURES FOR STATISTICAL COMPUTING IN PYTHON," IN *PROCEEDINGS OF THE 9TH PYTHON IN SCIENCE CONFERENCE*, 2010.

[132] A. A. HAGBERG, D. A. SCHULT AND P. J. SWART, "EXPLORING NETWORK STRUCTURE, DYNAMICS, AND FUNCTION USING NETWORKX," IN *PROCEEDINGS OF THE 7TH PYTHON IN SCIENCE CONFERENCE*, PASADENA, 2008.

[133] S. BEHNEL, M. FAASSEN, I. B. ANDHOLGER JOUKL, S. SAPIN, M.-A. PARENT, O. GRISEL, K. BUCHCIK, F. WAGNER, E. KROYMANN, P. EVERITT, V. NG, R. KERN, A. PAKULAT, D. SANKEL, M. KASPERSKI, S. DA SILVA AND P. OBERNDÖRFER, *LXML 4.6.3,* PYPI, ED., 2021.

[134] J. D. HUNTER, "MATPLOTLIB: A 2D GRAPHICS ENVIRONMENT," *COMPUTING IN SCIENCE ENGINEERING,* VOL. 9, PP. 90-95, 2007.

[135] M. L. WASKOM, "SEABORN: STATISTICAL DATA VISUALIZATION," *JOURNAL OF OPEN SOURCE SOFTWARE,* VOL. 6, P. 3021, 2021.

[136] P. VIRTANEN, R. GOMMERS, T. E. OLIPHANT, M. HABERLAND, T. REDDY, D. COURNAPEAU, E. BUROVSKI, P. PETERSON, W. WECKESSER, J. BRIGHT, S. J. VAN DER WALT, M. BRETT, J. WILSON, K. J. MILLMAN, N. MAYOROV, A. R. J. NELSON, E. JONES, R. KERN, E. LARSON, C. J. CAREY, İ. POLAT, Y. FENG, E. W. MOORE, J. VANDERPLAS, D. LAXALDE, J. PERKTOLD, R. CIMRMAN, I. HENRIKSEN, E. A. QUINTERO, C. R. HARRIS, A. M. ARCHIBALD, A. H. RIBEIRO, F. PEDREGOSA, P. VAN MULBREGT AND S. 1. CONTRIBUTORS, "SCIPY 1.0: FUNDAMENTAL ALGORITHMS FOR SCIENTIFIC COMPUTING IN PYTHON," *NATURE METHODS,* VOL. 17, P. 261–272, 2020.

[137] K. REITZ, C. BENFIELD, I. CORDASCO, N. PREWITT AND S. M. LARSON, *REQUESTS.*

[138] L. MCINNES, J. HEALY AND J. MELVILLE, "UMAP: UNIFORM MANIFOLD APPROXIMATION AND PROJECTION FOR DIMENSION REDUCTION," 2020.

[139] R. VAN HATTEM, *NUMPY-STL 2.16.0,* GITHUB, ED., 2021.

[140] J. MAITIN-SHEPARD, *NEUROGLANCER,* GITHUB, ED., 2020.

[141] S. SAALFELD, A. CARDONA, V. HARTENSTEIN AND P. TOMANČÁK, "CATMAID: COLLABORATIVE ANNOTATION TOOLKIT FOR MASSIVE AMOUNTS OF IMAGE DATA," *BIOINFORMATICS,* VOL. 25, P. 1984–1986, 8 2009.

[142] M. HELMSTAEDTER, K. L. BRIGGMAN AND W. DENK, "HIGH-ACCURACY NEURITE RECONSTRUCTION FOR HIGH-THROUGHPUT NEUROANATOMY.," *NATURE NEUROSCIENCE,* VOL. 14, NO. 8, PP. 1081-8, 7 2011.

[143] K. M. BOERGENS, M. BERNING, T. BOCKLISCH, D. BRÄUNLEIN, F. DRAWITSCH, J. FROHNHOFEN, T. HEROLD, P. OTTO, N. RZEPKA, T. WERKMEISTER, D. WERNER, G. WIESE, H. WISSLER AND M. HELMSTAEDTER, "WEBKNOSSOS: EFFICIENT ONLINE 3D DATA ANNOTATION FOR CONNECTOMICS," *NATURE METHODS,* VOL. 14, P. 691–694, 2017.

[144] T. ZHAO, D. J. OLBRIS, Y. YU AND S. M. PLAZA, "NEUTU: SOFTWARE FOR COLLABORATIVE, LARGE-SCALE, SEGMENTATION-BASED CONNECTOME RECONSTRUCTION," *FRONTIERS IN NEURAL CIRCUITS,* VOL. 12, P. 101, 2018.

[145] W. T. KATZ AND S. M. PLAZA, "DVID: DISTRIBUTED VERSIONED IMAGE-ORIENTED DATASERVICE," *FRONTIERS IN NEURAL CIRCUITS,* VOL. 13, P. 5, 2019.

[146] N. R. MOENIG, *AGGLOMERATION-PROOFREADING,* GITHUB, ED., 2020.

[147] S. DORKENWALD, N. L. TURNER, T. MACRINA, K. LEE, R. LU, J. WU, A. L. BODOR, A. A. BLECKERT, D. BRITTAIN, N. KEMNITZ, W. M. SILVERSMITH, D. IH, J. ZUNG, A. ZLATESKI, I. TARTAVULL, S.-C. YU, S. POPOVYCH, W. WONG, M. CASTRO, C. S. JORDAN, A. M. WILSON, E. FROUDARAKIS, J. BUCHANAN, M. TAKENO, R. TORRES, G. MAHALINGAM, F. COLLMAN, C. SCHNEIDER-MIZELL, D. J. BUMBARGER, Y. LI, L. BECKER, S. SUCKOW, J. REIMER, A. S. TOLIAS, N. M. DA COSTA, R. C. REID AND H. S. SEUNG, "BINARY AND ANALOG VARIATION OF SYNAPSES BETWEEN CORTICAL PYRAMIDAL NEURONS," *BIORXIV,* P. 2019.12.29.890319, 1 2019.

[148] C. M. SCHNEIDER-MIZELL, A. L. BODOR, F. COLLMAN, D. BRITTAIN, A. A. BLECKERT, S. DORKENWALD, N. L. TURNER, T. MACRINA, K. LEE, R. LU, J. WU, J. ZHUANG, A. NANDI, B. HU, J. BUCHANAN, M. M. TAKENO, R. TORRES, G. MAHALINGAM, D. J. BUMBARGER, Y. LI, T. CHARTRAND, N. KEMNITZ, W. M. SILVERSMITH, D. IH, J. ZUNG, A. ZLATESKI, I. TARTAVULL, S. POPOVYCH, W. WONG, M. CASTRO, C. S. JORDAN, E. FROUDARAKIS, L. BECKER, S. SUCKOW, J. REIMER, A. S. TOLIAS, C. ANASTASSIOU, H. S. SEUNG, R. C. REID AND N. MAÇARICO DA COSTA, "CHANDELIER CELL ANATOMY AND FUNCTION REVEAL A VARIABLY DISTRIBUTED BUT COMMON SIGNAL," *BIORXIV,* P. 2020.03.31.018952, 1 2020.

[149] E. PCHITSKAYA AND I. BEZPROZVANNY, "DENDRITIC SPINES SHAPE ANALYSIS–CLASSIFICATION OR CLUSTERIZATION? PERSPECTIVE," *FRONTIERS IN SYNAPTIC NEUROSCIENCE,* VOL. 12, P. 31, 2020.

[150] R. AREVALO, J. R. ALONSO, J. LARA, J. G. BRINON AND J. AIJON, "RUFFED CELLS IN THE OLFACTORY BULB OF FRESHWATER TELEOSTS. II. A GOLGI/EM STUDY OF THE RUFF," *JOURNAL FUR HIRNFORSCHUNG,* VOL. 32, PP. 477-484, 1991.

[151] J. R. ALONSO, J. LARA, J. J. MIGUEL AND J. AIJON, "RUFFED CELLS IN THE OLFACTORYBULB OF FRESHWATER TELEOSTS.," *J. ANAT.,* VOL. 155, PP. 101-107, 1987.

[152] T. KOSAKA AND K. HAMA, "PRESENCE OF THE RUFFED CELL IN THE OLFACTORY BULB OF THE CATFISH, PARASILURUS ASOTUS, AND THE SEA EEL, CONGER MYRIASTER," *J. COMP. NEUROL.,* VOL. 193, P. 103–117, 1980.

[153] T. KOSAKA, "RUFFED CELL: A NEW TYPE OF NEURON WITH A DISTINCTIVE INITIAL UNMYELINATED PORTION OF THE AXON IN THE OLFACTORY BULB OF GOLDFISH(CARASSIUS AURATUS): II. FINE STRUCTURE OF THE RUFFED CELL," *J. COMP.NEUROL.,* VOL. 193, P. 119–145, 1980.

[154] A. HAYAR, S. KARNUP, M. T. SHIPLEY AND M. ENNIS, "OLFACTORY BULB GLOMERULI: EXTERNAL TUFTED CELLS INTRINSICALLY BURST AT THETA FREQUENCY AND ARE ENTRAINED BY PATTERNED OLFACTORY INPUT," *J. NEUROSCI.,* VOL. 24, P. 1190, 2 2004.

[155] R. W. FRIEDRICH AND S. I. KORSCHING, "CHEMOTOPIC, COMBINATORIAL, AND NONCOMBINATORIAL ODORANT REPRESENTATIONS IN THE OLFACTORY BULB REVEALED USING A VOLTAGE-SENSITIVE AXON TRACER," *THE JOURNAL OF NEUROSCIENCE,* VOL. 18, P. 9977–9988, 12 1998.

[156] A. J. PINCHING AND T. P. S. POWELL, "THE NEUROPIL OF THE GLOMERULI OF THE OLFACTORY BULB," *J. CELL SCI.,* VOL. 9, P. 347, 9 1971.

[157] S. ZEPPILLI, T. ACKELS, R. ATTEY, N. KLIMPERT, K. D. RITOLA, S. BOEING, A. CROMBACH, A. T. SCHAEFER AND A. FLEISCHMANN, "MOLECULAR CHARACTERIZATION OF PROJECTION NEURON SUBTYPES IN THE MOUSE OLFACTORY BULB," *BIORXIV,* P. 2020.11.30.405571, 1 2020.

[158] T. IMAI, "CONSTRUCTION OF FUNCTIONAL NEURONAL CIRCUITRY IN THE OLFACTORY BULB," *SEMINARS IN CELL & DEVELOPMENTAL BIOLOGY,* VOL. 35, P. 180–188, 11 2014.

[159] G. M. SHEPHERD, "SYNAPTIC ORGANIZATION OF THE MAMMALIAN OLFACTORY BULB," *PHYSIOLOGICAL REVIEWS,* VOL. 52, P. 864–917, 10 1972.

[160] Y. SATO, N. MIYASAKA AND Y. YOSHIHARA, "MUTUALLY EXCLUSIVE GLOMERULAR INNERVATION BY TWO DISTINCT TYPES OF OLFACTORY SENSORY NEURONS REVEALED IN TRANSGENIC ZEBRAFISH," *J. NEUROSCI.,* VOL. 25, P. 4889, 5 2005.

[161] H. BAIER AND S. KORSCHING, "OLFACTORY GLOMERULI IN THE ZEBRAFISH FORM AN INVARIANT PATTERN AND ARE IDENTIFIABLE ACROSS ANIMALS," *J. NEUROSCI.,* VOL. 14, P. 219, 1 1994.

[162] S. WAGNER, A. L. GRESSER, A. T. TORELLO AND C. DULAC, "A MULTIRECEPTOR GENETIC APPROACH UNCOVERS AN ORDERED INTEGRATION OF VNO SENSORY INPUTS IN THE ACCESSORY OLFACTORY BULB," *NEURON,* VOL. 50, P. 697–709, 2006.

[163] S. KIKUTA, M. FLETCHER, R. HOMMA, T. YAMASOBA AND S. NAGAYAMA, "ODORANT RESPONSE PROPERTIES OF INDIVIDUAL NEURONS IN AN OLFACTORY GLOMERULAR MODULE," *NEURON,* VOL. 77, P. 1122–1135, 3 2013.

[164] Y. CHEN, X. CHEN, B. BASERDEM, H. ZHAN, Y. LI, M. B. DAVIS, J. M. KEBSCHULL, A. M. ZADOR, A. A. KOULAKOV AND D. F. ALBEANU, "WIRING LOGIC OF THE EARLY RODENT OLFACTORY SYSTEM REVEALED BY HIGH-THROUGHPUT SEQUENCING OF SINGLE NEURON PROJECTIONS," *BIORXIV,* P. 2021.05.12.443929, 1 2021.

[165] F. CAVARRETTA, S. D. BURTON, K. M. IGARASHI, G. M. SHEPHERD, M. L. HINES AND M. MIGLIORE, "PARALLEL ODOR PROCESSING BY MITRAL AND MIDDLE TUFTED CELLS IN THE OLFACTORY BULB," *SCIENTIFIC REPORTS,* VOL. 8, P. 7625, 2018.

[166] J. CHAPUIS AND D. A. WILSON, "BIDIRECTIONAL PLASTICITY OF CORTICAL PATTERN RECOGNITION AND BEHAVIORAL SENSORY ACUITY," *NAT NEUROSCI,* VOL. 15, P. 155–161, 1 2012.

[167] K. A. BOLDING AND K. M. FRANKS, "COMPLEMENTARY CODES FOR ODOR IDENTITY AND INTENSITY IN OLFACTORY CORTEX," *ELIFE,* VOL. 6, P. E22630, 2017.

[168] A. BOLDING KEVIN AND M. FRANKS KEVIN, "RECURRENT CORTICAL CIRCUITS IMPLEMENT CONCENTRATION-INVARIANT ODOR CODING," *SCIENCE,* VOL. 361, P. EAAT6904, 9 2018.

[169] N. MIYASAKA, K. MORIMOTO, T. TSUBOKAWA, S.-I. HIGASHIJIMA, H. OKAMOTO AND Y. YOSHIHARA, "FROM THE OLFACTORY BULB TO HIGHER BRAIN CENTERS: GENETIC VISUALIZATION OF SECONDARY OLFACTORY PATHWAYS IN ZEBRAFISH," *THE JOURNAL OF NEUROSCIENCE,* VOL. 29, P. 4756–4767, 4 2009.

[170] N. MIYASAKA, I. ARGANDA-CARRERAS, N. WAKISAKA, M. MASUDA, U. SÜMBÜL, H. S. SEUNG AND Y. YOSHIHARA, "OLFACTORY PROJECTOME IN THE ZEBRAFISH FOREBRAIN REVEALED BY GENETIC SINGLE-NEURON LABELLING," *NAT COMMUN,* VOL. 5, P. –, 4 2014.

[171] J. G. EDWARDS, A. GREIG, Y. SAKATA, D. ELKIN AND W. C. MICHEL, "CHOLINERGIC INNERVATION OF THE ZEBRAFISH OLFACTORY BULB," *J. COMP. NEUROL.,* VOL. 504, P. 631–645, 10 2007.

[172] F. MACRIDES AND S. P. SCHNEIDER, "LAMINAR ORGANIZATION OF MITRAL AND TUFTED CELLS IN THE MAIN OLFACTORY BULB OF THE ADULT HAMSTER," *J. COMP. NEUROL.,* VOL. 208, P. 419–430, 7 1982.

[173] R. TATTI, K. BHAUKAURALLY, O. GSCHWEND, R. P. SEAL, R. H. EDWARDS, I. RODRIGUEZ AND A. CARLETON, "A POPULATION OF GLOMERULAR GLUTAMATERGIC NEURONS CONTROLS SENSORY INFORMATION TRANSFER IN THE MOUSE OLFACTORY BULB," *NATURE COMMUNICATIONS,* VOL. 5, P. 3791, 2014.

[174] W.-L. LIU AND M. T. SHIPLEY, "INTRABULBAR ASSOCIATIONAL SYSTEM IN THE RAT OLFACTORY BULB COMPRISES CHOLECYSTOKININ-CONTAINING TUFTED CELLS THAT SYNAPSE ONTO THE DENDRITES OF GABAERGIC GRANULE CELLS," *J. COMP. NEUROL.,* VOL. 346, P. 541–558, 8 1994.

[175] H. P. R. ZIPPEL AND V. C.AND KORFF, "SIMULTANEOUS RECORDINGS FROM TWO PHYSIOLOGICALLY DIFFERENT TYPES OF RELAY NEURONS, MITRAL CELLS AND RUFFED CELLS, IN THE OLFACTORY BULB OF GOLDFISH," *CELLULAR AND MOLECULAR BIOLOGY (NOISY-LE-GRAND),* VOL. 45(3), PP. 327-37, 1999.

[176] H. P. ZIPPEL, M. GLOGER, S. NASSER AND S. WILCKE, "ODOUR DISCRIMINATION IN THE OLFACTORY BULB OF GOLDFISH: CONTRASTING INTERACTIONS BETWEEN MITRAL CELLS AND RUFFED CELLS.," *PHILOSOPHICAL TRANSACTIONS OF THE ROYAL SOCIETY B: BIOLOGICAL SCIENCES,* VOL. 355, P. 1229–1232, 9 2000.

[177] B. JUDKEWITZ, "ANALYSIS OF FUNCTIONAL CONNECTIVITY IN THE ZEBRAFISH OLFACTORY BULB," 2005.

[178] S. M. K. GLASAUER, R. WÄGER, M. GESEMANN AND S. C. F. NEUHAUSS, "MGLUR6B:EGFP TRANSGENIC ZEBRAFISH SUGGEST NOVEL FUNCTIONS OF METABOTROPIC GLUTAMATE SIGNALING IN RETINA AND OTHER BRAIN REGIONS," *J. COMP. NEUROL.,* P. N/A–N/A, 4 2016.

[179] E. SYKOVÁ, "EXTRASYNAPTIC VOLUME TRANSMISSION AND DIFFUSION PARAMETERS OF THE EXTRACELLULAR SPACE," *NEUROSCIENCE,* VOL. 129, P. 861–876, 2004.

[180] Y. OKUBO, H. SEKIYA, S. NAMIKI, H. SAKAMOTO, S. IINUMA, M. YAMASAKI, M. WATANABE, K. HIROSE AND M. IINO, "IMAGING EXTRASYNAPTIC GLUTAMATE DYNAMICS IN THE BRAIN," *PROC NATL ACAD SCI USA,* VOL. 107, P. 6526, 4 2010.

[181] G. SZAPIRO AND B. BARBOUR, "MULTIPLE CLIMBING FIBERS SIGNAL TO MOLECULAR LAYER INTERNEURONS EXCLUSIVELY VIA GLUTAMATE SPILLOVER," *NATURE NEUROSCIENCE,* VOL. 10, P. 735–742, 2007.

[182] A. NOMURA, R. SHIGEMOTO, Y. NAKAMURA, N. OKAMOTO, N. MIZUNO AND S. NAKANISHI, "DEVELOPMENTALLY REGULATED POSTSYNAPTIC LOCALIZATION OF A METABOTROPIC GLUTAMATE RECEPTOR IN RAT ROD BIPOLAR CELLS.," *CELL,* VOL. 77, NO. 3, PP. 361-9, 5 1994.

[183] E. YAKSI AND R. W. FRIEDRICH, "RECONSTRUCTION OF FIRING RATE CHANGES ACROSS NEURONAL POPULATIONS BY TEMPORALLY DECONVOLVED CA2+ IMAGING," *NAT METH,* VOL. 3, P. 377–383, 5 2006.

[184] M. GERAMITA AND N. N. URBAN, "DIFFERENCES IN GLOMERULAR-LAYER-MEDIATED FEEDFORWARD INHIBITION ONTO MITRAL AND TUFTED CELLS LEAD TO DISTINCT MODES OF INTENSITY CODING," *J. NEUROSCI.,* VOL. 37, P. 1428, 2 2017.

[185] G. LIU, E. FROUDARAKIS, J. M. PATEL, M. Y. KOCHUKOV, B. PEKAREK, P. J. HUNT, M. PATEL, K. UNG, C.-H. FU, J. JO, H.-K. LEE, A. S. TOLIAS AND B. R. ARENKIEL, "TARGET SPECIFIC FUNCTIONS OF EPL INTERNEURONS IN OLFACTORY CIRCUITS," *NATURE COMMUNICATIONS,* VOL. 10, P. 3369, 2019.

[186] T. MATSUNO, E. KIYOKAGE AND K. TOIDA, "SYNAPTIC DISTRIBUTION OF INDIVIDUALLY LABELED MITRAL CELLS IN THE EXTERNAL PLEXIFORM LAYER OF THE MOUSE OLFACTORY BULB," *J. COMP. NEUROL.,* VOL. 525, P. 2611–2611, 8 2017.

[187] M. COLONNIER, "SYNAPTIC PATTERNS ON DIFFERENT CELL TYPES IN THE DIFFERENT LAMINAE OF THE CAT VISUAL CORTEX. AN ELECTRON MICROSCOPE STUDY," *BRAIN RESEARCH,* VOL. 9, P. 268–287, 1968.

[188] L. J. MARTIN, C. D. BLACKSTONE, R. L. HUGANIR AND D. L. PRICE, "CELLULAR LOCALIZATION OF A METABOTROPIC GLUTAMATE RECEPTOR IN RAT BRAIN," *NEURON,* VOL. 9, P. 259–270, 1992.

[189] A. REINER AND J. LEVITZ, "GLUTAMATERGIC SIGNALING IN THE CENTRAL NERVOUS SYSTEM: IONOTROPIC AND METABOTROPIC RECEPTORS IN CONCERT," *NEURON,* VOL. 98, P. 1080–1098, 2018.

[190] K. KOSAKA, Y. AIKA, K. TOIDA AND T. KOSAKA, "STRUCTURE OF INTRAGLOMERULAR DENDRITIC TUFTS OF MITRAL CELLS AND THEIR CONTACTS WITH OLFACTORY NERVE TERMINALS AND CALBINDIN-IMMUNOREACTIVE TYPE 2 PERIGLOMERULAR NEURONS," *J. COMP. NEUROL.,* VOL. 440, P. 219–235, 11 2001.

[191] A. BOYD, J. STURGILL, C. POO AND J. ISAACSON, "CORTICAL FEEDBACK CONTROL OF OLFACTORY BULB CIRCUITS," *NEURON,* VOL. 76, P. 1161–1174, 12 2012.

[192] L. HUANG, K. UNG, I. GARCIA, K. B. QUAST, K. CORDINER, P. SAGGAU AND B. R. ARENKIEL, "TASK LEARNING PROMOTES PLASTICITY OF INTERNEURON CONNECTIVITY MAPS IN THE OLFACTORY BULB," *J. NEUROSCI.,* VOL. 36, P. 8856, 8 2016.

[193] K. A. SAILOR, M. T. VALLEY, M. T. WIECHERT, H. RIECKE, G. J. SUN, W. ADAMS, J. C. DENNIS, S. SHARAFI, G.-L. MING, H. SONG AND P.-M. LLEDO, "PERSISTENT STRUCTURAL PLASTICITY OPTIMIZES SENSORY INFORMATION PROCESSING IN THE OLFACTORY BULB," *NEURON,* VOL. 91, P. 384–396, 7 2016.

[194] J. TØNNESEN, G. KATONA, B. RÓZSA AND U. V. NÄGERL, "SPINE NECK PLASTICITY REGULATES COMPARTMENTALIZATION OF SYNAPSES," *NATURE NEUROSCIENCE,* VOL. 17, P. 678–685, 2014.

[195] Y. HAYASHI AND A. K. MAJEWSKA, "DENDRITIC SPINE GEOMETRY: FUNCTIONAL IMPLICATION AND REGULATION," *NEURON,* VOL. 46, P. 529–532, 2005.

[196] A. HOLTMAAT AND K. SVOBODA, "EXPERIENCE-DEPENDENT STRUCTURAL SYNAPTIC PLASTICITY IN THE MAMMALIAN BRAIN," *NATURE REVIEWS NEUROSCIENCE,* VOL. 10, P. 647–658, 2009.

[197] K. P. BERRY AND E. NEDIVI, "SPINE DYNAMICS: ARE THEY ALL THE SAME?," *NEURON,* VOL. 96, P. 43–55, 9 2017.

[198] J. A. MACK-BUCHER, J. LI AND R. W. FRIEDRICH, "EARLY FUNCTIONAL DEVELOPMENT OF INTERNEURONS IN THE ZEBRAFISH OLFACTORY BULB," *EUROPEAN JOURNAL OF NEUROSCIENCE,* VOL. 25, P. 460–470, 2007.

[199] D. C. WILLHITE, K. T. NGUYEN, A. V. MASURKAR, C. A. GREER, G. M. SHEPHERD AND W. R. CHEN, "VIRAL TRACING IDENTIFIES DISTRIBUTED COLUMNAR ORGANIZATION IN THE OLFACTORY BULB," *PROC NATL ACAD SCI USA,* VOL. 103, P. 12592, 8 2006.

[200] H. A. ARNSON AND B. W. STROWBRIDGE, "SPATIAL STRUCTURE OF SYNCHRONIZED INHIBITION IN THE OLFACTORY BULB," *J. NEUROSCI.,* VOL. 37, P. 10468, 10 2017.

[201] T. B. WOOLF, G. M. SHEPHERD AND C. A. GREER, "SERIAL RECONSTRUCTIONS OF GRANULE CELL SPINES IN THE MAMMALIAN OLFACTORY BULB," *SYNAPSE,* VOL. 7, P. 181–192, 3 1991.

[202] J. S. ISAACSON AND B. W. STROWBRIDGE, "OLFACTORY RECIPROCAL SYNAPSES: DENDRITIC SIGNALING IN THE CNS," *NEURON,* VOL. 20, P. 749–761, 4 1998.

[203] V. EGGER AND N. N. URBAN, "DYNAMIC CONNECTIVITY IN THE MITRAL CELL-GRANULE CELL MICROCIRCUIT," *SEMINARS IN CELL & DEVELOPMENTAL BIOLOGY,* VOL. 17, P. 424–432, 8 2006.

[204] V. LAGE-RUPPRECHT, L. ZHOU, G. BIANCHINI, S. S. AGHVAMI, M. MUELLER, B. RÓZSA, M. SASSO?-POGNETTO, V. EGGER, N. UCHIDA AND G. L. WESTBROOK, "PRESYNAPTIC NMDARS COOPERATE WITH LOCAL SPIKES TOWARD GABA RELEASE FROM THE RECIPROCAL OLFACTORY BULB GRANULE CELL SPINE," *ELIFE,* VOL. 9, P. E63737, 2020.

[205] I. SEGEV AND W. RALL, "COMPUTATIONAL STUDY OF AN EXCITABLE DENDRITIC SPINE," *JOURNAL OF NEUROPHYSIOLOGY,* VOL. 60, P. 499–523, 8 1988.

[206] C. KOCH AND A. ZADOR, "THE FUNCTION OF DENDRITIC SPINES: DEVICES SUBSERVING BIOCHEMICAL RATHER THAN ELECTRICAL COMPARTMENTALIZATION," *J. NEUROSCI.,* VOL. 13, P. 413, 2 1993.

[207] T. B. WOOLF AND C. A. GREER, "LOCAL COMMUNICATION WITHIN DENDRITIC SPINES: MODELS OF SECOND MESSENGER DIFFUSION IN GRANULE CELL SPINES OF THE MAMMALIAN OLFACTORY BULB," *SYNAPSE,* VOL. 17, P. 247–267, 8 1994.

[208] I. FUKUNAGA, J. T. HERB, M. KOLLO, E. S. BOYDEN AND A. T. SCHAEFER, "INDEPENDENT CONTROL OF GAMMA AND THETA ACTIVITY BY DISTINCT INTERNEURON NETWORKS IN THE OLFACTORY BULB," *NATURE NEUROSCIENCE,* VOL. 17, P. 1208–1216, 2014.

[209] A. GRELAT, L. BENOIT, S. WAGNER, C. MOIGNEU, P.-M. LLEDO AND M. ALONSO, "ADULT-BORN NEURONS BOOST ODOR-REWARD ASSOCIATION," *PROC NATL ACAD SCI USA,* VOL. 115, P. 2514, 3 2018.

[210] H. KATO, M. CHU, J. ISAACSON AND T. KOMIYAMA, "DYNAMIC SENSORY REPRESENTATIONS IN THE OLFACTORY BULB: MODULATION BY WAKEFULNESS AND EXPERIENCE," *NEURON,* VOL. 76, P. 962–975, 12 2012.

[211] C. K. REYHER, J. LUBKE, W. J. LARSEN, G. M. HENDRIX, M. T. SHIPLEY AND H. G. BAUMGARTEN, "OLFACTORY BULB GRANULE CELL AGGREGATES: MORPHOLOGICAL EVIDENCE FOR INTERPERIKARYAL ELECTROTONIC COUPLING VIA GAP JUNCTIONS," *J. NEUROSCI.,* VOL. 11, P. 1485, 6 1991.

[212] V. EGGER AND T. KUNER, "OLFACTORY BULB GRANULE CELLS: SPECIALIZED TO LINK COACTIVE GLOMERULAR COLUMNS FOR PERCEPT GENERATION AND DISCRIMINATION OF ODORS," *CELL AND TISSUE RESEARCH,* VOL. 383, P. 495–506, 2021.

[213] H. ZENG AND J. R. SANES, "NEURONAL CELL-TYPE CLASSIFICATION: CHALLENGES, OPPORTUNITIES AND THE PATH FORWARD," *NATURE REVIEWS NEUROSCIENCE,* VOL. 18, P. 530–546, 2017.

[214] F. SCALA, D. KOBAK, M. BERNABUCCI, Y. BERNAERTS, C. R. CADWELL, J. R. CASTRO, L. HARTMANIS, X. JIANG, S. LATURNUS, E. MIRANDA, S. MULHERKAR, Z. H. TAN, Z. YAO, H. ZENG, R. SANDBERG, P. BERENS AND A. S. TOLIAS, "PHENOTYPIC VARIATION OF TRANSCRIPTOMIC CELL TYPES IN MOUSE MOTOR CORTEX," *NATURE,* VOL. 598, P. 144–150, 2021.

[215] B. R. LEE, A. BUDZILLO, K. HADLEY, J. A. MILLER, T. JARSKY, K. BAKER, D. HILL, L. KIM, R. MANN, L. NG, A. OLDRE, R. RAJANBABU, J. TRINH, S. VARGAS, T. BRAUN, R. A. DALLEY, N. W. GOUWENS, B. E. KALMBACH, T. K. KIM, K. A. SMITH, G. SOLER-LLAVINA, S. SORENSEN, B. TASIC, J. T. TING, E. LEIN, H. ZENG, G. J. MURPHY, J. BERG, S. B. NELSON, L. CHEN, S. B. NELSON AND C. J. MCBAIN, "SCALED, HIGH FIDELITY ELECTROPHYSIOLOGICAL, MORPHOLOGICAL, AND TRANSCRIPTOMIC CELL CHARACTERIZATION," *ELIFE,* VOL. 10, P. E65482, 2021.

[216] K. A. FULTON AND K. L. BRIGGMAN, "PERMEABILIZATION-FREE EN BLOC IMMUNOHISTOCHEMISTRY FOR CORRELATIVE MICROSCOPY," *ELIFE,* VOL. 10, P. E63392, 2021.

[217] P. DE BOER, J. P. HOOGENBOOM AND B. N. G. GIEPMANS, "CORRELATED LIGHT AND ELECTRON MICROSCOPY: ULTRASTRUCTURE LIGHTS UP!," *NATURE METHODS,* VOL. 12, P. 503–513, 2015.

[218] N. ECKSTEIN, A. S. BATES, M. DU, V. HARTENSTEIN, G. S. X. E. JEFFERIS AND J. FUNKE, "NEUROTRANSMITTER CLASSIFICATION FROM ELECTRON MICROSCOPY IMAGES AT SYNAPTIC SITES IN DROSOPHILA," *BIORXIV,* P. 2020.06.12.148775, 1 2020.

[219] E. JONAS AND K. KORDING, "AUTOMATIC DISCOVERY OF CELL TYPES AND MICROCIRCUITRY FROM NEURAL CONNECTOMICS," *ELIFE,* VOL. 4, P. E04250, 4 2015.

[220] H. S. SEUNG, "READING THE BOOK OF MEMORY: SPARSE SAMPLING VERSUS DENSE MAPPING OF CONNECTOMES," *NEURON,* VOL. 62, P. 17–29, 2009.

[221] J. S. KIM, M. J. GREENE, A. ZLATESKI, K. LEE, M. RICHARDSON, S. C. TURAGA, M. PURCARO, M. BALKAM, A. ROBINSON, B. F. BEHABADI, M. CAMPOS, W. DENK, H. S. SEUNG AND THE EYEWIRERS, "SPACE-TIME WIRING SPECIFICITY SUPPORTS DIRECTION SELECTIVITY IN THE RETINA," *NATURE,* VOL. 509, P. 331–336, 5 2014.

[222] S.-Y. TAKEMURA, Y. ASO, T. HIGE, A. WONG, Z. LU, C. S. XU, P. K. RIVLIN, H. F. HESS, T. ZHAO, T. PARAG, S. BERG, G. HUANG, W. KATZ, D. J. OLBRIS, S. PLAZA, L. UMAYAM, R. ANICETO, L.-A. CHANG, S. LAUCHIE, O. OGUNDEYI, C. ORDISH, A. SHINOMIYA, C. SIGMUND, S. TAKEMURA, J. TRAN, G. C. TURNER, G. M. RUBIN AND L. K. SCHEFFER, "A CONNECTOME OF A LEARNING AND MEMORY CENTER IN THE ADULT DROSOPHILA BRAIN," *ELIFE,* VOL. 6, P. E26975, 7 2017.

[223] A. LITWIN-KUMAR AND S. C. TURAGA, "CONSTRAINING COMPUTATIONAL MODELS USING ELECTRON MICROSCOPY WIRING DIAGRAMS," *CURRENT OPINION IN NEUROBIOLOGY,* VOL. 58, P. 94–100, 10 2019.

[224] T. A. BRANCHEK AND G. STREISINGER, "PHOTORECEPTOR DEVELOPMENT IN THE ZEBRAFISH," *SOC. NEUROSCI. ABSTR.,* 1980.

[225] G. STREISINGER, C. WALKER, N. DOWER, D. KNAUBER AND F. SINGER, "PRODUCTION OF CLONES OF HOMOZYGOUS DIPLOID ZEBRA FISH (BRACHYDANIO RERIO)," *NATURE,* VOL. 291, P. 293–296, 1981.

[226] V. C. FLEISCH AND S. C. F. NEUHAUSS, "VISUAL BEHAVIOR IN ZEBRAFISH," *ZEBRAFISH,* VOL. 3, P. 191–201, 6 2006.

[227] P. MIKLAVC AND T. VALENTINÄ?IÄ?, "CHEMOTOPY OF AMINO ACIDS ON THE OLFACTORY BULB PREDICTS OLFACTORY DISCRIMINATION CAPABILITIES OF ZEBRAFISH DANIO RERIO," *CHEMICAL SENSES,* VOL. 37, P. 65–75, 1 2012.

[228] K. P. MUELLER AND S. C. F. NEUHAUSS, "AUTOMATED VISUAL CHOICE DISCRIMINATION LEARNING IN ZEBRAFISH (DANIO RERIO)." *JOURNAL OF INTEGRATIVE NEUROSCIENCE,* VOL. 11, NO. 1, PP. 73-85, 3 2012.

[229] A. VALENTE, K.-H. HUANG, R. PORTUGUES AND F. ENGERT, "ONTOGENY OF CLASSICAL AND OPERANT LEARNING BEHAVIORS IN ZEBRAFISH," *LEARNING & MEMORY,* VOL. 19, P. 170–177, 4 2012.

[230] VARIOUS AUTHORS, ZEBRAFISH PROTOCOLS FOR NEUROBEHAVIORAL RESEARCH, VOL. 66, A. V. K. UND ADAM MICHAEL STEWART, ED., HUMANA PRESS (SPRINGER SCIENCE+BUSINESS MEDIA), 2012.

[231] O. R. BRAUBACH, H.-D. WOOD, S. GADBOIS, A. FINE AND R. P. CROLL, "OLFACTORY CONDITIONING IN THE ZEBRAFISH (DANIO RERIO)," *BEHAVIOURAL BRAIN RESEARCH,* VOL. 198, P. 190–198, 3 2009.

[232] K.-H. HUANG, P. RUPPRECHT, T. FRANK, K. KAWAKAMI, T. BOUWMEESTER AND R. W. FRIEDRICH, "A VIRTUAL REALITY SYSTEM TO ANALYZE NEURAL ACTIVITY AND BEHAVIOR IN ADULT ZEBRAFISH," *NATURE METHODS,* VOL. 17, P. 343–351, 2020.

[233] M. F. WULLIMANN AND T. MUELLER, "TELEOSTEAN AND MAMMALIAN FOREBRAINS CONTRASTED: EVIDENCE FROM GENES TO BEHAVIOR," *J. COMP. NEUROL.,* VOL. 475, P. 143–162, 7 2004.

[234] C. SATOU, "EXPERIENCE-DEPENDENT REPRESENTATION OF ODOR VALUE IN TELENCEPHALON [CONFERENCE PRESENTATION]," IN *ZEBRAFISH NEURAL CIRCUITS & BEHAVIOR, CSHL, NOVEMBER 2019*.

6. APPENDIX

Manual of the agglomeration proofreading tool

MANUAL OF THE AGGLOMERATION PROOFREADING TOOL

INSTRUCTIONS FOR US KEYBOARD

The goal is to reconstruct whole cells in a segmentation by correcting mistakes of the agglomeration. Agglomeration mistakes are either false segment splits or false mergers. False segmentation mergers cannot be fixed with this tool, their location should be stored to correct otherwise. Reconstruction starts with one segment, usually containing the soma. From there follow along one neurite and add falsely split segments and remove falsely merged segments.

1. MERGING FALSE SPLITS

Example:

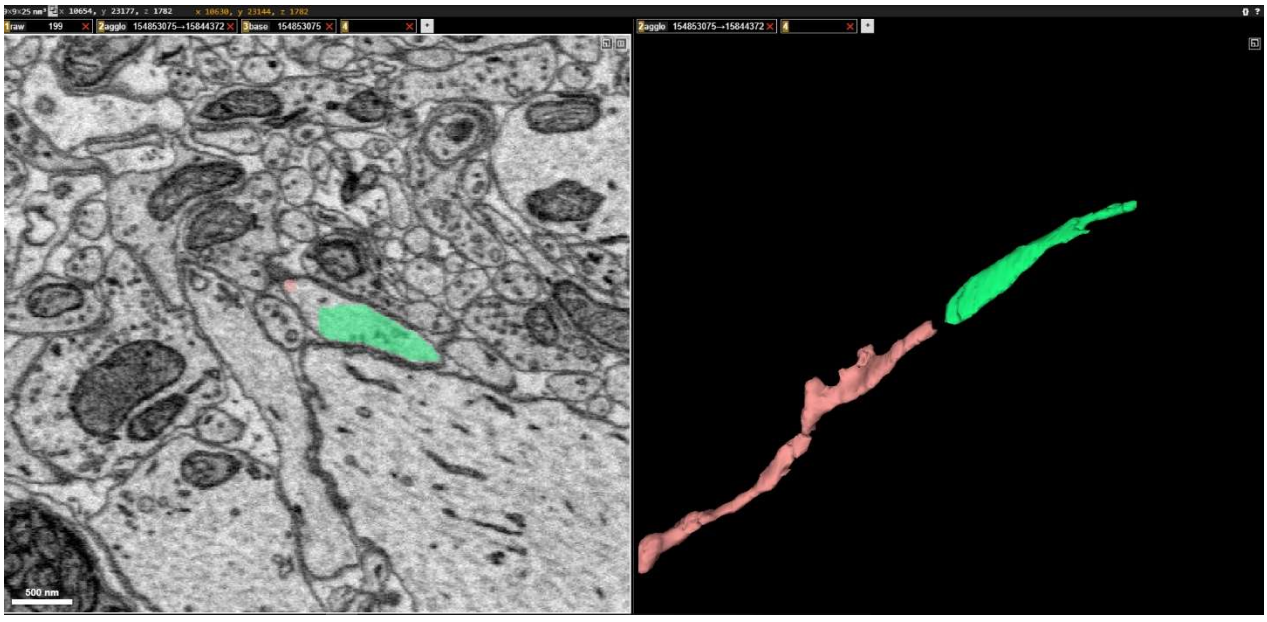

1. Move the cursor above the falsely split segment and press 'q', try to target a location close to the target branch!

2. Move the cursor above the target branch close to the falsely split segment and press 'd.'

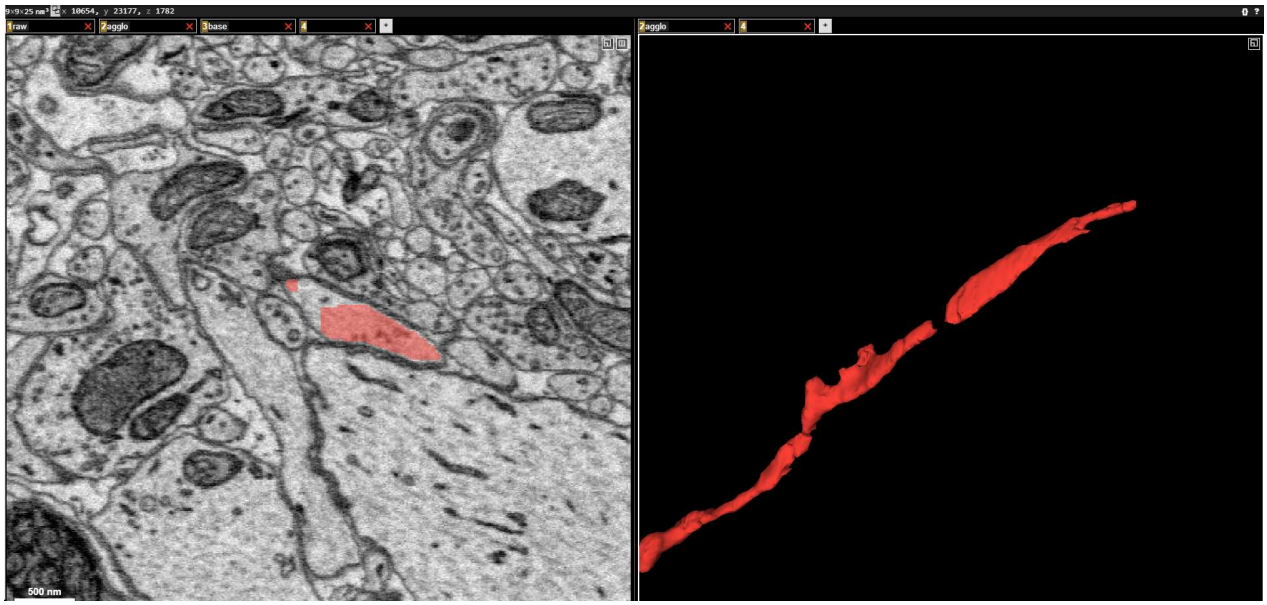

2. SPLITTING FALSE AGGLOMERATION MERGERS

Example:

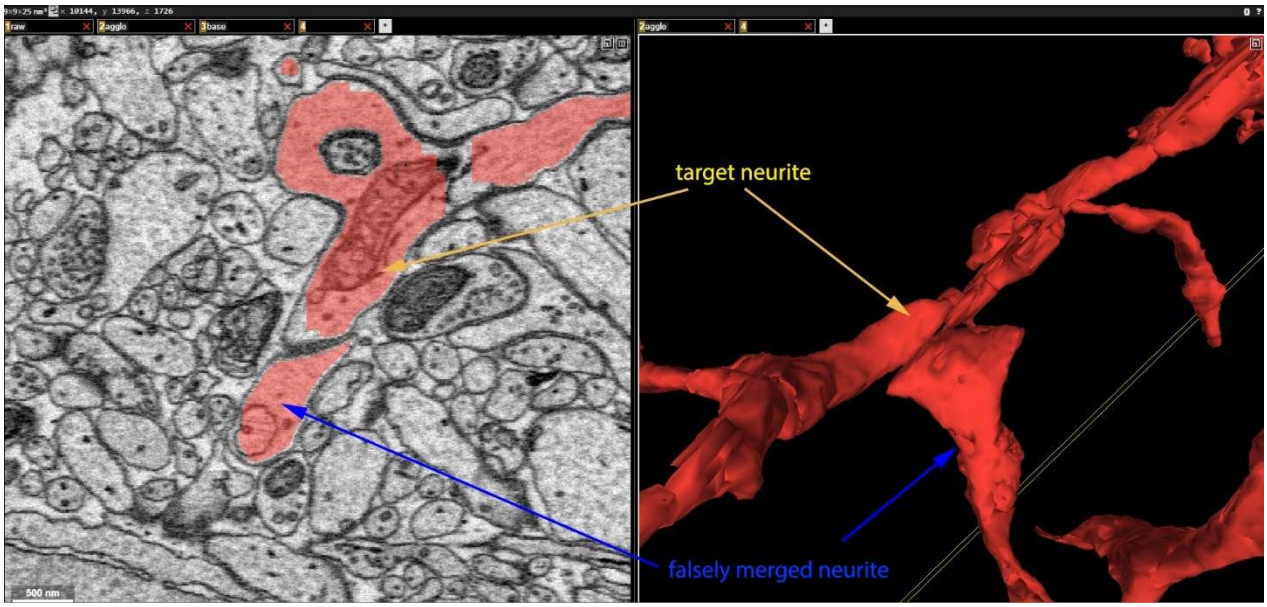

1. Move the cursor to one of the segments that is likely to be involved in the false merger and press 'c'. All segments connected to this segment are displayed. Playing with the opacity of the agglomeration layer 2 and the base volume layer 3 can help to determine the falsely merged segments.

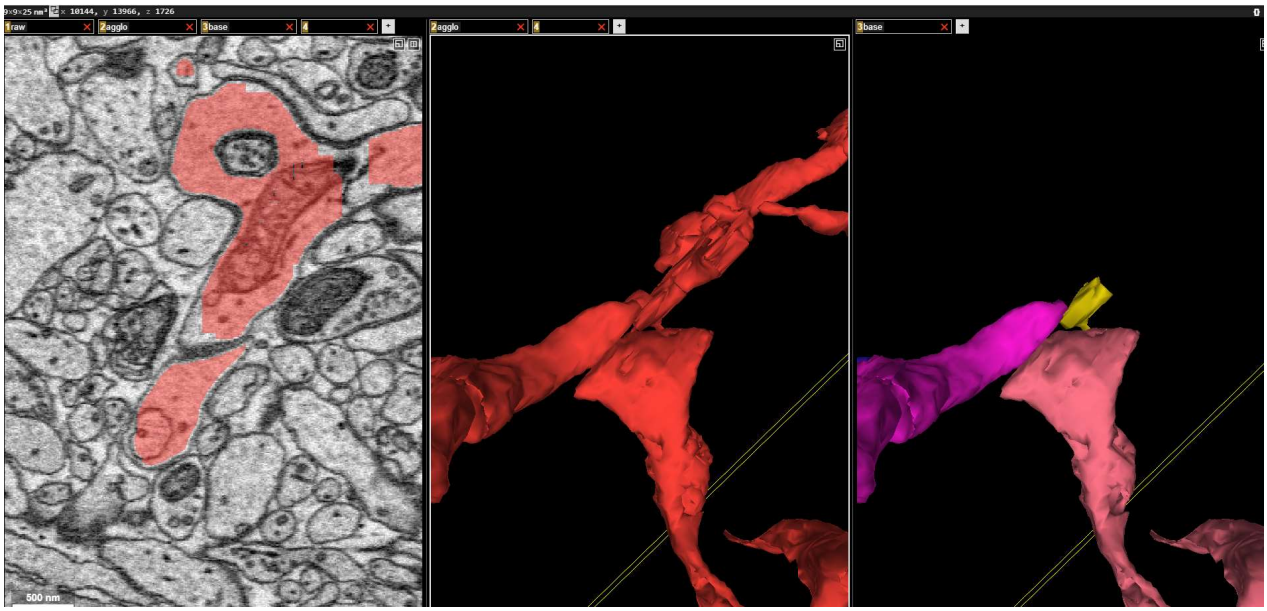

2. Find the wrongly merged pair:

- If the segment is not merged to one in the wrong branch, hover over the next segment in the base volume and press 'c' again.
- If a merged segment is found, move the cursor to this segment and split edges by pressing 'control + x'. The viewer will refresh.

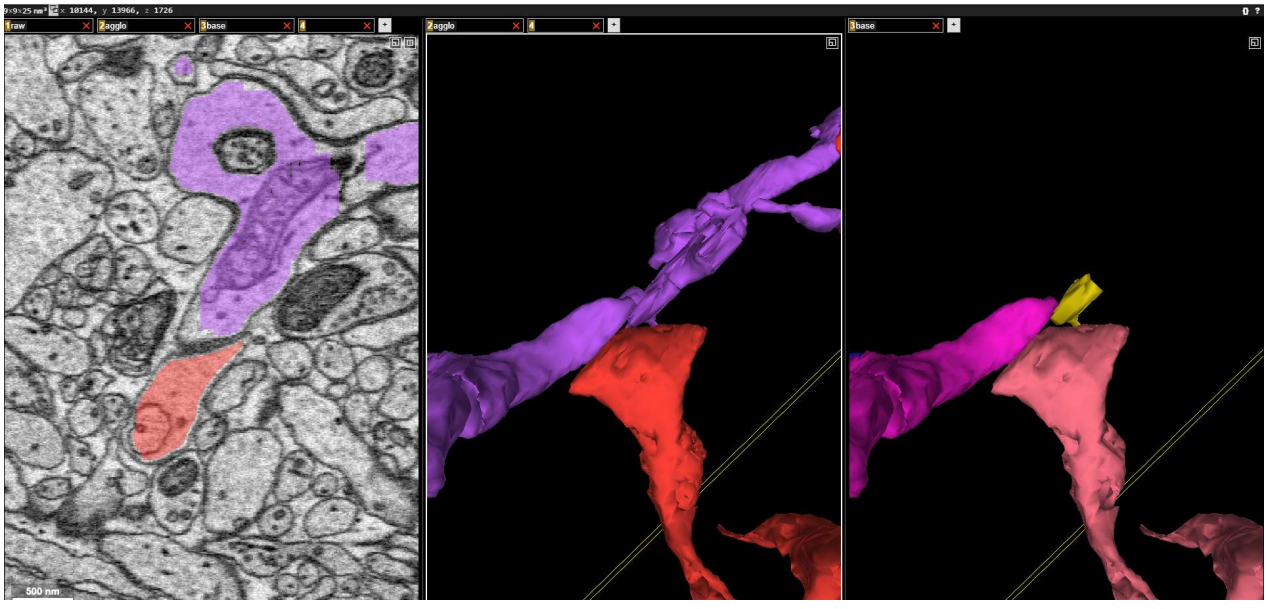

3. If the merged branches were split successfully, hover over the segment or branch that does not belong to the target neuron and confirm the split of the merger by pressing 'k'.

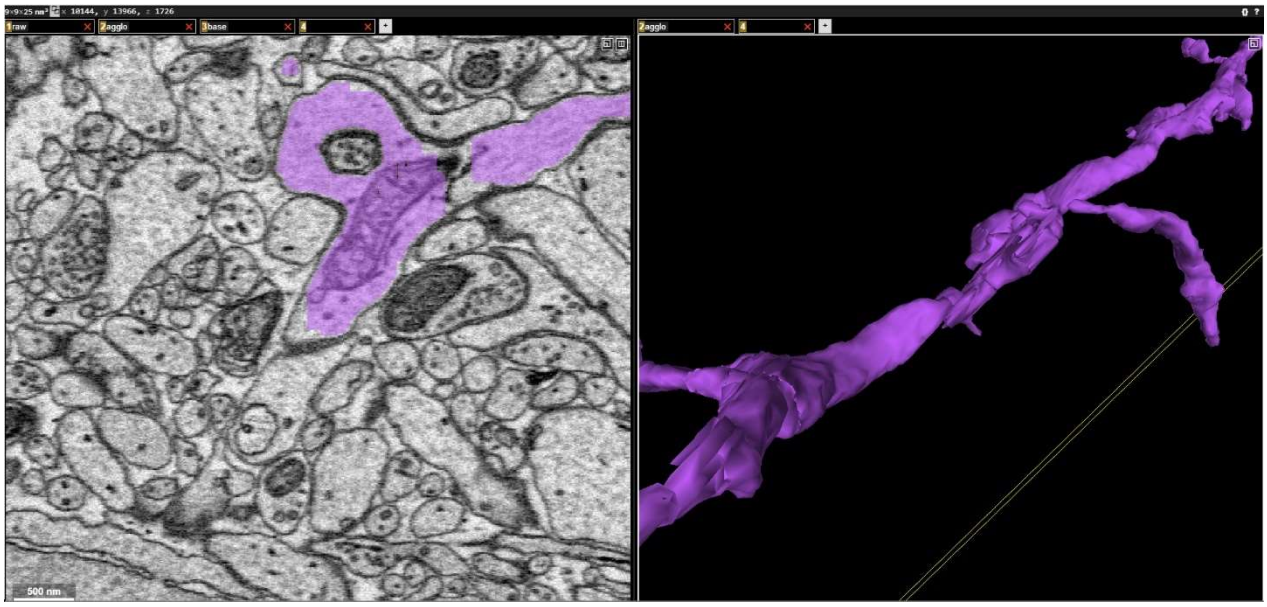

3. REMOVING GROUPS OF FALSELY MERGED SEGMENTS

This serves to remove larger groups of segments that should be split from the target branch. It does not preserve the connections of the segments to any other branch! This can be helpful to remove larger groups of segments covering membranes or extracellular space that are merged to the target neuron.

Example:

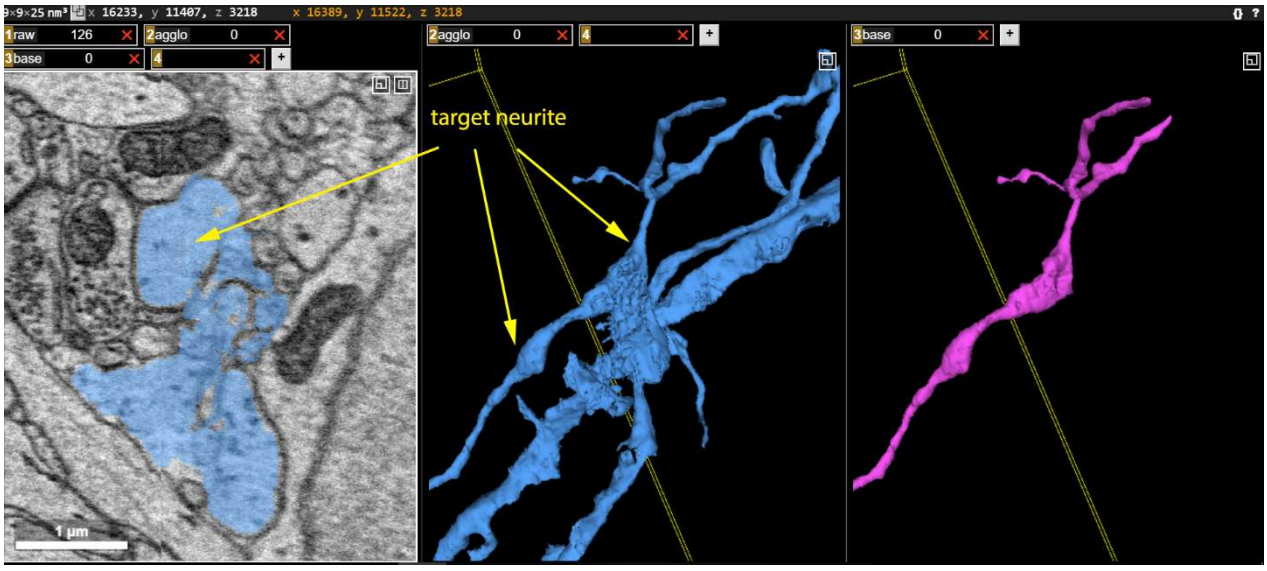

IMPORTANT: before using this, first make sure to empty the base volume viewport (press 'g').

1. Select any segment in the base volume that should be removed by hovering across the target segment and pressing t.

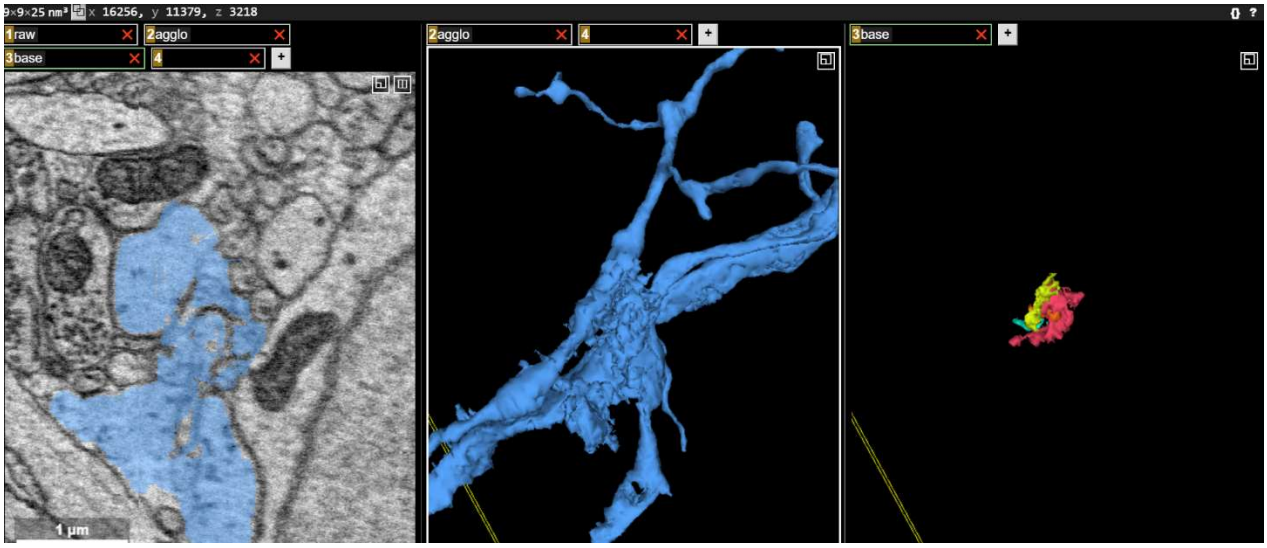

2. Press 'control+]' to split off the merged segments. The viewer updates and shows the segments in the neuron graph.

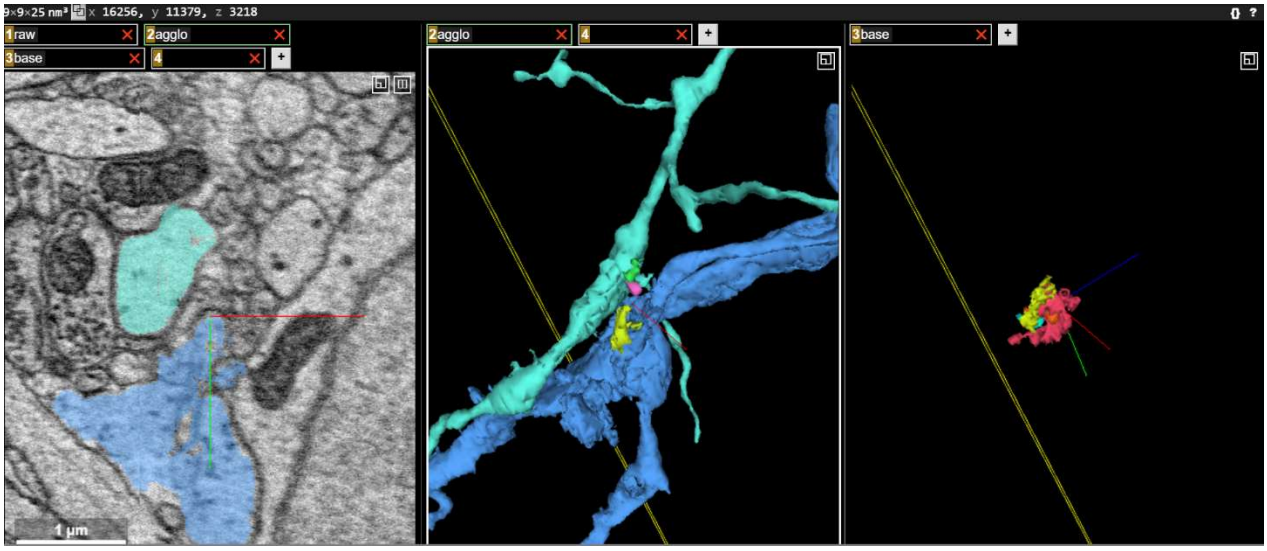

3. Segments that do not belong to the neuron that is reconstructed can be removed by moving the cursor to the segment and pressing 'shift+f'.

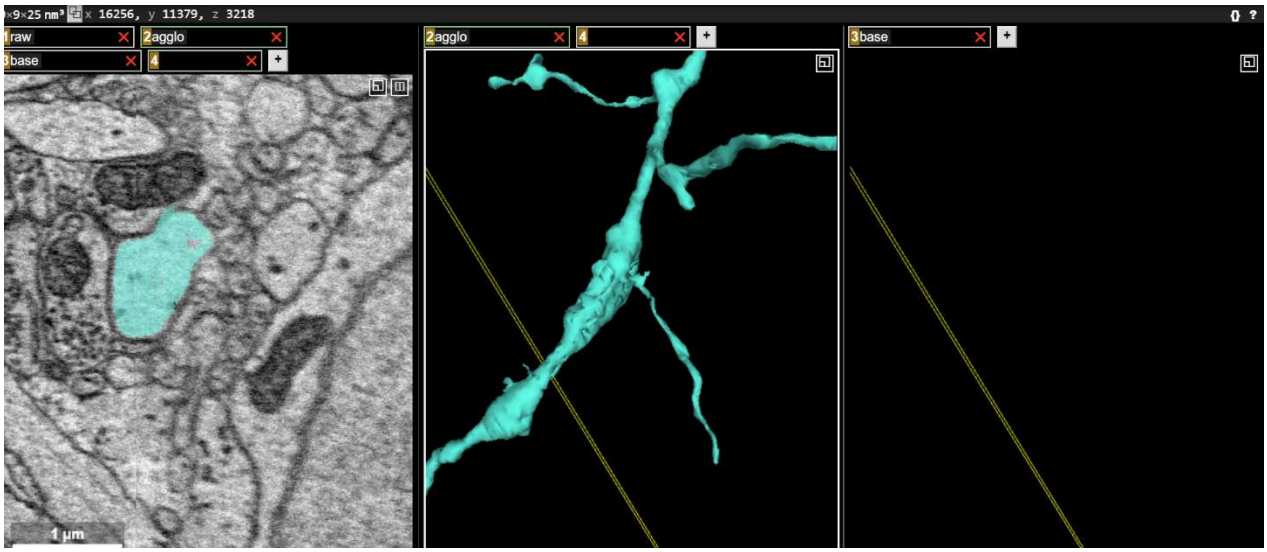

4. BRANCH POINTS

1. Set a branch point by moving the viewport location to the merge site (e.g. right click) and press 'y.'
2. Jump to the last unfinished branch location by pressing '7'.
3. Tag a branch point as visited by pressing 'control+r'. It will be annotated with an ellipsoid and the branch point will not be revisited when pressing '7'.
4. Remove a branch point annotation by hovering the cursor over the ellipsoid and press '0'.

5. TAGGING SEGMENTATION MERGER LOCATIONS

Move the viewport center to the merger site (e.g. right click) and press 'm'.